

UNIVERSITY OF OKLAHOMA  
GRADUATE COLLEGE

DEVELOPMENT OF NOVEL MATERIAL DESIGN STRATEGIES FOR HIGH-  
EFFICIENCY AND TUNABLE PHOTOLUMINESCENCE PROPERTIES

A DISSERTATION  
SUBMITTED TO THE GRADUATE FACULTY  
in partial fulfillment of the requirements for the  
Degree of  
DOCTOR OF PHILOSOPHY

By

TIELYR D. CREASON  
Norman, Oklahoma  
2022

DEVELOPMENT OF NOVEL MATERIAL DESIGN STRATEGIES FOR HIGH-  
EFFICIENCY AND TUNABLE PHOTOLUMINESCENCE PROPERTIES

A DISSERTATION APPROVED FOR THE  
DEPARTMENT OF CHEMISTRY AND BIOCHEMISTRY

BY THE COMMITTEE CONSISTING OF

Dr. Bayram Saparov, Chair

Dr. Daniel Glatzhofer

Dr. Yihan Shao

Dr. Ian Sellers

© Copyright by TIELYR D. CREASON 2022

All Rights Reserved

## Acknowledgments

First, I want to thank my advisor, Dr. Bayram Saparov, for his mentorship throughout this process. His passion for fundamental inorganic chemistry is infectious, spreading to the lab's students and visitors. He has always been enthusiastic about allowing me to explore new research directions for the lab. His support has allowed students to become more independent in their work as they investigate novel material classes. I would also like to thank Dr. Daniel Glatzhofer for his organic chemistry support and knowledge. Together, the two labs have learned from each other to develop better materials than either could have done alone.

Second, I would like to thank the larger Saparov Lab group, including the postdoctoral fellows, graduate students, and undergraduate students. The lab is an incredibly collaborative and caring team, helping not only in scientific matters but personal support as well. Specifically, I need to thank undergraduate students Timothy Mcwhorter and Isaiah Gilley for their years of assistance on projects. Without their contributions, I would not have been nearly as productive in developing novel materials and optimizing various synthetic methods.

Third, I would like to thank my fellow students and mentors at the University of Oklahoma for their knowledge and assistance with concepts and experiments. In particular, the Sellers group in physics has been a great help in completing various photoluminescence measurements and teaching me the theory along the way. In the laser lab, Dr. Vincent Whiteside took the time to educate me on the details of laser photoluminescence measurements and how to interpret the data. Dr. Douglas R. Powell of the Chemical Crystallography Lab has solved and assisted me in solving many novel crystal structures over the years. Collaborators outside of the University of Oklahoma have had major contributions to my work. Dr. Mao-Hua Du of Oak Ridge National Lab, completed

the majority of the DFT calculations that supported the experimental results.

Lastly, this work would not be possible without the unending support from my wife, daughter, siblings, and parents. There were never complaints about the long hours or additional hardships, only continued encouragement through it all. My wife Dana, in particular, deserves immense thanks for constantly pushing me forward and supporting me throughout the entire process.

## Abstract

New developments in the understanding of structural-optical property relationships of optoelectronic materials have led to rapid growth in energy-efficient solid-state lighting technologies. These improvements in the field of inorganic materials chemistry have led to new products, such as light-emitting diodes (LEDs) for residential lighting, scintillators for radiation detection, and luminescent inks for anti-counterfeiting applications. The emergence of lead halide perovskites has led to a paradigm shift in this area, with many groups around the globe working on both fundamental properties and practical applications of this diverse family. An unexplored alternative to the toxic nature of lead halides is the recently discovered families of earth-abundant and non-toxic copper(I) and silver halides. The structural-optical property relationships and physical properties of these new materials must be elucidated to continue development. This work focuses on understanding the optoelectronic properties of copper(I) and silver halides. The work also explores the strategy of utilizing organic cations as the source of emission, as opposed to more popular reliance on the metal halide polyhedra.

To better understand the history and fundamental science, the work begins with an introduction to down-converting metal halides in chapter 1. The information presented in the first chapter directly applies to the following chapter, as chapter 2 continues by investigating  $A_2CuX_3$  ( $A = K, Rb$  and  $X = Cl, Br$ ), a family of bright blue photoluminescent compounds with up to unity absolute photoluminescent quantum yield. A series of optical measurements were completed in order to thoroughly examine the effects of elemental substitution. The optical measurements were also supported with additional chemical purity and environmental stability test. The emission mechanism in these materials is established through a combination of spectroscopic and computational studies.

While the all-inorganic copper(I) halides answered some questions, many more were asked upon completion of the work. To further explore the impact of substituting the metal center, chapter 3 dives into the analogous silver halides in hopes of better understanding the varying emission mechanisms that can exist in these systems. These compounds display tunable, white emission, in stark contrast to their copper(I) counterparts. A broader elemental substitution study was conducted to understand the role of vacancies in the system. The work progressed beyond fundamental material design and continued into preliminary application research.

While extensive investigations of crystal and electronic structures and optical properties of all-inorganic group 11 metal halides have been conducted, a vast family of hybrid Cu(I) and Ag(I) materials remains unexplored. The last research component, chapter 4, changes directions away from metal-derived emission and explores the area of organic-derived emission. Although many organic compounds are known to be efficient light emitters, they are often unstable for practical application considerations. This work evaluates a novel method to stabilize and improve the photoluminescent emission while maintaining the same emission profile. The work opens the door to more hybrid organic-inorganic emitters. To tie everything together, chapter 5 concludes the work and discusses future directions.

# Table of Contents

<b>Chapter 1: Introduction .....</b>	<b>1</b>
1.1 Expanding Interest in Down-Converting Metal Halides .....	1
1.1.1 Historical Roots in Rare-earth Doped Oxides .....	2
1.1.2 Development of Metal Halide Perovskites .....	3
1.1.3 Emergence of Luminescent Copper(I) Halides.....	6
1.2 Historical overview of all-inorganic, ternary group 11 halides .....	9
1.3 Synthetic challenges of group 11 halides.....	14
1.3.1 Synthesis of Compounds Utilizing a Furnace.....	15
1.3.2 Solution Synthesis of Compounds .....	17
1.4 Origins of photoluminescence in metal halides .....	20
1.5 Applications of photoluminescence in metal halides.....	26
<b>Chapter 2: Development of Ternary Copper Halides for Ultrabright Blue Emission .....</b>	<b>31</b>
2.1 All-inorganic $\text{Rb}_2\text{CuCl}_3$ and $\text{Rb}_2\text{CuBr}_3$ for Blue Photoluminescence .....	31
2.1.1 Introduction.....	31
2.1.2 Experimental Synthesis and Methods for $\text{Rb}_2\text{CuX}_3$ .....	33
2.1.2.1 Reactants used in Rb.....	33
2.1.2.2 Synthesis of $\text{Rb}_2\text{CuBr}_3$ .....	33
2.1.2.3 Synthesis of $\text{Rb}_2\text{CuCl}_3$ .....	33
2.1.2.4 Powder X-ray Diffraction (PXRD) Measurements.....	34
2.1.2.5 Single crystal X-ray Diffraction (SXRD) Measurements.....	35
2.1.2.6 Thermogravimetry and Differential Scanning Calorimetry (TGA/DSC) Measurements.....	35
2.1.2.7 Optical Measurements.....	36
2.1.2.8 Computational Methods.....	37
2.1.3 Crystal Structure and Stability .....	39
2.1.4 Optical Properties of $\text{Rb}_2\text{CuX}_3$ .....	42
2.1.5 Band Structure and PDOS Calculations .....	46
2.1.6 Optical Cooling.....	49
2.1.7 Conclusions.....	50
2.2 All-inorganic $\text{K}_2\text{CuCl}_3$ and $\text{K}_2\text{CuBr}_3$ for Blue Emission and Dramatically Improved Stability .....	51
2.2.1 Introduction.....	51
2.2.2 Experimental Synthesis and Methods for $\text{K}_2\text{CuX}_3$ .....	53
2.2.2.1 Materials and Methods.....	53
2.2.2.2 Polycrystalline Powders of $\text{K}_2\text{CuX}_3$ .....	53
2.2.2.3 Flux growth of $\text{K}_2\text{CuCl}_3$ Single Crystals .....	53
2.2.2.4 $\text{K}_2\text{CuCl}_3$ Single Crystals via Slow Cooling of a Saturated Solution .....	54
2.2.2.5 Liquid-Liquid Diffusion Growth of $\text{K}_2\text{CuBr}_3$ Single Crystals .....	54



2.2.2.6 Vapor-Liquid Diffusion Growth of $K_2CuBr_3$ Single Crystals .....	54
2.2.2.7 Powder X-ray Diffraction (PXRD) Measurements.....	55
2.2.2.8 Single Crystal X-ray Diffraction (SCXRD).....	55
2.2.2.9 Thermogravimetry and Differential Scanning Calorimetry (TGA/DSC) Measurements .....	56
2.2.2.10 Optical Measurements .....	56
2.2.2.11 Computational Methods.....	57
2.2.3 Crystal Structure and Stability of $K_2CuX_3$ .....	59
2.2.4 Optical Properties of $K_2CuX_3$ .....	64
2.2.5 Radioluminescent Properties .....	66
2.2.6 Electronic Structure and Band Calculations .....	69
2.2.7 Conclusions.....	71
<b>Chapter 3: Tuning of White Light Emission via Silver Halides.....</b>	<b>73</b>
3.1 All-inorganic $A_2AgX_3$ (A=Rb, Cs; X=Cl,Br,I) for Tunable White Light Photoluminescence and Anti-counterfeiting Applications .....	73
3.1.1 Introduction.....	73
3.1.2 Experimental Synthesis and Methods for $A_2AgX_3$ .....	76
3.1.2.1 Materials .....	76
3.1.2.2 $Rb_2AgX_3$ (X = Cl, Br, I) Synthesis .....	76
3.1.2.3 $Cs_2AgX_3$ (X = Br, I) Synthesis .....	76
3.1.2.4 Ink preparation .....	77
3.1.2.5 Powder X-ray Diffraction (PXRD).....	77
3.1.2.6 Thermogravimetry and Differential Scanning Calorimetry (TGA/DSC).....	77
3.1.2.7 Optical Measurements .....	78
3.1.2.8 Microscopy .....	78
3.1.2.8 Computational Methods.....	79
3.1.3 Crystal Structure and Stability of the $A_2AgX_3$ Family .....	79
3.1.4 Optical Properties of $A_2AgX_3$ .....	82
3.1.5 Exciton Calculations and Emission Mechanism.....	87
3.1.6 Anti-counterfeiting Inks.....	93
3.1.7 Conclusion .....	97
3.2 $(NH_4)_2AgBr_3$ and $(NH_4)_2AgI_3$ with Halide Atmosphere Tunable Emission.....	97
3.2.1 Introduction.....	97
3.2.2 Synthesis and Characterization Methods.....	100
3.2.2.1 Materials and Methods.....	100
3.2.2.2 $(NH_4)_2AgX_3$ Single Crystals via Slow Cooling of a Saturated Solution .....	100
3.2.2.3 Powder X-ray Diffraction (PXRD) Measurements.....	100
3.2.2.4 Single Crystal X-ray Diffraction (SCXRD).....	101
3.2.2.5 Microscopy. ....	101
3.2.2.6 Thermogravimetry and Differential Scanning Calorimetry (TGA/DSC) Measurements .....	102
3.2.2.7 Optical Measurements .....	102
3.2.2.8 Computational Methods.....	102
3.2.3 Crystal Structure and Stability .....	103
3.2.4 Optical Properties.....	106

3.2.5 Electronic Band Structure .....	111
3.2.6 Conclusions.....	113
<b>Chapter 4: Design Novel Emitters Using Organic Emitters .....</b>	<b>114</b>
4.1 Hybrid Organic-Inorganic Indium Bromide with Organic Derived Bright Blue Emission .....	114
4.1.1 Introduction.....	114
4.1.2 Methods.....	116
4.1.2.1 Synthesis of RBr .....	116
4.1.2.2 Synthesis of RInBr <sub>4</sub> .....	117
4.1.2.3 Single Crystal X-Ray Diffraction (SXRD) Measurements.....	117
4.1.2.4 Powder X-ray Diffraction (PXRD) Measurements.....	118
4.1.2.5 Thermal Property Measurements .....	118
4.1.2.6 Optical Property Measurements.....	119
4.1.2.7 Computational Work.....	120
4.1.3 Crystal Structure .....	121
4.1.4 Optical Properties.....	124
4.1.5 Stability Measurements.....	129
4.1.6 Electronic Band Structure .....	132
4.1.7 Conclusions.....	134
<b>Chapter 5: Conclusion and Future Work.....</b>	<b>136</b>
5.1 Summary of Work Presented .....	136
5.2 Future Work .....	140
<b>References .....</b>	<b>142</b>
<b>Appendix: Supplemental Figures and Tables .....</b>	<b>156</b>
A1.1 Chapter 2 Figures and Tables.....	156
A1.2 Chapter 3 Figures and Tables.....	176
A1.3 Chapter 4 Figures and Tables.....	205

## Table of Tables

<b>Table 1.</b> Selected single-crystal data and structure refinement parameters for $\text{Rb}_2\text{CuCl}_3$ .....	41
<b>Table 2.</b> Selected single crystal data and structure refinement parameters for $\text{K}_2\text{CuX}_3$ .....	62
<b>Table 3.</b> A comparison of the photophysical properties of high efficiency blue emitters based on all-inorganic copper halides <sup>92, 111, 113, 117</sup> .....	65
<b>Table 4.</b> Calculated STE excitation and emission energies. ....	88
<b>Table 5.</b> Calculated emission energies from vacancies and STE. The energy of the lowest-energy exciton localized on the halogen/rubidium vacancy site is set to zero. ....	92
<b>Table 6.</b> A comparison of the photophysical properties of ternary $\text{A}_2\text{MX}_3$ ( $\text{A} = \text{K}, \text{Rb}, \text{Cs}; \text{M} = \text{Cu}, \text{Ag}; \text{X} = \text{Cl}, \text{Br}, \text{I}$ ) <sup>43, 117, 136, 154</sup> .....	109
<b>Table 7.</b> Single crystal data and structure refinement parameters for $\text{RInBr}_4$ .....	121
<b>Table 8.</b> A comparison of the photophysical properties of blue emitting hybrid organic-inorganic halides. <sup>3,18,40,54-59</sup> .....	131

## Table of Figures

- Figure 1.** The optical images of an isolated (a) ZJU-28 $\supset$ CsPbCl<sub>2</sub>Br, (b) ZJU-28 $\supset$ CsPbCl<sub>1.5</sub>Br<sub>1.5</sub>, (c) ZJU-28 $\supset$ CsPbClBr<sub>2</sub>, (d) ZJU-28 $\supset$ CsPbBr<sub>3</sub>, (e) ZJU-28 $\supset$ CsPbBr<sub>2</sub>I, (f) ZJU-28 $\supset$ CsPbBr<sub>1.5</sub>I<sub>1.5</sub> and (g) ZJU-28 $\supset$ CsPbBrI<sub>2</sub> microcrystals under excitation of 365 nm (for a–d) or 480 nm (for e–g). Scale bar, 50  $\mu$ m. (h) PL spectra of the ZJU-28 $\supset$ CsPbX<sub>3</sub> crystals. Reprinted with permission from reference 13. Copyright 2022 Royal Society of Chemistry.<sup>13</sup> ..... 4
- Figure 2.** Distribution of lead production worldwide in 2017 (open data from British Geological Survey). The inset shows the photo of mint plants grown in perovskite-contaminated soil within the campus of Fujian Agriculture and Forestry University, China (latitude 26.084, longitude 119.238). **b** The picture of mint plants grown on control soil (left) and **c** 250 mg kg<sup>-1</sup> Pb<sup>2+</sup> perovskite-contaminated soil (right). The range of lead content measured in the leaves, stem, and root is reported on the side of each picture. Reprinted with permission from reference 17. Copyright 2020 Nature.<sup>17</sup> ..... 6
- Figure 3.** a) Photograph of Cs<sub>3</sub>Cu<sub>2</sub>I<sub>5</sub>, a yellow phosphor, and its mixtures (from left to right: Cs<sub>3</sub>Cu<sub>2</sub>I<sub>5</sub>, mixture of 2:8, yellow phosphor) under UV illumination (top) and films prepared by kneading the powders into polydimethylsiloxane matrix (bottom). **b**) PL spectrum of the mixture of Cs<sub>3</sub>Cu<sub>2</sub>I<sub>5</sub> and yellow phosphor (mixing ratio = 2:8), **c**) CIE coordination of PL from the powder mixture, and **d**) current-density–luminance–voltage characteristic of the blue LED using a Cs<sub>3</sub>Cu<sub>2</sub>I<sub>5</sub> thin film as an emission layer, and (inset) its photo. Reprinted with permission from reference 23. Copyright 2018 Wiley.<sup>23</sup> ..... 8

**Figure 4.** Comparison of the crystal structures of the A-M-X (A = K, Rb, Cs, NH<sub>4</sub>, M = Cu(I), Ag, and X = Cl, Br, I) families. The left column displays a full structure, the middle column displays just the metal-halide polyhedra connectivity, and the right column describes the essential details of each family. A, M, and X are shown as orange, blue, and pink spheres, respectively. .... 11

**Figure 5.** (a-c) PXRD refined lattice parameters, and (d) unit cell volume shown as a function of halide content as alloying progresses from CsCu<sub>2</sub>Cl<sub>3</sub> (Cl) to CsCu<sub>2</sub>Br<sub>3</sub> (Br) to CsCu<sub>2</sub>I<sub>3</sub> (I). Reprinted with permission from reference 32. Copyright 2019 American Chemical Society.<sup>32</sup> ..... 13

**Figure 6.** Phase diagram for the RbBr–CuBr. Reprinted with permission from reference 34. Copyright 2001 Springer.<sup>34</sup> ..... 15

**Figure 7.** Salting-in intensity of a salt, dm<sup>1</sup>/dm<sup>2</sup>, vs. the concentration m of a component being added for the crystallization branches of (a) CuCl and (b) MCl. Reprinted with permission from reference 42. Copyright 2004 Springer Nature.<sup>42</sup> ..... 18

**Figure 8.** Diagram for diffusion crystal growth methods..... 19

**Figure 9.** Exciton levels for a simple band structure at  $k = 0$ . Reprinted with permission from reference 46. Copyright 2016 Springer Nature.<sup>46</sup> ..... 21

**Figure 10.** Schematic illustration of a tightly-bound exciton (Frenkel exciton) localized on one atom in a crystal. Reprinted with permission from reference 46. Copyright 2016 Springer Nature.<sup>46</sup> ..... 22

**Figure 11.** Schematic illustration of a weakly bound exciton (Mott-Wannier exciton) delocalized over several atoms in the crystal. Reprinted with permission from reference 46. Copyright 2016 Springer Nature.<sup>46</sup> ..... 22

**Figure 12.** (a) Schematic of various intrinsic photoluminescence phenomena, including band-to-band luminescence, exciton luminescence, STE luminescence, and cross luminescence. (b) Schematic of the energy level structure of STE (GS, ground state; FE, free exciton state; FC, free carrier state; STE, self-trapped exciton state;  $E_g$ , bandgap energy;  $E_b$ , exciton binding energy;  $E_{st}$ , self-trapping energy;  $E_d$ , lattice deformation energy;  $E_{PL}$ , emission energy). (c) Schematic of the nonradiative recombination process for STE when  $S$  is large. Orange circles represent excited electrons. Reprinted with permission from references 48. Copyright 2016 American Chemical Society.<sup>48</sup> ..... 23

**Figure 13.** Schematic depiction of pcWLEDs based on a NUV-LED and a mixture of RGB phosphors, and c a blue LED combined with a yellow phosphor, and their corresponding emission spectra in (b) and (d). Reprinted with permission from references 54 and 55. Copyright 2016 Springer Nature.<sup>54, 55</sup> ..... 27

**Figure 14.** Color gamut produced by an InGaN LED (circle),  $K_2SiF_6:Mn^{4+}$  (square), and  $RbLi(Li_3SiO_4)_2:Eu^{2+}$  (diamond), indicated by the gray dashed line, having an overlap area of 76% with the Rec. 2020 standard color gamut (white) when plotted on the 1931 CIE XYZ color space. The overlap area can be improved to 85% by using an InGaN LED,  $K_2GeF_6:Mn^{4+}$  (up-triangle), and  $\gamma-AlON:Mn^{2+}, Mg^{2+}$  (down-triangle). The NTSC color gamut (black) is provided for reference. Reprinted and adapted with permission from reference 8. Copyright 2022 American Chemical Society.<sup>8</sup> ..... 29

**Figure 15.** (a) A polyhedral view of the structure of  $Rb_2CuX_3$  projected along the  $b$ -axis, and (b) a close-up view of a segment of  $\infty 1CuX_3^{2-}$  chains showing the corner-sharing connectivity of the  $CuX_4$  tetrahedra. Rb, Cu, and X are shown in green, yellow, and red, respectively. . 39

**Figure 16.** Photos of as-prepared polycrystalline powders of (a)  $Rb_2CuBr_3$  and (b)  $Rb_2CuCl_3$ ,

and (c) single crystals of $\text{Rb}_2\text{CuCl}_3$ . .....	40
<b>Figure 17.</b> Room temperature optical absorption (circles), PLE (dashed lines) and PL (solid lines) of polycrystalline powders of $\text{Rb}_2\text{CuBr}_3$ (blue) and $\text{Rb}_2\text{CuCl}_3$ (red). The inset show the bright blue emission under UV irradiation. ....	42
<b>Figure 18.</b> Power dependence PL spectra for (a) $\text{Rb}_2\text{CuBr}_3$ and (b) $\text{Rb}_2\text{CuCl}_3$ . Insets show the corresponding plots of the PL intensity vs excitation power. ....	44
<b>Figure 19.</b> Time-resolved PL decay curve of $\text{Rb}_2\text{CuCl}_3$ crystals at room temperature. ....	45
<b>Figure 20.</b> Electronic band structure and density of states (DOS) for (a-b) $\text{Ru}_2\text{CuCl}_3$ and (c-d) $\text{Ru}_2\text{CuBr}_3$ . Note that the band gaps are underestimated due to the band gap error in the PBE calculation. ....	46
<b>Figure 21.</b> The partial charge densities of the hole (a) and the electron (b) in the exciton in $\text{Rb}_2\text{CuCl}_3$ . The Cu and the Cl atoms are represented by blue and green balls, respectively. The charge density at the isodensity surface is $0.001 \text{ e/Bohr}^3$ .....	48
<b>Figure 22.</b> Anti-Stokes photoluminescence spectra of a $\text{Rb}_2\text{CuCl}_3$ single crystal measured at ambient temperature and for different excitation wavelengths.....	50
<b>Figure 23.</b> Room temperature PXRD patterns (black) fitted using the Pawley method (red) for (a) $\text{K}_2\text{CuCl}_3$ and (b) $\text{K}_2\text{CuBr}_3$ prepared using solid-state synthesis. (c) A ball-and-stick representation of the 1D crystal structure of $\text{K}_2\text{CuX}_3$ viewed down the $b$ -axis.....	59
<b>Figure 24.</b> Photographs of $\text{K}_2\text{CuX}_3$ ( $X = \text{Cl}, \text{Br}$ ) samples: (a) A polycrystalline pellet of $\text{K}_2\text{CuCl}_3$ prepared using solid-state synthesis approach, (b) molten salt flux grown $\text{K}_2\text{CuCl}_3$ crystals, (c) $\text{K}_2\text{CuCl}_3$ crystals grown from slow cooling a saturated solution, (d) a 1 cm-long single crystal of $\text{K}_2\text{CuBr}_3$ grown using a liquid-liquid diffusion method, and (e) $\text{K}_2\text{CuBr}_3$ crystals via a liquid-vapor diffusion synthesis method. ....	60

- Figure 25.** (a) Room temperature photoluminescence excitation (PLE) (dashed lines) and photoluminescence emission (PL) (solid lines) of polycrystalline powders of  $\text{K}_2\text{CuBr}_3$  (blue) and  $\text{K}_2\text{CuCl}_3$  (red). (b) A comparison of the normalized photoluminescent quantum yield (PLQY) of  $\text{K}_2\text{CuCl}_3$  (plotted in black) against that of  $\text{Rb}_2\text{CuCl}_3$  (plotted in red) under continuous irradiation suggests a significantly improved photostability of  $\text{K}_2\text{CuCl}_3$  compared to  $\text{Rb}_2\text{CuCl}_3$ . ..... 64
- Figure 26.** Excitation-dependent PL measurements for (a)  $\text{K}_2\text{CuCl}_3$  and (b)  $\text{K}_2\text{CuBr}_3$ . (c) Room temperature time-resolved PL spectrum for  $\text{K}_2\text{CuCl}_3$ . (d) A radioluminescence spectrum of  $\text{K}_2\text{CuCl}_3$  with emission centered at 404 nm. .... 66
- Figure 27.** Calculated mean free path of photons in  $\text{K}_2\text{CuCl}_3$  (black),  $\text{K}_2\text{CuBr}_3$  (red),  $\text{Rb}_2\text{CuCl}_3$  (blue), and  $\text{Rb}_2\text{CuBr}_3$  (green). Sharp breaks correspond to the K and L edges in the constituent atoms. .... 68
- Figure 28.** Electronic band structures and DOS of  $\text{K}_2\text{CuCl}_3$  and  $\text{K}_2\text{CuBr}_3$ . .... 70
- Figure 29.** The partial charge density contours of the hole (a) and the electron (b) in the exciton in  $\text{K}_2\text{CuCl}_3$ . The Cu and Cl atoms are represented by blue and green balls, respectively. The charge density at the isodensity surface is  $0.001 \text{ e/bohr}^3$ . .... 71
- Figure 30.** Orthorhombic crystal structures of (a)  $\text{Cs}_2\text{AgBr}_3$  and (b)  $\text{Rb}_2\text{AgBr}_3$  viewed down the *b*-axes. Both compounds feature  $1\text{D } \infty 1\text{AgX}_3^{2-}$  chains (shown in red) separated by  $\text{A}^+$  cations. The difference in the packing of the  $\infty 1\text{AgX}_3^{2-}$  chains and  $\text{A}^+$  cations is emphasized by displaying (a) Cs1 and Cs2 in dark grey and light grey in  $\text{Cs}_2\text{AgBr}_3$  and (b) Rb1 and Rb2 in dark blue and light blue in  $\text{Rb}_2\text{AgBr}_3$ ; Ag and Br are shown in red and brown, respectively. .... 80
- Figure 31.** The room temperature PXRD patterns of (a)  $\text{Rb}_2\text{AgCl}_3$ , (b)  $\text{Rb}_2\text{AgBr}_3$ , (c)  $\text{Rb}_2\text{AgI}_3$ ,



(d) Cs <sub>2</sub> AgBr <sub>3</sub> , and (e) Cs <sub>2</sub> AgI <sub>3</sub> . The experimental patterns are plotted in red with the literature reference value plotted in black.....	81
<b>Figure 32.</b> Normalized room temperature photoluminescence excitation (PLE) and photoluminescence emission (PL) plots for (a) Rb <sub>2</sub> AgX <sub>3</sub> and (b) Cs <sub>2</sub> AgX <sub>3</sub> . Insets show the visible emission from samples when excited with their respective excitation maxima. ....	83
<b>Figure 33.</b> Excitation-dependent PL measurements results for (a) Rb <sub>2</sub> AgCl <sub>3</sub> , (b) Rb <sub>2</sub> AgBr <sub>3</sub> , (c) Rb <sub>2</sub> AgI <sub>3</sub> , (d) Cs <sub>2</sub> AgBr <sub>3</sub> , and (e) Cs <sub>2</sub> AgI <sub>3</sub> . .....	85
<b>Figure 34.</b> Time-resolved photoluminescence (TRPL) measurement results for (a) Rb <sub>2</sub> AgCl <sub>3</sub> , (b) Rb <sub>2</sub> AgBr <sub>3</sub> , (c) Rb <sub>2</sub> AgI <sub>3</sub> , (d) Cs <sub>2</sub> AgBr <sub>3</sub> , and (e) Cs <sub>2</sub> AgI <sub>3</sub> .....	86
<b>Figure 35.</b> Electronic band structure and density of states (DOS) of Rb <sub>2</sub> AgCl <sub>3</sub> (a-b), Rb <sub>2</sub> AgBr <sub>3</sub> (c-d), and Rb <sub>2</sub> AgI <sub>3</sub> (e-f), respectively. ....	87
<b>Figure 36.</b> A comparison of the normalized PL spectra of different Rb <sub>2</sub> AgI <sub>3</sub> samples prepared using a long (160 hours) and short thermal annealing (12 hours) times.....	90
<b>Figure 37.</b> The words “Saparov Lab” were written on black paper using the fabricated luminescent ink based on A <sub>2</sub> AgX <sub>3</sub> under normal light and UV light (365 nm). ....	94
<b>Figure 38.</b> The A <sub>2</sub> AgX <sub>3</sub> based luminescent inks can be used for fingerprints (FPs): (a, b) a print of a right thumb using Rb <sub>2</sub> AgI <sub>3</sub> and (c, d) a print of a left thumb using Cs <sub>2</sub> AgI <sub>3</sub> under normal light (a, c) and UV light (365 nm, b, d).....	96
<b>Figure 39.</b> (a) A polyhedral model of the 1D structure of (NH <sub>4</sub> ) <sub>2</sub> AgX <sub>3</sub> projected down the <i>b</i> -axis. (b) Isolated tetrahedral chains of ∞1AgX <sub>3</sub> 2 – demonstrating the 1D connectivity of corner-sharing AgX <sub>4</sub> tetrahedra. Silver, halide, nitrogen, and hydrogen are colored in grey, purple, blue, and pink, respectively. ....	104
<b>Figure 40.</b> Photographs of (a) (NH <sub>4</sub> ) <sub>2</sub> AgBr <sub>3</sub> and (b) (NH <sub>4</sub> ) <sub>2</sub> AgI <sub>3</sub> single crystals grown via	

hydrothermal synthesis method. ....	104
<b>Figure 41.</b> Room temperature photoluminescence excitation (PLE, blue lines) and photoluminescence emission (PL, red lines) spectra of single crystals of (a) $(\text{NH}_4)_2\text{AgBr}_3$ and (b) $(\text{NH}_4)_2\text{AgI}_3$ . ....	107
<b>Figure 42.</b> The Commission Internationale de l'Eclairage (CIE) color coordinates of $(\text{NH}_4)_2\text{AgBr}_3$ and $(\text{NH}_4)_2\text{AgI}_3$ . $(\text{NH}_4)_2\text{AgBr}_3$ is found to exhibit excitation-dependent light emission properties. A Planckian locus has been included to estimate correlated color temperature (CCT) for the various PL emissions of $(\text{NH}_4)_2\text{AgX}_3$ .....	108
<b>Figure 43.</b> Time-resolved PL plots for (a) $(\text{NH}_4)_2\text{AgBr}_3$ and (b) $(\text{NH}_4)_2\text{AgI}_3$ measured using a 299 nm excitation source. ....	110
<b>Figure 44.</b> Electronic band structures and DOS of (a-b) $(\text{NH}_4)_2\text{AgBr}_3$ and (c-d) $(\text{NH}_4)_2\text{AgI}_3$ ..	112
<b>Figure 45.</b> Synthesis of organic salt RBr. ....	117
<b>Figure 46.</b> A polyhedral view of the 0D crystal structure of $\text{RInBr}_4$ . C, N, M and Br atoms are shown in black, light blue, green and navy blue, respectively; H atoms are omitted for clarity. ....	121
<b>Figure 47.</b> (a) Photoluminescence emission (PL) and excitation (PLE) spectra of $\text{RInBr}_4$ and RBr. (b) Normalized photoluminescence quantum yield (PLQY) values of $\text{RInBr}_4$ and RBr under a continuous irradiation at their respective $\text{PLE}_{\text{max}}$ . ....	124
<b>Figure 48.</b> (a) A CIE 1931 chromaticity plot for $\text{RInBr}_4$ and (b) the luminescence color of the crystal. It has a clear match to the calculated color from the chromaticity plot. ....	125
<b>Figure 49.</b> Excitation wavelength dependent PL spectra of $\text{RInBr}_4$ . The optimal excitation wavelength is determined to be $\text{PLE}_{\text{max}} = 390$ nm. ....	126
<b>Figure 50.</b> Room temperature time-resolved PL data for $\text{RInBr}_4$ obtained using 3.5 eV excitation	

energy..... 128

**Figure 51.** (a) Electronic band structure and (b) density of states (DOS) of  $\text{RInBr}_4$  calculated using the PBE functional as well as (c) the DOS calculated using the more advanced hybrid PBE0 functional. Note that the PBE band gap in (a) and (b) is underestimated and the band gap is corrected by the PBE0 calculation in in (c)..... 133

**Figure 52.** (a) Conduction band minimum and (b) valence band maximum at the  $\Gamma$  point for  $\text{RInBr}_4$ . ..... 134

**Portions of this dissertation have been reprinted and/or adapted in part with permission of the publishers as follows:**

**Chapter 2:**

**Section 2.1** was adapted with permission from Creason, T. D.; Yangui, A.; Roccanova, R.; Strom, A.; Du, M.-H.; Saparov, B. Rb<sub>2</sub>CuX<sub>3</sub> (X = Cl, Br): 1D All-Inorganic Copper Halides with Ultrabright Blue Emission and Up-Conversion Photoluminescence. *Adv. Opt. Mat.* **2020**, 8 (2), 1901338. DOI: 10.1002/adom.201901338.

**Section 2.2** was adapted with permission from Creason, T. D.; McWhorter, T. M.; Bell, Z.; Du, M.-H.; Saparov, B. K<sub>2</sub>CuX<sub>3</sub> (X = Cl, Br): All-Inorganic Lead-Free Blue Emitters with Near-Unity Photoluminescence Quantum Yield. *Chem. Mat.* **2020**, 32 (14), 6197-6205. DOI: 10.1021/acs.chemmater.0c02098.

**Chapter 3:**

**Section 3.1** was adapted with permission from Kumar, P.\*; Creason, T. D.\*; Fattal, H.; Sharma, M.; Du, M. H.; Saparov, B. Composition-Dependent Photoluminescence Properties and Anti-Counterfeiting Applications of A<sub>2</sub>AgX<sub>3</sub> (A = Rb, Cs; X = Cl, Br, I). *Advanced Functional Materials* **2021**, 31 (48). DOI: 10.1002/adfm.202104941.

**Section 3.2** was adapted with permission from Creason, T. D. \*; Fattal, H. \*; Gilley, I. W.; McWhorter, T. M.; Du, M.-H.; Saparov, B. (NH<sub>4</sub>)<sub>2</sub>AgX<sub>3</sub> (X = Br, I): 1D Silver Halides with Broadband White Light Emission and Improved Stability. *ACS Mater. Au.* **2021**, 1 (1), 62-68. DOI: 10.1021/acsmaterialsau.1c00009.

**Chapter 4:**

**Chapter 4** was adapted with permission from Fattal, H.; Creason, T. D.; Delzer, C. J.; Yangui, A.; Hayward, J. P.; Ross, B. J.; Du, M.-H.; Glatzhofer, D. T.; Saparov, B. Zero-Dimensional Hybrid Organic–Inorganic Indium Bromide with Blue Emission. *Inorg. Chem.* **2021**, 60 (2), 1045-1054. DOI: 10.1021/acs.inorgchem.0c03164 From NLM PubMed-not-MEDLINE..

Tables and Figures in the Appendix have also been reprinted with permission from the above sources.

# **Chapter 1: Introduction**

## **1.1 Expanding Interest in Down-Converting Metal Halides**

The field of optoelectronic materials has rapidly grown in the past decade. Every facet, from understanding the fundamental nature of light-matter interactions to the design and commercialization of new devices, has been pushed forward to new heights. A critical area that has covered the broad gap between fundamental science to consumer devices is solid-state lighting (SSL). This area has created a feedback loop where new needs in the late-stage device space feed back into the materials design community to drive research into the structural-optical property relationships of the materials being utilized. The rapid nature of this cycle has driven innovation in the field at all levels. At this point, gains in basic-level research of optoelectronic materials can directly impact future SSL technologies.

Improvements in materials design can have impacts beyond the research lab. The U.S. Department of Energy (DOE) has identified SSL technology as a critical research area to support multiple priorities for the U.S. public interest.<sup>1</sup> Light emitting diodes (LEDs) based on SSL currently comprise approximately 35% of the U.S. total lighting market, with a set goal to reach 84% by 2035. If achieved, this would reduce the U.S. energy consumption from lighting by approximately 75%, a total savings of over 500 TWh annually.<sup>1</sup> To reach these goals, great strides must be made in multiple research areas, including novel materials design for SSL. One of the U.S. DOE's specific lighting platform technology R&D priorities is down converter technology.<sup>1</sup> This technology area is defined as the exploration and development of high-efficiency down-conversion materials to use with LEDs. Fundamentally, this is the conversion of higher energy light, for example, UV light, into lower energy light in the visible region. Many research gaps exist

in the fundamental understanding of why certain materials emit and how to design materials with specific emission profiles. From a purely practical perspective, the work presented in this dissertation is motivated by the need to develop new photoluminescent materials for down-conversion, with prospective applications in not only SSL, but in anti-counterfeiting, radiation detection, chemical and temperature sensors, etc. Fundamentally, the presented work contributes to the understanding of the structure-property relationships in brand-new materials families, which will aid the efforts to design novel light-emitting materials.

### **1.1.1 Historical Roots in Rare-earth Doped Oxides**

Within the area of down-conversion, two classes of materials have emerged as potential frontrunners in the future of down-conversion materials, rare-earth (RE) doped oxides and metal halide perovskites (MHPs). The first is the more technologically mature family of rare-earth (RE) doped oxides, which, as the name implies, rely on the doping of stable oxide host materials with often expensive RE metals.<sup>2</sup> The vast majority of commercialized LEDs on the market contain RE metals in their phosphor mixtures.<sup>3</sup> The most popular and among the best of this class of materials include commercialized oxides such as  $\text{BaMgAl}_{10}\text{O}_{17}:\text{Eu}^{2+}$ , which can reach photoluminescent down conversion efficiencies of up to 92.4 %.<sup>4</sup> While many of the optical properties of the rare-earth doped oxides are highly desirable, the synthetic challenges associated with the materials class are a disadvantage when compared to solution-processable materials.<sup>5</sup> Additionally, the starting precursors are only available in critically limited quantities worldwide, leading to price increases as the demand for LED lighting increases.<sup>6</sup> In order to incorporate the RE metal into the host matrix, the precursors must be finely ground and heated to relatively high processing temperatures, often exceeding 1000 K.<sup>7</sup> The total synthesis time is often on the time scale of weeks in order to allow for full incorporation of the dopant and to prevent impurities.<sup>7</sup> Once synthesized, post-

treatment is needed as many of the best materials are often hygroscopic, absorbing water from the air, as is the case for one of the best red emitters,  $\text{K}_2\text{SiF}_6:\text{Mn}^{4+}$ .<sup>8</sup>

From a novel materials design perspective, the options are often limited as the search for new host materials rarely leads to materials that beat the status quo. The difficulty in finding new materials is compounded by long synthesis times, limiting high throughput testing methods. Due to the nature of RE-doped oxides photoluminescence, the emission of the RE dopant is highly predictable. This means that even when a new host material is found, adding in a rare-earth dopant often produces the same emission as other host materials as long as the dopant is the same. These design challenges have led to slow improvements over the years, often relying on modifying best-in-class materials to be synthesized in the nanocrystal form to boost down conversion efficiency.<sup>3,</sup>

9

### **1.1.2 Development of Metal Halide Perovskites**

The other promising class of down-converters in the solid-state lighting field are the recently established metal halide perovskites (MHPs). The class is defined by a specific crystal structure type, precisely, a material with the same crystal structure as  $\text{CaTiO}_3$ .<sup>10</sup> For MHPs, this translates to the general formula of  $\text{ABX}_3$ ; in this structure, divalent B metals are octahedrally coordinated with the X anions. These octahedra are connected together in a three-dimensional lattice via the corner-shared anions, with the monovalent A cation filling the void space between the  $\text{BX}_6$  metal-anion octahedra. MHPs rose to popularity initially due to the rapid improvements in the area of photovoltaics. Hybrid organic-inorganic perovskites, such as formamidinium lead iodide,  $\text{FAPbI}_3$ , demonstrate outstanding performance in solar panels; derivative compositions based on this material recently set another record for power conversion efficiency of 25.4%.<sup>11</sup> To put the rapid progress into perspective, early perovskite-based solar cells fabricated as recently as

2009 were only at 3.8% power conversion efficiency.<sup>12</sup>

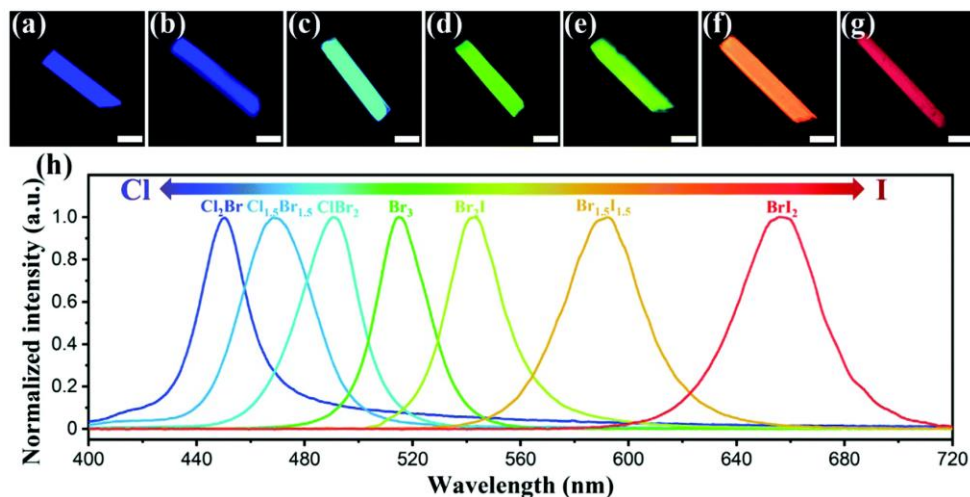


**Figure 1.** The optical images of an isolated (a) ZJU-28 $\supset$ CsPbCl<sub>2</sub>Br, (b) ZJU-28 $\supset$ CsPbCl<sub>1.5</sub>Br<sub>1.5</sub>, (c) ZJU-28 $\supset$ CsPbClBr<sub>2</sub>, (d) ZJU-28 $\supset$ CsPbBr<sub>3</sub>, (e) ZJU-28 $\supset$ CsPbBr<sub>2</sub>I, (f) ZJU-28 $\supset$ CsPbBr<sub>1.5</sub>I<sub>1.5</sub> and (g) ZJU-28 $\supset$ CsPbBrI<sub>2</sub> microcrystals under excitation of 365 nm (for a–d) or 480 nm (for e–g). Scale bar, 50  $\mu$ m. (h) PL spectra of the ZJU-28 $\supset$ CsPbX<sub>3</sub> crystals. Reprinted with permission from reference 13. Copyright 2022 Royal Society of Chemistry.<sup>13</sup>

The success in solar materials inspired the search in the area of photoluminescent materials for down conversion. One example that has garnered significant attention is CsPbX<sub>3</sub> (X = Cl, Br, and I) which has highly tunable PL emission properties, allowing high-intensity emission of nearly any color in the visible spectrum and reaching efficiencies of up to 90% when in the nanocrystalline form.<sup>14</sup> Early work in 2015 opened the door for many derivative compounds and post-synthetic modifications that now allow state-of-the-art MHPs to reach unity (100%) efficiency in down conversion.<sup>15</sup> An example of the now heavily optimized bright emission of CsPbX<sub>3</sub> is seen above in Figure 1. While these advances have led MHPs to enter early-stage commercialization in the solar and SSL industries, some problems intrinsic to the materials class remain.<sup>16</sup>

One issue frequently mentioned in the literature is the innate toxicity of lead.<sup>17</sup> While there will be many commercialization options where lead is not a problem, residential lighting will be



an uphill battle after decades of public awareness campaigns targeting the removal of lead from in-home products.<sup>16, 17</sup> The issue of lead toxicity is further exacerbated by the poor environmental stability of lead halide perovskites, which degrade into lead salts upon exposure to moisture.<sup>18</sup> Photographs showing the danger of lead toxicity in the environment are shown below in Figure 2. Pertaining to SSL specifically, perovskites are great for monochromatic emission due to the nature of the emission mechanism, discussed in a later section. However, MHPs must be combined into a composite coating to produce the broad white light emission needed for many lighting applications.<sup>19</sup> Lastly, when looking at recent trends in improving perovskite photoluminescence, the majority of the perovskites studied are in the nanocrystal phase, which can be a hindrance for certain SSL applications.

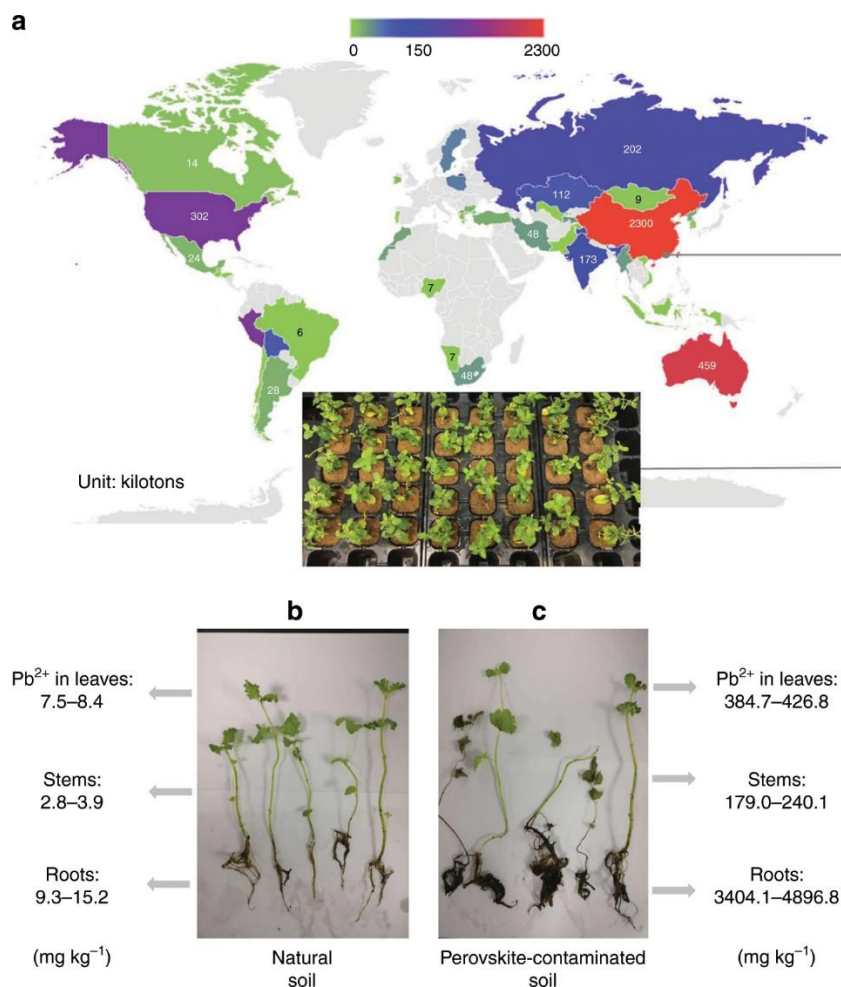


**Figure 2.** Distribution of lead production worldwide in 2017 (open data from British Geological Survey). The inset shows the photo of mint plants grown in perovskite-contaminated soil within the campus of Fujian Agriculture and Forestry University, China (latitude 26.084, longitude 119.238). **b** The picture of mint plants grown on control soil (left) and **c**  $250\ mg\ kg^{-1}\ Pb^{2+}$  perovskite-contaminated soil (right). The range of lead content measured in the leaves, stem, and root is reported on the side of each picture. Reprinted with permission from reference 17. Copyright 2020 Nature.<sup>17</sup>

### 1.1.3 Emergence of Luminescent Copper(I) Halides

The fundamental and stability challenges associated with both RE-doped oxides and MHPs inspired work in the area of lead-free metal halide photoluminescence. This is a rapidly expanding area of interest, with many alternatives being proposed. Many focus on materials that are isoelectronic to the lead by investigating the use of Sn or Bi halides. However, these alternatives carry many of the same stability issues, with only comparable at best performance.<sup>20, 21, 22</sup> This has

pushed some outside of the p-block and into transition metals. Among the most impactful reports that informed this dissertation was the discovery of the photoluminescent properties of  $\text{Cs}_3\text{Cu}_2\text{I}_5$ . First reported in 2018 by Taehwan Jun et al. and later in 2019 by Rachel Rocanova et al., the compound was the first bulk, lead-free metal halides to display near-unity down conversion efficiency (PLQY of almost 100%).<sup>23,24</sup> The new class of materials had great preliminary phosphor results under UV illumination, as seen below in Figure 3. The high-intensity emission was also in the blue region, an area that is traditionally more difficult to design materials for due to the tendency to form mid-gap states that quench the emission or contribute to low energy emission leading to low color purity.<sup>19</sup> These exciting results opened up a new opportunity to research ternary group 11 halides as a potential material for solid-state lighting.

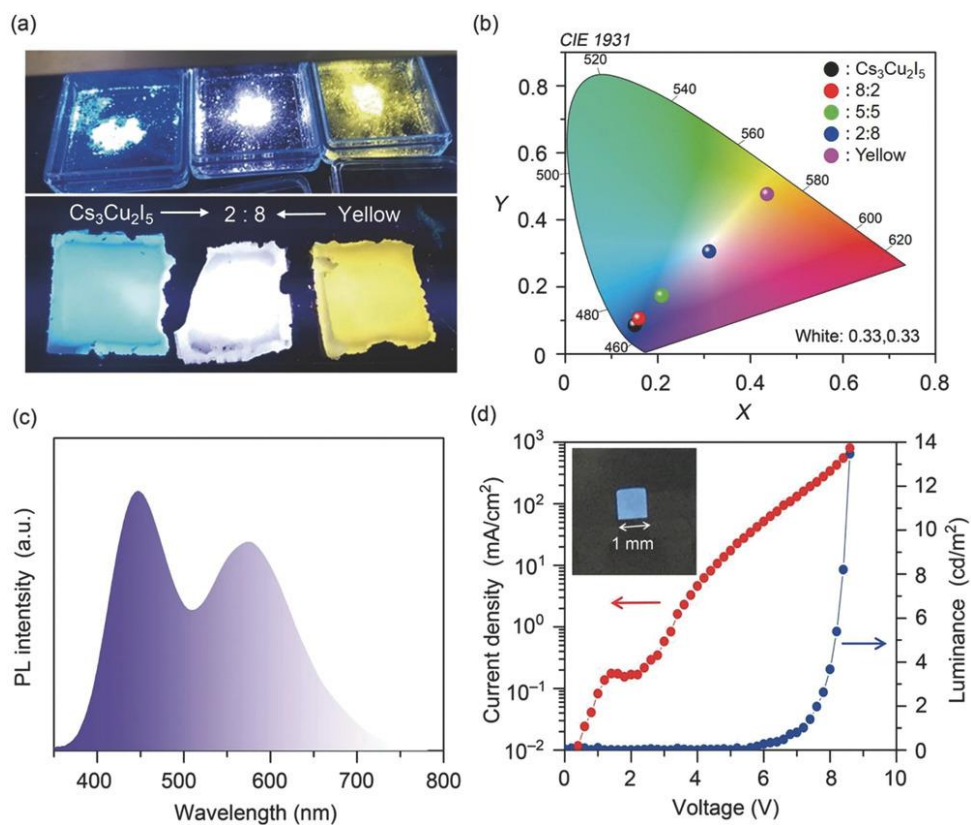


**Figure 3.** a) Photograph of Cs<sub>3</sub>Cu<sub>2</sub>I<sub>5</sub>, a yellow phosphor, and its mixtures (from left to right: Cs<sub>3</sub>Cu<sub>2</sub>I<sub>5</sub>, mixture of 2:8, yellow phosphor) under UV illumination (top) and films prepared by kneading the powders into polydimethylsiloxane matrix (bottom). b) PL spectrum of the mixture of Cs<sub>3</sub>Cu<sub>2</sub>I<sub>5</sub> and yellow phosphor (mixing ratio = 2:8), c) CIE coordination of PL from the powder mixture, and d) current-density–luminance–voltage characteristic of the blue LED using a Cs<sub>3</sub>Cu<sub>2</sub>I<sub>5</sub> thin film as an emission layer, and (inset) its photo. Reprinted with permission from reference 23. Copyright 2018 Wiley.<sup>23</sup>

The structure-optical property relationships of multinary copper (I) and the isoelectronic silver halides are poorly understood, and the literature is underdeveloped relative to the RE-doped oxides and MHPs. Prior to this work, the majority of the work available in the literature was either original reports of structures, broad searches for new materials with high ionic conductivity, or evaluating organometallic copper(I) structures for photoluminescence. In chapter 2 of this work, all-inorganic copper(I) halides were investigated by characterizing the A<sub>2</sub>CuX<sub>3</sub> family as a model system to understand the intrinsic photoluminescence emission and the effects of elemental

substitution on both optical and physical properties. The hypothesis initially was that the emission could be improved or tuned by anion or cation substitution, as seen in MHPs. The work in chapter 3 covers the work done to investigate the changes made when silver replaces the luminescent emission center of copper (I) halides. The project was undertaken with the hope that a high  $Z$  substitution could improve the scintillation capabilities with better X-ray absorption, but as research always goes, new interesting optical properties were discovered. Chapter 4 explores an uncommon route to high-efficiency photoluminescence by incorporating organic emitters into a high band gap hybrid material. This research strategy opens the door to improving organic-derived photoluminescence from a stability perspective and increasing efficiency while maintaining a previously selected emission profile. Chapter 5 briefly concludes the work presented and discusses future directions.

In order to set the stage for the main body of the work, the following sections in chapter 1 present background information that may be necessary to contextualize the work presented in the later chapters. The introduction continues with a historical perspective on ternary group 11 halides and their crystal structures relevant to the larger body of work. This is followed by an overview of the synthetic challenges and ways to overcome them associated with group 11 metal halides. Lastly, the origins of photoluminescence and their applications are briefly covered in sections 1.4 and 1.5, respectively.

## **1.2 Historical overview of all-inorganic, ternary group 11 halides**

There is a plethora of historical data involving all-inorganic ternary group 11 halides; Pearson's database alone reports over 840 distinct entries.<sup>25</sup> To narrow the field, the relevant work for this background section will only focus on ternary monovalent copper and silver halides. Gold halides are an ongoing area of interest, with potential future studies. While the optoelectronic

interest in ternary copper and silver halides has only emerged recently, the family of compounds has been known as far back as 1827 by P. Boullay, who initially reported them in the *Annales de Chimie et de Physique*.<sup>26</sup> The family mostly sat unexplored until investigated by Dr. Clara Brink of the famous Dr. Anton Eduard van Arkel group at Leiden University. In her work, Dr. Brink primarily investigated the compositionally versatile  $A_2MX_3$  ( $A = K, Rb, Cs, NH_4, M = Cu(I), Ag,$  and  $X = Cl, Br, I$ ) family, which has the prototypes  $K_2CuCl_3$  and  $K_2AgI_3$ .<sup>27</sup> Two prototypes exist as there are technically two different structures, however they are incredibly similar with only minor differences discussed below. This classification into two types was made by S. Hull in their 2004 work systematically exploring the family.<sup>28</sup> All copper(I) halides fall into type two, with silver halides split between type one and two. This family can be seen below in Figure 4 as the first listed structural family.

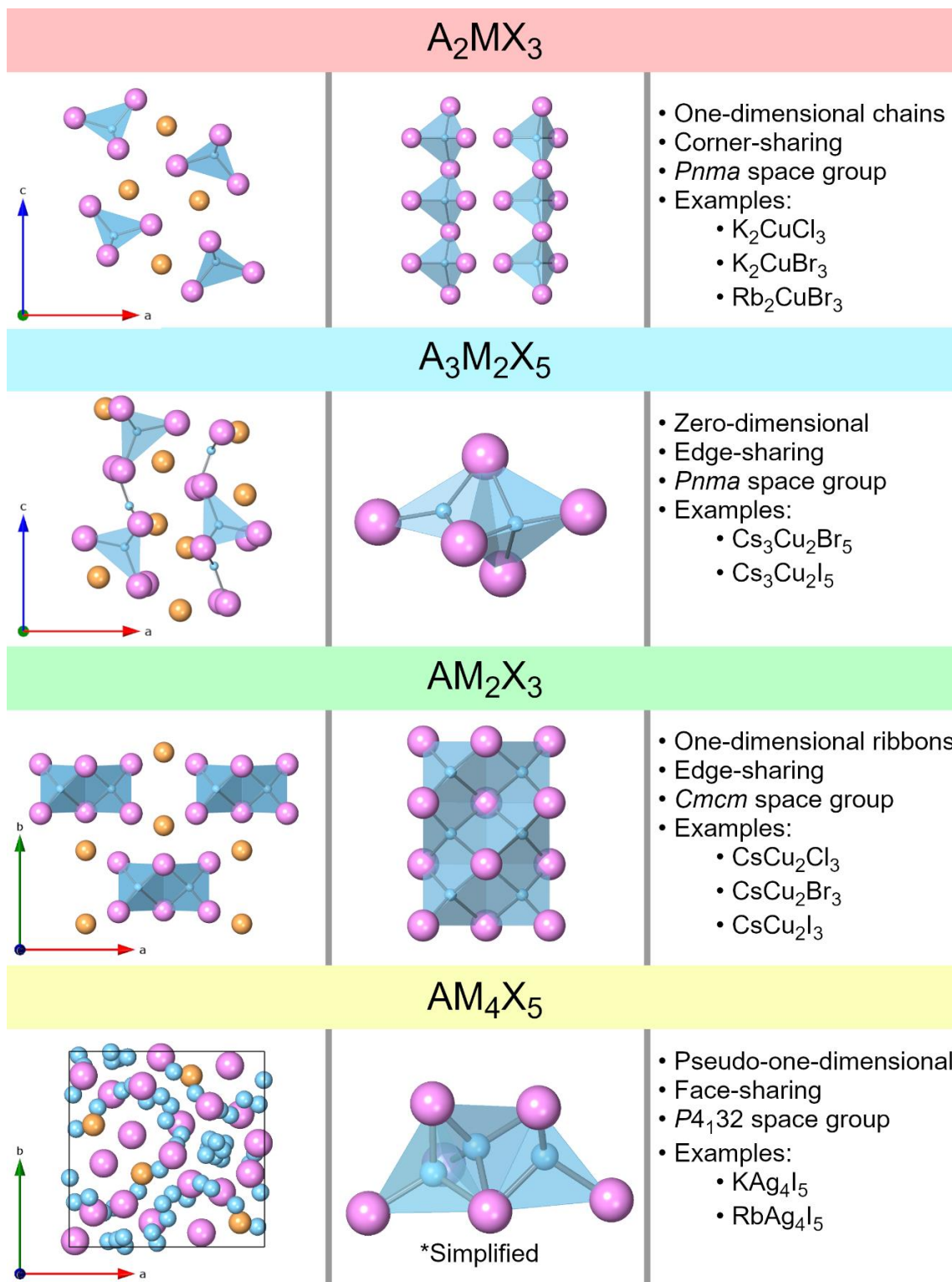


**Figure 4.** Comparison of the crystal structures of the A-M-X (A = K, Rb, Cs, NH<sub>4</sub>, M = Cu(I), Ag, and X = Cl, Br, I) families. The left column displays a full structure, the middle column displays just the metal-halide polyhedra connectivity, and the right column describes the essential details of each family. A, M, and X are shown as orange, blue, and pink spheres, respectively.

The structural family falls into the *Pnma* space group and is composed of copper(I) or silver-centered tetrahedra with halide ions forming the corners.<sup>27</sup> The metal-halide tetrahedra are corner-sharing to form a one-dimensional chain down the b-axis, as seen in Figure 4. The void space between the chains is filled by  $A^+$  cations, which can be a group 1 metal such as cesium, rubidium, or potassium.<sup>28</sup> The  $A^+$  cation can also comprise small molecules such as ammonium.<sup>29</sup> The differences between type one and type two, as classified by Hull, is simply the packing of the  $A^+$  cations between the metal halide chains.<sup>28</sup> The metal-halide tetrahedra are all regular with bond angles and distances within the expected range as defined by Shannon ionic radii.<sup>30</sup> Attempts to distort the structure through a solid solution of either the metal or the halide sites have been made; however, these endeavors were not successful, as reported in this work.

A closely related structure to the  $A_2MX_3$  compounds is the family  $AM_2X_3$  ( $A = K, Rb, Cs, NH_4, M = Cu(I), Ag,$  and  $X = Cl, Br, I$ ). This structure was also discovered by Dr. Clara Brink in 1954 with the prototype  $CsCu_2Cl_3$ .<sup>31</sup> All compounds in the family form in the *Cmcm* space group. Similar to the  $A_2MX_3$  family, the structure is composed of metal halide tetrahedra that form one-dimensional chains through the *c*-axis.<sup>31</sup> A notable difference is that the tetrahedra are edge-sharing, meaning that the chains are more appropriately referred to as ribbons or nanowires.<sup>32</sup> The nature of the double ribbons is seen in Figure 4 above. This structure is also more complex, with distortion in the tetrahedra and facile solid solution formation. The distortion in the tetrahedra follows the trend of decreasing distortion from  $CsCu_2Cl_3$  to  $CsCu_2Br_3$  to  $CsCu_2I_3$ . Distortion in the lattice is reportedly a beneficial feature as it is believed to enhance the photoluminescence emission in more distorted compounds.<sup>32</sup> The solid solution of the halides is easily achieved through simple stoichiometric loading of the precursors. The lattice parameters of the solid solution structures approximate Vegard's law, as seen below in Figure 5.<sup>32</sup>



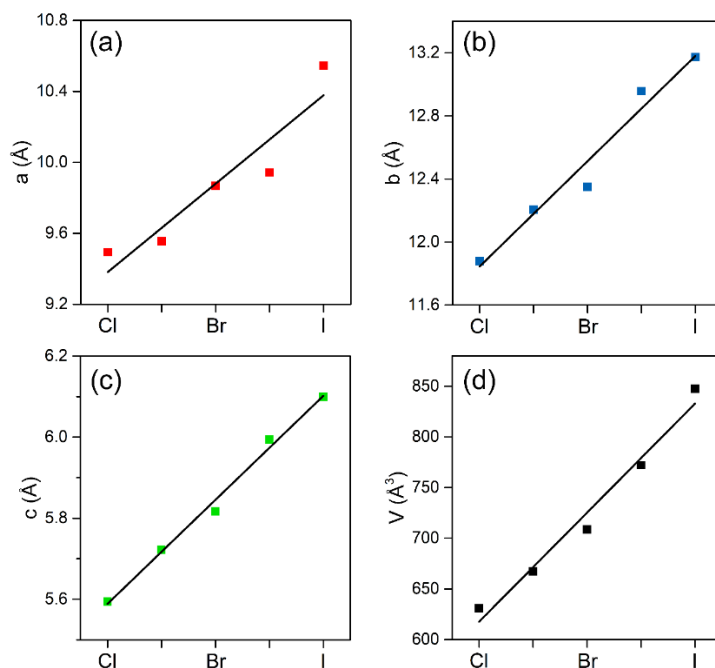


**Figure 5.** (a-c) PXRD refined lattice parameters, and (d) unit cell volume shown as a function of halide content as alloying progresses from  $\text{CsCu}_2\text{Cl}_3$  (Cl) to  $\text{CsCu}_2\text{Br}_3$  (Br) to  $\text{CsCu}_2\text{I}_3$  (I). Reprinted with permission from reference 32. Copyright 2019 American Chemical Society.<sup>32</sup>

Other prominent ternary group 11 metal halide compounds are known to exist. These, however, are generally isolated compositions and less of families that are open to elemental substitution. One of the most impactful in recent years regarding optoelectronic properties is  $\text{Cs}_3\text{Cu}_2\text{Br}_{5-x}\text{I}_x$ . This compound, mentioned above in section 1.1, is a zero-dimensional structure comprised of isolated edge-sharing tetrahedra and trigonal planar species.<sup>24</sup> Another low-dimensional structure is that of  $\text{CsAgX}_2$  ( $X=\text{Cl}, \text{Br}$ ), which forms edge-sharing trigonal bipyramidal metal-halide chains down the b-axis, similar to the above structures.<sup>28</sup> The last structure of note is  $\text{A}Ag_4\text{I}_5$  ( $A=\text{Rb}, \text{K}$ ); while discovered in 1960, the compound has reemerged recently due to its potential battery applications since the material is known to have superionic behavior.<sup>28, 33</sup> The structure is quite different from the others discussed as it is comprised of face-sharing iodide tetrahedra with  $\text{Ag}^+$  and  $\text{Rb}^+$  in void space. More all-inorganic structures are predicted, such as  $\text{Rb}_3\text{CuCl}_4$ , yet many of these are based on phase diagrams and not yet

synthesized.<sup>34</sup> A myriad of hybrid and organometallic group 11 halides are also known, though they are outside the scope of this work and are excluded.

When searching for prior work not focused on the structure or synthesis of ternary group 11 halides, the literature is relatively sparse. Throughout the 1990s, there were multiple papers published by T. Awano that investigated the formation of self-trapped holes in ternary silver halides when exposed to high doses of gamma radiation.<sup>29, 35</sup> This work serves as the basis for the formation of halide vacancies in the ternary silver halides discussed in chapter 3. The other main body of work was published by S. Hull in a study mentioned above. In this work, all known  $(\text{AgX})_x-(\text{MX})_{1-x}$  and  $(\text{CuX})_x-(\text{MX})_{1-x}$  ( $= \text{K, Rb and Cs; X=Cl, Br and I}$ ) compounds were systematically grown as pellets and tested for superionic properties. Unfortunately, only the known  $\text{KAg}_4\text{I}_5$  and  $\text{RbAg}_4\text{I}_5$  were confirmed to be superionic due to the presence of weakly bound silver in the structure.<sup>28</sup> From an optical properties perspective, the work mentioned above regarding  $\text{Cs}_3\text{Cu}_2\text{X}_5$  and  $\text{CsCu}_2\text{X}_3$  were the only all-inorganic compounds reported prior to this work.<sup>23, 24, 32</sup> There is extensive literature on binary salts going back as far as 1949, where they have since been used as model systems to study exciton properties.<sup>36</sup>

### **1.3 Synthetic challenges of group 11 halides**

Ternary group 11 halides present a significant synthetic challenge since many of the target compounds are unstable, and so are their precursors. Both copper(I) halides and silver halides are light sensitive, with copper(I) halides photooxidizing to copper(II) and silver halides photoreducing down to elemental silver.<sup>37</sup> Additionally, copper(I) halides are air and moisture-sensitive, readily forming oxides and hydrates when only briefly exposed. This ultimately translates to the copper(I) halides needing to be utilized in air-free environments or with a potent reducing agent. Silver halides, on the other hand, need to be made ideally in the dark or, at a minimum, in low-light

conditions.<sup>38</sup>

There are two general synthetic approaches for forming these compounds: synthesis in a furnace or solutions synthesis. The first method of furnace synthesis can further be broken down into three sub-methods, melt growth, solid-state synthesis, and flux growth.<sup>39</sup> In the case where a phase diagram is previously reported or can be generated, furnace-based synthesis becomes a more viable route. A phase diagram allows one to target specific temperatures and stoichiometric loadings, eliminating the need to set up many additional reactions. Without a phase diagram, the synthesis becomes more of a trial-and-error process, especially in the case where previous compounds either in the same structural family were not reported.

### 1.3.1 Synthesis of Compounds Utilizing a Furnace

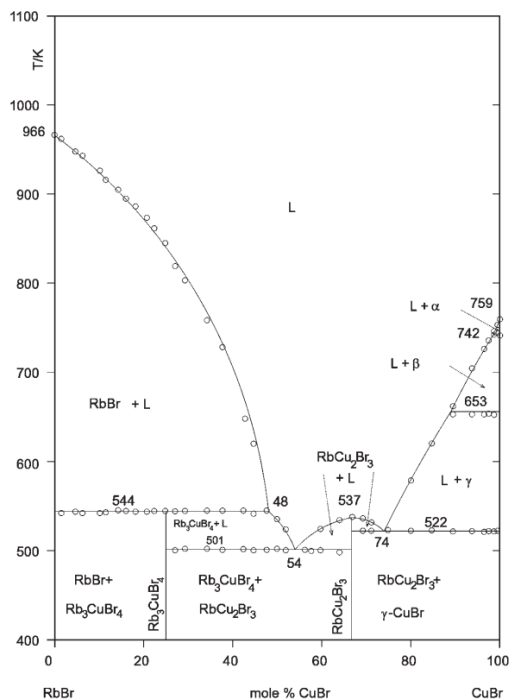


**Figure 6.** Phase diagram for the RbBr–CuBr. Reprinted with permission from reference 34. Copyright 2001 Springer.<sup>34</sup>

Starting with melt growth, this is the most desirable method if accessible as the crystallinity

and purity are much higher than the other furnace-based methods. This method loads and grinds stoichiometric precursors into a fine polycrystalline powder and then seals them in an inert ampule and atmosphere, such as a fused silica ampule under vacuum. The ampule is then heated through the liquidus line on the phase diagram, annealed at a high temperature to homogenize the liquid, and then slowly cooled through the liquidus line to induce crystallization of the target compound. The target compound must have a eutectic transition directly at stoichiometric loading to the liquid phase to pursue this advantageous method. In the RbBr-CuBr phase diagram above in Figure 6, the only compound with this eutectic transition is  $\text{RbCu}_2\text{Br}_3$ .

When implementing the solid-state synthesis method, commonly referred to as "shake and bake" or "beat and heat," the requirements are less strict regarding placement on the phase diagram. This method is often used when melt growth is inaccessible due to a peritectic decomposition of the target compound; this is when a target material degrades to solid and liquid instead of straight to liquid. A peritectic decomposition can be seen above in Figure 6 with the compound labeled  $\text{Rb}_3\text{CuBr}_4$  (actually likely to be  $\text{Rb}_2\text{CuBr}_3$ ), at which point heating above 544K, RbBr plus liquid is formed. The pre-heating preparation is similar to melt growth, with the difference being that the ground powders are pelletized before being placed in the ampule. The sample is then heated slowly to a target temperature determined by the phase diagram, generally 20 K below the peritectic decomposition temperature. The temperature is selected based on Tammann Rule, which states that for a target composition to form, the sample needs to be annealed at  $2/3$  or greater temperature relative to the peritectic decomposition point.<sup>40</sup> The sample is then annealed for extended periods of time to allow for solid diffusion to occur. Finally, the polycrystalline pellet is cooled and checked for purity. If large impurities exist, the process is repeated, starting with the regrinding of the pellet. The major disadvantage of this method is that there always exists some amount of

impurities, and the crystallinity is poor. When looking at most ternary group 11 halides, this method is often tried in first attempts as it yields a polycrystalline powder from which preliminary measurements can be made.

The last furnace synthesis method, flux growth, requires the most technical skill. To utilize flux growth, one must adjust the loading ratio so that when cooling the sample, the composition will go from the liquid phase to the target compound plus the liquid phase. For example, in Figure 6, one might target 48% CuBr in order to make  $\text{Rb}_3\text{CuBr}_4$ . Once the precursors are ground in the specified ratio, they are loaded into the bottom of a Canfield crucible. The sample is then heated with a profile similar to a melt growth and then slowly cooled through the liquidus line. While still hot, the sample is then pulled from the furnace, inverted, and centrifuged. Inside the Canfield crucible, a filter will separate the crystals from flux; these can be extracted once the ampule has cooled to room temperature. The advantage of this method is that single crystals can still be grown when melt growth is not accessible. However, it requires fine technical skill and careful consideration of the phase diagram.

### **1.3.2 Solution Synthesis of Compounds**

The advantage of switching synthetic styles over to the solution method is that single crystals can be grown at low temperatures and often quicker than furnace-based methods. The primary disadvantage is that few guiding principles allow one to plan the solvent composition, precursor loading composition, and heating profiles. In short, more trial and error is needed for solution methods, but when successful, the optimized growth produces larger crystals in usually less time. The first approach with solution synthesis is often to use basic batch methods where one either slowly evaporates a saturated solution or cools a saturated solution.<sup>41</sup> The first step is to select a solvent that all precursors are highly soluble in. Next, the solvent is heated to just below

the boiling, and the precursors are added in a stoichiometric ratio until the solution has reached saturation. From there, the solution is cooled or evaporated. The fundamental basis is the same for either technique, one must reduce the amount of material that can stay dissolved in the solution, and hopefully, crystals of the target material will come out if the target is more thermodynamically preferred relative to the precursors.

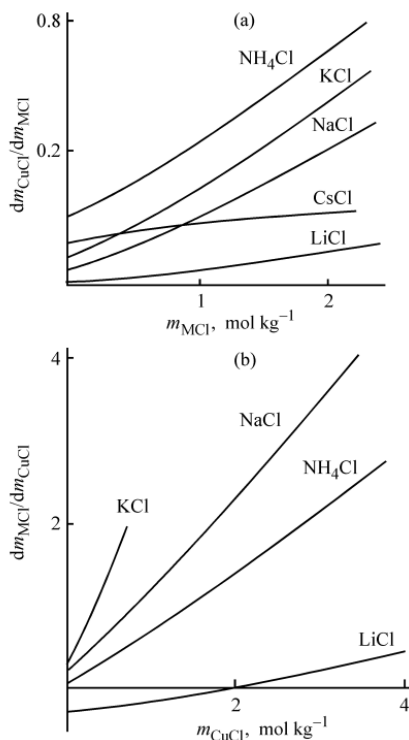


**Figure 7.** Salting-in intensity of a salt,  $dm_1/dm_2$ , vs. the concentration  $m$  of a component being added for the crystallization branches of (a)  $CuCl$  and (b)  $MCl$ . Reprinted with permission from reference 42. Copyright 2004 Springer Nature.<sup>42</sup>

As it applies to all-inorganic copper(I) and silver halides, the precursors are typically  $AX$  and  $CuX$ , where  $A$  is the  $A^+$  cation and  $X$  is the halide. If looking at group 1 metals as the  $A^+$  cation, hydrohalic acid is usually an ideal solvent. An interesting solubility study was done in 2004 by L.V. Stepakova, which found that as the concentration of  $AX$  in water increased, the solubility of  $CuX$  also dramatically increased (see Figure 7 above). Due to this effect, as well as the common ion effect, the hydrohalic acid needs to be diluted with water to allow the  $AX$  to dissolve fully.

Other considerations need to be made when working with copper(I) halides; a key issue is that the solution either needs to be kept air free or a potent reducing agent needs to be added to prevent the oxidation of copper(I) to copper(II).

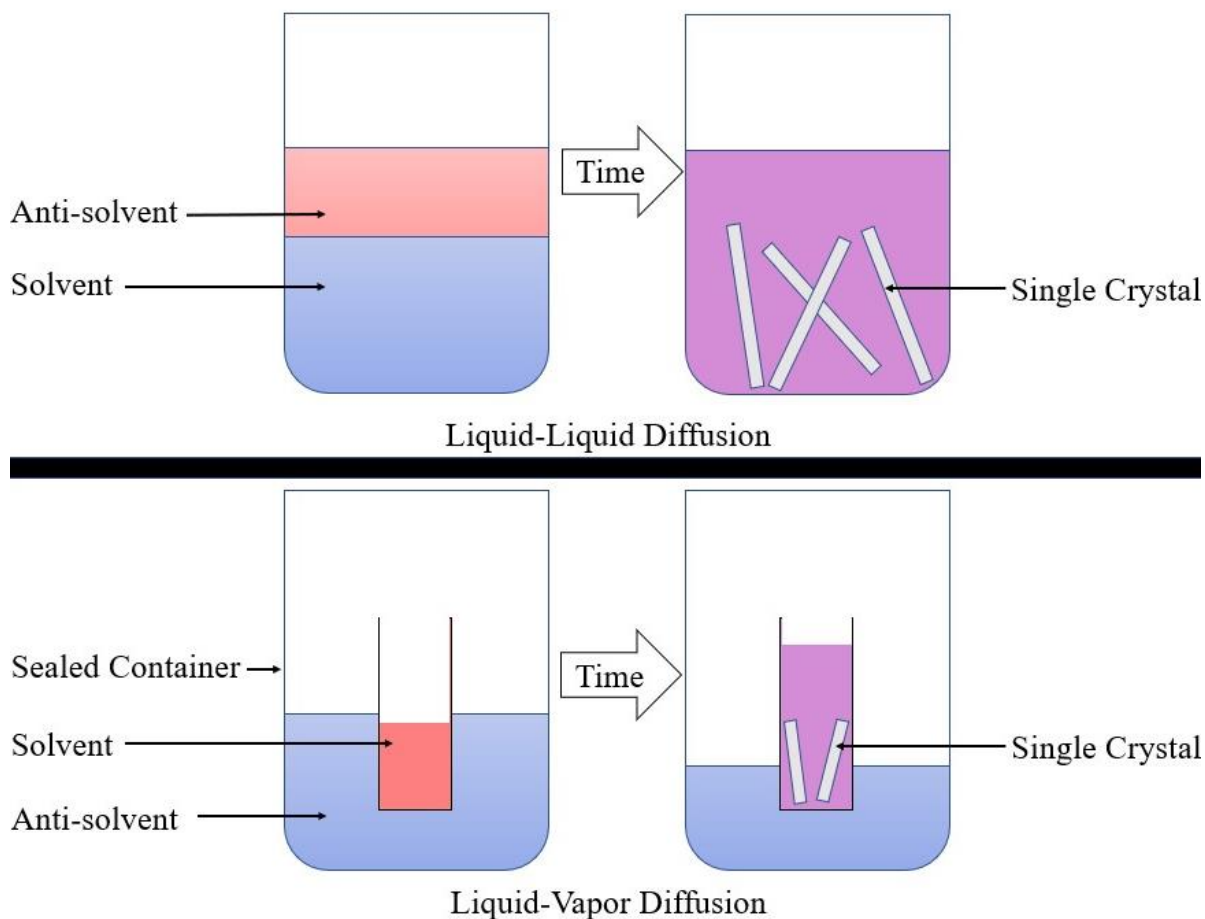


**Figure 8.** Diagram for diffusion crystal growth methods.

Beyond simple batch methods, the other primary solution synthesis technique is through the use of solvent/antisolvent diffusion. For this method, the preparation is the same as above, except the precursors, are dissolved at room temperature, requiring more solvent. The solution is then exposed to an antisolvent, a solvent with low precursor solubility. Exposure techniques can be as simple as layering the antisolvent on top of the solvent, in which case crystals will grow at the interface. More complex techniques require a volatile antisolvent so that in a sealed container,

the antisolvent will evaporate into the container atmosphere and then slowly condense inside the same vial as the solvent. Regardless of the diffusion method used, the advantage over batch methods is that one has more control over the crystal growth rate and crystals can still be grown when heating a solution is not a viable option, as is the case with many organic solvents. The disadvantage is that there is now, even more to optimize, such as finding a good solvent/antisolvent pair for any set of precursors and optimizing the ratio of the solvent and antisolvent. For group 11 halides, commonly used solvent/antisolvent pairs include DMF/DCM and HX/MeOH.<sup>43</sup>

### **1.4 Origins of photoluminescence in metal halides**

Photoluminescence is a process by which matter absorbs light of a particular energy level in the form of photons and then reemits light of a different energy level in the form of photons.<sup>44</sup> This is the fundamental process utilized in many modern technologies, including lighting, displays, anti-counterfeiting, and many other essential use cases.<sup>19</sup> To understand what gives rise to photoluminescent properties, one can start with the electronic band structure of a material. While the fundamentals of electronic band structure warrant an entire college course, it can have a simplified definition as the range of energy levels in which electrons can reside in a solid.<sup>45</sup> In a semiconductor, the energy band that is immediately below the fermi level of a solid is the valence band (VB) of a material. This is the highest energy band that electrons can access in the ground state at 0 K. Directly above the fermi level is the conduction band (CB), this is the lowest unoccupied energy band in a solid at the ground state. Difference in energy level between the CB and the VB is defined as the band gap of a material. An example of this can be seen below in Figure 9.



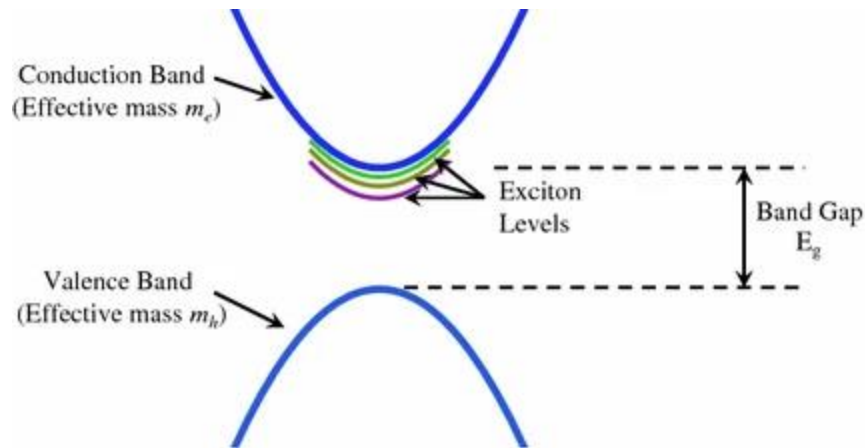


**Figure 9.** Exciton levels for a simple band structure at  $k = 0$ . Reprinted with permission from reference 46. Copyright 2016 Springer Nature.<sup>46</sup>

Upon incident exposure to light, if the energy of the photon is great than the band gap of a material, an electron is promoted from the VB into the CB. Simultaneously, a hole is generated in the previous place of the electron in the VB. This hole can be modeled as a point of positive charge. Due to Coulombic attraction, the electron-hole interaction can be modeled as a quasi-particle referred to as an exciton. Coulombic attraction can be quantified in part as the exciton binding energy; this can allow energy levels to exist below the conduction band. Once formed, excitons have two quantities. The first is the pseudomomentum of the electron-hole pair. This is the vector sum of the individual electron and hole momenta. This allows the exciton to be modeled as traveling through the structure of the solid. The second quantity is relative momentum, which determines the internal structure and classification of the exciton. Excitons are generally classified into two types: a Frenkel exciton or a Mott-Wannier exciton.

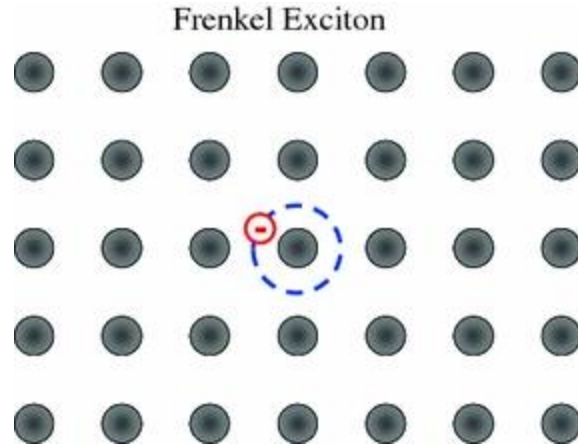


**Figure 10.** Schematic illustration of a tightly-bound exciton (Frenkel exciton) localized on one atom in a crystal. Reprinted with permission from reference 46. Copyright 2016 Springer Nature.<sup>46</sup>

Frenkel excitons are tightly bound excitons localized to a single point in the crystal lattice. The radius of the said exciton is approximately equal to interatomic spacing.<sup>47</sup> These are common in high band gap crystals, such as alkali halides. They are also commonly seen in organic crystals or noble gas crystals.

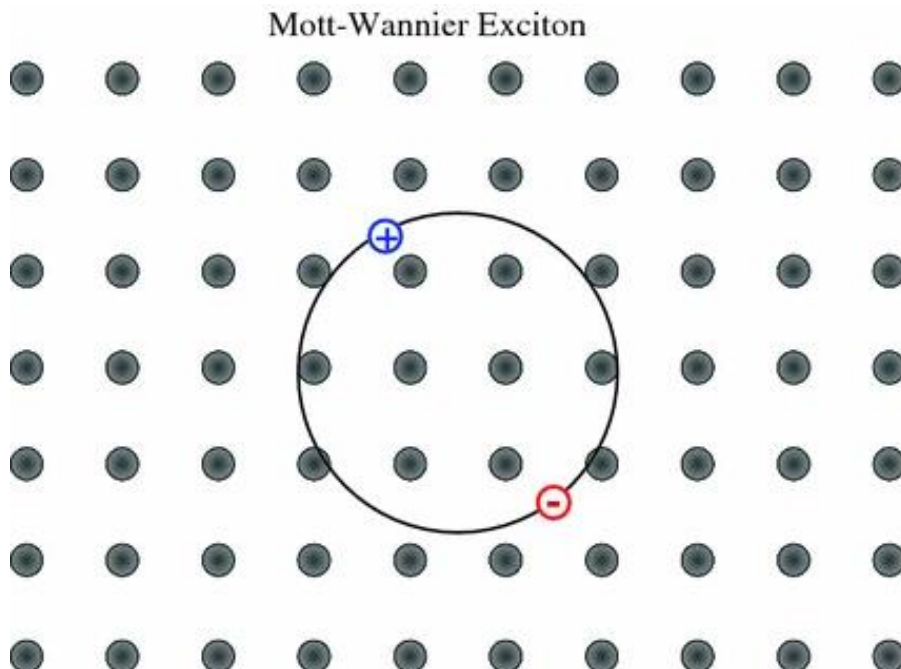


**Figure 11.** Schematic illustration of a weakly bound exciton (Mott-Wannier exciton) delocalized over several atoms in the crystal. Reprinted with permission from reference 46. Copyright 2016 Springer Nature.<sup>46</sup>

In contrast to Frenkel excitons, Mott-Wannier excitons are weakly bound and delocalized over an area larger than the lattice constant of the crystal. This exciton is modeled as a two-particle system that is weakly interacting.<sup>46</sup> These excitons are commonly observed in semiconducting materials such as GaN or CdTe. The binding energy is often in the single to double-digit mEv range, substantially lower than what is commonly seen in Frenkel excitons.<sup>47</sup> When an exciton has low binding energy and can move freely through a crystalline lattice, it is considered to be a free exciton. If the exciton is heavily localized to a small area of the lattice, such as being localized on a defect, it is considered a bound exciton.

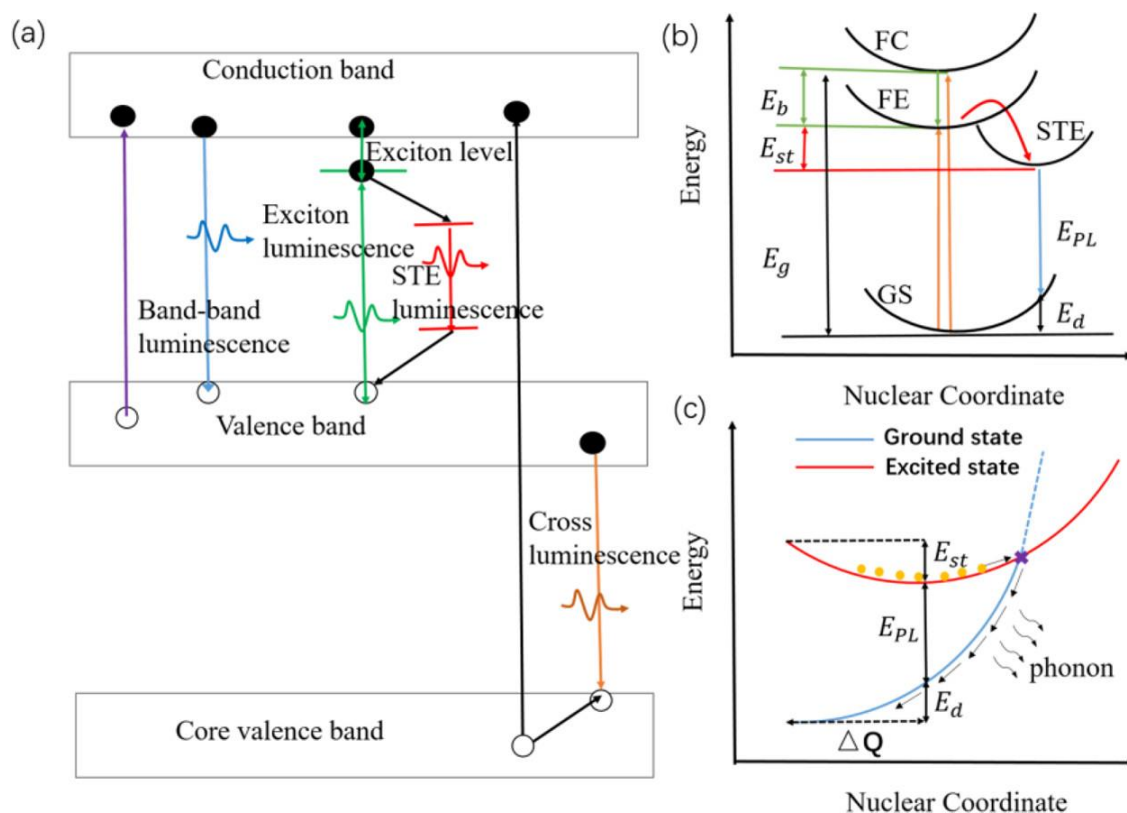


**Figure 12.** (a) Schematic of various intrinsic photoluminescence phenomena, including band-to-band luminescence, exciton luminescence, STE luminescence, and cross luminescence. (b) Schematic of the energy level structure of STE (GS, ground state; FE, free exciton state; FC, free carrier state; STE, self-trapped exciton state;  $E_g$ , bandgap energy;  $E_b$ , exciton binding energy;  $E_{st}$ , self-trapping energy;  $E_d$ , lattice deformation energy;  $E_{PL}$ , emission energy). (c) Schematic of the nonradiative recombination process for STE when  $S$  is large. Orange circles represent excited electrons. Reprinted with permission from reference 48. Copyright 2016 American Chemical Society.<sup>48</sup>

Returning to the topic of photoluminescence, the process begins with the excitation of an electron to the VB from the CB. The now-formed exciton will interact with vibrations in the crystal lattice (referred to as phonons). A formed exciton can recombine by the excited electron returning to the bound hold in the VB from the CB. This transition emits a photon with energy equal to the difference between the excitonic state and VB. The process can be seen above in Figure 12. In excitonic photoluminescence, the energy level of the emitted light is lower than that of the absorbed light; the emission energy is equal to the difference between the band gap and the exciton binding energy. The emission profile of materials that have free-exciton derived emission is often characterized by a narrow full width at half maximum (FWHM) and having a relatively short lifetime on the scale of picoseconds to nanoseconds. In free exciton emission, the Stoke's shift, or absorption and emission energy difference, is relatively small.

While many emission mechanisms are relevant to low-dimensional metal halides, two, in particular, will be covered in this background section: defect emission and self-trapped exciton emission. Defect emission is a form of extrinsic emission where an exciton localizes on a defect or imperfection in the crystal lattice. A typical example is surface halide vacancies where exposure to vacuum, environmental effects, or other phenomena will leave vacancies where halides should be present. This emission is characteristically below the band gap with a profile that can take many different forms. The emission can be broad or have multiple shoulders if multiple defect sites are present. One method to differentiate defect emission from intrinsic emission is excitation power-dependent photoluminescence.<sup>49, 50</sup> In this method, excitation power is increased, and the corresponding photoluminescence intensity is integrated and fitted to a power growth function. If the line is linear, then the emission is said to be intrinsic to the material. However, if at high-power excitation, the emission intensity begins to saturate, then the emissive defect sites are also being

saturated, and therefore the emission is extrinsic.

The other emission mechanism relevant to this work is self-trapped excitons, more commonly seen in recent years than years prior. A flexible crystal lattice deforms upon interaction with a charge carrier (electron/hole) in this emission mechanism. This self-trapped exciton (STE) is similar in nature to that of a small polaron. The charge carrier distorts the lattice, which leads to the creation of a local potential well. The charge carrier is trapped by its own distortion in the potential well. The exciton, in this case, is considered a self-trapped exciton (STE). Upon recombination, the photoluminescence emission of an STE can differ substantially from a FE. Since the FE and STE exist in thermal equilibrium as a distribution of locally disordered states, the photoluminescence emission is often quite broad, and the lower energy of the exciton leads to a large Stoke's shift.<sup>51</sup> A visual comparison is seen above in Figure 12 (a). Another characteristic of STE-derived emission is longer lifetimes, often in the nanosecond to microsecond range. When exposed to different excitation wavelengths, the overall profile of the emission does not shift, and one does not expect the appearance of new shoulders, indicating other emission mechanisms present. When lowering the temperature of a sample, most emission mechanisms lead to an increase in photoluminescence emission intensity; however, in STEs, it is not uncommon for the emission intensity to drop as structural deformation requires overcoming a thermal barrier to occur.<sup>52, 53</sup> With excitation power-dependent photoluminescence measurements, STEs behave similarly to other intrinsic mechanisms and have a linear response.

One significant benefit of a material with STE photoluminescence is that the efficiency of downconversion can be quite high. The absolute photoluminescence quantum yield (PLQY) is a key metric by which down-conversion materials are compared. In PLQY measurements, an integrating sphere is used to determine the number of photons emitted and absorbed by a sample.

The ratio of the number of photons at a particular emission wavelength over the number of photons absorbed at the excitation wavelength is PLQY. Materials with high PLQY values are often used as phosphors, discussed in the next section, and implemented in other technologies. It was the high PLQY values in  $\text{Cs}_3\text{Cu}_2\text{I}_5$ , that inspired part of the research in chapters 2 and 3.

### **1.5 Applications of photoluminescence in metal halides**

While it may not be apparent, photoluminescent materials and technology incorporating them are commonly found in many household devices. As mentioned in the first section, solid-state lighting often relies on photoluminescent materials in the form of a phosphor. The term phosphor refers to a wavelength down-converting material; in a standard LED lightbulb, there typically is a yellow phosphor layer on top of a blue LED. This is one of the two common ways to produce white light needed for residential and commercial lighting. The other standard method is to use a UV LED with a combination of phosphors. This gives access to a broader color gamut needed to fulfill the lighting needs of different environments, such as an office or restaurant lighting. A comparison between the two phosphor designs is seen below in Figure 13.

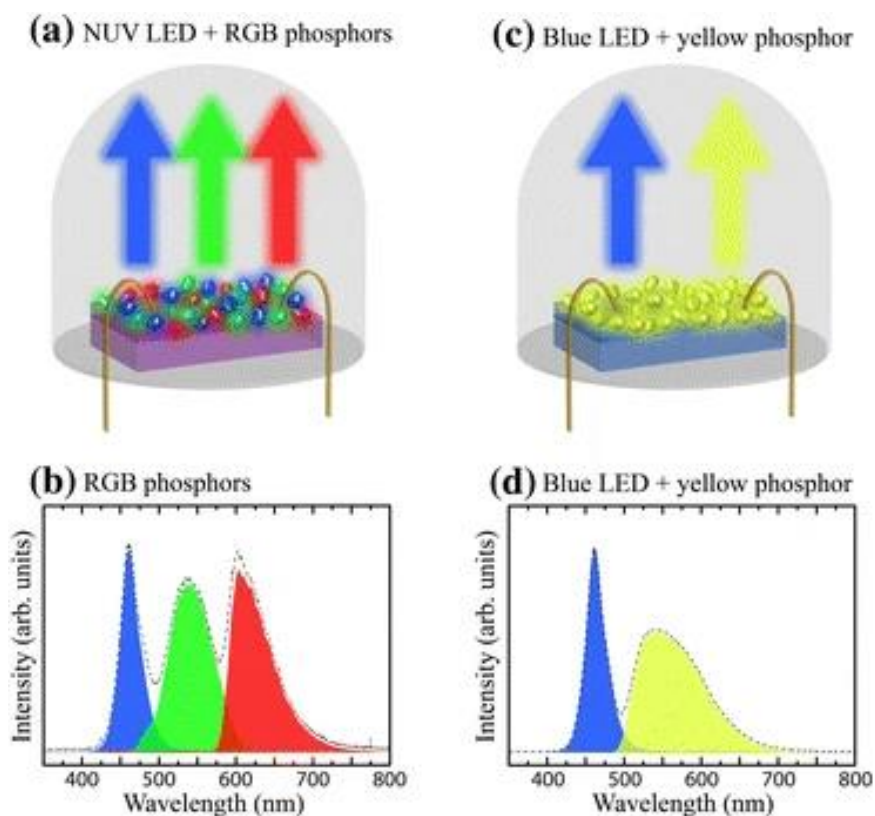


**Figure 13.** Schematic depiction of pcWLEDs based on a a NUV-LED and a mixture of RGB phosphors, and c a blue LED combined with a yellow phosphor, and their corresponding emission spectra in (b) and (d). Reprinted with permission from references 54 and 55. Copyright 2016 Springer Nature.<sup>54, 55</sup>

In order for a phosphor to be considered viable for future commercialization, three key metrics are considered.<sup>55</sup> The first is the efficiency, or more specifically, the absolute PLQY of material from the excitation source to the desired emission profile. This is more specific than simply the highest obtainable PLQY, as the efficiency often varies as excitation energy changes. A material might have great PLQY values from a 220 nm excitation source, but if a UV chip of the energy cannot be made, then the PLQY value is not applicable. The other consideration from PLQY is that only the emission within the visible light region is applicable. If the emission is so broad that it extends into the NIR region, the PLQY value is overestimated.<sup>8</sup>

The following key metric for a phosphor is stability. This broad category encompasses multiple stability types, including environmental and thermal stability. Many commercialized RE-

doped oxides have environmental stability issues, specifically hygroscopicity, where the materials absorb water from the air, leading to degradation. These issues can be overcome with encapsulation or mixing the phosphor into a polymer host material, however, added manufacturing complexity is less desirable. Thermal stability is a problem where as the material is heated, it may change the emission profile or, even worse, degrade into a non-luminescent compound. The standard for stability is a minimum of 353 K; however, a higher temperature allowance is more desirable as it can open up more use cases or make manufacturing more manageable.<sup>8</sup> Thermal stability is a category in which RE-doped oxides often outperform their metal halide counterparts.

The last key metric is dependent on the design of the LED-phosphor combination that is being implemented. If targeting a UV LED with three phosphors, the phosphors in question should have high color purity and be at the edge of the RGB triangle for the particular application. This color purity is plotted on a CIE, which displays how any particular emission spectrum looks to the human eye from a single point on a color palette. Many RGB triangles can be drawn on a CIE plot; however, the common ones include NTSC, which is the old television standard in the US, or the Rec. 2020, which is the new 2020 tv display standard. If three phosphors are at the corner of an RGB triangle, then any color within that triangle can be easily reproduced. For example, in Figure 14 below, the Rec. 2020 triangle is drawn, which requires a green phosphor with emission near pure 530 nm.



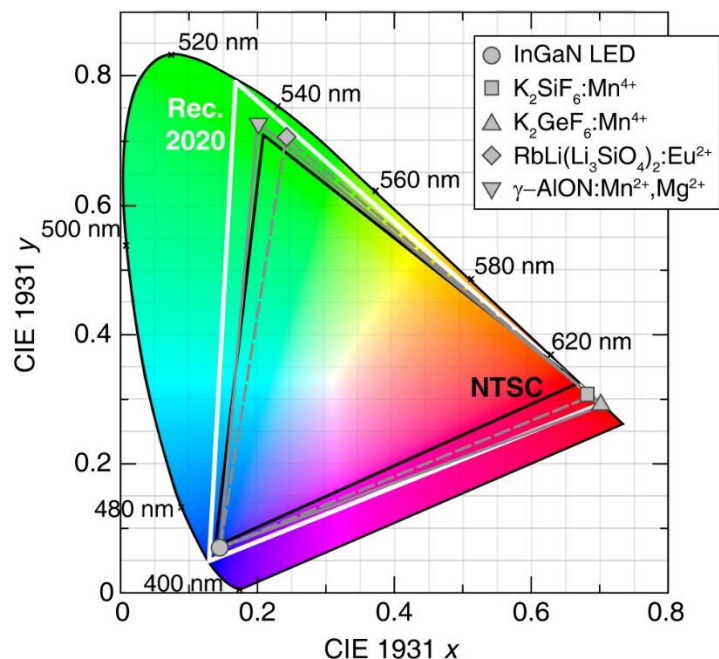


**Figure 14.** Color gamut produced by an InGaN LED (circle),  $\text{K}_2\text{SiF}_6:\text{Mn}^{4+}$  (square), and  $\text{RbLi}(\text{Li}_3\text{SiO}_4)_2:\text{Eu}^{2+}$  (diamond), indicated by the gray dashed line, having an overlap area of 76% with the Rec. 2020 standard color gamut (white) when plotted on the 1931 CIE XYZ color space. The overlap area can be improved to 85% by using an InGaN LED,  $\text{K}_2\text{GeF}_6:\text{Mn}^{4+}$  (up-triangle), and  $\gamma\text{-AlON}:\text{Mn}^{2+}, \text{Mg}^{2+}$  (down-triangle). The NTSC color gamut (black) is provided for reference. Reprinted and adapted with permission from reference 8. Copyright 2022 American Chemical Society.<sup>8</sup>

When utilizing a single phosphor, a prominent target is single-phase white light emission. In this design, a UV or blue-emitting LED is combined with one phosphor that can imitate broadband white light emission seen in a traditional incandescent bulb. The emission spectrum needs to be so broad that it can cover the entire visible spectrum. The key metric is the color rendering index (CRI) or color quality scale (CQS).<sup>8</sup> Both measure how well a color can be rendered when illuminated by the LED-phosphor combination. If the CRI or CQS is poor, a fruit may look slightly off or unappetizing. It can also make it hard to differentiate colors under a poor CRI compound.

Beyond solid-state lighting and phosphors, many other photoluminescence applications are utilized in the modern world. An example is the use of anti-counterfeiting inks in currency

production. In many high-value currencies, the physical notes will photoluminesce when exposed to UV light. Clerks can check this visually in a matter of seconds to ensure that a bill is legitimate. The United States utilizes this technology on the new \$100 bills. When designing materials for luminescent ink applications, many requirements carry over from LED phosphors. The main difference is that instead of a particular emission spectrum, one will generally optimize for long-term stability and durability.

In conclusion, the background information for the work in the following chapters has been laid out above. Chapter 2 provides insight into the  $A_2CuX_3$  family of copper (I) halides and the effects of elemental substitution on optical properties and environmental stability. Chapter 3 follows by investigating the nature of multiple photoluminescent emission mechanisms in the related  $A_2AgX_3$  family. Next, chapter 4 explores the concept of using organic cations as the emission source instead of the widespread reliance on metal halide polyhedra. Finally, chapter 5 concludes by laying out future work and directions.

## **Chapter 2: Development of Ternary Copper Halides for Ultrabright Blue Emission**

As discussed in chapter 1, copper(I) halides are an emerging area with the potential to be lead-free, solution-processable alternatives for solid-state lighting. However, prior to this work, few papers thoroughly investigated the impact of elemental substitution and the complete emission mechanism. Chapter 2 below delves into such topics by using the family  $A_2CuX_3$  as a model to understand the intricacies of the system. The first section utilizes Rb as the A cation and is the introduction to the family. While the optical properties were impressive, the stability left large areas for potential improvement. This was remedied in the second section of the chapter by replacing Rb with K, leading to significant stability improvements. This work has been summarized as publications in *Advanced Optical Materials* and *Chemistry of Materials*.<sup>43, 56</sup>

### **2.1 All-inorganic $Rb_2CuCl_3$ and $Rb_2CuBr_3$ for Blue Photoluminescence**

#### **2.1.1 Introduction**

The United States Department of Energy (DOE) projects an estimated energy cost savings of \$630 billion from 2015 to 2035 if reliable solid-state lighting technologies can be developed and DOE goals are met.<sup>57</sup> For the cost-effective implementation of light-emitting diodes (LEDs), development of new inexpensive light emitters is an urgent need. Owing to their outstanding photophysical properties including tunable band gaps and emission colors, high photoluminescent quantum yields (PLQY) and excellent color purity, metal halide perovskite LEDs (PeLEDs) have been attracting increased attention in recent years.<sup>58, 59</sup> Thus, high external quantum efficiency (EQE) green and near-infrared (NIR) light-emitting PeLEDs have already been developed including a recent report of a NIR-emitting PeLED with a high EQE of 21.6%.<sup>60</sup> However, the

development of efficient blue-emitting halides has historically lagged behind, although recent reports show some progress in this area.<sup>58, 59</sup> Notable examples include highly efficient blue emission with PLQY over 70% from CsPbBr<sub>3</sub> and its mixed analog CsPb(Br/Cl)<sub>3</sub>,<sup>61</sup> Cu<sup>2+</sup>-doped CsPb<sub>1-x</sub>Cu<sub>x</sub>X<sub>3</sub> (X = Br, Cl) quantum dots,<sup>62</sup> and from exfoliated crystals of (C<sub>6</sub>H<sub>5</sub>CH<sub>2</sub>NH<sub>3</sub>)<sub>2</sub>PbBr<sub>4</sub>.<sup>58</sup> These materials have also been incorporated into blue PeLEDs with external quantum efficiency (EQE) values up to 1.5% for PEA<sub>2</sub>A<sub>n-1</sub>Pb<sub>n</sub>X<sub>3n+1</sub><sup>59</sup> and 9.5% for Cs<sub>x</sub>FA<sub>1-x</sub>PbBr<sub>3</sub>.<sup>63</sup> Despite the remarkable progress in the last few years, these deep blue emitters are predominantly low-dimensional or nanostructured lead halide perovskites, which usually suffer from the lead toxicity and poor stability.<sup>58, 59</sup> In principle, other Pb-free low-dimensional halides should also demonstrate increased charge localization and enhanced excitonic properties observed in lead halide perovskites, yielding efficient blue emitters that are free of toxic Pb such as in the case of recently reported copper halides Cs<sub>3</sub>Cu<sub>2</sub>X<sub>5</sub> and CsCu<sub>2</sub>X<sub>3</sub>.<sup>24, 64</sup> In this work, we provide further evidence of the validity of this conjecture through preparation of all-inorganic nontoxic Rb<sub>2</sub>CuX<sub>3</sub> (X = Cl, Br), which exhibit near-unity PLQY blue emission. The remarkably high PLQY demonstrated by these compounds is attributed to the creation of self-trapped excitons (STEs) within their one-dimensional (1D) crystal structure. Moreover, for Rb<sub>2</sub>CuCl<sub>3</sub>, our preliminary results indicate a net phonon-assisted anti-Stokes photoluminescence (ASPL), and an optical cooling efficiency of ~ 32% at room temperature. Note that optical cooling by ASPL (also known as upconversion PL) was previously reported in several rare earth-based materials,<sup>65</sup> semiconductors such as CdS<sup>66</sup> and more recently in a few hybrid organic-inorganic<sup>67, 68</sup> and all-inorganic perovskites type materials.<sup>69</sup> This process takes place as a result of a light excitation energy below the band gap of the material producing a non-equilibrium electron distribution. Then, the exciting photon first interacts with the lattice leading to phonon absorption followed by blue-

shifted luminescence. This mechanism leads to the extraction of the heat energy from the lattice by emitting a higher energy photon, which cools down the material. The advantages of metal halides is their high PLQY photoemission properties and the relatively low trap-states density which are important parameters for optical cooling.<sup>70</sup> For example, exceptionally strong ASPL and a remarkable optical cooling of 58.7 K was observed in the exfoliated crystals of two-dimensional (2D) layered perovskite  $(\text{C}_6\text{H}_5\text{C}_2\text{H}_4\text{NH}_3)_2\text{PbI}_4$ .<sup>67</sup>

## **2.1.2 Experimental Synthesis and Methods for $\text{Rb}_2\text{CuX}_3$**

### **2.1.2.1 Reactants used in Rb**

The starting reagents were used as received: (i) rubidium chloride (99%, Acros Organics), (ii) copper(I) chloride (>99%, Sigma-Aldrich), (iii) rubidium bromide (99%, Alfa Aesar), (iv) copper(I) bromide (>99%, Alfa Aesar), (v) hydrochloric acid (37% wt, Sigma-Aldrich).

### **2.1.2.2 Synthesis of $\text{Rb}_2\text{CuBr}_3$ .**

A 2:1 stoichiometric amount of RbBr and CuBr were ground under an inert atmosphere, pressed into a pellet, then sealed under vacuum. The pellet was annealed at 225°C for 48 hours and slowly cooled to room temperature over 18 hrs. A second grinding and annealing was performed to ensure the homogeneity of the resulting product.

### **2.2.2.3 Synthesis of $\text{Rb}_2\text{CuCl}_3$ .**

Solid-state synthesis following the above described procedure for  $\text{Rb}_2\text{CuBr}_3$  was used to obtain a polycrystalline powder sample of  $\text{Rb}_2\text{CuCl}_3$ . For single crystal growth, a 2:1 stoichiometric amount of RbCl and CuCl w

ere separately dissolved in sparged concentrated HCl, under inert atmosphere. Then, the CuCl solution was added dropwise to the RbCl solution and heated at 95°C for 3 hours followed

by a slow cooling to room temperature. Colorless needle-like crystals of  $\text{Rb}_2\text{CuCl}_3$  were formed overnight (Figure 16).

#### **2.1.2.4 Powder X-ray Diffraction (PXRD) Measurements.**

To check the phase identity and purity of  $\text{Rb}_2\text{CuX}_3$  powder samples, we measured PXRD on a Rigaku Miniflex600 equipped with D/tex detector and a Ni-filtered  $\text{Cu-K}\alpha$  radiation source. Data were collected at room temperature in the  $3\text{--}90^\circ$  ( $2\theta$ ) range, with a step size of  $0.02^\circ$ . The obtained PXRD data were fitted using the Pawley refinement method.<sup>71</sup> we confirmed the good matching between the measured and calculated PXRD patterns of  $\text{Rb}_2\text{CuX}_3$  ( $\text{X} = \text{Cl}, \text{Br}$ ). Presence of a minor impurity peak at  $\sim 26^\circ$  (Figure A1) corresponding to the unreacted starting material  $\text{RbBr}$  was noted for the  $\text{Rb}_2\text{CuBr}_3$  samples, which is consistent with a previous report on the  $\text{Rb}_2\text{CuBr}_3$  preparation.<sup>28</sup> A PXRD pattern measured on a single crystal of  $\text{Rb}_2\text{CuCl}_3$  was fully indexed using the single crystal X-ray diffraction (SXR) data (Figure A2).

To test their air-stability, samples were left on a laboratory bench in ambient conditions and periodic PXRD were performed. Lead chlorides and bromides are known to exhibit high air stability compared to lead iodides.<sup>72</sup> Indeed, single crystals of  $\text{Rb}_2\text{CuCl}_3$  do not exhibit any noticeable degradation when left in ambient air (Figure A3). However, polycrystalline powder of  $\text{Rb}_2\text{CuCl}_3$  kept in ambient air shows noticeable signs of degradation after one day with decomposition products including  $\text{Rb}_2\text{CuCl}_4 \cdot 2\text{H}_2\text{O}$  and  $\text{RbCl}$  (Figure A4). The formation of the hydrate product  $\text{Rb}_2\text{CuCl}_4 \cdot 2\text{H}_2\text{O}$  is indicative of the fact that the material's stability depends on the humidity of the environment. The oxidation of Cu results in a visual change of powder color from white to light green (Figure A5a-b). In contrast,  $\text{Rb}_2\text{CuBr}_3$  shows a markedly better air stability with no significant changes up to 1 week in air, however, prolonged exposure over a period of 2 months leads to the emergence of  $\text{RbBr}$  as the major phase (Figure A4). Note that it

has been previously reported that CuBr is more stable than CuCl in ambient atmosphere,<sup>73,74</sup> which is consistent with our observation of better air stability of Rb<sub>2</sub>CuBr<sub>3</sub> compared to Rb<sub>2</sub>CuCl<sub>3</sub>.

#### **2.1.2.5 Single crystal X-ray Diffraction (SXRD) Measurements.**

Single crystal X-ray diffraction (SXRD) data were collected on a Bruker D8 Quest with a Kappa geometry goniometer, an Incoatec Imus X-ray source (graphite monochromated Mo-K $\alpha$  ( $\lambda$  = 0.71073 Å) radiation), and a Photon II detector. The data were corrected for absorption using the semiempirical method based on equivalent reflections, and the structures were solved by intrinsic phasing methods (SHELXT) as embedded in the APEX3 v2015.5-2 program. Site occupancy factors were checked by freeing occupancies of each unique crystallographic site. All atoms were refined with anisotropic displacement parameters and site occupancy factors were checked by freeing occupancies of each unique crystallographic site. Details of the data collection and crystallographic parameters are summarized in Table 1. Additional information on the crystals structures investigations can be obtained in the form of a Crystallographic Information File (CIF), which were deposited in the Cambridge Crystallographic Data Centre (CCDC) database (deposition number 1955726).

#### **2.1.2.6 Thermogravimetry and Differential Scanning Calorimetry (TGA/DSC) Measurements.**

Simultaneous thermogravimetric analysis and differential scanning calorimetry (TGA/DSC) were measured on ~10 mg of polycrystalline powder samples of Rb<sub>2</sub>CuX<sub>3</sub> on a TA Instruments SDT 650 thermal analyzer system. Samples were heated up at a rate of 5 °C/min from 25 to 475 °C under an inert flow of dry nitrogen gas (flow rate of 100 mL/min)..

It is worth noticing that in practical applications, such as down conversion phosphors for optically pumped white LEDs, the device temperature under continuous operation often exceeds

70 °C, a fact that makes the thermal stability of the emitter material an important parameter for consideration. Unlike most hybrid organic-inorganic lead halide perovskites,  $\text{Rb}_2\text{CuX}_3$  show no significant weight loss up to 475°C (Figure A6), which is in agreement with reports on similar all-inorganic metal halides such as  $\text{Cs}_3\text{Cu}_2\text{Br}_{5-x}\text{I}_x$ <sup>24</sup> and  $\text{Rb}_4\text{Ag}_2\text{BiBr}_9$ .<sup>75</sup> Moreover, DSC data show that  $\text{Rb}_2\text{CuCl}_3$  and  $\text{Rb}_2\text{CuBr}_3$  are thermally stable up to 274 and 271 °C, respectively, at which they undergo peritectic decompositions, which is in excellent agreement with the reported phase diagrams.<sup>34, 76</sup> The thermal properties of  $\text{Rb}_2\text{CuX}_3$  are similar to those reported in several metal halides all inorganic compounds such as  $\text{Cs}_2\text{SnI}_6$ .<sup>77</sup>

#### **2.1.2.7 Optical Measurements.**

Room temperature PL and PLE measurements were performed on polycrystalline powders of  $\text{Rb}_2\text{CuX}_3$  (X = Br, Cl) and single crystals of  $\text{Rb}_2\text{CuCl}_3$  on a Jobin Yvon Fluorolog-3 spectrofluorometer (HORIBA company) equipped with a Xenon lamp and a Quanta-φ integrating sphere using the two-curve method in a varied range from 280 to 860 nm. For lifetime measurements, a Time-Correlated Single Photon Counting (TCSPC) system including a DeltaHub DH-HT High throughput TCSPC controller and NanoLED NL-C2 Pulsed Diode Controller was used. For light source a 299 nm NanoLED diode was selected, which has a <1.2 ns pulse duration.

Additional confirmatory PLQY measurements were performed on single crystals of  $\text{Rb}_2\text{CuCl}_3$  using a Jobin Horiba FluoroMax4 equipped with a 150 W Xenon lamp and an R928 PMT detector. The Quanta-φ integrating sphere (15 cm) with a PTFE cup as the sample holder and a PTFE stub as the blank was used for the four-curve analysis. Typical methods used a 0.1 second integration time (0.5 nm increment) for the absorbance region and 0.1 second integration time (1 nm increment) for the luminescence region with a 3 nm bandpass on excitation and emission slits for both. When necessary, optical filters were used to attenuate the signal to



appropriate levels and to reduce scattering. Radiometric (red), sphere, and dark count corrections were applied during data acquisition, while corrections for neutral density and long pass filters and integration time differences were applied in the final calculation of PLQY in the FluorEssence™ analysis package for Quantum Yield (FluorEssence v3.8.0.60, Origin v8.6001).

Quantum yield is then determined by:

$$Quantum\ Yield = \left( \frac{Em_s - Em_b}{Ex_b - Ex_s} \right) * 100$$

where  $Ex_s$  and  $Ex_b$  are the integrated excitation profiles of the sample and the blank and  $Em_s$  and  $Em_b$  are the integrated emission profiles of the sample and blank respectively. An Area Balance Factor is applied in the FluorEssence software which accounts for changes in integration times between excitation and emission scans and for the use of neutral density filters.

#### **2.1.2.8 Computational Methods**

Our calculations were based on density functional theory (DFT) as implemented in the VASP code.<sup>78</sup> The kinetic energy cutoff of the plane-wave basis is 369 eV. The projector augmented wave method was used to describe the interaction between ions and electrons.<sup>79</sup> The unit cell contains four formula units of  $Rb_2CuX_3$  ( $X = Cl, Br$ ). The lattice parameters were fixed at the experimentally measured values while the atomic positions were optimized until the force on each atom is less than 0.02 eV/Å. A  $1 \times 5 \times 1$  supercell was used to model localized excitons in  $Rb_2CuCl_3$ . A single  $\Gamma$  point was used for Brillouin zone integration. The convergence test shows that doubling the k-point mesh density in the directions perpendicular to the 1D chain direction (axis b) results in a small change in the total energy (0.4 meV/atom), indicating negligible inter-chain coupling.

The electronic band structure of  $Rb_2CuCl_3$  and  $Rb_2CuBr_3$  were calculated using Perdew-Burke-Ernzerhof (PBE) exchange-correlation functional.<sup>80</sup> The band gap and excitonic properties

of  $\text{Rb}_2\text{CuCl}_3$  were further calculated using the more advanced hybrid PBE0 functional,<sup>81</sup> which has 25% non-local Fock exchange. The inclusion of a fraction of Fock exchange significantly improves the band gap energy<sup>81, 82</sup> and the description of charge localization in insulators.<sup>83, 84, 85</sup> Previous PBE0 calculations have provided critical understanding of the structural and electronic properties of self-trapped and dopant-bound excitons in halides.<sup>85, 86</sup> The total energy of an exciton was calculated by fixing the occupation numbers of the electron and hole-occupied eigenlevels [ $\Delta$  self-consistent field ( $\Delta$ SCF) method<sup>87</sup>]. The  $\Delta$ SCF method can be easily used in  $\text{Rb}_2\text{CuCl}_3$  because the electron and hole are both highly localized and each occupies one single eigenlevel deep inside the band gap.<sup>88</sup> The  $\Delta$ SCF method combined with the hybrid PBE0 functional allows excited-state structural relaxation and has shown accurate results in exciton excitation and emission energies in many compounds.<sup>88-91, 92</sup> Following Franck-Condon principle, the optical excitation and emission energies were obtained by calculating the total energy differences between the excited and the ground states using PBE0-optimized ground-state and excited-state structures, respectively.

### 2.1.3 Crystal Structure and Stability

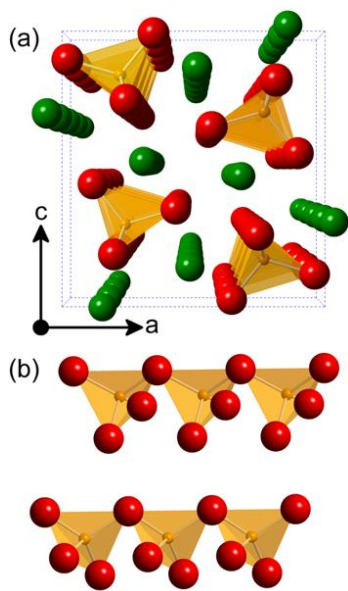


**Figure 15.** (a) A polyhedral view of the structure of  $\text{Rb}_2\text{CuX}_3$  projected along the  $b$ -axis, and (b) a close-up view of a segment of  $[\text{CuX}_3]^{2-}$  chains showing the corner-sharing connectivity of the  $\text{CuX}_4$  tetrahedra. Rb, Cu, and X are shown in green, yellow, and red, respectively.

$\text{Rb}_2\text{CuX}_3$  ( $X = \text{Br}, \text{Cl}$ ) crystallize in the orthorhombic space group  $Pnma^{28}$  featuring 1D  $[\text{CuX}_3]^{2-}$  chains separated by  $\text{Rb}^+$  cations (Figure 15 and Table 1). The anionic  $[\text{CuX}_3]^{2-}$  chains are made of corner-sharing  $[\text{CuX}_4]$  tetrahedra along the  $b$ -axis.  $\text{Rb}_2\text{CuX}_3$  can be prepared both as polycrystalline powder samples or grown as single crystals using solid-state synthesis and solvent evaporation techniques, respectively (Figure 16).

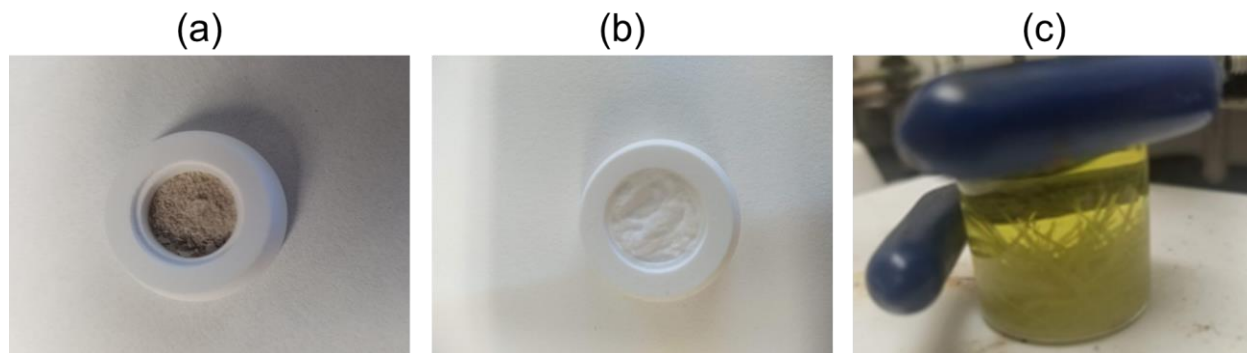


**Figure 16.** Photos of as-prepared polycrystalline powders of (a)  $\text{Rb}_2\text{CuBr}_3$  and (b)  $\text{Rb}_2\text{CuCl}_3$ , and (c) single crystals of  $\text{Rb}_2\text{CuCl}_3$ .

The presence of monovalent  $\text{Cu}^+$  cations in these materials and their ionic nature makes them susceptible to degradation in ambient air (Figures A3-4, see SI for further details) However, larger single crystals of  $\text{Rb}_2\text{CuCl}_3$  do not exhibit any noticeable degradation when left in ambient air (Figure A3). On the other hand, our thermogravimetric analysis (TGA) measurements suggest that unlike most hybrid organic-inorganic lead halide perovskites,  $\text{Rb}_2\text{CuX}_3$  show no significant weight loss up to  $475^\circ\text{C}$  (Figure A6), which is in agreement with the reports of improved thermal stability of all-inorganic metal halides such as  $\text{Cs}_3\text{Cu}_2\text{Br}_{5-x}\text{I}_x$ ,<sup>24</sup>  $\text{Rb}_4\text{Ag}_2\text{BiBr}_9$ ,<sup>75</sup> and  $\text{Cs}_2\text{SnI}_6$ .<sup>77</sup> Differential scanning calorimetry (DSC) data show that  $\text{Rb}_2\text{CuCl}_3$  and  $\text{Rb}_2\text{CuBr}_3$  have peritectic decompositions at  $274$  and  $271^\circ\text{C}$ , respectively, consistent with the reported phase diagrams.<sup>34, 76</sup>

**Table 1.** Selected single-crystal data and structure refinement parameters for Rb<sub>2</sub>CuCl<sub>3</sub>

Formula	Rb <sub>2</sub> CuCl <sub>3</sub>
Formula weight (g/mol)	340.83
Temperature (K)	100(2)
Radiation, wavelength (Å)	Mo Kα, 0.71073
Crystal system	Orthorhombic
Space group	Pnma
Z	4
Unit cell parameters (Å)	$a = 12.4457(5)$ $b = 4.19998(12)$ $c = 12.9345(5)$
Volume (Å <sup>3</sup> )	676.11(4)
Density ( $\rho_{\text{calc}}$ ) (g/cm <sup>3</sup> )	3.348
Absorption coefficient ( $\mu$ ) (mm <sup>-1</sup> )	18.585
$\theta_{\text{min}} - \theta_{\text{max}}$ (°)	2.27 – 30.53
Reflections collected	13558
Independent reflections	1145
$R^a$ indices ( $I > 2\sigma(I)$ )	$R_1 = 0.0178$ $wR_2 = 0.0545$
Goodness-of-fit on $F^2$	1.065
Largest diff. peak and hole (e <sup>-</sup> /Å <sup>3</sup> )	0.730 and -1.044

$${}^aR_1 = \sum ||F_0| - |F_c|| / \sum |F_0|; wR_2 = |\sum |w(F_0^2 - F_c^2)|^2 / \sum |wF_0^2|^{1/2}$$

where  $w = 1/|\sigma^2 F_0^2 + (AP)^2 + BP|$ , with  $P = (F_0^2 + 2F_c^2)/3$  and weight coefficients A and B

### 2.1.4 Optical Properties of $\text{Rb}_2\text{CuX}_3$

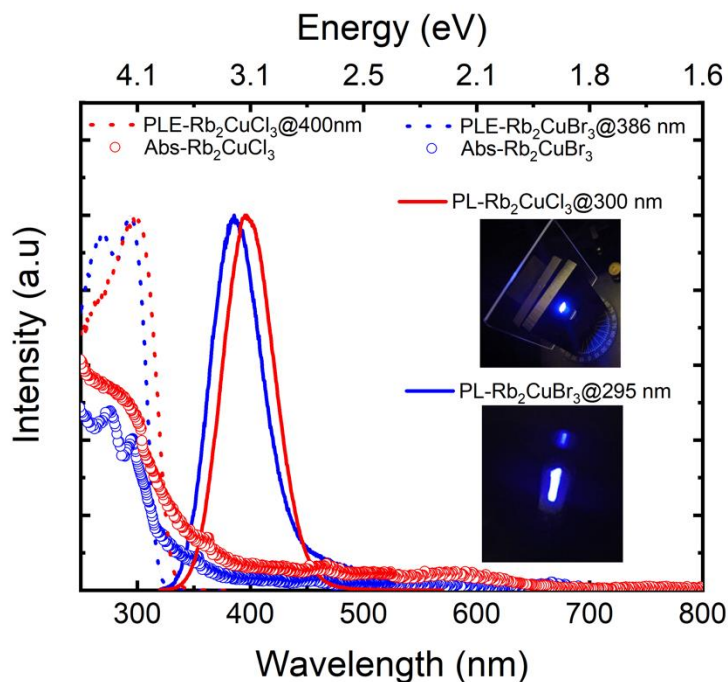


**Figure 17.** Room temperature optical absorption (circles), PLE (dashed lines) and PL (solid lines) of polycrystalline powders of  $\text{Rb}_2\text{CuBr}_3$  (blue) and  $\text{Rb}_2\text{CuCl}_3$  (red). The inset show the bright blue emission under UV irradiation.

Optical absorption spectra of polycrystalline powder samples of  $\text{Rb}_2\text{CuX}_3$  show two features at  $\sim 276$  and  $\sim 300$  nm. Upon UV irradiation, the room temperature PL spectra of polycrystalline powders of  $\text{Rb}_2\text{CuX}_3$  show a very bright blue emission (Figure 17). The PL maxima are located at  $\sim 385$  and  $395$  nm, with full width at half maximum (FWHM) values of 54 and 52 nm and relatively small Stokes shifts of 85 and 93 nm for  $\text{Rb}_2\text{CuBr}_3$  and  $\text{Rb}_2\text{CuCl}_3$ , respectively. Usually, low-dimensional (1D and 0D) metal halides materials emit strongly Stokes shifted spectra due to significant structural distortions in excited states.<sup>93</sup> In contrast, our PL results on  $\text{Rb}_2\text{CuX}_3$  are notably different for several reasons. First,  $\text{Rb}_2\text{CuX}_3$  are among the few blue emitters with a near UV excitation and relatively small Stokes shift blue emission,<sup>94</sup> which is advantageous given the small energy loss between photoluminescence excitation (PLE) and emission (PL) spectra.

Secondly, the measured PL linewidths of 54 and 52 nm for  $\text{Rb}_2\text{CuBr}_3$  and  $\text{Rb}_2\text{CuCl}_3$ , respectively, are among the lowest for highly-efficient blue emitting bulk samples.<sup>58</sup> Note that obtaining materials that combine efficient blue emission with narrow emission linewidth is a recognized challenge, and the best literature-reported narrow blue emitters are  $(\text{C}_6\text{H}_5\text{CH}_2\text{NH}_3)_2\text{PbBr}_4$  nanoplates and  $\text{CsPbX}_3$  quantum dots, which unlike our bulk samples are obtained through nanostructuring.<sup>58</sup> Finally, the visibly bright blue emission is corroborated by the high PLQY values of 64 and 85 % measured on polycrystalline powders of  $\text{Rb}_2\text{CuBr}_3$  and  $\text{Rb}_2\text{CuCl}_3$ , respectively (see Figure A7). PLE spectra measured on polycrystalline  $\text{Rb}_2\text{CuX}_3$  for emission wavelengths of 386 and 400 nm show maxima at 295 and 300 nm, accompanied with a shoulder at 270 and 265 nm for  $\text{Rb}_2\text{CuBr}_3$  and  $\text{Rb}_2\text{CuCl}_3$ , respectively, which coincide with the measured absorption spectra (see Figure 17). Furthermore, we also measured room temperature PL/PLE on single crystals of  $\text{Rb}_2\text{CuCl}_3$ , which match the PL/PLE of the bulk powder sample (see Figure A8). Importantly, a unity ( $\sim 100\%$ ) PLQY value was measured on single crystals of  $\text{Rb}_2\text{CuCl}_3$  (see Figure A7), which is the record high for known blue emitters.<sup>24, 58</sup> The difference in the measured PLQY values with respect to the nature of sample (i.e., PLQY of 85% for a powder sample vs 100% for single crystals) is mainly due to the fact that single crystals contain less surface defects than polycrystalline powders and thin films. This is also consistent with the literature results on other copper halides<sup>23</sup> including PLQY values of 60% and 90% reported for thin films and single crystals of  $\text{Cs}_3\text{Cu}_2\text{I}_5$ , respectively.<sup>24</sup> However, despite record high PLQY value for  $\text{Rb}_2\text{CuCl}_3$ , its photostability must be further improved for device considerations as our periodic measurements of PLQY under continuous irradiation at its  $\text{PLE}_{\text{max}}$  yielded  $\sim 75\%$  loss in PLQY in 1 hour (see Figure A9).

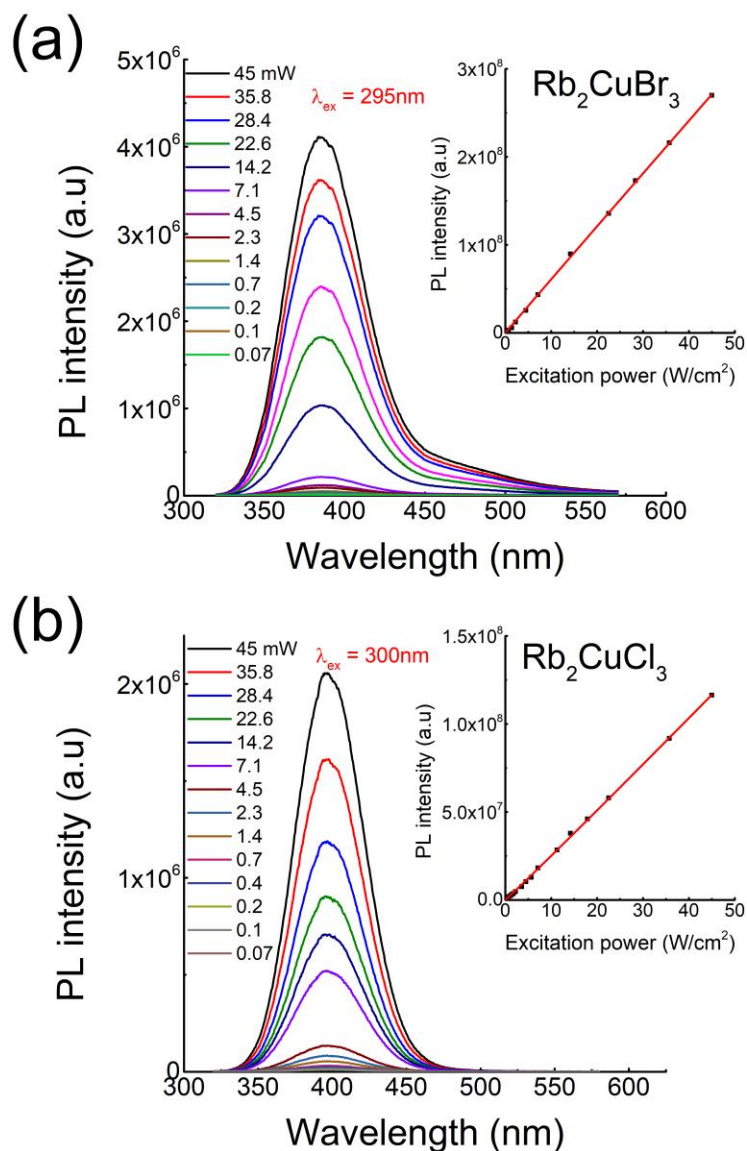


**Figure 18.** Power dependence PL spectra for (a)  $\text{Rb}_2\text{CuBr}_3$  and (b)  $\text{Rb}_2\text{CuCl}_3$ . Insets show the corresponding plots of the PL intensity vs excitation power.

To understand the photophysical origin of the highly efficient blue-emission of  $\text{Rb}_2\text{CuX}_3$ , we measured its excitation and power dependence PL spectra at ambient temperature (see Figure A10). Results show that  $\text{Rb}_2\text{CuX}_3$  compounds have excitation-dependent emission shapes and a linear dependence of the PL intensity as a function of excitation power. This fact suggests the intrinsic nature of  $\text{Rb}_2\text{CuX}_3$  blue emission, and the absence of saturation at high excitation power excludes the presence of permanent defects emissions.<sup>75, 95</sup> Therefore, we attribute this intense



blue-emission to STEs often observed in metal halide all-inorganic systems.<sup>22-24, 75, 96</sup>

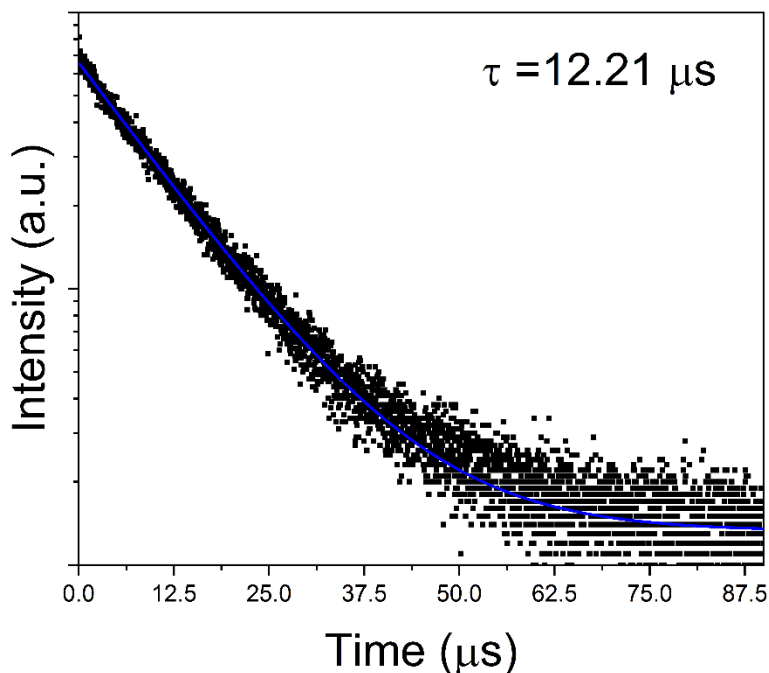


**Figure 19.** Time-resolved PL decay curve of  $\text{Rb}_2\text{CuCl}_3$  crystals at room temperature.

Based on our single exponential fitting of the time-resolved PL data for  $\text{Rb}_2\text{CuCl}_3$  single crystals (Figure 19), a decay lifetime of  $12.21 \mu\text{s}$  was extracted. Long lifetime emission from STEs have also been reported for other metal halides including the related  $\text{Cs}_3\text{Cu}_2\text{I}_5$ . On the other hand, PL of  $\text{Rb}_2\text{CuX}_3$  can also be compared to that of binary copper halides.<sup>23</sup> It has been previously reported that  $\gamma\text{-CuX}$  ( $X = \text{Br}, \text{Cl}$ ) have significant light emission properties in the 300-400 nm spectral range, suitable for novel UV/blue light applications.<sup>73, 74, 97</sup> Here, we also measured the room temperature emission spectra of  $\gamma\text{-CuX}$  (Figure A11), that show a UV-blue light emission with the presence of two PL peaks at 384 and 395 nm for  $\gamma\text{-CuCl}$  and at 422 and 433 nm for  $\gamma\text{-CuBr}$ , in agreement with the previous reports.<sup>97, 98</sup> However, the measured PLQY values of  $\gamma\text{-CuX}$  are very low ( $< 0.5\%$ ). The remarkable enhancement of emission efficiency of the ternary halides  $\text{Rb}_2\text{CuX}_3$  compared to the binary parents  $\text{CuX}$  is mainly due to the quantum confinement effect

resulting from the reduction of structural dimensionality from 3D corner-sharing tetrahedra for  $\gamma$ -CuX (the zincblende structure) to 1D for  $\text{Rb}_2\text{CuX}_3$ , a well-known effect that results in higher exciton binding energies ( $E_b$ ) and improved exciton stabilities.<sup>50, 72, 99-101</sup> Here, based on the optical absorption measurements for  $\text{Rb}_2\text{CuCl}_3$  (Figure 17), the exciton binding energy could be estimated as  $E_b = E_g - E_{\text{ex}} = 390 \text{ meV}$ ,<sup>102</sup> where  $E_g = 4.49 \text{ eV}$  and  $E_{\text{ex}} = 4.10 \text{ eV}$  are the band gap energy and the exciton energy, respectively. The high  $E_b$  values are characteristic of low dimensional metal halide materials.<sup>64, 101, 103</sup>

### 2.1.5 Band Structure and PDOS Calculations

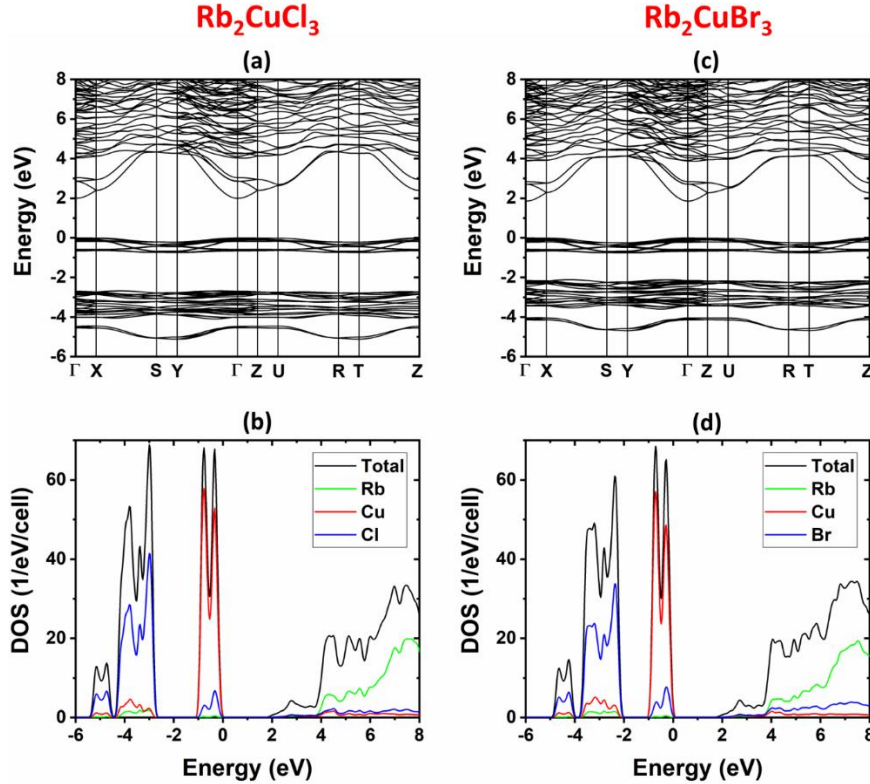


**Figure 20.** Electronic band structure and density of states (DOS) for (a-b)  $\text{Ru}_2\text{CuCl}_3$  and (c-d)  $\text{Ru}_2\text{CuBr}_3$ . Note that the band gaps are underestimated due to the band gap error in the PBE calculation.

To further investigate the main origin of the ultrabright blue emission of  $\text{Rb}_2\text{CuX}_3$ , we

carried out DFT calculations (SI). Figure 20 shows the calculated electronic band structure and density of states (DOS) plots.  $\text{Rb}_2\text{CuBr}_3$  has a direct band gap at the  $\Gamma$  point. In contrast, the band gap of  $\text{Rb}_2\text{CuCl}_3$  is slightly indirect – the conduction band minimum (CBM) is at the  $\Gamma$  point while the valence band maximum (VBM) is located between the  $\Gamma$  and the Z points. However, the top of the valence band between the  $\Gamma$  and the Z points is extremely flat as can be seen in Figure 20a; the energy of the top valence band is changed by only 0.002 eV from the  $\Gamma$  point to the VBM, which is negligible. Thus, the band gap of  $\text{Rb}_2\text{CuCl}_3$  is nearly direct. The DOS projected to each atomic species (Figures 20b-d) shows that the valence band is mainly made up of Cu-3d orbitals hybridized with halogen p orbitals while the conduction band has a mixed character of Cu-4s, Rb-5s, and halogen-p. The valence band is narrow, resulting from the localized nature of Cu-3d orbitals, while the conduction band is dispersive not only along the 1D chain direction (Y axis) but also along directions perpendicular to the chain. Thus, the electronic structure of  $\text{Rb}_2\text{CuCl}_3$  and  $\text{Rb}_2\text{CuBr}_3$  do not have the 1D character.

The calculated band gaps of  $\text{Rb}_2\text{CuCl}_3$  and  $\text{Rb}_2\text{CuBr}_3$  are 1.99 eV and 1.85 eV, respectively, which are expected to be underestimated due to the well-known band gap error in the PBE calculation but are consistent with previous PBE calculations.<sup>104</sup> Since the valence bands of both halides have mainly the Cu-3d character, their band gaps are weakly dependent on the type of the halogen atom. The Br-4p band in  $\text{Rb}_2\text{CuBr}_3$  is closer in energy to the Cu-3d band than the Cl-3p band in  $\text{Rb}_2\text{CuCl}_3$ , thus having a stronger hybridization with the Cu-3d band. As a result, the Cu-3d band in  $\text{Rb}_2\text{CuBr}_3$  is pushed up higher than that in  $\text{Rb}_2\text{CuCl}_3$ , resulting in a higher VBM and a slightly smaller band gap.

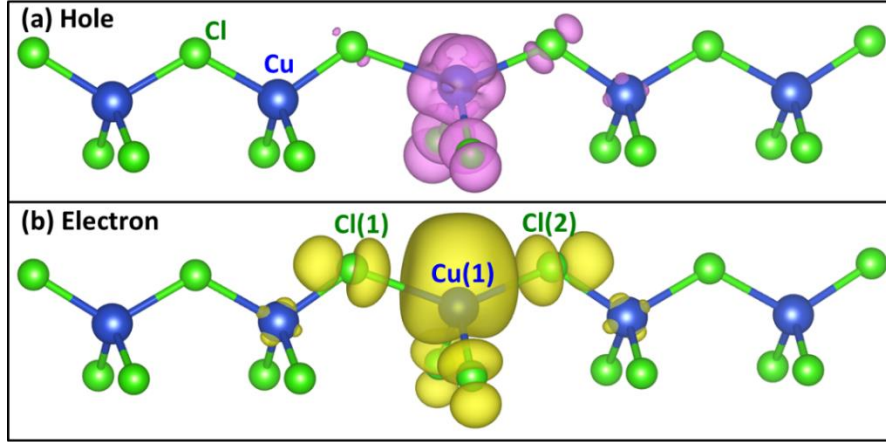


**Figure 21.** The partial charge densities of the hole (a) and the electron (b) in the exciton in  $\text{Rb}_2\text{CuCl}_3$ . The Cu and the Cl atoms are represented by blue and green balls, respectively. The charge density at the isodensity surface is  $0.001 \text{ e/Bohr}^3$ .

We further studied excitonic properties using more advanced PBE0 calculations which provide much improved description of the band gap and charge localization in insulators. Since the electronic structures of  $\text{Rb}_2\text{CuCl}_3$  and  $\text{Rb}_2\text{CuBr}_3$  have the similar characteristics as shown in Figure 20, we focus on the exciton in  $\text{Rb}_2\text{CuCl}_3$ . The PBE0 calculation increases the band gap of  $\text{Rb}_2\text{CuCl}_3$  at the  $\Gamma$  point to 4.51 eV, which present a good agreement with the experimental band gap estimated based on the optical absorption data shown in Figure 17. The excited-state structural relaxation leads to a strong local structural distortion. The resulting localized STE is shown in Figure 21. The exciton self-localization around a Cu ion on the 1D Cu-Cl chain significantly weakens two Cu-Cl bonds (Cu(1)-Cl(1) and Cu(1)-Cl(2) in Figure 21). The calculated Cu(1)-Cl(1) and Cu(1)-Cl(2) bond lengths are 2.85 Å and 2.61 Å, which are 16.3% and 6.5% longer than the Cu-Cl bond length of 2.45 Å at the ground state. The calculated exciton emission energy based on the relaxed STE structure is 2.88 eV, close to the experimentally measured peak emission energy (3.14 eV or 395 nm). The good agreement between the calculated and measured exciton excitation/emission energies validates the excited-state theoretical modeling and supports the predicted exciton self-trapping as shown in Figure 21.

### 2.1.6 Optical Cooling

For  $\text{Rb}_2\text{CuCl}_3$ , the unity PLQY blue emission and noticeable overlap between the absorption and emission spectra (see Figure 17) suggest a possible optical cooling due to PL upconversion.<sup>65, 67</sup> As shown in Figure 17, the optical absorption spectra of  $\text{Rb}_2\text{CuX}_3$  show a long band tail that quenches only at a very low energy ( $\sim 1.9$  eV), suggesting a high probability to have phonon-assisted ASPL above the 1.9 eV (650 nm) energy. As a preliminary study, we measured the ASPL spectra of the highly emissive single crystals of  $\text{Rb}_2\text{CuCl}_3$  using different excitation wavelengths in the 490-650 nm range (Figure 22). Results show the presence of upconversion PL with the maximum emission observed under 520 nm excitation. Note that the other possible mechanisms of ASPL include defect/impurity effects and two-photon absorption. However, since the lowest excitation peak is observed at 300 nm, the two-photon absorption mechanism would necessitate  $\text{PLE}_{\text{max}}$  of 600 nm for ASPL instead of the observed 520 nm. The defect effects are largely ruled out based on the observed unity PLQY for the  $\text{Rb}_2\text{CuCl}_3$  single crystals, which have also been shown to be free of impurities using the X-ray methods (SI).

According to the previous studies based on Sheik-Bahae theory,<sup>65, 67, 69, 105</sup> the optical cooling efficiency can be estimated from the following equation:

$$\eta_C = \eta_{PL} \frac{E_{em}}{E_{ex}} - 1,$$

where  $\eta_C$  and  $\eta_{PL}$  are the cooling and PL efficiency, respectively, and  $E_{em}$  and  $E_{ex}$  present the emission and excitation energies. Considering the fact that single crystals of  $\text{Rb}_2\text{CuCl}_3$  shows a 100% PLQY, and the maximum ASPL occurs at 395 nm (3.14 eV) under 520 nm (2.385 eV), using the above equation, an optical cooling efficiency of  $\sim 32\%$  is estimated. This value is similar to the highest values recently reported for hybrid perovskite<sup>67, 106</sup> and all inorganic metal halides.<sup>69,</sup>

<sup>107</sup> Further detailed spectroscopic investigations including Raman spectroscopy is in progress to

better understand the physical origin of the observed ASPL of  $\text{Rb}_2\text{CuCl}_3$ .

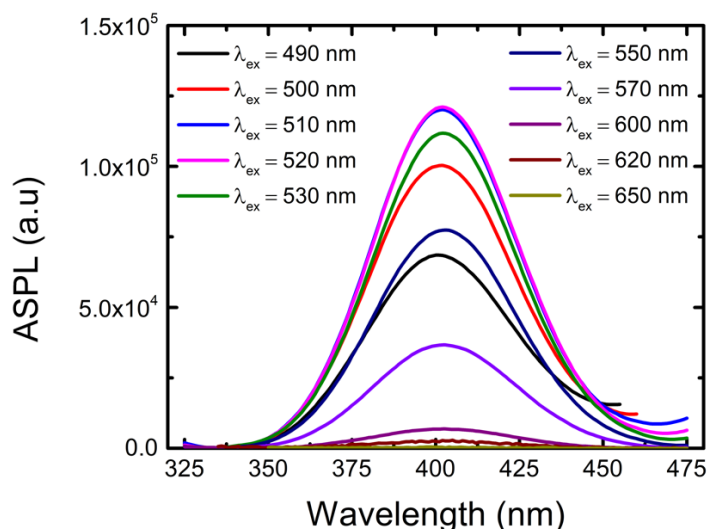


**Figure 22.** Anti-Stokes photoluminescence spectra of a  $\text{Rb}_2\text{CuCl}_3$  single crystal measured at ambient temperature and for different excitation wavelengths.

### 2.1.7 Conclusions

In summary, we report the photophysical properties of bulk and single crystal samples of all-inorganic metal halide materials  $\text{Rb}_2\text{CuX}_3$  ( $X = \text{Br}, \text{Cl}$ ), which exhibit one-dimensional crystal structures featuring anionic  ${}_{\infty}^1[\text{CuX}_3]^{2-}$  ribbons separated by  $\text{Rb}^+$  cations. These materials simultaneously show remarkably high blue emission efficiency and narrow emission linewidths: PLQY values of 64% to 100% and FWHM values of 54 and 52 nm for  $\text{Rb}_2\text{CuBr}_3$  and  $\text{Rb}_2\text{CuCl}_3$ , respectively, are among the record values in each category for bulk samples. Furthermore, the measured Stokes shifts of 85 and 93 nm for  $\text{Rb}_2\text{CuBr}_3$  and  $\text{Rb}_2\text{CuCl}_3$ , respectively, are unusually small for low-dimensional multinary halides, and can be advantageous for practical applications given the comparatively low energy loss between emission and excitation. Based on excitation-, time- and power-dependent PL studies, the physical origin of the emission is attributed to STEs, which is further supported by DFT calculations suggesting the presence of enhanced excitonic

interactions. Moreover,  $\text{Rb}_2\text{CuCl}_3$  shows an ASPL that could provide up to 32% optical cooling efficiency, shown for the first time for Pb-free metal halides in this work. Importantly, discoveries of highly-efficient blue emitters based on nontoxic and inexpensive copper paves a way for the consideration of low-cost and environmentally-friendly copper halides for optoelectronic devices.

## **2.2 All-inorganic $\text{K}_2\text{CuCl}_3$ and $\text{K}_2\text{CuBr}_3$ for Blue Emission and Dramatically Improved Stability**

### **2.2.1 Introduction**

In the last few decades, significant efforts have been devoted to developing earth-abundant, luminescent materials and nanomaterials that demonstrate high stability and photoluminescence (PL) quantum yield.<sup>108</sup> Among these, multinary metal halides, especially halide perovskites and their structural derivatives, have been the focus of much attention owing to their high-efficiency white, blue, red and green emission.<sup>20, 109, 110, 111</sup> Development of high-efficiency blue emitters has lagged compared to red and green emitters due to the higher energy optical transition required for obtaining blue emission.<sup>111, 112, 113</sup> Despite remarkable structural diversity and optoelectronic properties, lead halide perovskites have their own drawbacks such as poor air stability, photoinstability, and toxicity, which could prevent their commercialization.<sup>114</sup>

Recently, several families of copper halides emerged as promising alternatives to luminescent lead halides. These include near-unity green photoluminescence in  $\text{Cs}_3\text{Cu}_2\text{Cl}_5$  and near-unity blue emission in  $\text{Cs}_3\text{Cu}_2\text{X}_5$  ( $\text{X} = \text{Br}, \text{I}$ ) and  $\text{Rb}_2\text{CuX}_3$  ( $\text{X} = \text{Cl}, \text{Br}$ ), to name just a few.<sup>92, 111, 115-117</sup> Tunable blue, green and yellow emission has also been observed for the  $\text{CsCu}_2\text{X}_3$  family, however, the measured photoluminescence quantum yield (PLQY) values are lower compared to the aforementioned families.<sup>118</sup> In all of these families, luminescence is attributed to the self-trapped excitons (STEs), which are induced by strong charge localization within low-dimensional

crystal structures of these copper halides. The formation of STEs is accompanied by a significant excited state structural reorganization, typically leading to a very strong room temperature photoluminescence (PL) emission with large Stokes shifts. Given the importance of structural distortions in light emission in metal halides, narrow structural changes can lead to a significant change in the observed luminescence behavior of materials. A recent high-pressure study of CsCu<sub>2</sub>I<sub>3</sub> confirms this conjecture as a remarkable enhancement of luminescence and changes in STE emission is observed for this material due to the structural evolution of the material under pressure.<sup>119</sup>

Here, we report the preparation and characterization of K<sub>2</sub>CuX<sub>3</sub> (X= Cl, Br), which are the chemically pressurized form of the bright blue emitting Rb<sub>2</sub>CuX<sub>3</sub>.<sup>111, 116, 117</sup> Along with the bright blue emission, Rb<sub>2</sub>CuX<sub>3</sub> have recently shown a strong potential as sensitive X-ray scintillator materials.<sup>116, 117</sup> Despite their excellent fundamental optical properties, Rb<sub>2</sub>CuX<sub>3</sub> contain intrinsically radioactive Rb and the photostability of Rb<sub>2</sub>CuX<sub>3</sub> is poor with a reported ~75% drop in PLQY in only an hour of UV exposure.<sup>111, 117</sup> In contrast, K<sub>2</sub>CuX<sub>3</sub> reported in this work show markedly improved air stability and photostability while preserving their ultrabright blue emission behavior. In this work, K<sub>2</sub>CuX<sub>3</sub>(X = Cl, Br) single crystals and polycrystalline powders were prepared via five different preparation methods including traditional solid-state methods, flux growth, slow cooling of a saturated solution, liquid-liquid diffusion, and liquid-vapor diffusion. Structural characterizations were performed using powder and single crystal X-ray diffraction methods. Optical properties of K<sub>2</sub>CuX<sub>3</sub> were studied using a combined computational and experimental approach through photoluminescence spectroscopy and density functional theory (DFT) methods. This work highlights the strong potential of inexpensive and earth-abundant copper halides for practical applications, which can be further fine-tuned through chemical



substitution experiments.

## **2.2.2 Experimental Synthesis and Methods for $K_2CuX_3$**

### **2.2.2.1 Materials and Methods**

The starting reactants: potassium chloride (99%, J.T. Baker), copper(I) chloride (>99%, Sigma-Aldrich), potassium bromide (99%, Sigma-Aldrich) and copper(I) bromide (>99%, Alfa Aesar) were used as received. For high temperature synthesis experiments, the fused silica tubes were first annealed at 300 °C for 2 hours before quickly transferring to a nitrogen filled glovebox for long term storage. All manipulations of reactants and products were performed in a nitrogen-filled glovebox.

### **2.2.2.2 Polycrystalline Powders of $K_2CuX_3$**

Polycrystalline powder samples of  $K_2CuX_3$  (X= Cl, Br) were prepared by grinding a 2:1 stoichiometric amount of KX and CuX for approximately 30 minutes under a nitrogen atmosphere. Then, the mixtures were pressed into pellets and sealed under vacuum in quartz tubes. The sealed ampoules were heated to 210 °C over the course of 4 hours, held at this temperature for 72 hours and cooled to room temperature over 18 hours. Each sample goes through this heating and cooling cycle at least twice, with a grinding in between, to ensure the complete consumption of reactants.

### **2.2.2.3 Flux growth of $K_2CuCl_3$ Single Crystals**

For single crystal growth experiments using molten salt as flux, a 21:29 molar ratio of KCl and CuCl were ground for approximately 30 minutes under a nitrogen atmosphere. The mixtures were then loaded into alumina crucibles. The crucibles were sealed inside evacuated quartz ampoules and placed into a furnace. The reaction mixtures were heated to 300 °C over 4 hours, held at this temperature for 10 hours, cooled to 170 °C over 130 hours and at this temperature for 336 hours. The liquid flux was removed via centrifugation and single crystals of  $K_2CuCl_3$  were

isolated.

#### **2.2.2.4 $\text{K}_2\text{CuCl}_3$ Single Crystals via Slow Cooling of a Saturated Solution**

$\text{K}_2\text{CuCl}_3$  single crystals of up to 20 mm in length with 1 mm in diameter were prepared by mixing stoichiometric amounts of KCl and CuCl in a 6M HCl solution. In order to prevent oxidation, samples were loaded in a nitrogen glovebox and sealed with white rubber Suba-Seal septa. A Schlenk line was used with an oil bubbler to constantly flow nitrogen over the samples. Approximately 5% by volume  $\text{H}_3\text{PO}_2$ , was added to the KCl solution. Both solutions were heated at 100 °C until fully dissolved and clear. The CuCl solution was added dropwise to the KCl solution and allowed to mix for 1 hour. The samples were then cooled to room temperature for 6 hours. Colorless needle crystals of  $\text{K}_2\text{CuCl}_3$  were collected and washed in methanol.

#### **2.2.2.5 Liquid-Liquid Diffusion Growth of $\text{K}_2\text{CuBr}_3$ Single Crystals**

$\text{K}_2\text{CuBr}_3$  single crystals of up to 1 cm in lengths were prepared by mixing stoichiometric amounts of KBr and CuBr in a 4M HBr solution. In order to prevent oxidation samples were loaded in a nitrogen glovebox and sealed with white rubber Suba-Seal septa. A Schlenk line was used with an oil bubbler to constantly flow nitrogen over the samples. Approximately 10% by volume  $\text{H}_3\text{PO}_2$  was added to the KBr solution. Both solutions were fully dissolved and clear at room temperature. The CuBr was then added dropwise to KBr and the solutions were mixed for 1 hour at room temperature. An equal volume of methanol to HBr was layered on top of the HBr solution. Long (up to 1 cm) colorless needle crystals grew overnight, which were collected and washed in methanol.

#### **2.2.2.6 Vapor-Liquid Diffusion Growth of $\text{K}_2\text{CuBr}_3$ Single Crystals**

$\text{K}_2\text{CuBr}_3$  single crystals of 0.5 cm in size were prepared by mixing stoichiometric amounts of KBr and CuBr in a 4M HBr solution. In order to prevent oxidation, samples were loaded in a

nitrogen glovebox and sealed with white rubber Suba-Seal septa. A Schlenk line was used with an oil bubbler to constantly flow nitrogen over the samples. Approximately 10% by volume  $\text{H}_3\text{PO}_2$  was added to the KBr solution. Both solutions were fully dissolved and clear at room temperature. The CuBr was then added dropwise to KBr and the solutions were mixed for 1 hour at room temperature. The sample was then transferred to a test tube which was suspended from the top of a sealed glass jar with excess methanol at the bottom. The jar was placed in an oil bath at 60 °C, where 0.5 cm crystals grew over the course of 5 days. Crystals were washed in methanol.

#### **2.2.2.7 Powder X-ray Diffraction (PXRD) Measurements**

In order to establish bulk purity of samples, PXRD measurements were periodically taken on a Rigaku Miniflex600 equipped with D/tex detector and a Ni-filtered Cu-K $\alpha$  radiation source. Data was collected at room temperature in the 3–90° (2 $\theta$ ) range, with a step size of 0.02°. The obtained PXRD patterns were refined using the decomposition method. To test the air-stability of  $\text{K}_2\text{CuX}_3$ , powdered samples were left on a laboratory bench under ambient conditions (thermostat set at 20 °C and relative humidity of 30%) and periodic PXRD experiments were performed to monitor the changes. To quantify the sample composition changes, the Reference Intensity Ratio (RIR) quantitative analysis was performed using the PDXL2 program.

#### **2.2.2.8 Single Crystal X-ray Diffraction (SCXRD)**

Single crystal X-ray diffraction (SXRD) data was collected on a Bruker D8 Quest with a Kappa geometry goniometer, an Incoatec Imus X-ray source (graphite monochromated Mo-K $\alpha$  ( $\lambda = 0.71073 \text{ \AA}$ ) radiation), and a Photon II detector. The data was corrected for absorption using the semiempirical method based on equivalent reflections, and the structures were solved by intrinsic phasing methods (SHELXT) as embedded in the APEX3 v2015.5-2 program. Site occupancy factors were checked by freeing occupancies of each unique crystallographic site. Details of the

data collection and crystallographic parameters are given in Table 1. Atomic coordinates, equivalent isotropic displacement parameters, and selected interatomic distances and bond angles are provided in Table A1 and Table A2 in the Supporting Information (SI). Additional information on the crystals structures investigations can be obtained in the form of a Crystallographic Information File (CIF), which were deposited in the Cambridge Crystallographic Data Centre (CCDC) database (deposition numbers 1989799 and 1989800)

### **2.2.2.9 Thermogravimetry and Differential Scanning Calorimetry (TGA/DSC)**

#### **Measurements**

Simultaneous thermogravimetric analysis and differential scanning calorimetry (TGA/DSC) were measured on ~15 mg of polycrystalline powder of  $K_2CuX_3$  on a TA Instruments SDT 650 thermal analyzer system. Sample was heated up from 25 to 475 °C under an inert flow of dry nitrogen gas at a rate of 100 mL/min, with a heating rate of 5 °C/min.

### **2.2.2.10 Optical Measurements**

Room temperature photoluminescence emission (PL) and photoluminescence excitation (PLE) measurements were performed on polycrystalline powders of  $K_2CuX_3$  ( $X = Cl, Br$ ) and single crystals of  $K_2CuCl_3$  on a Jobin Yvon Fluorolog-3 spectrofluorometer (HORIBA company) equipped with a Xenon lamp and a Quanta- $\phi$  integrating sphere using the two-curve method in a varied range from 280 to 860 nm. For lifetime measurements, a Time-Correlated Single Photon Counting (TCSPC) system including a DeltaHub DH-HT high throughput TCSPC controller and NanoLED NL-C2 pulsed diode controller was used. For light source, a 299 nm NanoLED diode was selected, which has a <1.2 ns pulse duration.

Photoluminescence quantum yield was determined by:

$$Quantum\ Yield = \left( \frac{Em_s - Em_b}{Ex_b - Ex_s} \right) * 100$$

where  $E_{x_s}$  and  $E_{x_b}$  are the integrated excitation profiles of the sample and the blank and  $E_{m_s}$  and  $E_{m_b}$  are the integrated emission profiles of the sample and blank respectively. An Area Balance Factor is applied in the FluorEssence software which accounts for changes in integration times between excitation and emission scans and for the use of neutral density filters. For the photostability measurement, a polycrystalline  $K_2CuCl_3$  sample was placed inside the Quanta- $\phi$  integrating sphere on the Jobin Yvon Fluorolog-3 spectrofluorometer. The sample was then exposed to the full power of the Xenon lamp of the spectrofluorometer at its PL excitation maximum of 291 nm. Periodic PLQY measurements were taken every 5 minutes under these conditions for a total of 60 minutes.

For radioluminescence (RL) measurements, a  $K_2CuCl_3$  polycrystalline pellet sample with  $\sim 5 \times 5 \times 3 \text{ mm}^3$  dimensions was fixed on a wooden stick using silicone optical grease (Bicron BC-630), and placed in an X-ray beam at the focal point of the optics of a Princeton Instruments Acton SP2150 UV-VIS spectrometer (see Figure A12) housed in the lead-lined irradiation cabinet. This instrument uses a Hamamatsu R928 photomultiplier tube (PMT) to receive light from a diffraction grating and mirror system scanned to cover the range from 200 to 650 nm. Data were collected as a function of wavelength at increments of 2 nm under irradiation with bremsstrahlung X rays at 200 kVp, 20 ma ( $\sim 25 \text{ Gy/h}$ ). For each wavelength, 4 measurements were averaged with 250 ms integration time per measurement to reduce noise. For completeness, we ran an identical measurement of the wooden stick covered with optical grease to rule out the unlikely possibility that the grease was the source of the luminescence (Figure A13).

#### **2.2.2.11 Computational Methods**

Our calculations were based on density functional theory (DFT) as implemented in the VASP code.<sup>78</sup> The kinetic energy cutoff of the plane-wave basis is 295 eV. The projector

augmented wave method was used to describe the interaction between ions and electrons.<sup>79</sup> Lattice parameters were fixed at the experimentally measured values while the atomic positions were optimized until the force on each atom is less than 0.02 eV/Å.

The electronic band structure and density of states (DOS) were calculated using Perdew-Burke-Ernzerhof (PBE) exchange-correlation functional.<sup>80</sup> The band gaps were corrected and excitonic properties were studied by using the hybrid PBE0 functional.<sup>81</sup> The inclusion of 25% Fock exchange in the PBE0 functional significantly improves the band gap energy<sup>81, 82</sup> and the description of charge localization in insulators.<sup>83, 85, 120</sup> The total energy of an exciton was calculated by fixing the occupation numbers of the electron and hole-occupied eigenlevels [ $\Delta$  self-consistent field ( $\Delta$ SCF) method<sup>87</sup>]. Following Franck-Condon principle, the optical excitation and emission energies were obtained by calculating the total energy differences between the excited and the ground states using PBE0-optimized ground-state and excited-state structures, respectively. The  $\Delta$ SCF method combined with the hybrid PBE0 functional allows excited-state structural relaxation and has shown accurate results in exciton excitation and emission energies in many low-dimensional metal halides and oxides,<sup>88, 89, 121, 122</sup> including 1D and 0D copper halides.<sup>92,</sup>

111, 123

### 2.2.3 Crystal Structure and Stability of $K_2CuX_3$

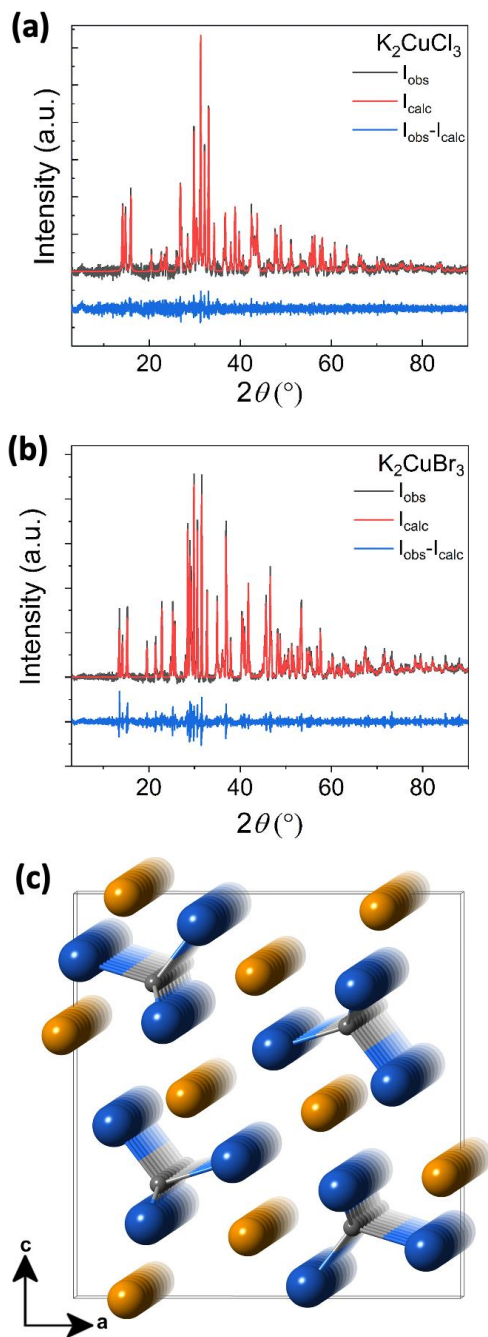


**Figure 23.** Room temperature PXRD patterns (black) fitted using the Pawley method (red) for (a)  $K_2CuCl_3$  and (b)  $K_2CuBr_3$  prepared using solid-state synthesis. (c) A ball-and-stick representation of the 1D crystal structure of  $K_2CuX_3$  viewed down the  $b$ -axis.

The optical photographs of single crystals and polycrystalline pellet of  $K_2CuCl_3$  and  $K_2CuBr_3$  obtained using solid-state heating, solution grown, liquid-liquid and liquid-vapor

diffusion are illustrated in Figure 21. Such ease of preparation using multiple differing approaches can be advantageous for the potential practical applications of the  $K_2CuX_3$  compounds. Notably, the use of excess molten salt as a reactive flux is demonstrated for the first time for  $A_2CuX_3$  ( $A = K, Rb$ ;  $X = Cl, Br$ ) compounds. Although this approach produces high quality needle crystals of  $K_2CuCl_3$  (Figure 24), presence of dark-colored impurities and inclusions are noticeable due to a rapid oxidation of the surface  $CuCl$  self-flux.

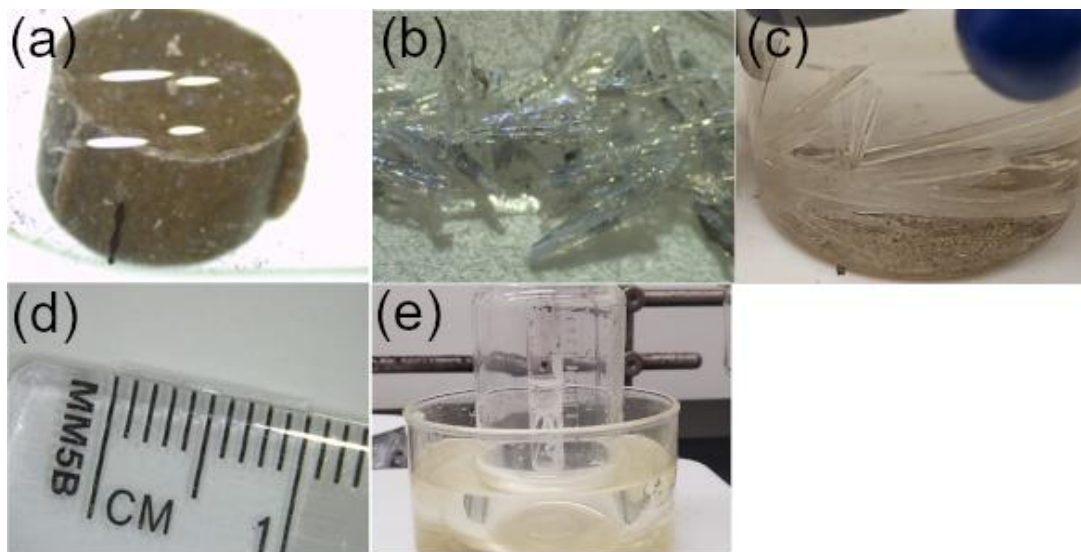


**Figure 24.** Photographs of  $K_2CuX_3$  ( $X = Cl, Br$ ) samples: (a) A polycrystalline pellet of  $K_2CuCl_3$  prepared using solid-state synthesis approach, (b) molten salt flux grown  $K_2CuCl_3$  crystals, (c)  $K_2CuCl_3$  crystals grown from slow cooling a saturated solution, (d) a 1 cm-long single crystal of  $K_2CuBr_3$  grown using a liquid-liquid diffusion method, and (e)  $K_2CuBr_3$  crystals via a liquid-vapor diffusion synthesis method.

To compare the purity and stability of samples prepared using various synthetic methods, we performed regular room temperature PXRD measurements; PXRD patterns of  $K_2CuCl_3$  and  $K_2CuBr_3$  prepared using solid state synthesis approach are provided in Figure 23. As mentioned above, the flux-grown crystals of  $K_2CuCl_3$  form black impurity pieces when exposed to air. However, after an initial surface oxidation, no further noticeable changes occur for the flux-grown crystals. Single crystals of  $K_2CuX_3$  grown using the solution methods were also left in ambient air and showed no signs of degradation. In contrast, a polycrystalline powder sample of  $K_2CuCl_3$



prepared using solid-state synthesis and kept in ambient air shows signs of degradation after one day resulting in the formation of a small amount of KCuO impurity (Figure A14). There is a gradual increase of the KCuO impurity peak (up to estimated 6%) over a 2-months period. However, the crystallinity and peak intensities for  $\text{K}_2\text{CuCl}_3$  remain unchanged. Therefore, the formation of the KCuO impurity in powder samples exposed to the ambient lab environment are attributed to the oxidation of the leftover reactants in our samples. In fact, during our solid-state synthesis experiments, we noted that while smaller scale (total mass < 0.5g) reactions produce phase pure samples based on PXRD, larger scale reactions (total mass > 1 g) tend to show leftover reactant peaks in PXRD patterns. Thus, solid-state synthesis preparation of 1.5 g sample of  $\text{K}_2\text{CuBr}_3$  yielded a sample with a minor amount of unreacted CuBr impurity (~2%) after multiple grinding and annealing procedures (Figure A15). Unlike  $\text{K}_2\text{CuCl}_3$ , no change was noted for  $\text{K}_2\text{CuBr}_3$  over the three weeks tested. These results suggest that the  $\text{K}_2\text{CuBr}_3$  polycrystalline powders are stable under ambient air and moisture, whereas  $\text{K}_2\text{CuCl}_3$  samples show minor degradation due to the oxidation of leftover reactants. Notably,  $\text{K}_2\text{CuX}_3$  exhibit greatly improved air-stability compared to the heavier  $\text{Rb}_2\text{CuX}_3$  analogs. Thus, more than half (~56%) of a polycrystalline sample of  $\text{Rb}_2\text{CuCl}_3$  degraded forming RbCl and  $\text{Rb}_2\text{CuCl}_4 \cdot 2\text{H}_2\text{O}$  impurities when left in air under identical conditions for only a month.<sup>111</sup>

**Table 2.** Selected single crystal data and structure refinement parameters for K<sub>2</sub>CuX<sub>3</sub>.

Formula	K <sub>2</sub> CuCl <sub>3</sub>	K <sub>2</sub> CuBr <sub>3</sub>
Formula weight (g/mol)	248.09	381.47
Temperature (K)	100(2)	100(2)
Radiation, wavelength (Å)	Mo K $\alpha$ , 0.71073	Mo K $\alpha$ , 0.71073
Crystal system	Orthorhombic	Orthorhombic
Space group	Pnma	Pnma
Z	4	4
Unit cell parameters (Å)	$a = 11.9388(5)$	$a = 12.5112(10)$
	$b = 4.1112(2)$	$b = 4.2939(3)$
	$c = 12.5095(5)$	$c = 13.1645(10)$
Volume (Å <sup>3</sup> )	614.00(5)	707.22(9)
Density ( $\rho_{\text{calc}}$ ) (g/cm <sup>3</sup> )	2.684	3.583
Absorption coefficient ( $\mu$ ) (mm <sup>-1</sup> )	6.068	21.085
$\theta_{\text{min}} - \theta_{\text{max}}$ (°)	2.358 – 30.53	2.246 – 33.799
Reflections collected	8078	11844
Independent reflections	1623	1579
$R^a$ indices ( $I > 2\sigma(I)$ )	$R_1 = 0.0215$	$R_1 = 0.0316$
	$wR_2 = 0.0498$	$wR_2 = 0.0731$
Goodness-of-fit on $F^2$	1.006	1.009
Largest diff. peak and hole (e <sup>-</sup> /Å <sup>3</sup> )	0.623 and -0.568	1.197 and -1.153

$${}^aR_1 = \sum ||F_0| - |F_c|| / \sum |F_0|; WR_2 = |\sum |w(F_0^2 - F_c^2)|^2 / \sum |wF_0^2|^2|^{1/2}$$

where  $w = 1/|\sigma^2 F_0^2 + (AP)^2 + BP|$ , with  $P = (F_0^2 + 2F_c^2)/3$  and weight coefficients A and B

The results of SCXRD experiments are summarized in Tables 2, A1, and A2.  $K_2CuX_3$  are isostructural with the previously reported  $Rb_2CuX_3$ <sup>111</sup> and crystallize in the orthorhombic space group  $Pnma$  featuring 1D  $\infty^1[CuX_3]^{2-}$  chains separated by  $K^+$  cations (Figure 23c). The polyanionic  $\infty^1[CuX_3]^{2-}$  are formed via corner sharing copper halide tetrahedra extending along the  $b$ -axis. The room temperature PXRD patterns of single crystals can be indexed based on the simulated pattern from the SCXRD data (Figure A16). The measured bond distances and angles within the 1D  $\infty^1[CuX_3]^{2-}$  chains in  $A_2CuX_3$  ( $A = K, Rb; X = Cl, Br$ ) are similar (Table A2). Thus, the Cu-X bond distances are in the range 2.3319(4) – 2.3916(2) Å for  $K_2CuCl_3$ , nearly identical to the 2.3363(6) – 2.4243(3) Å range reported for  $Rb_2CuCl_3$ .<sup>111</sup> For  $K_2CuBr_3$ , the Cu – X distances range from 2.4529(8) to 2.5215(4) Å; the Cu – Br bond lengths are longer than the Cu – Cl distances in accordance with the Shannon ionic radii trends for the halides.<sup>30</sup> Since alkali metals are not directly involved in the optical transitions observed for the ternary alkali copper halides, and given the similarity in the 1D  $\infty^1[CuX_3]^{2-}$  ribbons, similar optical properties can be expected for  $K_2CuX_3$  and  $Rb_2CuX_3$ .

The thermal stability of  $K_2CuCl_3$  and  $K_2CuBr_3$  was evaluated by thermogravimetric analysis (TGA) and differential scanning calorimetry (DSC) measurements (Figure A17). Based on the TGA results,  $K_2CuX_3$  polycrystalline powder samples show no significant weight loss up to 460°C. These results are consistent with the improved thermal stability reported for all-inorganic metal halides such as  $Rb_2CuCl_3$ ,  $Rb_4Ag_2BiBr_9$ ,  $Cs_3Cu_2Br_{5-x}I_x$ ,  $Cs_2SnI_6$  etc. as compared to hybrid organic-inorganic metal halides.<sup>92, 111, 124</sup> The obtained DSC results indicate a single thermal event for each sample, which have been assigned to the peritectic decompositions of  $K_2CuCl_3$  and  $K_2CuBr_3$  at 274 and 271 °C, respectively. These results are in a good agreement with the reported  $KX - CuX$  phase diagrams.<sup>125</sup>

## 2.2.4 Optical Properties of $K_2CuX_3$

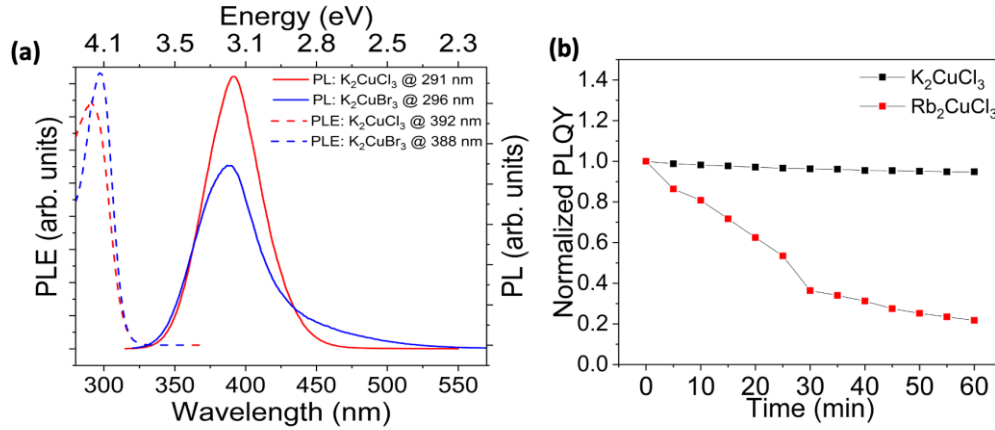


**Figure 25.** (a) Room temperature photoluminescence excitation (PLE) (dashed lines) and photoluminescence emission (PL) (solid lines) of polycrystalline powders of  $K_2CuBr_3$  (blue) and  $K_2CuCl_3$  (red). (b) A comparison of the normalized photoluminescent quantum yield (PLQY) of  $K_2CuCl_3$  (plotted in black) against that of  $Rb_2CuCl_3$  (plotted in red) under continuous irradiation suggests a significantly improved photostability of  $K_2CuCl_3$  compared to  $Rb_2CuCl_3$ .

The optical properties of as-synthesized  $K_2CuX_3$  were explored by photoluminescence spectroscopy. The photoluminescence excitation (PLE) and emission (PL) spectra for polycrystalline powders of  $K_2CuCl_3$  and  $K_2CuBr_3$  are provided in Figure 25a. A comparison between room temperature PL spectra for single crystals and polycrystalline powder samples of  $K_2CuCl_3$  is provided in Figure A18. Under UV irradiation,  $K_2CuCl_3$  and  $K_2CuBr_3$  show a bright blue emission with PL maxima at 392 and 388 nm, respectively. The corresponding PLE spectra for  $K_2CuCl_3$  and  $K_2CuBr_3$  show maxima at 291 and 296 nm, respectively. In combination, the measured PL and PLE peaks yield the Stokes shift values of 101 nm and 92 for  $K_2CuCl_3$  and  $K_2CuBr_3$ , respectively. The observed bright blue emission is attributed to the self-trapped excitons (STEs) in photoexcited  $K_2CuX_3$ .<sup>110, 116</sup> For compounds with STE-based emission, the measured Stokes shifts of ~100 nm is relatively small as compared to other low-dimensional (1D and 0D) metal halides.<sup>88, 90, 126</sup> Furthermore, the measured PL peaks for  $K_2CuX_3$  are noticeably narrower with full width at half maximum (FWHM) ~ 54 nm compared to other STE based emitters

including blue emitting copper halides such as  $\text{Cs}_3\text{Cu}_2\text{Br}_5$  and  $\text{Cs}_3\text{Cu}_2\text{I}_5$  (Table 3).<sup>92, 111, 113, 117</sup> Finally, blue emission with PLQY values of 96.58% and 55% measured for polycrystalline powder samples of  $\text{K}_2\text{CuCl}_3$  and  $\text{K}_2\text{CuBr}_3$ , respectively, are among the highest reported to date. In combination, higher color purity blue emission with greater energy efficiency distinguishes the  $\text{A}_2\text{CuX}_3$  family from other known efficient blue emitters

**Table 3.** A comparison of the photophysical properties of high efficiency blue emitters based on all-inorganic copper halides<sup>92, 111, 113, 117</sup>

<b>Compound</b>	<b>PLQY (%)</b>	<b>PL<sub>max</sub> (nm)</b>	<b>PLE<sub>max</sub> (nm)</b>	<b>Stokes shift (nm)</b>	<b>FWHM (nm)</b>	<b>Ref</b>
$\text{K}_2\text{CuCl}_3$	96.58	392	291	101	54	this work
$\text{K}_2\text{CuBr}_3$	55	388	296	92	54	this work
$\text{Rb}_2\text{CuCl}_3$	100	400	300	100	52	[110]
$\text{Rb}_2\text{CuBr}_3$	98.6	385	300	85	~54	[116]
$\text{Cs}_3\text{Cu}_2\text{I}_5$	91.2	445	290	155	~175	[112]
$\text{Cs}_3\text{Cu}_2\text{Br}_5$	50.1	455	298	157	75	[90]

Given the fact that  $\text{K}_2\text{CuX}_3$  are isostructural to  $\text{Rb}_2\text{CuX}_3$ , we attribute the mechanism of blue emission in  $\text{K}_2\text{CuX}_3$  to the highly stable STEs, which form upon the photoexcitation of these materials. The results of excitation-dependent and time-resolved PL measurements (Figure 26) further support the attribution of blue emission in  $\text{K}_2\text{CuX}_3$  to STEs. The observed excitation-dependent PL spectra are indicative of a single radiative transition mechanism (Figure 26a-b). From the time-resolved PL measurements a lifetime of 12.97  $\mu\text{s}$  was extracted for  $\text{K}_2\text{CuCl}_3$  (Figure 26). This lifetime value is in a good agreement with the lifetime of 12.21  $\mu\text{s}$  reported for  $\text{Rb}_2\text{CuCl}_3$ .<sup>111</sup> Interestingly, the measured optical properties of  $\text{A}_2\text{CuX}_3$  suggest a very weak dependence of PL properties on both the alkali A and halogen X sites (Table 3), which is in contrast to the observed significant changes in the PL properties of lead halides upon halogen substitution

such as in case of the  $\text{CsPbX}_3$  family.<sup>14</sup> Such unusually weak dependence of optical properties on the A and X sites in  $\text{A}_2\text{CuX}_3$  is due to the intricacies of their band structures (*vide infra*). Although the optical properties of  $\text{Rb}_2\text{CuX}_3$  and  $\text{K}_2\text{CuX}_3$  are similar,  $\text{K}_2\text{CuX}_3$  reported in this work are found to exhibit both greater air stability (*vide supra*) and photostability compared to  $\text{Rb}_2\text{CuX}_3$  (Figure 25). One of the key drawbacks of the high efficiency blue emitter  $\text{Rb}_2\text{CuCl}_3$ , for example, is that a 75% drop in PLQY is observed over the course of one hour under UV radiation.<sup>117</sup> In contrast,  $\text{K}_2\text{CuCl}_3$  shows only a 5% drop within the same time frame (Figure 25).

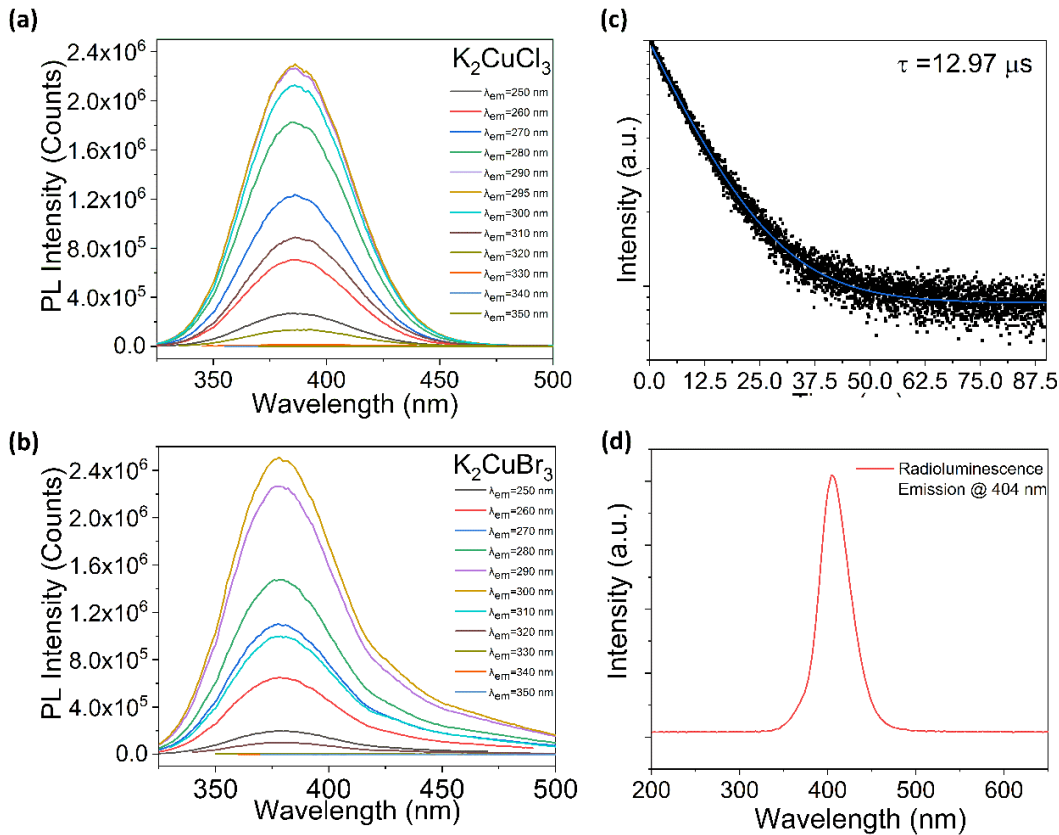


**Figure 26.** Excitation-dependent PL measurements for (a)  $\text{K}_2\text{CuCl}_3$  and (b)  $\text{K}_2\text{CuBr}_3$ . (c) Room temperature time-resolved PL spectrum for  $\text{K}_2\text{CuCl}_3$ . (d) A radioluminescence spectrum of  $\text{K}_2\text{CuCl}_3$  with emission centered at 404 nm.

### 2.2.5 Radioluminescent Properties

In the literature,  $\text{Rb}_2\text{CuX}_3$  have been identified as potential materials for radiation detection applications.<sup>116, 117</sup> To evaluate the potential of  $\text{K}_2\text{CuX}_3$  for X-ray detection applications, we

measured radioluminescence (RL) spectrum from a polycrystalline pellet of  $\text{K}_2\text{CuCl}_3$ . Under irradiation with bremsstrahlung X rays at 200 kVp, 20 ma ( $\sim 25$  Gy/h), the bright peak at 404 nm seen in Figure 26 appeared. This peak is in the same region as the room temperature PL emission under UV irradiation suggesting the same STE-based emission mechanism. The wavelength of the RL emission is optimal for use with PMTs and Si photomultipliers because these devices are optimized for the detection of light between 360 and 450 nm. Small samples, such as the one investigated here, are useful for the detection of  $\alpha/\beta$  radiation because the ranges of these particles in solid matter is small. The range of the 4.2 MeV alpha particles from  $^{238}\text{U}$ , is only  $\sim 20$   $\mu\text{m}$  (as calculated by the SRIM-2013 code) in  $\text{K}_2\text{CuCl}_3$ , making thin wafers, whether pressed polycrystalline material or single crystals, sufficient for efficient detection.<sup>127</sup> This form factor is suitable for health physics survey and ion beam instrumentation.

The considerations for X and gamma rays require accounting for the cross section for electromagnetic radiation causing the ejection of electrons and the range of electrons in  $\text{K}_2\text{CuCl}_3$ . The former determines the size of a compact or crystal needed for the efficient conversion of X and gamma rays to electrons, whereas the latter determines the efficiency with which ionization energy will be deposited in the crystal. Using photon cross section data available from NIST<sup>128</sup>, and the densities of analogous copper halides, the mean free paths of photons between 1 and 100 keV are shown in Figure 27 for  $\text{K}_2\text{CuCl}_3$ ,  $\text{K}_2\text{CuBr}_3$ ,  $\text{Rb}_2\text{CuCl}_3$ , and  $\text{Rb}_2\text{CuBr}_3$ . Based on our calculations,  $\text{A}_2\text{CuX}_3$  ( $\text{A} = \text{K}, \text{Rb}; \text{X} = \text{Cl}, \text{Br}$ ) have similar X-ray absorption properties. Among these,  $\text{K}_2\text{CuCl}_3$  has the longest attenuation length, meaning it is the least absorptive, whereas the heavier  $\text{Rb}_2\text{CuX}_3$  analogs have better absorption properties. However, Rb is intrinsically radioactive (a beta emitter), which significantly limits the useful size of  $\text{Rb}_2\text{CuX}_3$  crystals for spectroscopy applications. For example, at a density of  $3.83$   $\text{g}/\text{cm}^3$ , we estimate that a  $\text{Rb}_2\text{CuBr}_3$

crystal would have an intrinsic activity of 1193 Bq/cm<sup>3</sup>. By comparison, a NaI(Tl) crystal (comparable density and attenuation length) with dimensions 5 x 10 x 40 cm<sup>3</sup> sees a natural background (at ORNL) of about 900 Bq, making its observed background rate about 0.5 Bg/cm<sup>3</sup>.

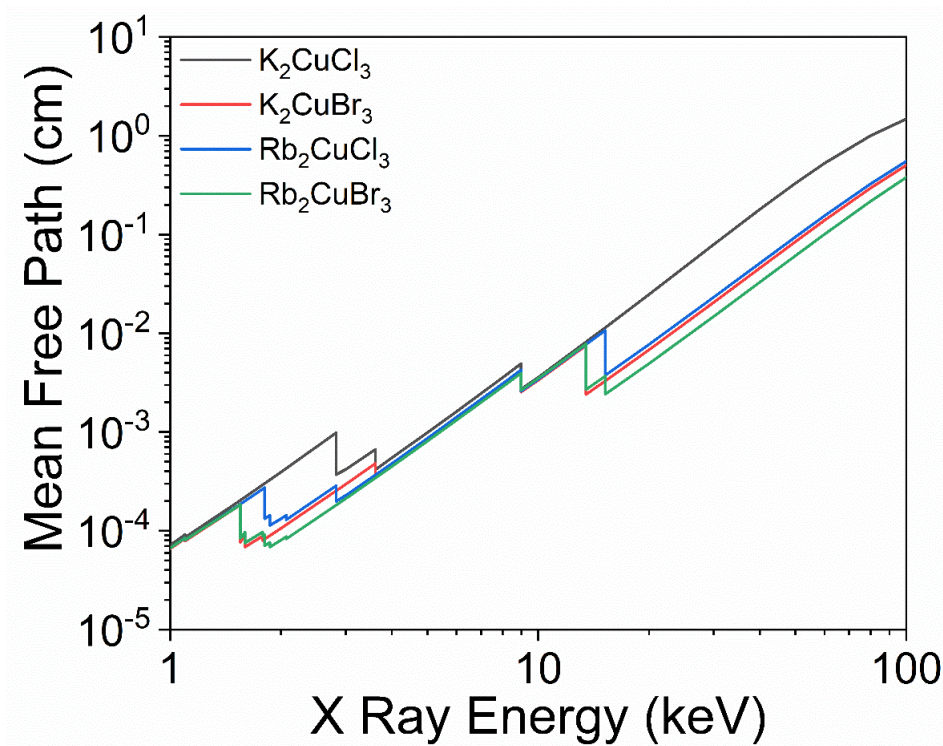


**Figure 27.** Calculated mean free path of photons in K<sub>2</sub>CuCl<sub>3</sub> (black), K<sub>2</sub>CuBr<sub>3</sub> (red), Rb<sub>2</sub>CuCl<sub>3</sub> (blue), and Rb<sub>2</sub>CuBr<sub>3</sub> (green). Sharp breaks correspond to the K and L edges in the constituent atoms.

In medical applications, the bremsstrahlung end point energy is often not more than 100 keV, which puts the most probable emitted X ray between 20 and 50 keV. At these energies and below, compacts and crystals need not be thicker than 1 mm for efficient absorption of the X rays. Since the photoelectric effect is the dominant process at these energies, electrons ejected from atoms will have energies ~10 keV lower than the ionizing photon. The range of 40 keV electrons in the material becomes the important parameter determining the skin depth that defines the region of total energy deposition. Electrons originating closer to the surface than the range of 40 keV



electrons have a high probability of not depositing their full energy in the detector. Using the NIST ESTAR code <sup>129</sup>, we estimate the continuous slowing down approximation (CSDA) range of these electrons to be 15.8  $\mu\text{m}$ , making the totally absorbing thickness of a 1 mm thick detector at least 0.97 mm. We write “at least” here because CSDA range assumes a straight-line path for the electron, whereas in reality, electrons suffer many large-angle scatterings because the primary scatterers are other electrons. Therefore, we conclude that  $\text{K}_2\text{CuCl}_3$  should be a viable detector material for medical applications.

The ranges of 1 - 2 MeV electrons and gamma rays (typical energies from terrestrial radioactive sources) are large,  $\sim 2.2 - 4.8$  mm (CSDA) and  $\sim 5$  cm (mfp), respectively, necessitating the use of transparent single crystals because pressed polycrystalline compacts thicker than 0.5 – 1 mm are opaque to the RL emission. The heavier halides members of this family will be more likely to find use in high-energy gamma ray detectors because of their higher average atomic number and densities. It will be necessary to produce larger single crystals (at least  $5 \text{ mm} \times 5 \text{ mm} \times 5 \text{ mm}$ ) to measure the light yield (number of scintillation photons/deposited MeV) with monoenergetic X or gamma ray sources. Thus, our preliminary investigations of radiation detection properties of  $\text{K}_2\text{CuX}_3$  have highlighted the potential of this family for further, more in-depth studies.

## **2.2.6 Electronic Structure and Band Calculations**

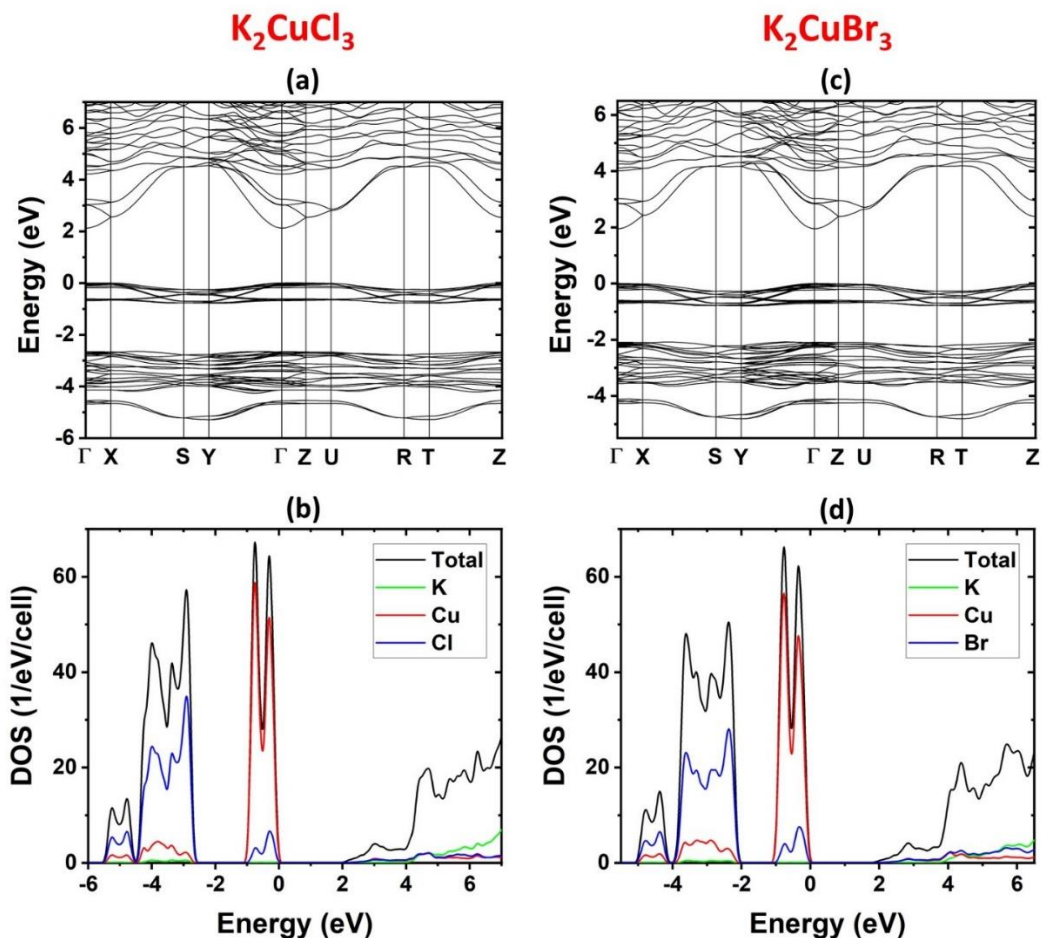


**Figure 28.** Electronic band structures and DOS of  $\text{K}_2\text{CuCl}_3$  and  $\text{K}_2\text{CuBr}_3$ .

The electronic band structures of  $\text{K}_2\text{CuX}_3$  ( $X = \text{Cl}, \text{Br}$ ) are shown in Figure 28. Both compounds exhibit direct band gaps at the  $\Gamma$  point. The PBE-calculated band gaps of  $\text{K}_2\text{CuCl}_3$  and  $\text{K}_2\text{CuBr}_3$  are 2.13 eV and 1.95 eV, respectively. These PBE band gaps are expected to be underestimated due to the well-known band gap error in the PBE calculation. The hybrid PBE0 calculations increase the band gaps of  $\text{K}_2\text{CuCl}_3$  and  $\text{K}_2\text{CuBr}_3$  to 4.63 eV and 4.32 eV, respectively. The DOS plots in Figure 28 show that the valence (conduction) band is primarily derived from the Cu-3d (Cu-4s) orbitals hybridized with halogen p orbitals. Since both the conduction and valence band edges are dominated by Cu states, the calculated band gaps are weakly dependent on the halogen.

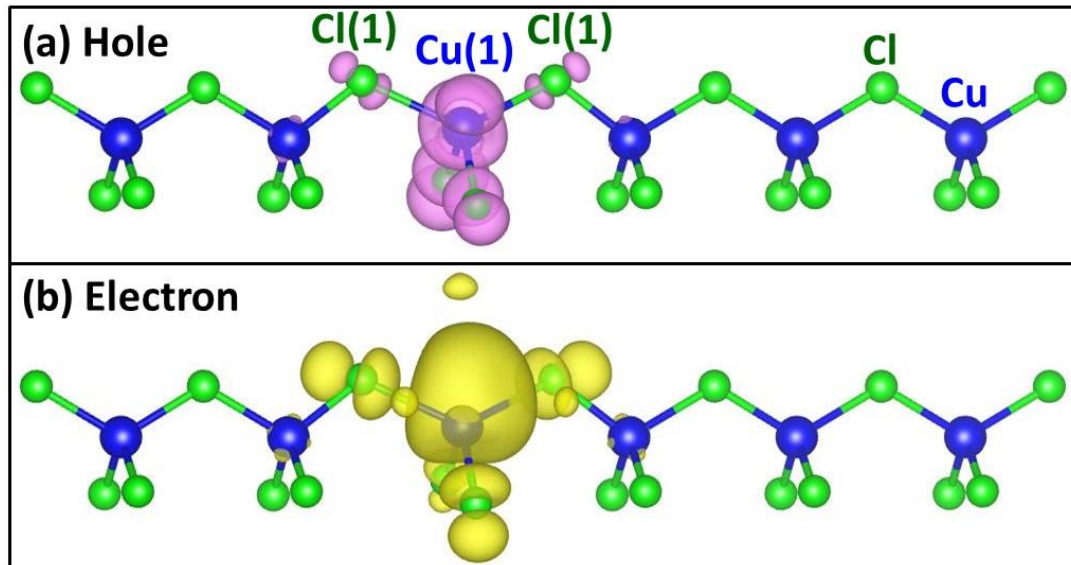


**Figure 29.** The partial charge density contours of the hole (a) and the electron (b) in the exciton in  $\text{K}_2\text{CuCl}_3$ . The Cu and Cl atoms are represented by blue and green balls, respectively. The charge density at the isodensity surface is  $0.001 \text{ e/bohr}^3$ .

To understand the origin of the optical emission in  $\text{K}_2\text{CuX}_3$ , we calculated the excitonic properties in  $\text{K}_2\text{CuCl}_3$ . Despite the dispersive conduction band, the localization of an exciton is found to be strong, leading to significant local structural distortion, which in turn traps the exciton, forming a STE. A STE is centered at a Cu ion, causing elongation of the two adjacent Cu-Cl bonds [Cu(1)-Cl(1) and Cu(1)-Cl(2) in Figure 29] along the 1D chain direction from  $2.41 \text{ \AA}$  to  $2.68 \text{ \AA}$  (a 11% increase). The partial charge density contours of the hole and electron in a STE are shown in Figure 29b. The binding energy of the STE (relative to a pair of free electron and hole) in  $\text{K}_2\text{CuCl}_3$  is calculated to be  $1.06 \text{ eV}$ . The calculated STE emission energy is  $2.85 \text{ eV}$ , in reasonable agreement with the experimental value of  $3.16 \text{ eV}$  ( $392 \text{ nm}$ ) and the observed RL peak at  $3.07 \text{ eV}$  ( $404 \text{ nm}$ ). These results suggest the STE as the origin of the observed emission in  $\text{K}_2\text{CuCl}_3$ . The observed optical emission in  $\text{K}_2\text{CuBr}_3$  is similar to that in  $\text{K}_2\text{CuCl}_3$ , indicating the same emission mechanism.

### 2.2.7 Conclusions

In summary, we report preparation and optical properties of all-inorganic copper halides  $K_2CuX_3$  ( $X=Cl, Br$ ).  $K_2CuX_3$  demonstrate narrow blue emission with FWHM values of  $\sim 50$  nm, very high PLQY values up to unity, and relatively small Stokes shifts for this class of materials. Interestingly, the measured optical properties of  $K_2CuX_3$  show very weak dependence on A site or X site substitutions. Our computational investigations suggest that both the conduction and valence band edges are primarily made of Cu states, which explains the weak dependence of the observed optical properties on the halogen and alkali metal. Based on our combined experimental and computational work, the blue emission in  $K_2CuX_3$  is attributed to excitons localized within the  $\infty[CuX_3]^{2-}$  chains centered at a copper ion. Importantly,  $K_2CuX_3$  are found to exhibit significantly improved air- and photo-stability compared to other analogous copper halides.  $K_2CuCl_3$  also exhibits radioluminescence at a wavelength similar to the blue emission from PL when exposed to bremsstrahlung X-rays. The combination of inexpensive and earth-abundant chemical composition, high efficiency blue emission and much improved stability of  $K_2CuX_3$  makes these compounds attractive for consideration for practical optical and radiation detection applications.

## Chapter 3: Tuning of White Light Emission via Silver Halides

While the results from chapter 2 were quite promising in many aspects, a disadvantage of the family is that the emission will likely always be blue when using copper(I) halides in that particular structure. This is due to the singular emission mechanism of highly localized STEs formed on the copper(I) site. Chapter 3 moves beyond copper(I), utilizing silver as the metal center. The substitution presents new opportunities and new challenges in terms of synthesis. However, the most prominent change is the PL emission switch from a narrow blue emission to a broad white light. The first section focuses on using group 1 metals as the A cation, and the second section incorporates the ammonium cation. This work is summarized as publications in *Advanced Functional Materials* and *ACS Materials Au*.<sup>130, 131</sup>

### 3.1 All-inorganic $A_2AgX_3$ (A=Rb, Cs; X=Cl,Br,I) for Tunable White Light Photoluminescence and Anti-counterfeiting Applications

#### 3.1.1 Introduction

In the past decade, multinary metal halides have been receiving increased attention due to their wide range of applications, including photodetectors, light-emitting diodes (LEDs), and solar cells.<sup>19, 100, 132, 133-137</sup> Significant progress has recently been made to develop structurally unique metal halides to tune their functional properties for specific applications. Lead halides receive the most attention among various metal halides due to their outstanding photophysical properties, such as the low threshold for lasing, tunable band gaps, and photoluminescence (PL) in the entire visible spectral range, to name just a few.<sup>14, 61, 134, 135, 138, 139</sup> Despite their excellent optical and electronic properties, the toxicity of lead and instability of lead halides in humid environments are among the significant concerns in this field.<sup>135, 137</sup> Therefore, considerable efforts have been devoted to developing alternative eco-friendly lead-free metal halides with improved stability.<sup>23, 43, 53, 75, 117,</sup>

<sup>136, 140, 141</sup> The initial focus for the replacement of Pb was on the same group elements, Sn and Ge, which yielded several exciting materials, but with much lower stability than the parent lead halides.<sup>77, 142</sup>

In recent years, the search for Pb-free alternatives was expanded to include halides of antimony (Sb), bismuth (Bi), and copper (Cu). The latter, Cu(I) halides, are interesting for optical applications.<sup>23, 32, 43, 53, 64, 73, 117, 136, 141, 143, 144</sup> They combine many of the desirable attributes for practical applications such as eco-friendly, earth-abundant and inexpensive elemental compositions, simple processing, and high-efficiency light emission with photoluminescence quantum yield (PLQY) values approaching unity. The most prominent members of these recently discovered Cu(I) halide light emitters include  $\text{Cs}_3\text{Cu}_2(\text{Br},\text{I})_5$ ,  $\text{Rb}_2\text{CuX}_3$ , and  $\text{K}_2\text{CuX}_3$  ( $\text{X} = \text{Cl}, \text{Br}$ ), which demonstrate near-unity PLQY blue emission at room temperature.<sup>23, 43, 136, 144</sup> Interestingly, as is evident from this list, the light emission properties of Cu(I) halides are very weakly dependent on the alkali metal and halogen sites, and therefore, their substitutions do not provide a route for tuning their PL emission. This observation is in stark contrast to the all-inorganic lead halides such as the  $\text{CsPbX}_3$ , for which the wide range tunability of their PL emission is one of their noted advantages.<sup>133, 134, 145, 146</sup> The reason for the notably low tunability of PL properties of Cu(I) halides lies in the intricacies of their band structures: the top of the valence band and the bottom of the conduction band are dominated by Cu  $3d$  and  $4s$  orbitals, respectively.<sup>147</sup> Therefore, to change band structures and consequently light emission properties of copper(I) halides, a strategy can be formulated centered around the replacement of Cu(I) with a different metal such as Ag(I). Such substitution is also expected to improve the stability of Cu(I) halides, which is currently one of the significant barriers for considerations of Cu(I) halides for practical applications as materials such as  $\text{Rb}_2\text{CuX}_3$  have been shown to degrade in humid air rapidly.<sup>136</sup> In contrast, the monovalent

oxidation state is preferred by silver, and therefore, degradation via oxidation is unlikely to occur in Ag(I) halides.

The recently discovered ternary Cu(I) halides have been explored for varieties of applications such as in high-efficiency LEDs, fast scintillation and dynamic X-ray imaging.<sup>136, 148,</sup>  
<sup>149</sup> In addition, highly luminescent materials can also be candidates for anti-counterfeiting applications due to their chemical durability, unique optical properties, low cost, difficulty in their duplications, and good concealment.<sup>150</sup> Estimated economic losses reached \$1.7 trillion in 2015 due to counterfeiting, and this value has been increasing.<sup>151</sup> Various luminescent materials, including quantum dots, organic dyes, metal-organic frameworks (MOFs), lanthanide-based materials, and lead halides, have been tested for anti-counterfeiting applications.<sup>150, 151</sup> Here, we report a facile method of preparation of a new family of candidate materials for anti-counterfeiting applications –  $A_2AgX_3$  ( $A = Rb, Cs$ ;  $X = Cl, Br, I$ ), which are substitution analogs of brightly luminescent blue-emitting  $A_2CuX_3$ . Confirming our materials design ideas, the replacement of Cu(I) with Ag(I) has a significant impact on the electronic band structures, and consequently, the light emission properties of  $A_2AgX_3$ . Furthermore, we report a strategy for fabricating luminescent inks based on  $A_2AgX_3$ , which are used for high-end anti-counterfeiting labels with demonstrated stability in water, under heating and ultrasonication. The obtained materials were characterized using X-ray diffraction (PXRD) and optical spectroscopy methods. Our experimental work is complemented by comprehensive density functional theory (DFT) calculations, which suggest the much more significant contribution of halogen- $p$  orbitals in the valence band of  $A_2AgX_3$ , as well as composition-dependent multi-excitonic emission including emissions from defect-bound excitons (DBEs) and self-trapped excitons (STEs), explaining the observed more tunable and starkly different PL properties. Our combined experimental and computational work shows that

Ag(I) halides are an exciting new class of highly luminescent multinary halides with improved stability.

### **3.1.2 Experimental Synthesis and Methods for $A_2AgX_3$**

#### **3.1.2.1 Materials**

Rubidium chloride (99%, Alfa Aesar), rubidium bromide (99%, Alfa Aesar), rubidium iodide (99%, Alfa Aesar), cesium bromide (>99%, Sigma-Aldrich), cesium iodide (>99%, Sigma-Aldrich), silver chloride (>99%, Alfa Aesar), silver bromide (99.5%, Alfa Aesar), silver iodide (99.999%, Alfa Aesar), polymethyl methacrylate (PMMA) (Sigma-Aldrich), and toluene (>99.5%, Sigma-Aldrich) were purchased and used as received.

#### **3.1.2.2 $Rb_2AgX_3$ (X = Cl, Br, I) Synthesis**

$Rb_2AgX_3$  (X = Cl, Br, I) were synthesized by a facile solid-state method. Stoichiometric amounts of starting materials, RbX and AgX, were weighed precisely and ground for 30 minutes for homogeneous mixing inside a nitrogen-filled glove box. The grounded mixtures were pressed into pellets, then sealed under approximately 5 mTorr vacuum. The pellets of  $Rb_2AgCl_3$ ,  $Rb_2AgBr_3$ , and  $Rb_2AgI_3$  were annealed at 260 °C, 268 °C and 260 °C for 60 hours, 60 hours, and 96 hours, respectively. This procedure was repeated by regrinding the collected pellets, re-pelletizing, and annealing under the same conditions to ensure sample homogeneity and total consumption of reactants. To test the sample-to-sample variation in the optical properties,  $Rb_2AgI_3$  samples with a short annealing time of 12 hours were also prepared.

#### **3.1.2.3 $Cs_2AgX_3$ (X = Br, I) Synthesis**

$Cs_2AgX_3$  (X = Br, I) were also synthesized using solid-state techniques. Stoichiometric 2:1 ratios of CsX and AgX were weighed precisely and ground for 30 minutes for homogeneous mixing inside a nitrogen-filled glove box, pressed into pellets, and sealed under approximately



5mTorr vacuum. The  $\text{Cs}_2\text{AgBr}_3$  and  $\text{Cs}_2\text{AgI}_3$  pellets were annealed at  $260^\circ\text{C}$  and  $240^\circ\text{C}$  for 160 hours and 80 hours, respectively, and cooled to room temperature over 12 hours. The obtained samples were then re-ground and pelletized again for a repeated annealing to improve the sample homogeneity and purity.

#### **3.1.2.4 Ink preparation**

To prepare luminescent inks, 2 g of polymethyl methacrylate (PMMA) was added into 5 ml of toluene and stirred at room temperature until PMMA completely dissolved. Then, as-synthesized  $\text{A}_2\text{AgX}_3$  (R= Rb, Cs, X= Cl, Br, I) polycrystalline powder samples (200 mg) were dispersed in this solution and stirred overnight, followed by sonication for 1 hour. Finally,  $\text{A}_2\text{AgX}_3$  (R= Rb, Cs, X= Cl, Br, I) based luminescent inks were used for writing a security code for anti-counterfeiting and printing latent fingerprints.

#### **3.1.2.5 Powder X-ray Diffraction (PXRD)**

Powder X-ray powder diffraction (PXRD) measurements were taken on a Rigaku Miniflex600 equipped with a D/tex detector and a Rigaku Ultima IV diffractometer, both with a Ni-filtered  $\text{Cu-K}\alpha$  radiation source. Data were collected at room temperature in the  $3 - 90^\circ$  ( $2\theta$ ) range, with a step size of  $0.02^\circ$ . For evaluating materials stability, periodic PXRD experiments were taken on powder samples of  $\text{A}_2\text{AgX}_3$  left in the dark under ambient air conditions at  $19.7^\circ\text{C}$ .

#### **3.1.2.6 Thermogravimetry and Differential Scanning Calorimetry (TGA/DSC)**

The thermal stability of polycrystalline powders of  $\text{A}_2\text{AgX}_3$  (R= Rb, Cs, X= Cl, Br, I) was examined through thermogravimetric analysis and differential scanning calorimetry (TGA/DSC) measurements using a TA Instruments SDT 650 thermal analyzer system. The samples were heated from  $25$  to  $450^\circ\text{C}$  with a heating rate of  $5^\circ\text{C}/\text{min}$  under an inert flow of dry nitrogen gas at a rate of  $100\text{ mL}/\text{min}$ .

### 3.1.2.7 Optical Measurements

Optical properties of polycrystalline powders of  $A_2AgX_3$  were studied using a Jobin Yvon Fluorolog-3 spectrofluorometer (Horiba) equipped with a Xenon lamp (450 W) and Quanta-φ integrating sphere. For each sample, photoluminescence emission (PL), photoluminescence excitation (PLE), and photoluminescence quantum yield (PLQY) measurements were performed from 270 to 750 nm. Time-resolved photoluminescence (TRPL) measurements were taken using a Time-Correlated Single Photon Counting (TCSPC) system that includes a DeltaHub DH-HT high throughput TCSPC controller and NanoLED NL-C2 pulsed diode controller. For TRPL measurements, a 299 nm NanoLED diode with a <1.2 ns pulse duration was used as an excitation source. In order to fit the data, the following equations were used:

$$I(t) = \sum_i^n \alpha_i \exp\left(\frac{-t}{\tau_i}\right)$$
$$\alpha_1 = \frac{B_1}{(B_1 + B_2)} \quad \alpha_2 = \frac{B_2}{(B_1 + B_2)}$$

Fitting parameters are available in Table A3.

Quantum yield is determined by:

$$\text{Quantum Yield} = \left( \frac{Em_s - Em_b}{Ex_b - Ex_s} \right) \times 100$$

$Ex_s$  and  $Ex_b$  are the integrated excitation profiles of the sample, and the blank and  $Em_s$  and  $Em_b$  are the integrated emission profiles of the sample and blank, respectively. An Area Balance Factor is applied in the FluorEssence software, which accounts for changes in integration times between excitation and emission scans and the use of neutral density filters.

### 3.1.2.8 Microscopy

A [Thermo Quattro S field-emission environmental Scanning Electron Microscope \(FE-](#)

[ESEM](#)) was utilized to obtain the SEM images. The aliquots of the inks were placed on top of clean silicon plate and images were collected using the back-scattered detector.

### **3.1.2.8 Computational Methods**

Our calculations were based on density functional theory (DFT) as implemented in the VASP code.<sup>78</sup> The kinetic energy cutoff of the plane-wave basis is 262 eV. The projector augmented wave method was used to describe the interaction between ions and electrons.<sup>79</sup> The lattice parameters were fixed at the experimentally measured values while the atomic positions were optimized until the force on each atom is less than 0.02 eV/Å. The electronic band structure and density of states (DOS) were calculated using Perdew-Burke-Ernzerhof (PBE) exchange-correlation functional<sup>80</sup>, and the band gap was further corrected using the hybrid PBE0 functional.<sup>81</sup>

The optimized ground- and excited-state structures [including the structures of self-trapped excitons (STE) and defect-bound excitons] were obtained by using the hybrid PBE0 functional,<sup>81</sup> which has 25% non-local Fock exchange. The occupation numbers of the electron- and hole-occupied eigenlevels are fixed [ $\Delta$  self-consistent field ( $\Delta$ SCF) method<sup>87</sup>] for the total energy calculation of an exciton and throughout the entire excited-state structural relaxation process. Following the Franck-Condon principle, the excitation and emission energies of an exciton were calculated by taking the energy difference between the excited and the ground state energies using the relaxed ground-state and excited-state structures, respectively.

### **3.1.3 Crystal Structure and Stability of the A<sub>2</sub>AgX<sub>3</sub> Family**

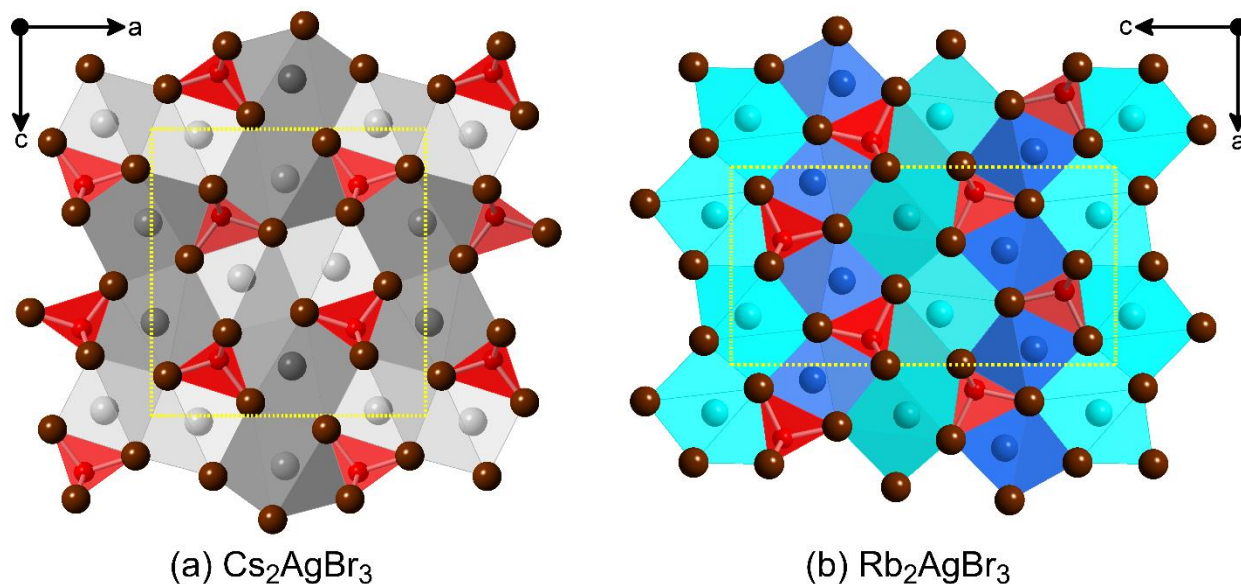


**Figure 30.** Orthorhombic crystal structures of (a)  $\text{Cs}_2\text{AgBr}_3$  and (b)  $\text{Rb}_2\text{AgBr}_3$  viewed down the  $b$ -axes. Both compounds feature  $1\text{D } \infty^1[\text{AgX}_3]^{2-}$  chains (shown in red) separated by  $\text{A}^+$  cations. The difference in the packing of the  $\infty^1[\text{AgX}_3]^{2-}$  chains and  $\text{A}^+$  cations is emphasized by displaying (a) Cs1 and Cs2 in dark grey and light grey in  $\text{Cs}_2\text{AgBr}_3$  and (b) Rb1 and Rb2 in dark blue and light blue in  $\text{Rb}_2\text{AgBr}_3$ ; Ag and Br are shown in red and brown, respectively.

$\text{A}_2\text{AgX}_3$  crystallize in the orthorhombic space group  $Pnma$  featuring  $1\text{D } \infty^1[\text{AgX}_3]^{2-}$  chains separated by  $\text{A}^+$  cations (Figure 30). In this family, the use of the larger  $\text{Cs}^+$  cation results in the  $\text{K}_2\text{CuCl}_3$  type structure, i.e.,  $\text{Cs}_2\text{AgX}_3$  are isostructural to  $\text{A}_2\text{CuX}_3$ . In contrast, the  $\infty^1[\text{AgX}_3]^{2-}$  chains are packed differently with respect to the  $\text{A}^+$  cations in the case of the  $\text{K}_2\text{AgI}_3$  type compounds  $\text{Rb}_2\text{AgX}_3$  and  $\text{K}_2\text{AgX}_3$  featuring the smaller alkali cations  $\text{Rb}^+$  and  $\text{K}^+$  (Figure 30).

To determine the bulk purity and environmental stability of the as prepared  $\text{A}_2\text{AgX}_3$  samples, periodic PXRD measurements were taken over four weeks at room temperature. This data was then fitted to the previously published structures of these compounds to ensure excellent purity.<sup>28</sup> The room temperature PXRD patterns of  $\text{A}_2\text{AgX}_3$  are illustrated in Figure 31(a-e). Our PXRD results suggest that the preparation method employed in this work is an effective route for syntheses of high purity and high crystallinity  $\text{A}_2\text{AgX}_3$  materials. Furthermore,  $\text{Rb}_2\text{AgX}_3$  are found to have significantly improved air stability with no measurable changes for the samples left in

ambient air for four weeks (Figure A19). This contrasts with the reported poor stability of  $\text{Rb}_2\text{CuX}_3$  ( $\text{X} = \text{Cl}, \text{Br}$ ), which show noticeable degradation in days and are largely degraded in bulk within a month.<sup>136</sup>

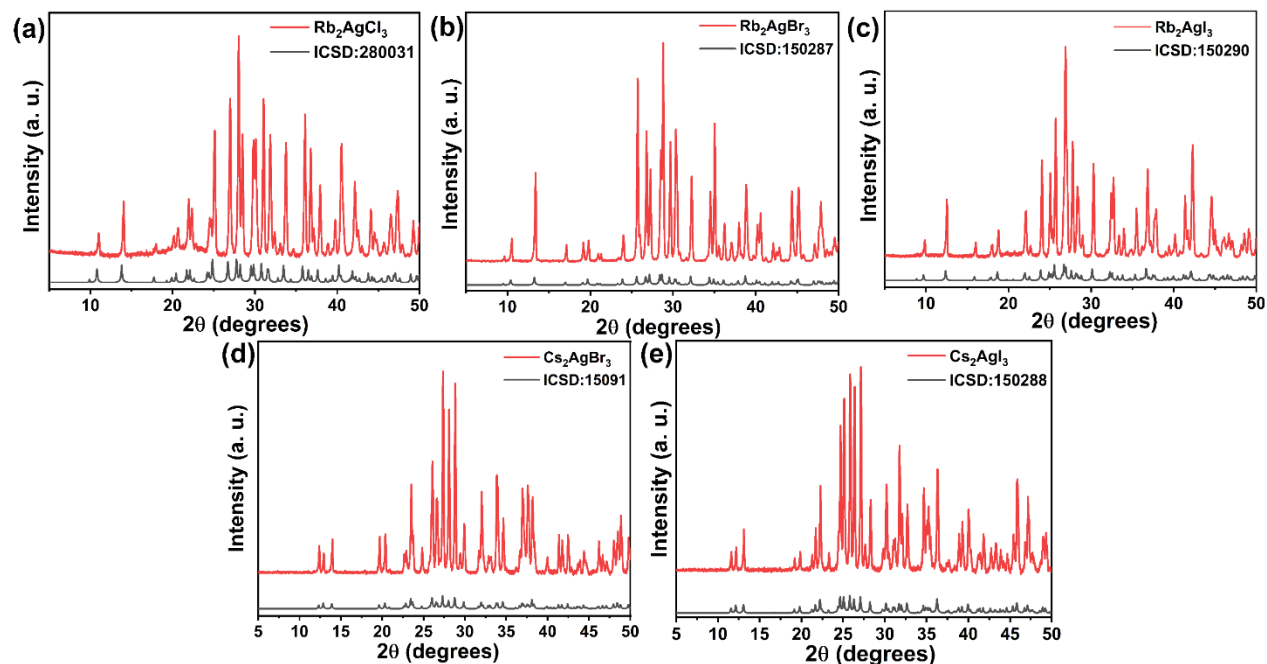


**Figure 31.** The room temperature PXRD patterns of (a)  $\text{Rb}_2\text{AgCl}_3$ , (b)  $\text{Rb}_2\text{AgBr}_3$ , (c)  $\text{Rb}_2\text{AgI}_3$ , (d)  $\text{Cs}_2\text{AgBr}_3$ , and (e)  $\text{Cs}_2\text{AgI}_3$ . The experimental patterns are plotted in red with the literature reference value plotted in black.

Moreover, the thermal stability of  $\text{Rb}_2\text{AgCl}_3$ ,  $\text{Rb}_2\text{AgBr}_3$ , and  $\text{Rb}_2\text{AgI}_3$  was also evaluated by heating polycrystalline powder samples at 100 °C for 48 hours, which suggests that these compounds are structurally stable under these conditions (Figure A20). Thermogravimetric analysis (TGA) measurements suggest that  $\text{A}_2\text{AgX}_3$  show no significant loss in weight up to 450 °C (Figure A21). This observation is consistent with the improved thermal stability of all-inorganic metal halides such as  $\text{Rb}_2\text{CuX}_3$ ,  $\text{Rb}_4\text{Ag}_2\text{BiBr}_9$ ,  $\text{Cs}_3\text{Cu}_2\text{Br}_{5-x}\text{I}_x$ , and  $\text{Cs}_2\text{SnI}_6$  as compared to hybrid organic-inorganic metal halides.<sup>23, 75, 77, 136, 144</sup> The differential scanning calorimetry (DSC) results demonstrate that  $\text{Rb}_2\text{AgCl}_3$ ,  $\text{Rb}_2\text{AgBr}_3$ ,  $\text{Rb}_2\text{AgI}_3$ ,  $\text{Cs}_2\text{AgBr}_3$ , and  $\text{Cs}_2\text{AgI}_3$  show peritectic decompositions at 303.4 °C, 296.9 °C, 303.4 °C, 297.4 °C, 257.9 °C, and 252.8 °C, respectively,

which matches with the reported phase diagram for compounds that were previously studied (Figure A21).<sup>152</sup>

### **3.1.4 Optical Properties of $A_2AgX_3$**

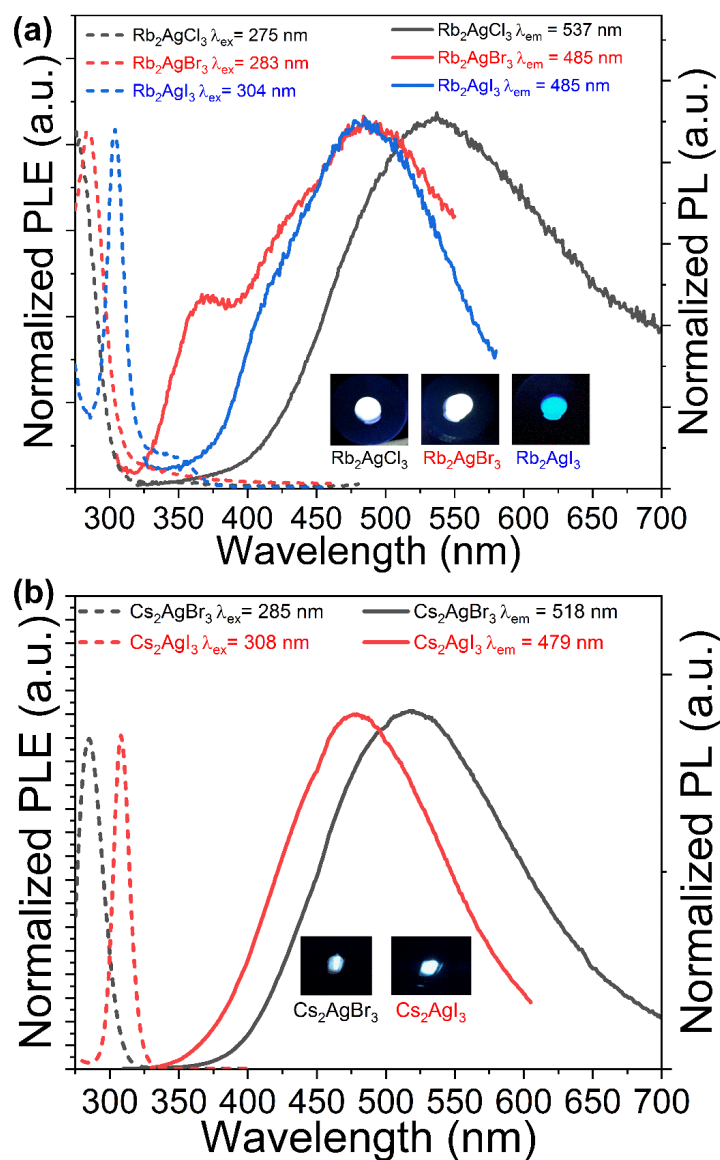


**Figure 32.** Normalized room temperature photoluminescence excitation (PLE) and photoluminescence emission (PL) plots for (a) Rb<sub>2</sub>AgX<sub>3</sub> and (b) Cs<sub>2</sub>AgX<sub>3</sub>. Insets show the visible emission from samples when excited with their respective excitation maxima.

Photoluminescence excitation (PLE) and emission (PL) spectra of A<sub>2</sub>AgX<sub>3</sub> are provided in Figure 32. PLE spectra of Rb<sub>2</sub>AgCl<sub>3</sub>, Rb<sub>2</sub>AgBr<sub>3</sub>, Rb<sub>2</sub>AgI<sub>3</sub>, Cs<sub>2</sub>AgBr<sub>3</sub>, and Cs<sub>2</sub>AgI<sub>3</sub> show sharp excitation bands centered at 280 nm, 284 nm, 304 nm, 285 nm, and 308 nm, respectively, which give broad emission peaks with maxima at 534 nm, 484 nm, 483 nm, 518 nm, and 479 nm, respectively. The obtained PLE spectra are strikingly similar to that of A<sub>2</sub>CuX<sub>3</sub>, with PLE maxima at virtually the same wavelength.<sup>43, 53, 117, 136</sup> In contrast, the PL emission spectra are both

significantly red-shifted and have a larger full width at half-maximum (FWHM) than the  $A_2CuX_3$  counterparts.<sup>43, 53, 117, 136</sup> This broadband emission causes the  $A_2AgX_3$  compounds to have a white or bluish-white emission compared to Cu(I) analogs  $A_2CuX_3$ , which are all blue emitters.<sup>43, 53, 147</sup> Based on our PL and PLE results,  $Rb_2AgCl_3$ ,  $Rb_2AgBr_3$ ,  $Rb_2AgI_3$ ,  $Cs_2AgBr_3$ , and  $Cs_2AgI_3$  exhibit large Stokes shift values of 254 nm, 200 nm, 179 nm, 233 nm, and 171 nm, respectively. The observed large Stokes shifts in low-dimensional metal halides are typically a sign of light emission originating from self-trapped excitons (STEs) and defect-bound excitons (DBEs).<sup>48, 53, 117, 143, 147, 153, 154</sup> Notably, the large Stokes shift values for  $A_2AgX_3$  are approximately double of what is observed in the  $A_2CuX_3$  compounds, which is explained below by the difference in the main emission mechanisms, i.e., the DBE emission in  $A_2AgX_3$  vs. the STE emission in  $A_2CuX_3$ .<sup>43, 136, 147</sup> This observation is also consistent with the previous work on doped NaF samples, which also showed a stronger lattice coupling for  $Ag^+$  compared  $Cu^+$  doping.<sup>155</sup>

The measured PL properties of  $A_2AgX_3$  show tunability through substitution including some changes with substitutions on the  $A^+$  cation site and more pronounced changes via the substitutions on the halide site. The composition dependence of PL in  $A_2AgX_3$  is in stark contrast with the nearly complete lack of tunability observed for the analogous blue-emitting  $Rb_2CuX_3$  and  $K_2CuX_3$ .<sup>147</sup> The weak tunability of PL properties of  $A_2CuX_3$  has been explained by the fact that the Cu states dominate the states around the band gap and that the STEs formed in these compounds are localized around the Cu sites.<sup>43, 136, 147</sup> In comparison, our results on  $A_2AgX_3$  suggest that defects play a more significant role in their PL properties. We find that certain members of this system exhibit both DBEs and STEs (see the computational analysis section below), which in combination provide broader and more tunable light emission properties.



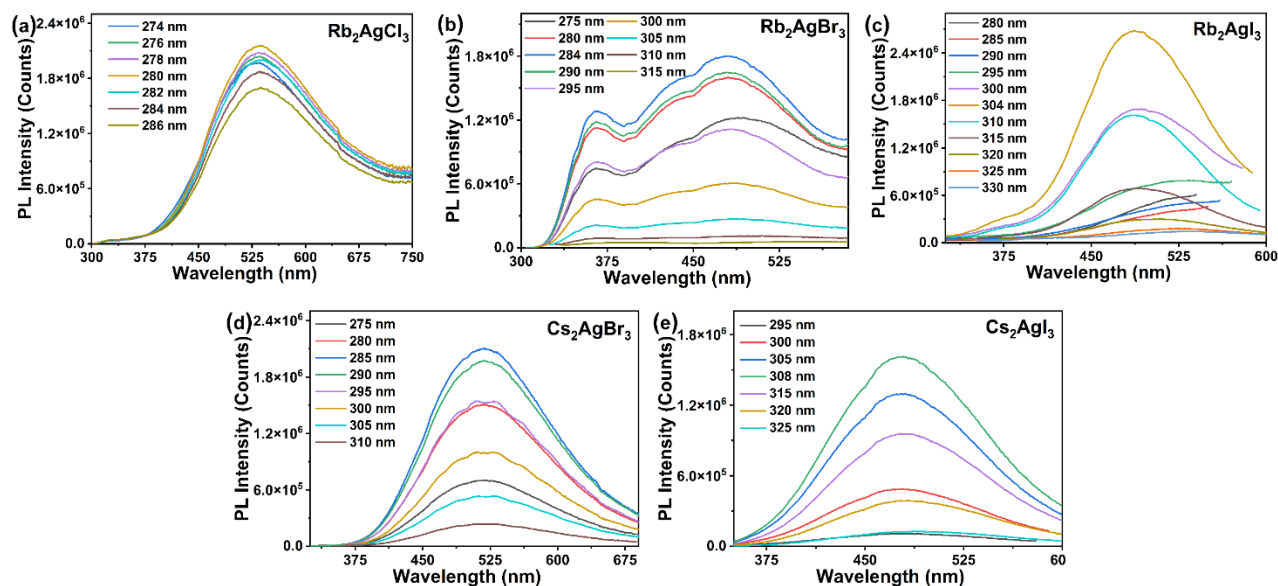


**Figure 33.** Excitation-dependent PL measurements results for (a)  $\text{Rb}_2\text{AgCl}_3$ , (b)  $\text{Rb}_2\text{AgBr}_3$ , (c)  $\text{Rb}_2\text{AgI}_3$ , (d)  $\text{Cs}_2\text{AgBr}_3$ , and (e)  $\text{Cs}_2\text{AgI}_3$ .

To better understand the light emission properties of  $\text{A}_2\text{AgX}_3$ , excitation wavelength-dependent PL spectra (Figure 33) were measured. Most notable changes occur for  $\text{Rb}_2\text{AgI}_3$ , in which higher excitation energy causes a small red shift in the PL emission. Other members of the  $\text{A}_2\text{AgX}_3$  have largely preserved PL peak shapes and positions. In addition, we performed PLE measurements for a variety of emission wavelengths, which confirmed that the observed PL emission peaks were all related to a singular PLE maximum in each of the compounds (Figure A22). These measurements reveal that in each of  $\text{A}_2\text{AgX}_3$ , a single photoexcited state is the source of their respective PL emission spectra, including the case of  $\text{Rb}_2\text{AgBr}_3$ , which clearly shows the presence of multiple emission centers (Figure 32). The case of  $\text{Rb}_2\text{AgBr}_3$  is particularly interesting because its measured photophysical properties indicate the presence of two emission centers, which are assigned to DBE and STE centers (see below). In combination with the observed large Stokes shifts and broad emission spectra, our in-depth PL results are suggestive of primarily defect-bound exciton emission in  $\text{A}_2\text{AgX}_3$ .

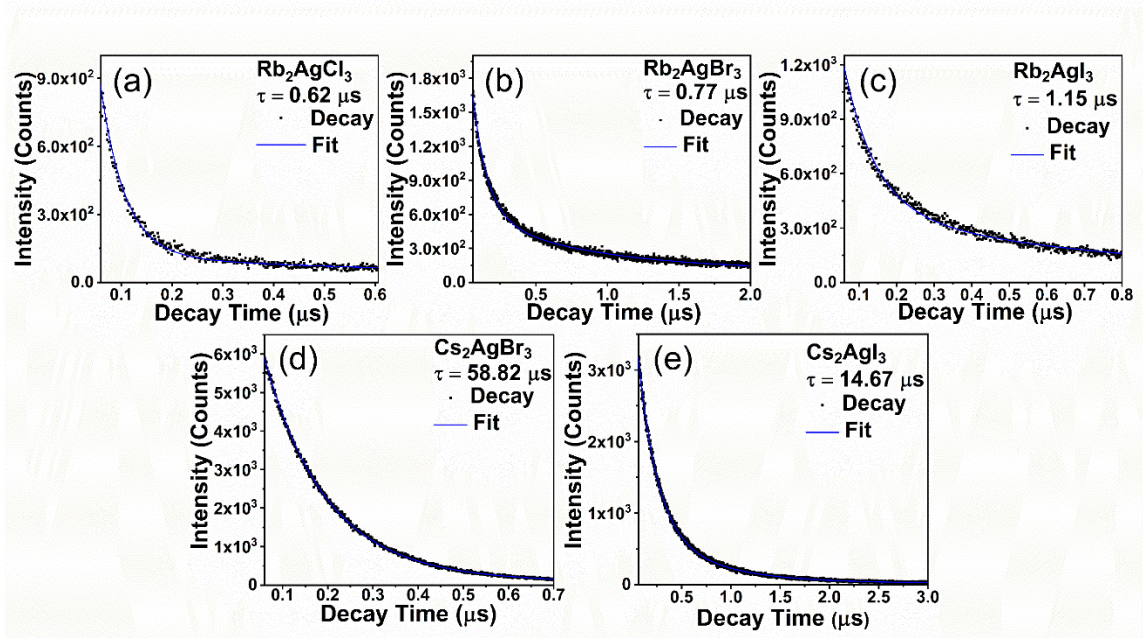


**Figure 34.** Time-resolved photoluminescence (TRPL) measurement results for (a)  $\text{Rb}_2\text{AgCl}_3$ , (b)  $\text{Rb}_2\text{AgBr}_3$ , (c)  $\text{Rb}_2\text{AgI}_3$ , (d)  $\text{Cs}_2\text{AgBr}_3$ , and (e)  $\text{Cs}_2\text{AgI}_3$ .

The lifetime of PL emission from any luminescent material is an essential parameter for the potential practical applications of luminescent materials. For example, for certain photodetector and sensing applications, luminescent materials with faster decay rates are more desirable, while luminescent materials with longer decay are more suitable for signal or self-luminous light source applications.<sup>156, 157</sup> For  $\text{A}_2\text{AgX}_3$ , the TRPL decay profiles and their exponential fits are provided in Figure A34; the decay profiles were fitted with double-exponential function as where  $\tau_1$  and  $\tau_2$  are the decay lifetimes of the luminescence, and A1 and A2 are the weighting parameters. The fitting results of our TRPL data are provided in Table A3. The observed average lifetime of  $\text{Rb}_2\text{AgCl}_3$ ,  $\text{Rb}_2\text{AgBr}_3$ ,  $\text{Rb}_2\text{AgI}_3$ ,  $\text{Cs}_2\text{AgBr}_3$ , and  $\text{Cs}_2\text{AgI}_3$  polycrystalline powders are 0.62  $\mu\text{s}$ , 0.77  $\mu\text{s}$ , 1.15  $\mu\text{s}$ , 58.82  $\mu\text{s}$ , and 14.67  $\mu\text{s}$ , respectively. These lifetimes are on par with the  $\sim 10\text{-}12$   $\mu\text{s}$  lifetimes reported in  $\text{A}_2\text{CuX}_3$  compounds, which have triplet-STE-based emission, suggesting a similar triplet-exciton-based light emission in  $\text{A}_2\text{AgX}_3$ . In contrast, free exciton emission is characterized by significantly faster emission on the

nanosecond scale.<sup>158</sup>

### 3.1.5 Exciton Calculations and Emission Mechanism

Electronic band structures and DOS of  $\text{Rb}_2\text{AgX}_3$  ( $X = \text{Cl}, \text{Br}, \text{I}$ ) obtained by PBE calculations are shown in Figure 35. The band gap of  $\text{Rb}_2\text{AgCl}_3$  is direct at the  $\Gamma$  point, while those of  $\text{Rb}_2\text{AgBr}_3$  and  $\text{Rb}_2\text{AgI}_3$  are slightly indirect. The conduction band minima (CBM) of both  $\text{Rb}_2\text{AgBr}_3$  and  $\text{Rb}_2\text{AgI}_3$  are located at the  $\Gamma$  point, while their valence band maxima (VBM) at the X point are slightly higher than those at the  $\Gamma$  point by 0.01 eV. The direct band gaps of all three halides calculated using both the PBE and hybrid PBE0 functionals are shown in Table A4.

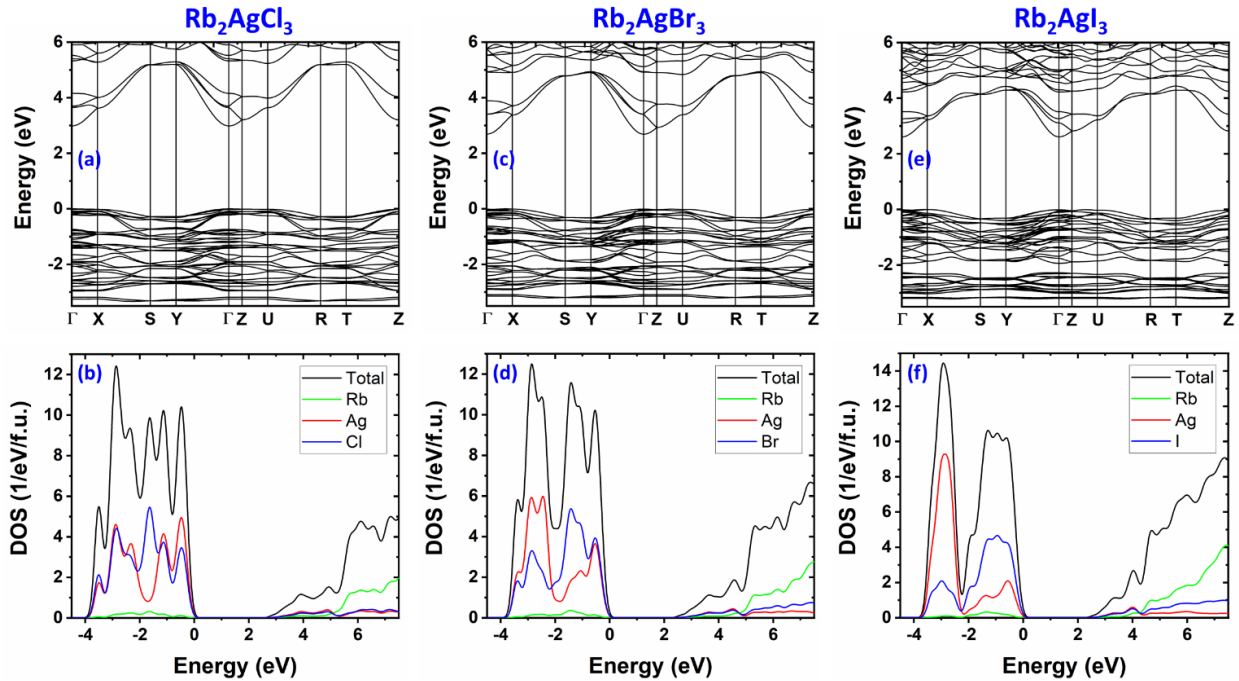


**Figure 35.** Electronic band structure and density of states (DOS) of  $\text{Rb}_2\text{AgCl}_3$  (a-b),  $\text{Rb}_2\text{AgBr}_3$  (c-d), and  $\text{Rb}_2\text{AgI}_3$  (e-f), respectively.

Figure 35 shows that the conduction band of  $\text{Rb}_2\text{AgX}_3$  is made up of Ag-5s orbitals, which hybridize with halogen- $p$  orbitals, while the valence band is a mixing of Ag-4d and halogen- $p$  states. The band gaps follow the normal decreasing trend from  $\text{Rb}_2\text{AgCl}_3$ ,  $\text{Rb}_2\text{AgBr}_3$ , to  $\text{Rb}_2\text{AgI}_3$ ,

consistent with the red shift of excitation energies observed in the experiments. This is in contrast to  $\text{Rb}_2\text{CuX}_3$  and  $\text{K}_2\text{CuX}_3$ , in which Cu-3d orbitals dominate the valence band, and thus the band gap is nearly independent on the type of the halogen ion.

**Table 4.** Calculated STE excitation and emission energies.

$\text{Rb}_2\text{AgCl}_3$		$\text{Rb}_2\text{AgBr}_3$		$\text{Rb}_2\text{AgI}_3$	
Excitation	Emission	Excitation	Emission	Excitation	Emission
4.821 eV	3.842 eV	4.436 eV	3.692 eV	4.203 eV	3.222 eV
(257 nm)	(323 nm)	(280 nm)	(336 nm)	(295 nm)	(385 nm)

To better understand the multi-excitonic nature of light emission in this family, calculations of excitonic properties were carried out for  $\text{Rb}_2\text{AgX}_3$  (Tables 4-5). The calculated exciton excitation energies in  $\text{Rb}_2\text{AgX}_3$  (X = Cl, Br, I) are 4.821 eV, 4.436 eV, and 4.203 eV, in good agreement with the experimentally observed values of 4.509 eV, 4.381 eV, and 4.078 eV, respectively. The strong excited-state structural relaxation (similar to that reported in  $\text{Rb}_2\text{CuX}_3$ ) leads to the formation of a STE.<sup>136</sup> The calculated STE emission energies of 3.842 eV, 3.692 eV, 3.222 eV in  $\text{Rb}_2\text{AgX}_3$  (X = Cl, Br, I) are much higher in energy than the main PL peaks of 2.309 eV, 2.556 eV, 2.556 eV, respectively (Table 4). Previous calculations utilizing the same computational method showed that calculated STE emission energies in low-dimensional halides agree well with PL peak energies with errors typically less than 0.3 eV.<sup>121</sup> The large differences between calculated STE emission energies and the observed main PL peak energies suggest that the main PL peaks in Figure 32(a) are likely due to other sources, such as native defects. We further investigated excitons trapped by vacancies ( $V_{\text{Rb}}^-$ ,  $V_{\text{Ag}}^-$ , and  $V_{\text{X}}^+$ ), which are typically the main defects in halides. There are three inequivalent halogen X sites, two inequivalent Rb sites, and one Ag

sites in  $\text{Rb}_2\text{AgX}_3$ , which are shown in Figure A23. The calculated DBE emission energies are shown in Table 5; a comparison of calculated and experimental transition energy levels for  $\text{Rb}_2\text{AgX}_3$  is provided in Figure A24. The calculated emission energies of excitons trapped by the most stable halogen vacancy ( $V_{X3}^+$ ) are 2.477 eV in  $\text{Rb}_2\text{AgCl}_3$  and 2.322 eV in  $\text{Rb}_2\text{AgBr}_3$ , which are in good agreement with the observed main PL peaks at 2.309 eV and 2.556 eV in the two respective compounds. For  $\text{Rb}_2\text{AgI}_3$ , the calculated emission energies of  $V_{Ag}^-$  (2.919 eV) and  $V_{Rb2}^-$  (2.935 eV) are reasonably close to the observed main PL peak at 2.556 eV. Therefore, we tentatively assign the main PL peaks in  $\text{Rb}_2\text{AgCl}_3$  and  $\text{Rb}_2\text{AgBr}_3$  to the halogen vacancy and that in  $\text{Rb}_2\text{AgI}_3$  to cation vacancies. In addition, the metastable halogen vacancy ( $V_{X2}^+$  in  $\text{Rb}_2\text{AgCl}_3$  and  $\text{Rb}_2\text{AgBr}_3$ ) could also contribute to the broad PL peak because its energy is just slightly higher than the most stable halogen vacancy. There is also a minor peak at 3.416 eV (363 nm) in the PL spectrum of  $\text{Rb}_2\text{AgBr}_3$  (Figure A25), which is close to the calculated STE emission energy of 3.692 eV (336 nm). This suggests that some (but not all) excitation energy in  $\text{Rb}_2\text{AgBr}_3$  is transferred from the triplet STE to defects, leading to emission by both STEs and defects, while, in  $\text{Rb}_2\text{AgCl}_3$  and  $\text{Rb}_2\text{AgI}_3$ , STEs are likely quickly trapped by defects, resulting in the quenching of the STE emission. The observation of significant contributions of both STE and DBE to the PL of  $\text{Rb}_2\text{AgBr}_3$  suggests that the timescale of STE trapping by defects is competitive to the STE emission time; therefore, it is reasonable to expect that the DBE emission time is comparable to even longer than the STE emission time, which is consistent with the measured long lifetimes of PL emission. The dual band emission mechanism in  $\text{Rb}_2\text{AgBr}_3$  is responsible for its unusual white light emission.

The presence of halogen vacancy defects in ternary silver halides has been known and reported in the literature.<sup>29, 153</sup> Previously, the PL peak observed in  $\text{Rb}_2\text{AgBr}_3$  was assigned to

neutral  $V_{Br}$  ( $V_{Br1}^0$ ) rather than  $V_{Br3}^+$  proposed in this work.<sup>153</sup> Note that the cation and anion vacancies in a large-gap halide are usually ionized and compensate each other, resulting in charge neutrality. At the +1 charge state,  $V_{Br1}^+$  is less stable than  $V_{Br3}^+$  and the calculated emission energy of  $V_{Br1}^+$  is much lower than the observed main PL peak, as shown in Table 5. On the other hand, our calculated band gap (5.10 eV) and STE emission energy (3.692 eV) in  $Rb_2AgBr_3$  are in excellent agreement with those reported previously (5.1 eV and 3.7 eV).<sup>153</sup> This emission mechanism is also supported by the literature precedent of analogous ternary silver halides.<sup>131</sup>

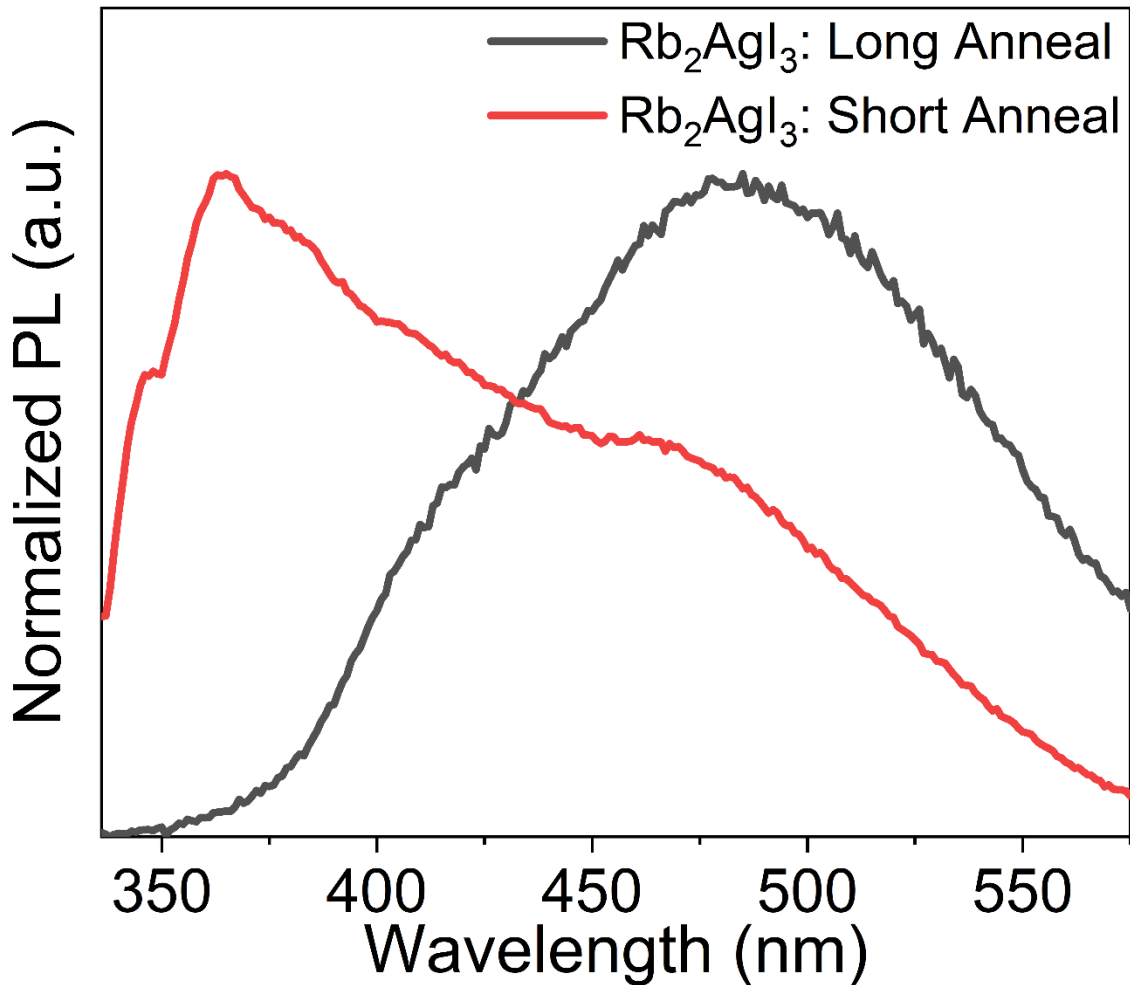


**Figure 36.** A comparison of the normalized PL spectra of different  $Rb_2AgI_3$  samples prepared using a long (160 hours) and short thermal annealing (12 hours) times.

As another supporting evidence for the significant role of defects in determining the

photophysical properties of  $A_2AgX_3$ , previously it was reported that the pulling of vacuum on a  $Rb_2AgBr_3$  sample significantly increases the intensity of the defect PL peak.<sup>153</sup> To test this further, we prepared  $Rb_2AgI_3$  using two differing techniques: (i) the more reliable method of sample preparation involved annealing of the sample in a vacuum sealed ampoule under 5 mTorr for 80 hours, followed by regrinding and reannealing for another 80 hours. The second method involved only a short annealing time of 12 hours. The PL spectra for resultant samples are starkly different (Figure A36), suggesting the dominant STE emission for the second sample with short annealing time. The emission energy for this sample matches well with the calculated STE transition energy (Figure A24 and Table 4). In contrast, the longer annealing produces a sample with a predominant DBE emission. However, we note that the STE/DBE intensity ratio significantly varies from sample to sample.

**Table 5.** Calculated emission energies from vacancies and STE. The energy of the lowest-energy exciton localized on the halogen/rubidium vacancy site is set to zero.

	Rb <sub>2</sub> AgCl <sub>3</sub>		Rb <sub>2</sub> AgBr <sub>3</sub>		Rb <sub>2</sub> AgI <sub>3</sub>	
	Energy (meV)	Emission	Energy (meV)	Emission	Energy (meV)	Emission
$V_{X1}^+$	134	0.712 eV (1742 nm)	214	1.325 (936 nm)	156	1.15011 (1078 nm)
$V_{X2}^+$	4	2.582 eV (480 nm)	42	2.433 eV (510 nm)	56	2.197 eV (564 nm)
$V_{X3}^+$	0	2.477 eV (501 nm)	0	2.322 eV (534 nm)	0	1.995 eV (621 nm)
$V_{Rb1}^-$	34	3.630 eV (342 nm)	90	3.453 eV (359 nm)	167	2.104 eV (589 nm)
$V_{Rb2}^-$	0	3.665 eV (338 nm)	0	3.520 eV (352 nm)	0	2.935 eV (422 nm)
$V_{Ag}^-$	N/A	3.782 eV (328 nm)	N/A	3.580 eV (346 nm)	N/A	2.919 eV (425 nm)
STE	N/A	3.842 eV (323 nm)	N/A	3.692 eV (336 nm)	N/A	3.222 eV (385 nm)
Exp. emission		2.309 eV (537 nm)		2.556 eV (485 nm)		2.556 eV (485 nm)

Advantageously, Pb-free all-inorganic A<sub>2</sub>AgX<sub>3</sub> not only demonstrate improved air- and thermal-stability as compared to many of the known lead halide perovskites and analogous copper(I) halides, but also show visibly bright room-temperature light emission properties. The estimated PLQY values for fresh samples were 1.52%, 0.37%, 6.37% and 14.41% for Rb<sub>2</sub>AgBr<sub>3</sub>, Rb<sub>2</sub>AgI<sub>3</sub>, Cs<sub>2</sub>AgBr<sub>3</sub> and Cs<sub>2</sub>AgI<sub>3</sub>, respectively. Note that these are conservative estimates since



$A_2AgX_3$  are broadband emitters and our PLQY measurement ranges are constrained by the excitation energy and its overtones. This is especially the case for the  $Rb_2AgX_3$  species, including  $Rb_2AgCl_3$ , for which PLQY cannot be accurately estimated due to its high excitation energy. It is also previously reported that solid-state grown samples often significantly under report the PLQY when compared to single crystals.<sup>136</sup> Finally, a major difference between Ag(I) and Cu(I) halides is that in the former, defects play a lot more significant role in their photophysical behaviors. Therefore, the lower lying defect bands could also be routes for nonradiative recombination in this system. Notwithstanding the lower PLQYs of Ag(I) halides,  $A_2AgX_3$  are also found to have improved photostability (Figure A26). Thus, under a continuous UV irradiation,  $Cs_2AgX_3$  display only a small (< 8%) drop in PLQY values, indicating a significant improvement in photostability as compared to Cu(I) analogs such as  $Rb_2CuCl_3$ .<sup>136</sup> As for  $Rb_2AgX_3$ , the recorded increase in PLQY is due to both increased relative error of low PLQY of these compounds and formation of defects under continuous irradiation.

### **3.1.6 Anti-counterfeiting Inks**

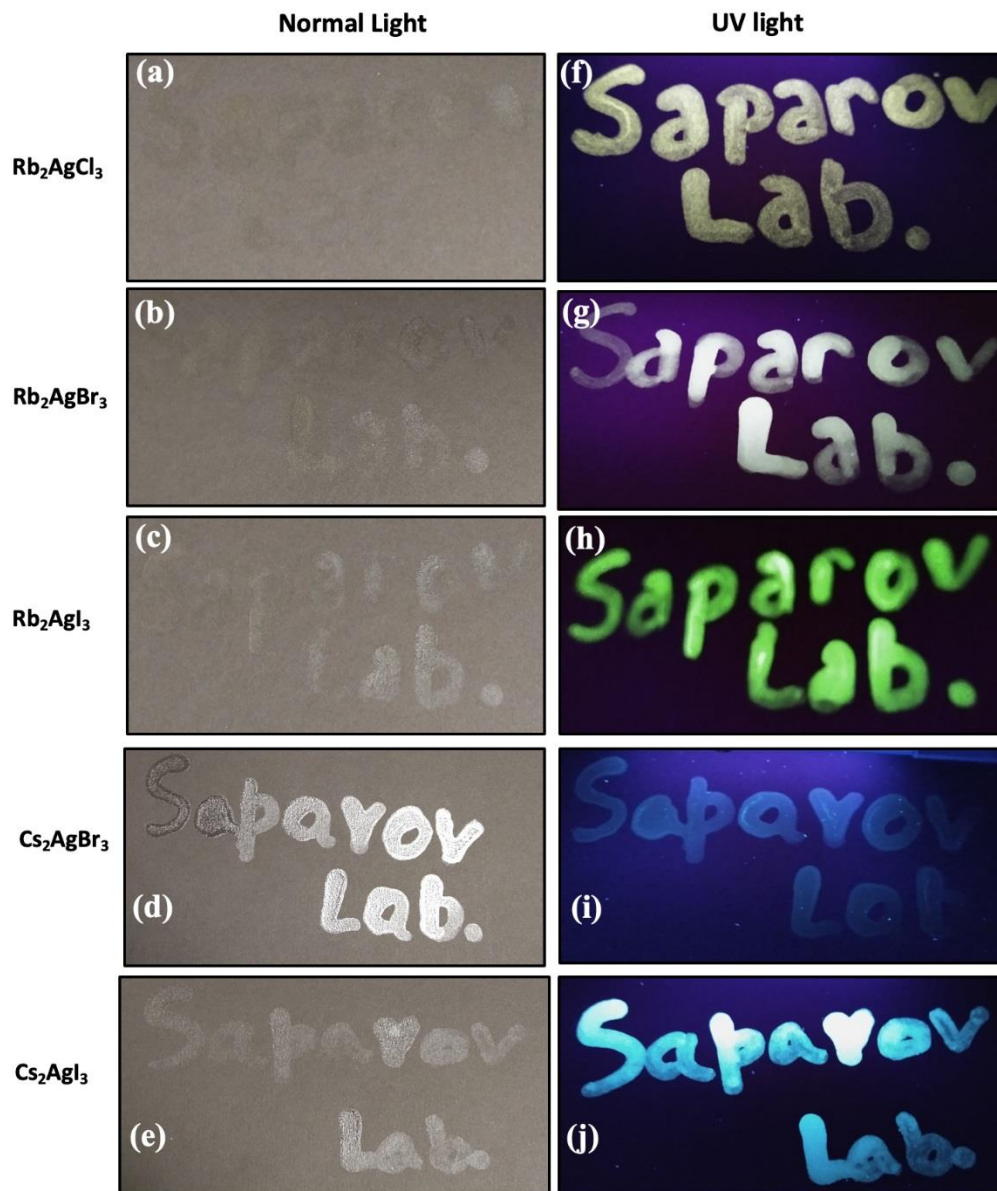


**Figure 37.** The words “Saparov Lab” were written on black paper using the fabricated luminescent ink based on  $\text{A}_2\text{AgX}_3$  under normal light and UV light (365 nm).

Much improved environmental stability and PL tunability of  $\text{A}_2\text{AgX}_3$  allows their consideration for practical uses such as anti-counterfeiting. The counterfeiting and duplicity of valuable documents such as diplomas, certificates, and currency are a rising critical problem worldwide. Recently, lead-based metal halides have been used for anti-counterfeiting applications, however, the presence of toxic lead remains a major issue.<sup>150, 151</sup> We prepared luminescent inks to

validate the feasibility of the as-prepared  $A_2AgX_3$  for anti-counterfeiting applications. The fabricated inks contain  $A_2AgX_3$  individual particles with sizes ranging from approximately 500 nm to a micron and much larger micron scale aggregates (Figure A27). For the proof of concept, the words “**Saparov Lab**” were printed on black paper using the fabricated luminescent ink based on  $A_2AgX_3$  (Figure 37). Interestingly, all five members of  $A_2AgX_3$  show unique emission colors, creating a possibility of multicolor patterns. Furthermore, to demonstrate the versatility of  $A_2AgX_3$  based luminescent inks, we prepared prints on a variety of surfaces and colors, including white weighing papers (Figure A28), colored papers (Figure A29), and transparent polyethylene bags, which can be utilized for commercial packing (Figure A30). In all cases, clearly discernible prints are observed under UV excitation. Our results reveal that the color of the printing surfaces does not affect the printed code words. Therefore, the  $A_2AgX_3$  luminescent inks reported in this work can be used on any color surface, which is a significant advantage over other reported materials for anti-counterfeiting applications.

For potential practical applications of the  $A_2AgX_3$  inks, the printed patterns' stability and durability are of the highest importance. The results suggest that the printed patterns using the  $A_2AgX_3$  inks are water stable (Figure A31). Moreover, only a minimal luminescence intensity loss is observed under heating at elevated temperatures of 60 °C and 80 °C (Figure A21). The mechanical stability of printed patterns was also tested by ultrasonication for 30 minutes at 25 kHz (Figure A32). The printed patterns on transparent polyethylene bags did not disappear entirely even after ultrasonication in water, which is a testament to the remarkable durability of the  $A_2AgX_3$  based inks.

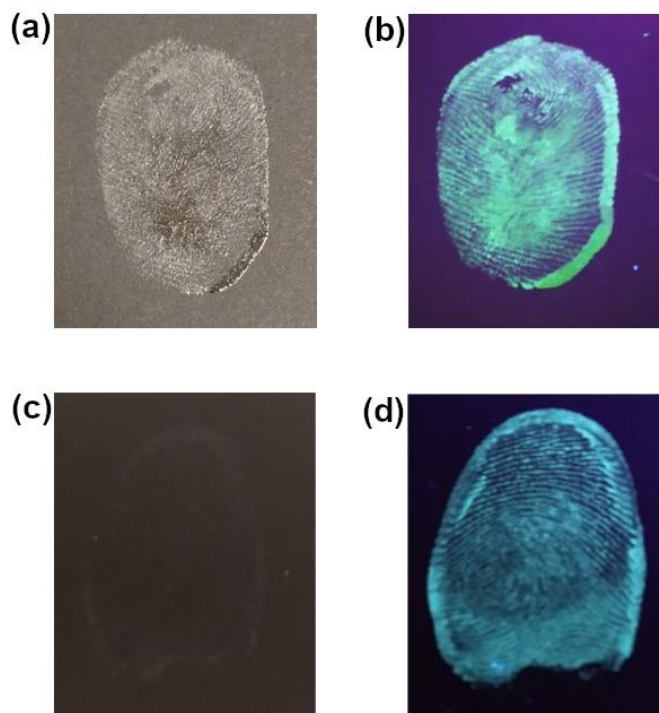


**Figure 38.** The  $A_2AgX_3$  based luminescent inks can be used for fingerprints (FPs): (a, b) a print of a right thumb using  $Rb_2AgI_3$  and (c, d) a print of a left thumb using  $Cs_2AgI_3$  under normal light (a, c) and UV light (365 nm, b, d).

Fingerprints (FPs) and latent fingerprints (LFPs) are commonly used for medical diagnosis, national security and policing, control of access, and forensic investigations.<sup>159</sup> However, metal halide-based light emitters are underexplored for LFPs. Consequently, in addition to the anti-counterfeiting application of  $A_2AgX_3$  based luminescent ink, we also explored their potential use in LFPs. The LFPs based  $Rb_2AgI_3$  (right thumb) and  $Cs_2AgI_3$  (left thumb) based luminescent inks were deposited on black paper. The deposited thumb impression is visible in normal light and shows bright fluorescence emission in UV light, which can be early observed and identified (Figure 38).

In summary, our results suggest that the  $A_2AgX_3$  based luminescent inks are viable candidates for advanced LFPs and anti-counterfeiting applications. The  $A_2AgX_3$  inks are versatile and can be printed on any surface with any color background, including polyethylene surfaces. The possibility of printing  $A_2AgX_3$ -based patterns on polyethylene surfaces with high water and

mechanical stability is particularly noted and can pave the way for applying these and related metal halides for commercial use.

### **3.1.7 Conclusion**

We report a facile method of preparation of  $A_2AgX_3$  ( $A = Rb, Cs$ ;  $X = Cl, Br$ ), which exhibit broadband PL emission spectra attributed to vacancy-bound excitons (DBEs) and in the case of  $Rb_2AgBr_3$  STEs as well.  $A_2AgX_3$  demonstrate markedly improved photo-, air- and thermal-stability compared to the high efficiency blue emitting Cu(I) analogs  $A_2CuX_3$ . Moreover, the measured optical properties show that PL emission properties of  $A_2AgX_3$  are sensitive to A and X site substitutions, which is in stark contrast to the notable lack of tunability of PL properties of  $A_2CuX_3$ . The computational investigations reveal that the PL in  $Rb_2AgX_3$  ( $X = Cl, Br, I$ ) are dominated by the emission by vacancy-bound excitons with a minor contribution from the STE in the case of  $Rb_2AgBr_3$  and the experimentally observed halogen dependence of the PL properties can be explained by the different type of defects involved in light emission. Tunability of PL properties of  $A_2AgX_3$  and their much-improved stability allows their consideration for practical applications, which is demonstrated in this work by the preparation of  $A_2AgX_3$  based luminescent inks for fingerprint detection and anti-counterfeiting applications. Our printed security patterns using the  $A_2AgX_3$  inks are stable in water, under heat, and ultrasonication, further confirming the stability of  $A_2AgX_3$ . In combination, lead-free and earth-abundant elemental compositions, simple processing, high-efficiency tunable light emission, and improved environmental stability of  $A_2AgX_3$  makes them attractive alternatives to toxic lead halide perovskites and unstable copper(I) halides for practical applications.

## **3.2 $(NH_4)_2AgBr_3$ and $(NH_4)_2AgI_3$ with Halide Atmosphere Tunable Emission**

### **3.2.1 Introduction**

Novel ternary metal halides have garnered significant attention in the past decade for prospective light emission applications such as solid-state lighting and radiation detection.<sup>54, 117, 141, 145, 157</sup> Among the most prominent examples are cesium and methylammonium lead halide perovskites, particularly in their nanoparticle forms, demonstrating tunable and highly-efficient light emission properties.<sup>133, 134, 138, 145, 146</sup> However, the toxic nature of lead poses a challenge from an environmental perspective, and lead halide perovskites are known to exhibit poor stability in ambient air conditions.<sup>134, 135, 137</sup> Furthermore, the preparation of high-quality nanoparticles of lead halide perovskites involves lengthy and complicated synthesis methods.<sup>133, 134, 138, 146, 160</sup> These challenges hinder the prospects of lead halide perovskites for commercialization and use in practical applications.

High-efficiency light emitters based on lead-free alternative metal halides have been developed in the past few years in the form of ternary copper(I) halides. Notable examples include compounds such as  $\text{Cs}_3\text{Cu}_2\text{X}_5$  ( $\text{X} = \text{Cl}, \text{Br}, \text{or I}$ ) and  $\text{A}_2\text{CuX}_3$  ( $\text{A}=\text{K or Rb}, \text{X} = \text{Cl or Br}$ ), which were found to have record-breaking blue light emission efficiencies with room temperature photoluminescence quantum yield (PLQY) values up to 100%.<sup>23, 43, 53, 117, 136, 144, 148</sup> Of these,  $\text{A}_2\text{CuX}_3$  compounds have been attracting attention due to recent improvements in their stability and demonstration of their potential in radiation detection applications.<sup>43, 53</sup> Light emission in these low-dimensional copper(I) halides, including the  $\text{A}_2\text{CuX}_3$  family, has been attributed to self-trapped excitons (STEs), which are formed through structural reorganizations that occur in the excited state, leading to charge localization on distorted metal halide polyhedra.<sup>96, 147</sup> These trapped excitons form mid-gap states that have significantly red-shift the emission peaks relative to the absorption energies. Such exciton trapping is ubiquitously observed in lower-dimensional metal halides as the energy barrier is lower for structural distortion, emphasizing the roles of

chemistry and structural dimensionality in the photoemission properties of metal halides. Despite their outstanding optical emission properties, the members of the  $A_2CuX_3$  family are all blue emitters, and substitutions on the A and X sites in  $A_2CuX_3$  have shown only negligible impacts on the optical properties.<sup>43, 53, 136, 147, 148</sup> Such unusual lack of tunability of the photoluminescence (PL) properties in the  $A_2CuX_3$  family is due to the fact that electronic transitions take place primarily between copper(I) orbitals.<sup>43, 136</sup> To bring PL tunability to this family, a strategy based on the substitution of Cu(I) with alternative metals (e.g., with Ag) can be proposed. The validity of this approach was recently demonstrated for the  $A_2AgX_3$  ( $A = Rb, Cs$ ;  $X = Cl, Br$ ), which exhibit tunable broadband emission spectra attributed to STEs and defect-bound excitons (DBEs).<sup>153, 154</sup> There has also been an increasing interest in hybrid variants of ternary silver halides, such as the white light emitting  $(H_2DABCO)[Ag_2X_4(DABCO)]$  and  $(HDABCO)_3Ag_5Cl_8$ .<sup>161</sup> These all-inorganic and hybrid compounds have set the stage for ternary silver halides as potential white light emitters, with PLQY's of up to 27%.<sup>153</sup>

Here, we report the preparation and characterization of  $(NH_4)_2AgX_3$  ( $X = Br$  and  $I$ ). Although not isostructural,  $(NH_4)_2AgX_3$  exhibit very similar structures to that of  $A_2CuX_3$ , based on 1D  $[AgX_3]^{2-}$  chains made of tetrahedral  $AgX_4$  units separated by  $NH_4^+$  cations.<sup>28</sup> Substitution of alkali metal cations with  $NH_4^+$  is both cost-effective and also removes the issues associated with the intrinsic radioactivity of alkali metals such as Rb used in  $Rb_2CuX_3$ , expanding the potential of  $(NH_4)_2AgX_3$  for radiation detection applications. Large cm-sized colorless needles were synthesized through a hydrothermal preparation method. Both single crystal and powder X-ray diffraction methods were used to characterize structure and bulk purity. In stark contrast to Cu(I) analogs,  $(NH_4)_2AgX_3$  exhibit white light emission properties. Detailed investigations, including density functional theory (DFT) calculations and optical spectroscopy measurements, were

performed to elucidate this white light emission mechanism. Based on our combined experimental and computational work, low dimensional silver halides constitute an exciting new family of nontoxic and rare-earth free luminescent metal halides with tunable optical properties.

### **3.2.2 Synthesis and Characterization Methods**

#### **3.2.2.1 Materials and Methods**

The starting reactants: ammonium bromide (>99.99%, Aldrich), silver bromide (99.5%, Alfa Aesar), ammonium iodide (>99%, Sigma-Aldrich), and silver iodide (99.999%, Alfa Aesar) were used as received. All solvents were obtained via Sigma – Aldrich and used as received, including hypophosphorous acid (50%), hydrobromic acid (48%), and hydroiodic acid (47%). All manipulations of reactants and products were performed in a nitrogen-filled glovebox.

#### **3.2.2.2 (NH<sub>4</sub>)<sub>2</sub>AgX<sub>3</sub> Single Crystals via Slow Cooling of a Saturated Solution**

(NH<sub>4</sub>)<sub>2</sub>AgX<sub>3</sub> single crystal measuring up to 1.5 cm in length were prepared by mixing stoichiometric amounts of NH<sub>4</sub>X (X = Br, I) and AgX in a 6M HX solution. A combined 1.5 grams of reagents were added to a 20 mL glass scintillation vial wrapped in an aluminum foil, then 10.0 mL of the corresponding acid was added. H<sub>3</sub>PO<sub>2</sub> (~5% by volume) was added to the resultant solution. The vial was then capped and placed in the center of a box furnace and heated at 130 °C until all reactants fully dissolved, producing a clear solution. The box furnace was held at 130 °C for 6 hours, followed by slow cooling to 25 °C over 105 hours. The obtained products are composed of long colorless needle crystals of (NH<sub>4</sub>)<sub>2</sub>AgX<sub>3</sub> with small binary AgX impurity crystals on the surface as confirmed by the powder X-ray diffraction (PXRD) measurements. Larger needle crystals with minimal surface impurities were carefully collected and washed in isopropyl alcohol (see Figure 40).

#### **3.2.2.3 Powder X-ray Diffraction (PXRD) Measurements**



To establish the samples' bulk purity, PXRD measurements were taken on a Rigaku Miniflex600 equipped with a D/tex detector and a Ni-filtered Cu-K $\alpha$  radiation source. Data were collected at room temperature in the 3–90° (2 $\theta$ ) range, with a step size of 0.02°. The obtained PXRD patterns were refined using the decomposition method. To test the air-stability of (NH<sub>4</sub>)<sub>2</sub>AgX<sub>3</sub>, powdered samples were left on a laboratory bench under ambient conditions (thermostat set at 20 °C and relative humidity of 30%), and periodic PXRD experiments were performed to monitor the changes. The reference intensity ratio (RIR) quantitative analysis was performed using the PDXL2 program to quantify the sample composition changes.

#### **3.2.2.4 Single Crystal X-ray Diffraction (SCXRD)**

Single crystal X-ray diffraction (SXRD) data were collected on a Bruker D8 Quest with a Kappa geometry goniometer, an Incoatec I $\mu$ S X-ray source (graphite monochromated Mo-K $\alpha$  ( $\lambda$  = 0.71073 Å) radiation), and a Photon II detector. The data were corrected for absorption using the semiempirical method based on equivalent reflections, and the structures were solved by intrinsic phasing methods (SHELXT) as embedded in the APEX3 v2015.5-2 program. Site occupancy factors were checked by freeing occupancies of each unique crystallographic positions. Details of the data collection and crystallographic parameters are given in Table A5. Atomic coordinates, equivalent isotropic displacement parameters, and selected interatomic distances and bond angles are provided in Table A6 and Table A7 in the appendix. Additional information on the crystals structures investigations can be obtained in the form of a Crystallographic Information File (CIF), which was deposited in the Cambridge Crystallographic Data Centre (CCDC) database (deposition numbers 2031391 and 2031392).

**3.2.2.5 Microscopy.** A Thermo Quattro S field-emission environmental Scanning Electron Microscope (FE-ESEM) was utilized to obtain the SEM images. Optical images of crystals were

captured on Leica S6D microscope with Leica EC4 digital camera attachment.

### 3.2.2.6 Thermogravimetry and Differential Scanning Calorimetry (TGA/DSC)

#### Measurements

Simultaneous thermogravimetric analysis and differential scanning calorimetry (TGA/DSC) measurements were performed on a TA Instruments SDT 650 thermal analyzer system. Polycrystalline powder samples of  $(\text{NH}_4)_2\text{AgX}_3$  (~15 mg) were placed in 90  $\mu\text{L}$  alumina crucibles with the corresponding caps and heated from 25 to 450  $^\circ\text{C}$  with a heating rate of 5  $^\circ\text{C}/\text{min}$  under an inert flow of dry nitrogen gas at a rate of 100 mL/min.

### 3.2.2.7 Optical Measurements

Room temperature photoluminescence emission (PL) and photoluminescence excitation (PLE) measurements were performed on single crystals of  $(\text{NH}_4)_2\text{AgX}_3$  on a Jobin Yvon Fluorolog-3 spectrofluorometer (HORIBA company) equipped with a Xenon lamp with a range from 280 to 750 nm. Commission Internationale de l'Eclairage (CIE) color coordinates were generated from PL spectra in Origin 2019. For lifetime measurements, a Time-Correlated Single Photon Counting (TCSPC) system including a DeltaHub DH-HT high throughput TCSPC controller and NanoLED NL-C2 pulsed diode controller was used. A 299 nm NanoLED diode was selected for the light source, which has a <1.2 ns pulse duration. In order to fit the data, the following equations were used:

$$I(t) = \sum_i^n \alpha_i \exp\left(\frac{-t}{\tau_i}\right)$$
$$\alpha_1 = \frac{B_1}{(B_1 + B_2)} \quad \alpha_2 = \frac{B_2}{(B_1 + B_2)}$$

The fitting parameters calculated in this study are available in Table A8.

**3.2.2.8 Computational Methods.** Our calculations were based on density functional

theory (DFT) as implemented in the VASP code.<sup>78</sup> The kinetic energy cutoff of the plane-wave basis is 400 eV. The projector augmented wave method was used to describe the interaction between ions and electrons.<sup>79</sup> The lattice parameters were fixed at the experimentally measured values while the atomic positions were optimized until the force on each atom is less than 0.02 eV/Å. The electronic band structure and density of states (DOS) were calculated using Perdew-Burke-Ernzerhof (PBE) exchange-correlation functional<sup>80</sup> and the band gap was further corrected using the hybrid PBE0 functional.<sup>81</sup>

### 3.2.3 Crystal Structure and Stability

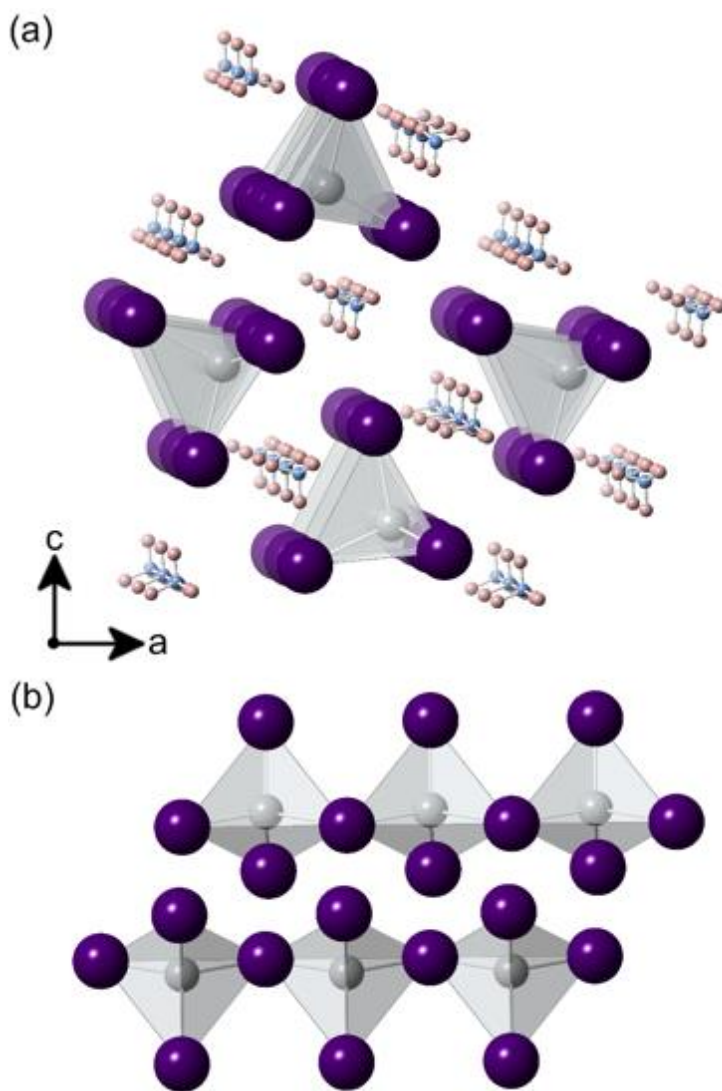


**Figure 39.** (a) A polyhedral model of the 1D structure of  $(\text{NH}_4)_2\text{AgX}_3$  projected down the  $b$ -axis. (b) Isolated tetrahedral chains of  ${}_{\infty}^1[\text{AgX}_3]^{2-}$  demonstrating the 1D connectivity of corner-sharing  $\text{AgX}_4$  tetrahedra. Silver, halide, nitrogen, and hydrogen are colored in grey, purple, blue, and pink, respectively.

$(\text{NH}_4)_2\text{AgBr}_3$  and  $(\text{NH}_4)_2\text{AgI}_3$  are isostructural compounds crystallizing with the  $\text{K}_2\text{AgI}_3$  type structure in the  $Pnma$  space group (Tables A5-7).<sup>28</sup> Their structure consists of  $1\text{D } {}_{\infty}^1[\text{AgX}_3]^{2-}$  tetrahedral chains extending along the  $b$ -axis, which are separated by  $[\text{NH}_4]^+$  ions (Figure 39).  $(\text{NH}_4)_2\text{AgBr}_3$  has Ag-Br bond lengths ranging from 2.6934(3) – 2.7139(6) Å and Br – Ag – Br angles ranging from 101.239(19) – 109.664(14)°. These are fairly similar to  $\text{Rb}_2\text{AgBr}_3$ , where Ag-Br bond lengths range from 2.6925 – 2.7224 Å and Br – Ag – Br angles range from 103.65 – 117.14°. Compared to  $(\text{NH}_4)_2\text{AgBr}_3$ ,  $(\text{NH}_4)_2\text{AgI}_3$  features slightly less distorted tetrahedra, with Ag-I bond lengths ranging from 2.8345(7) – 2.8647(4) Å and I – Ag – I angles from 104.982(19) – 109.505(12)°. The bond lengths are within the expected range compared to  $\text{K}_2\text{AgI}_3$ , where Ag-I bond lengths range from 2.8093 – 2.8525 Å and I – Ag – I angles are from 103.90 – 113.83°.<sup>162</sup> Note that the  $\text{K}_2\text{AgI}_3$  type structure is similar to the  $\text{K}_2\text{CuCl}_3$  type structure adopted by the  $\text{A}_2\text{CuX}_3$  family, which have recently been reported as ultrabright blue emitters with prospective applications in solid-state lighting and radiation detection applications.<sup>43, 117, 136, 148</sup> The differences between the two structure types are in the packing of the chains relative to the A cationic site.<sup>28</sup>

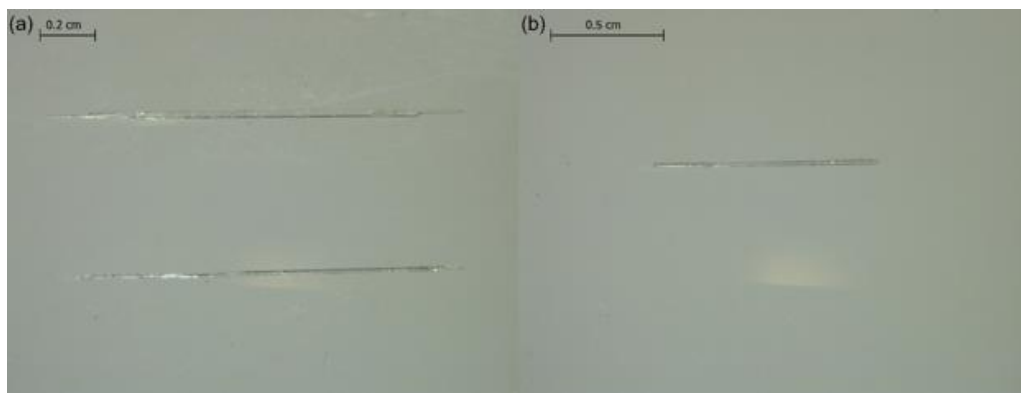


**Figure 40.** Photographs of (a)  $(\text{NH}_4)_2\text{AgBr}_3$  and (b)  $(\text{NH}_4)_2\text{AgI}_3$  single crystals grown via hydrothermal synthesis method.

Large single crystals of  $(\text{NH}_4)_2\text{AgBr}_3$  and  $(\text{NH}_4)_2\text{AgI}_3$  measuring up to 1.5 cm long are effortlessly obtained through a hydrothermal process (Figure 40). To confirm bulk purity, a portion of these crystals were ground thoroughly for room temperature PXRD measurements (Figure A33). Based on our PXRD results, high purity samples with no noticeable impurities are obtained through hydrothermal synthesis. Since  $\text{Ag}^+$  naturally photodegrades to Ag, the stability of this compound was monitored.<sup>163</sup> To evaluate their stability, the materials were stored under ambient air conditions for approximately 10 hours/day between the PXRD scans. The environmental conditions were set at 20 °C and a relative humidity of 30%. Over three weeks, no significant signs of degradation were observed (Figure A34); however, a relatively small drop in peak intensities was recorded. The fact that the sample purity is preserved when kept in air for two weeks is a significant improvement over the stability demonstrated by the related copper(I) halides such as  $\text{Rb}_2\text{CuCl}_3$ .<sup>136</sup> Previous studies of copper halides have shown that over time, copper often oxidizes into the divalent state.<sup>43, 136</sup> Here, we observe potential practical benefits of replacing Cu(I) with Ag(I) in high-efficiency light-emitting group 11 elements – unlike Cu(I), Ag(I) is less likely to oxidize in air, which results in the enhanced air stability of Ag(I) halides.

To evaluate the thermal stability of  $(\text{NH}_4)_2\text{AgBr}_3$  and  $(\text{NH}_4)_2\text{AgI}_3$ , simultaneous thermogravimetric analysis (TGA) and differential scanning calorimetry (DSC) measurements were performed (Figure A35). The results are consistent with other compounds in the  $\text{A}_2\text{AgX}_3$  and  $\text{A}_2\text{CuX}_3$  families; a single distinct thermal event is seen for  $(\text{NH}_4)_2\text{AgI}_3$  at 272.44 °C. For  $(\text{NH}_4)_2\text{AgBr}_3$ , there is a similar event at 259.22 °C and a second event at 416.49 °C. The first thermal event is hypothesized to be a peritectic decomposition point, which is accompanied by the evaporation and loss of the ammonium salt. The weight loss of 42% and 55% at 272.44 °C and 259.22 °C approximately matches the 51% and 55% weight of the ammonium salt ( $\text{NH}_4\text{Br}$  and

NH<sub>4</sub>I, respectively) in (NH<sub>4</sub>)<sub>2</sub>AgBr<sub>3</sub> and (NH<sub>4</sub>)<sub>2</sub>AgI<sub>3</sub>, respectively. For (NH<sub>4</sub>)<sub>2</sub>AgBr<sub>3</sub>, the second event at 416.49 °C is hypothesized to be the melting transition of the residual ammonium bromide and silver bromide mixture. This conjecture is based on the approximation of the second point to the respective silver halide melting point.

### 3.2.4 Optical Properties

To evaluate the optical properties of (NH<sub>4</sub>)<sub>2</sub>AgX<sub>3</sub>, room-temperature photoluminescence excitation (PLE) and photoluminescence emission (PL) were measured for both compounds (Figure 41). Immediately noticeable is that the PL and PLE plots are different for (NH<sub>4</sub>)<sub>2</sub>AgBr<sub>3</sub> and (NH<sub>4</sub>)<sub>2</sub>AgI<sub>3</sub>. While significant changes in the PL properties of all-inorganic lead halides such as CsPbX<sub>3</sub> occur upon halogen substitution, the A<sub>2</sub>CuX<sub>3</sub> family are known as efficient and narrow blue emitters with a lack of tunability of their PL properties.<sup>43, 53, 117, 134, 136, 145, 148</sup> This unusually weak dependence of light emission properties of A<sub>2</sub>CuX<sub>3</sub> on the halogen site substitutions has been explained by the fact that conduction band minimum (CBM) and valence band maximum (VBM) are dominated by Cu(I) orbitals in their electronic band structures<sup>43, 136, 147</sup>. The substitution of Cu(I) with Ag(I) is, therefore, expected to directly impact the bands around the optical gap, changing orbital contributions to the VBM and CBM, and consequently resulting in significant changes to the observed PL properties of (NH<sub>4</sub>)<sub>2</sub>AgX<sub>3</sub> in comparison to their Cu(I) analogs.

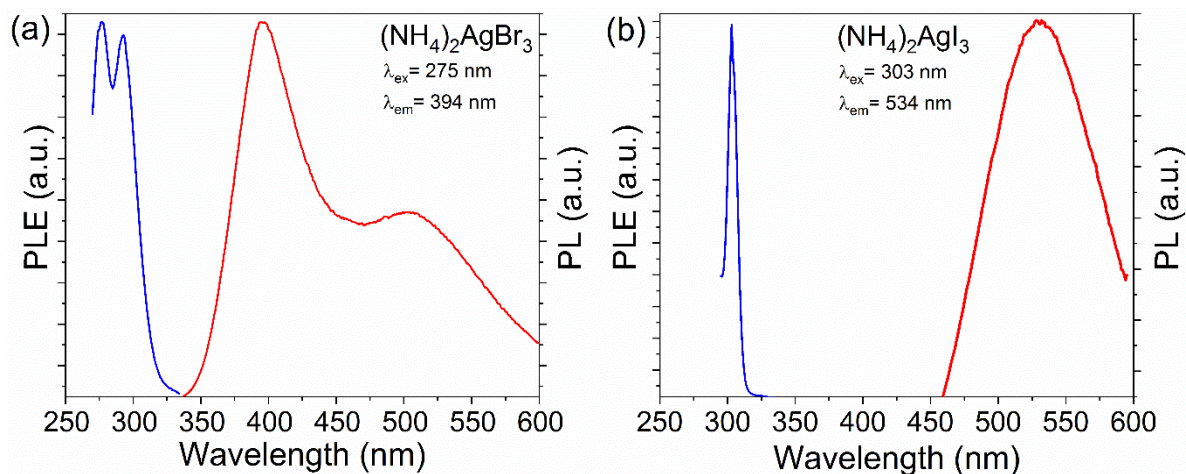


**Figure 41.** Room temperature photoluminescence excitation (PLE, blue lines) and photoluminescence emission (PL, red lines) spectra of single crystals of (a)  $(\text{NH}_4)_2\text{AgBr}_3$  and (b)  $(\text{NH}_4)_2\text{AgI}_3$ .

In the present case,  $(\text{NH}_4)_2\text{AgBr}_3$  has a broad white emission, with a maximum at 394 nm and a shoulder peak at 524 nm, and the corresponding PLE plot shows two maxima at 275 and 290 nm. The two excitation transitions are also clearly seen in the diffuse reflectance plots measured on polycrystalline powder samples (Figure A36 (a)). A small transition in the diffuse reflectance at  $\sim 2.5$  eV is attributed to a minor impurity of AgBr on the surface. In comparison,  $(\text{NH}_4)_2\text{AgI}_3$  has a relatively red-shifted PL peak with a maximum at 534 nm with a corresponding PLE peak at 303 nm. A small transition in the diffuse reflectance also occurs in  $(\text{NH}_4)_2\text{AgI}_3$  at  $\sim 2.8$  eV, this is attributed to a minor impurity of AgI on the surface. The double peak emission of  $(\text{NH}_4)_2\text{AgBr}_3$  is indicative of a multi-exciton emission, specifically the presence of a higher energy self-trapped exciton (STE) and a lower energy defect-bound (DBE) emission, analogous to the PL properties reported for  $\text{Rb}_2\text{AgBr}_3$ .<sup>153</sup> Furthermore, unlike the PL plot for  $(\text{NH}_4)_2\text{AgBr}_3$ , there is no high energy peak for  $(\text{NH}_4)_2\text{AgI}_3$ , indicating a single emission mechanism attributed solely to DBEs located on iodine vacancies within the tetrahedral chain. The halogen-dependence of emission properties of silver halides is explained by the fact that the halogen vacancies ( $V_{\text{Br}}$ ) have been shown to trap excitons leading to DBE emission in  $\text{Rb}_2\text{AgBr}_3$ . Similarly, starkly different

photoemission properties have been reported for  $\text{Cs}_2\text{AgCl}_3$  and  $\text{Cs}_2\text{AgBr}_3$ .<sup>154</sup>

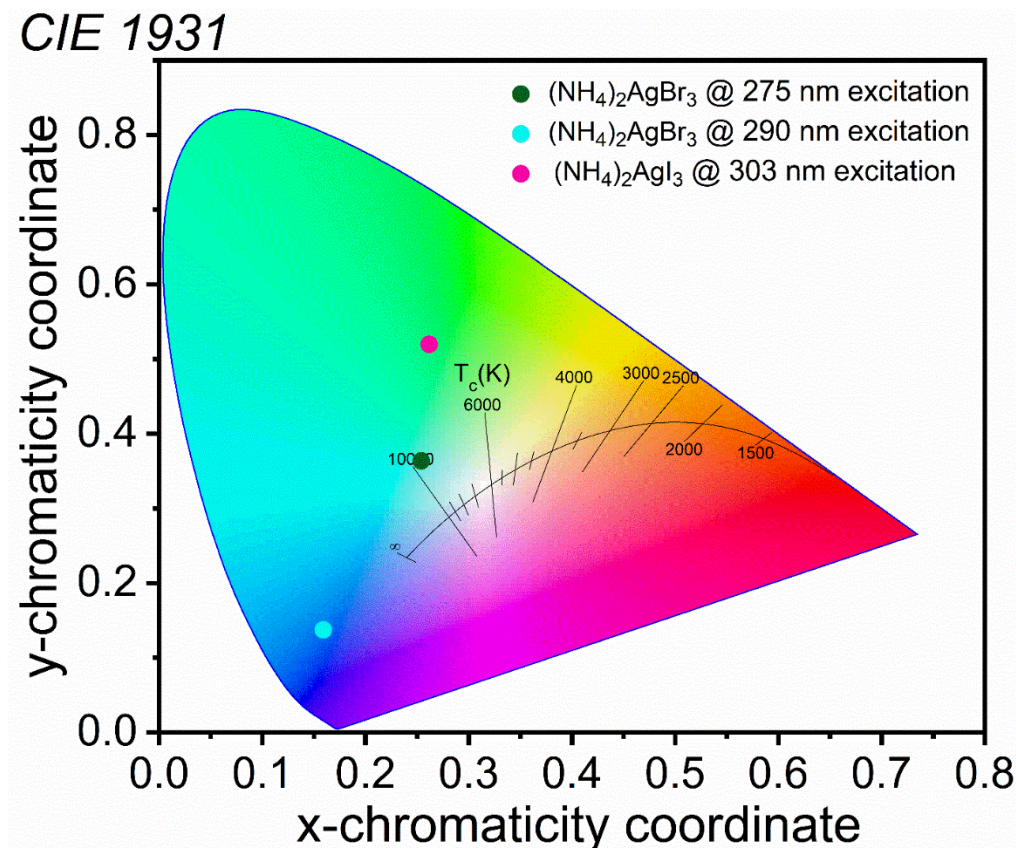


**Figure 42.** The Commission Internationale de l’Eclairage (CIE) color coordinates of  $(\text{NH}_4)_2\text{AgBr}_3$  and  $(\text{NH}_4)_2\text{AgI}_3$ .  $(\text{NH}_4)_2\text{AgBr}_3$  is found to exhibit excitation-dependent light emission properties. A Planckian locus has been included to estimate correlated color temperature (CCT) for the various PL emissions of  $(\text{NH}_4)_2\text{AgX}_3$ .

For both  $(\text{NH}_4)_2\text{AgX}_3$  compounds, the PLE plots are comparable to that of  $\text{K}_2\text{CuCl}_3$  and  $\text{K}_2\text{CuBr}_3$ , which show maxima at 291 and 296 nm, respectively. The notable broadness of the PL peaks for the  $(\text{NH}_4)_2\text{AgX}_3$  compounds results in a visible white or near-white light emission. Namely,  $(\text{NH}_4)_2\text{AgBr}_3$  has a significantly broader emission with a full width at half maximum (FWHM) value of 142 nm compared to the FWHM of 54 nm reported for  $\text{A}_2\text{CuX}_3$ .<sup>43, 136</sup>  $(\text{NH}_4)_2\text{AgI}_3$  has a slightly smaller FWHM of 114 nm due to the lack of a lower energy shoulder; however, this FWHM value is still more than twice that of the blue-emitting copper(I) halides (Table 6). The broadness of these peaks further supports the attribution of DBEs as the emission



mechanism as opposed to narrow STE peaks seen in the analogous Cu(I) compounds.<sup>43, 52, 53, 117, 136, 164</sup> The narrower emission peak for (NH<sub>4</sub>)<sub>2</sub>AgI<sub>3</sub> yields a greenish-white emission color with the Commission Internationale de l'Eclairage (CIE) color coordinates of (0.23, 0.53) compared to the white emission with the CIE coordinates of (0.25, 0.36) by (NH<sub>4</sub>)<sub>2</sub>AgBr<sub>3</sub>. The correlated color temperature for (NH<sub>4</sub>)<sub>2</sub>AgBr<sub>3</sub> is 9273 K, calculated based on CIE coordinates. CIE 1931 plots generated from PL emission spectra can be found in Figure 42. Finally, the Stokes shifts of (NH<sub>4</sub>)<sub>2</sub>AgBr<sub>3</sub> and (b) (NH<sub>4</sub>)<sub>2</sub>AgI<sub>3</sub> are 119 nm and 231 nm, respectively, which are comparable to the Stokes shifts demonstrated by other analogous low-dimensional metal halides with excitonic light emission properties (Table 6).

**Table 6.** A comparison of the photophysical properties of ternary A<sub>2</sub>MX<sub>3</sub> (A = K, Rb, Cs; M = Cu, Ag; X = Cl, Br, I)<sup>43, 117, 136, 154</sup>

Compound	PL <sub>max</sub> (nm)	PLE <sub>max</sub> (nm)	Stokes shift (nm)	Lifetime (μs)	FWHM (nm)	Ref
(NH <sub>4</sub> ) <sub>2</sub> AgBr <sub>3</sub>	394	275	119	0.995	142	This work
(NH <sub>4</sub> ) <sub>2</sub> AgI <sub>3</sub>	534	303	231	1.25	114	This work
Cs <sub>2</sub> AgCl <sub>3</sub>	397	250	147	0.068	-	153
Cs <sub>2</sub> AgBr <sub>3</sub>	524	292	232	0.114	-	153
Cs <sub>2</sub> AgI <sub>3</sub>	595	310	285	0.135	-	153
K <sub>2</sub> CuCl <sub>3</sub>	392	291	101	12.97	54	41
K <sub>2</sub> CuBr <sub>3</sub>	388	296	92	-	54	41
Rb <sub>2</sub> CuCl <sub>3</sub>	400	300	100	12.21	52	135
Rb <sub>2</sub> CuBr <sub>3</sub>	385	300	85	-	~54	116

In addition to stark differences to the PL properties of Cu(I) halides, we also note distinct variation of light emission properties in Ag(I) halides depending on the A site cation, e.g.,

$(\text{NH}_4)_2\text{AgBr}_3$ ,  $\text{Rb}_2\text{AgBr}_3$  and  $\text{Cs}_2\text{AgBr}_3$  have PL emission peaks at 394, 484 and 518 nm, respectively. Similarly, the PL spectra of  $(\text{NH}_4)_2\text{AgI}_3$ ,  $\text{Rb}_2\text{AgI}_3$  and  $\text{Cs}_2\text{AgI}_3$  feature peaks at 534, 483 and 579 nm, respectively. Such sensitivity of light emission properties of low-dimensional ternary metal halides on the A cation site is unusual as A site cations typically have no direct contribution to the states in the vicinity of the optical band gap. Here, both for bromides and iodides, PLE peak positions are largely identical, but both PL peak positions and shapes as evidenced by the varying FWHM values are strongly dependent on the nature of the A cation. We attribute the observed impact of the A cations such as  $\text{NH}_4^+$  to their hydrogen bonding capabilities, which can impact the local coordination around the B metal cation, leading to starkly different PL emission properties. The change in emission mechanism from STEs in Copper (I) halides to STEs and DBEs in silver halides also account for the significantly increased broadness in FWHM. Similar observations are made by comparing the reported PL properties of hybrid organic-inorganic copper halides such as green-emitting  $(\text{MA})_4\text{Cu}_2\text{Br}_6$  and all-inorganic copper halides such as blue-emitting  $\text{Rb}_2\text{CuBr}_3$ .<sup>143</sup>

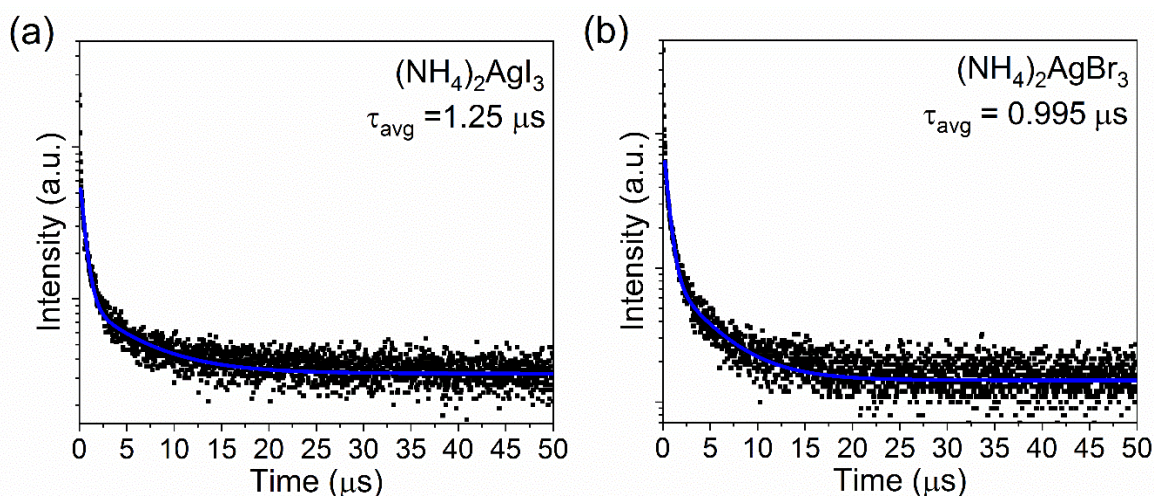


**Figure 43.** Time-resolved PL plots for (a)  $(\text{NH}_4)_2\text{AgBr}_3$  and (b)  $(\text{NH}_4)_2\text{AgI}_3$  measured using a 299 nm excitation source.

To further probe the photoluminescence emission mechanism of the  $(\text{NH}_4)_2\text{AgX}_3$

compounds, additional photoluminescence spectroscopy measurements were performed. First, surface defects as the source of emission were ruled out. Single crystals were ground with PL taken before and after grinding (Figure A37), which showed only a decrease in emission intensities, ruling out surface defects as the significant source of PL emission in these compounds. Instead, we observe nearly two-fold reduction in PL intensity for powder samples, suggesting the presence of surface trap states that may quench PL. A comparison of crystal size before and after grinding can be seen in Figure A38. Excitation wavelength-dependent emission was done to determine whether multiple emission mechanisms were at play. For  $(\text{NH}_4)_2\text{AgBr}_3$ , there is a loss of intensity in the lower energy excitation peak when the excitation energy is lowered (Figure A39), suggesting multi-excitonic nature of emission; the emission primarily varies in the lower energy peak, this is consistent with the assignment of this peak to DBEs. However, the PL emission profile does not change with excitation energy for  $(\text{NH}_4)_2\text{AgI}_3$ , suggesting an only DBE-based photoemission mechanism for this material (Figure A40). Next, time-resolved PL was done, in which a two-exponential fitting was used to determine the average lifetimes of PL emission for  $(\text{NH}_4)_2\text{AgX}_3$ , which yields similar average lifetimes of 0.995  $\mu\text{s}$  and 1.25  $\mu\text{s}$  for  $(\text{NH}_4)_2\text{AgBr}_3$  and  $(\text{NH}_4)_2\text{AgI}_3$ , respectively, shown in Figure 43. While these values are approximately one-tenth of the lifetimes reported for the STE dominated  $\text{A}_2\text{CuX}_3$  single crystals, they are significantly longer than fast emission lifetimes expected for a singlet emission from free exciton recombination. Therefore, the measured TRPL results further support the attribution of emission to DBEs in  $(\text{NH}_4)_2\text{AgX}_3$ .

### **3.2.5 Electronic Band Structure**

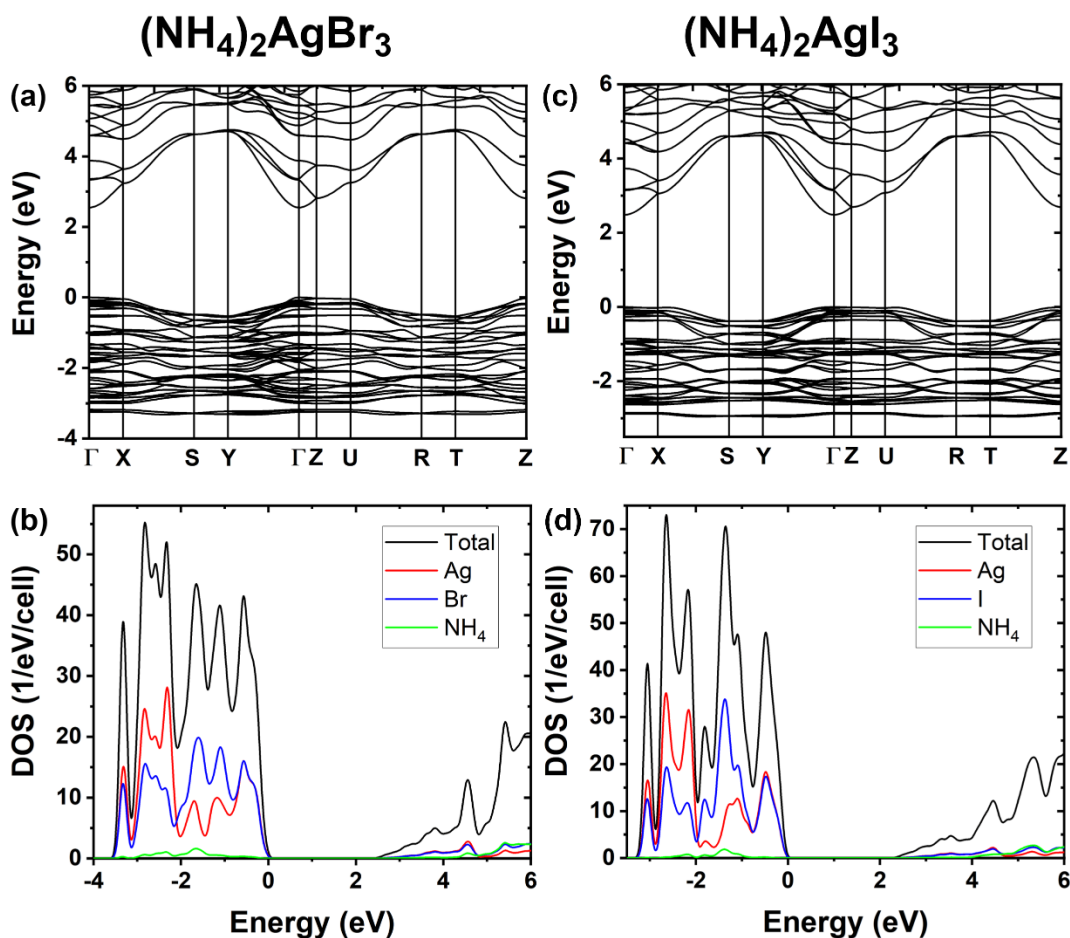


**Figure 44.** Electronic band structures and DOS of (a-b)  $(\text{NH}_4)_2\text{AgBr}_3$  and (c-d)  $(\text{NH}_4)_2\text{AgI}_3$ .

Electronic band structures and DOS of  $(\text{NH}_4)_2\text{AgX}_3$  ( $X = \text{Br}, \text{I}$ ) obtained by PBE calculations are shown in Figure 44. Both compounds exhibit a direct band gap at the  $\Gamma$  point. The calculated PBE band gaps are 2.55 eV and 2.49 eV for  $(\text{NH}_4)_2\text{AgBr}_3$  and  $(\text{NH}_4)_2\text{AgI}_3$ , respectively; they are corrected by the hybrid PBE0 calculation to 4.58 eV and 4.50 eV. The projected DOS in Figure 44 shows that the conduction band of  $(\text{NH}_4)_2\text{AgX}_3$  is made up of Ag-5s orbitals, which hybridize with halogen- $p$  orbitals, while the valence band is a mixing of Ag-4d and halogen- $p$  states. The hybridization between Ag-4d and halogen- $p$  in  $(\text{NH}_4)_2\text{AgX}_3$  is significantly stronger than that between Cu-3d and halogen- $p$  in  $\text{Rb}_2\text{CuX}_3$  and  $\text{K}_2\text{CuX}_3$ .<sup>43, 136</sup> This stronger contribution opens the door for further halide tunability of emission spectra for similar ternary silver halides.

The band gaps follow the normal decreasing trend from  $(\text{NH}_4)_2\text{AgBr}_3$  to  $(\text{NH}_4)_2\text{AgI}_3$ , consistent with the red shift of excitation energies observed in the experiment. Further and in-depth exciton calculations are needed in the future to better model the defects and emission mechanism in this family.

### 3.2.6 Conclusions

We report the hydrothermal synthesis and broadband white light emission properties of  $(\text{NH}_4)_2\text{AgX}_3$  ( $X = \text{Br}, \text{I}$ ), which are substitution analogs of the ultrabright blue-emitting  $\text{A}_2\text{CuX}_3$  family. Unlike the  $\text{A}_2\text{CuX}_3$  family,  $(\text{NH}_4)_2\text{AgX}_3$  are shown to exhibit light emission properties that are sensitive to A and X site substitutions. The tunability of photoemission in  $(\text{NH}_4)_2\text{AgX}_3$  through halogen substitution is explained by the greater contribution of the halogen- $p$  states to the valence and conduction bands. In addition,  $(\text{NH}_4)_2\text{AgBr}_3$  exhibits a dual emission mechanism attributed to self-trapped excitons and bromine vacancy  $V_{\text{Br}}$  bound excitons. The presence of multiple emission peaks for  $(\text{NH}_4)_2\text{AgBr}_3$  results in broad PL emission spectra covering the entire visible spectrum yielding white emission with the CIE coordinates of (0.25, 0.36). Our combined experimental and theoretical work on  $(\text{NH}_4)_2\text{AgX}_3$  suggests that substitution of Cu(I) with Ag(I) in  $\text{A}_2\text{CuX}_3$  not only provides a route for PL tunability but also significantly improves materials' stability. In conclusion, ternary silver halides are attractive alternatives to toxic lead halide perovskites and unstable copper(I) halides.

## Chapter 4: Design Novel Emitters Using Organic Emitters

The popular way to design and develop hybrid organic-inorganic metal halides is to rely on tuning the metal-halide polyhedra. While this method is somewhat reliable, the scope of possible combinations has some limits. The emission often becomes unpredictable, as few studies thoroughly understand the emission mechanisms and how they relate to structural properties. This work explores one route around this by utilizing an organic compound as the emission source. While this has challenges mentioned in the text below, it allows one to have a predictable emission profile. Organic emitters are often associated with stability problems; these are overcome by the methods described in the main text. This work has been summarized as a publication in the journal *Inorganic Chemistry*.<sup>165</sup>

### 4.1 Hybrid Organic-Inorganic Indium Bromide with Organic Derived Bright Blue Emission

#### 4.1.1 Introduction

In recent years, low-dimensional metal halides have received increased attention due to their outstanding light emission properties attributed to strong charge localization and enhanced excitonic properties.<sup>1-9</sup> Among these, hybrid organic-inorganic and all-inorganic lead halides have been the focus of most attention with notable examples including zero-dimensional (0D)  $\text{Cs}_4\text{PbBr}_6$  with efficient green emission, and one-dimensional (TDMP) $\text{PbBr}_4$  with broadband white emission.<sup>10-13</sup> However, despite the remarkable advancement in the development of lead halide phosphors, the innate toxicity of lead and the issues regarding their long term air stability are obstacles to potential commercialization of these materials.<sup>14</sup> Unlike higher dimensional metal halides, there are virtually no structural restrictions for 0D metal halides (e.g., size factors as

outlined by the tolerance factor for perovskites). Therefore, in principle, a far greater diversity of chemical compositions and crystal structures can be explored in the 0D metal halides family. In the search for lead-free light emitters, brightly luminescent 0D metal halides have recently been expanded to include halides of Sn, Cu, Zn, Mn etc.<sup>15-21</sup> Among these, materials such as  $A_2CuX_3$  ( $A = K, Rb$ ;  $X = Cl, Br$ ) demonstrate high photoluminescence quantum yield (PLQY) values measuring up to unity, which allows their consideration for LED and radiation detection applications.<sup>17,21-24</sup> However, for potential practical applications, stability of metal halides under irradiation, ambient air, and other relevant conditions must be further improved.<sup>22</sup>

In the literature, halides containing trivalent metal cations have received less attention than halides based on divalent metal cations.<sup>25</sup> In particular, halides of  $Sb^{3+}$  and  $Bi^{3+}$  have been studied as isoelectronic alternatives to unstable  $Sn^{2+}$  and toxic  $Pb^{2+}$ , respectively.<sup>26-30</sup> In comparison, halides of group 13 elements (Al, Ga, In) have been underexplored with only a few known members reported in the literature so far including compounds  $Cs_2InBr_5 \cdot H_2O$ ,<sup>31</sup> and  $(C_4H_{14}N_2)_2In_2Br_{10}$ ,<sup>32</sup>  $(C_4H_7N_2)_4[InBr_6][InBr_4] \cdot 2H_2O$ ,<sup>33</sup>  $(C_4H_{10}N)_6[InBr_6][InBr_4]_3 \cdot H_2O$ ,<sup>34</sup> and the mixed-valent indium compounds  $CsInX_3$  ( $X = Br, Cl$ ).<sup>35</sup> Interestingly, indium can form structures based on both octahedral and tetrahedral coordination geometry. Photoluminescence (PL) studies on  $Cs_2InBr_5 \cdot H_2O$ , and  $(C_4H_{14}N_2)_2In_2Br_{10}$  show that the compounds emit in the red region (670 - 695 nm) with PLQY values ranging from 3 to 33%, attributed to self-trapped excitons (STEs) localized on the inorganic sublattice.<sup>31,32</sup>

Herein, we report preparation and efficient sky-blue emission properties of a novel hybrid organic-inorganic indium halide  $RInBr_4$ , where  $R =$  trimethyl-(4-stilbenyl) methylammonium cation,  $C_{14}H_{22}N^+$ . In this study, an alternative approach has been taken wherein a previously known efficient light emitter, stilbene, has been modified in a novel fashion by adding a tri-methylated

ammonium group to one of the two phenyl rings. Stilbene is known to exhibit high efficiency light emission properties, but has poor photostability.<sup>36,37</sup> This stilbene derivative was then used as the organic cation for the formation of the novel RInBr<sub>4</sub>, which is, to the best of our knowledge, one of the few known pseudo-ternary hybrid organic-inorganic indium(III) halide to date. The novel compound was structurally characterized using X-ray diffraction (XRD) methods. We find that RInBr<sub>4</sub> demonstrates high-efficiency blue emission with a PLQY value of 16.36%, which is a two-fold increase compared to the PLQY of 8.15% measured for the organic precursor salt RBr. We discuss the origin of the sky-blue emission from RInBr<sub>4</sub> based on our combined optical spectroscopy and Density Functional Theory (DFT) results.

## **4.1.2 Methods**

### **4.1.2.1 Synthesis of RBr**

A round bottom flask was charged with (*E*)-4-methylstilbene (3.9 g), N-bromosuccinimide (3.7 g), 2,2'-azobis(2-methylpropionitrile) (0.060 g), and 50 mL benzene. A condenser was attached, and the solution was heated to gently reflux solvent overnight. The solution was cooled, transferred to a separatory funnel, and washed with a solution of NaOH (3.0 g) in 50 mL distilled water. The benzene layer was dried over sodium sulfate, filtered, and the solvent was removed under reduced pressure. Most of the solid residue (5.1 g) was dissolved in 90 mL acetonitrile in a round bottom flask fitted with an inlet adaptor and magnetic stirrer. The flask and contents were cooled in an ice bath and, with stirring, trimethylamine gas, generated from ca. trimethylamine hydrochloride (4.0 g) and ca. NaOH (1.8 g) in a small amount of water, was allowed to condense into the flask. After 24 hours, the procedure was repeated, followed by another 24 h stirring. Diethyl ether (70 mL) was added with stirring and the solid white precipitate was collected using suction filtration, washed twice with diethyl ether, dried by pulling air through it, and stored in a



desiccator to give 4.80 g (72% overall yield) of the desired trimethylammonium bromide salt RBr, mp. 227 - 228 °C (lit. 226 °C).<sup>69</sup> Scheme 1 shows the synthesis of the organic salt RBr. <sup>1</sup>H-NMR (300 MHz, DCCl<sub>3</sub>): □ 7.65 (d, 2H, J = 8.3 Hz), 7.59 (d, 2H, 8.0 Hz), 7.55 – 7.51 (m, 2 H), 7.42 – 7.29 (m, 3H) 7.19 (d, 1 H, J = 16.5 Hz), 7.10 (d, 1 H, J = 16.3 Hz), 5.05 (s, 2H), 3.43 (s, 9H).

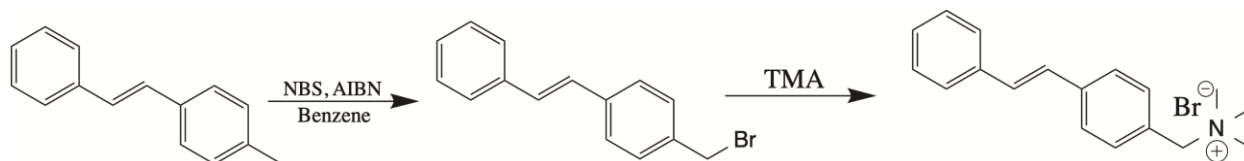


**Figure 45.** Synthesis of organic salt RBr.

#### 4.1.2.2 Synthesis of RInBr<sub>4</sub>

Reactants were dissolved in methanol in separate vials. Indium(III) bromide (>99%, Aldrich) dissolved completely in methanol forming a dark yellow solution. The organic precursor salt RBr had to be sonicated briefly (<5 minutes) for a complete dissolution in methanol. The resulting solution was light yellow. Both solutions were filtered and the indium(III) bromide solution was added dropwise to the organic solution. The reaction mixture was sonicated for 30 minutes and left to evaporate at room temperature. Light yellow block-shaped crystals were formed overnight (Figure A50).

#### 4.1.2.3 Single Crystal X-Ray Diffraction (SXRD) Measurements

Single crystal X-ray diffraction (SXRD) data were collected at 100(2) K on a Bruker D8 Quest with a Kappa geometry goniometer, an Incoatec Imus X-ray source (graphite monochromated Mo-K $\alpha$  ( $\lambda = 0.71073$  Å) radiation), and a Photon II detector. The data were corrected for absorption using the semiempirical method based on equivalent reflections, and the

structures were solved by intrinsic phasing methods (SHELXT) as embedded in the APEX3 v2015.5-2 program. All atoms were refined with anisotropic displacement parameters and site occupancy factors were checked by freeing occupancies of each unique crystallographic site. Details of the data collection, crystallographic parameters and atomic coordinates are summarized in Tables 7, A9, and A10. Additional information on the crystals structure investigations can be obtained in the form of a Crystallographic Information File (CIF), which was deposited in the Cambridge Crystallographic Data Centre (CCDC) database (deposition number 1991390).

#### **4.1.2.4 Powder X-ray Diffraction (PXRD) Measurements**

In order to establish bulk purity, PXRD measurements were performed on a Rigaku Miniflex600 benchtop diffractometer with a D/tex detector and a Ni-filtered Cu-K $\alpha$  radiation source. The scans were done with room temperature measurements in the 3-90° ( $2\theta$ ) range using a step size of 0.02°. The PXRD data were fitted using the Pawley method (Figure A51). Room-temperature PXRD measurements were also taken on a single crystal using the above-described conditions. In order to test for air and moisture stability of the compounds, periodic PXRD measurements were taken on samples stored in open air (thermostat set to 20 °C and 30% relative humidity).

#### **4.1.2.5 Thermal Property Measurements**

Simultaneous thermogravimetric analysis (TGA) and differential scanning calorimetry (DSC) measurements were performed on a polycrystalline powdered sample of RInBr<sub>4</sub> and RBr on a TA Instruments SDT 650 thermal analyzer system. Samples were heated up from 25 to 250 °C under an inert flow of dry nitrogen gas at a rate of 100 mL/min, with a heating rate of 5 °C/min.

Melting point measurements for RInBr<sub>4</sub> and RBr were run on a Mel – Temp apparatus, 110/120VAC, 50/60 Hz, 200W. The heating element was set to 50 volts, and the measurements

took 15 minutes and 20 minutes for RInBr<sub>4</sub> and RBr, respectively. The samples were loaded in the capillary tubes (0.8 – 1.1 × 90 mm).

#### **4.1.2.6 Optical Property Measurements**

Photoluminescence emission (PL) and excitation (PLE) measurements were performed at room temperature using a Jobin Yvon Fluorolog-3 spectrofluorometer (HORIBA company) equipped with a Xenon lamp and a Quanta-φ integrating sphere. PL and PLE experiments were conducted on a single crystal and polycrystalline powder sample of RInBr<sub>4</sub>, and a powdered sample of the precursor organic salt RBr. For lifetime measurements, a Time-Correlated Single Photon Counting (TCSPC) system including a DeltaHub DH-HT high throughput TCSPC controller and NanoLED NL-C2 pulsed diode controller was used. For light source, a 350 nm NanoLED diode was selected, which has a <1.2 ns pulse duration. Low temperature PL was collected under excitation by the 325 nm line of a HeCd laser (Kimmon Electric HeCd dual-wavelength laser, model: IK552R-F). The sample was placed on the cold finger of a helium closed-cycle cryostat, and the measurements were performed at 4 K.

For the photostability measurements, a single crystal of RInBr<sub>4</sub> and a powder sample of RBr were placed inside the Quanta-φ integrating sphere on the Jobin Yvon Fluorolog-3 spectrofluorometer. The samples were then exposed to the full power of the Xenon lamp of the spectrofluorometer at the PL excitation maximum of 391 nm and 398 nm for RInBr<sub>4</sub> and RBr, respectively. Periodic PLQY measurements were taken every 5 minutes under these conditions over 60 minutes.

Room temperature diffuse reflectance spectra of polycrystalline powder of RInBr<sub>4</sub> were measured using a high-resolution PerkinElmer LAMBDA 750 UV–vis–NIR spectrometer equipped with a 100 mm InGaAs integrating sphere attachment. The diffuse reflectance data were

converted to pseudo absorption spectra according to the Kubelka-Munk equation,  $FI = \alpha/S = (1-R)^2/(2R)$ , where R is the reflectance,  $\alpha$  is the absorption coefficient, S is the scattering coefficient.

#### **4.1.2.7 Computational Work**

Our calculations are based on DFT as implemented in the VASP code.<sup>70</sup> The kinetic energy cutoff of the plane-wave basis is 400 eV. The projector augmented wave method was used to describe the interaction between ions and electrons.<sup>71</sup> The lattice parameters were fixed at the experimentally measured values while the atomic positions were optimized until the force on each atom is less than 0.02 eV/Å. The electronic band structure and density of states (DOS) of RInBr<sub>4</sub> were calculated using Perdew-Burke-Ernzerhof (PBE) exchange-correlation functional.<sup>72</sup> The band gap was further corrected, and the DOS was recalculated by using the hybrid PBE0 functional, which has 25% non-local Fock exchange. The inclusion of a fraction of Fock exchange significantly improves the calculation of the band gap energy.<sup>66-68</sup>

### 4.1.3 Crystal Structure

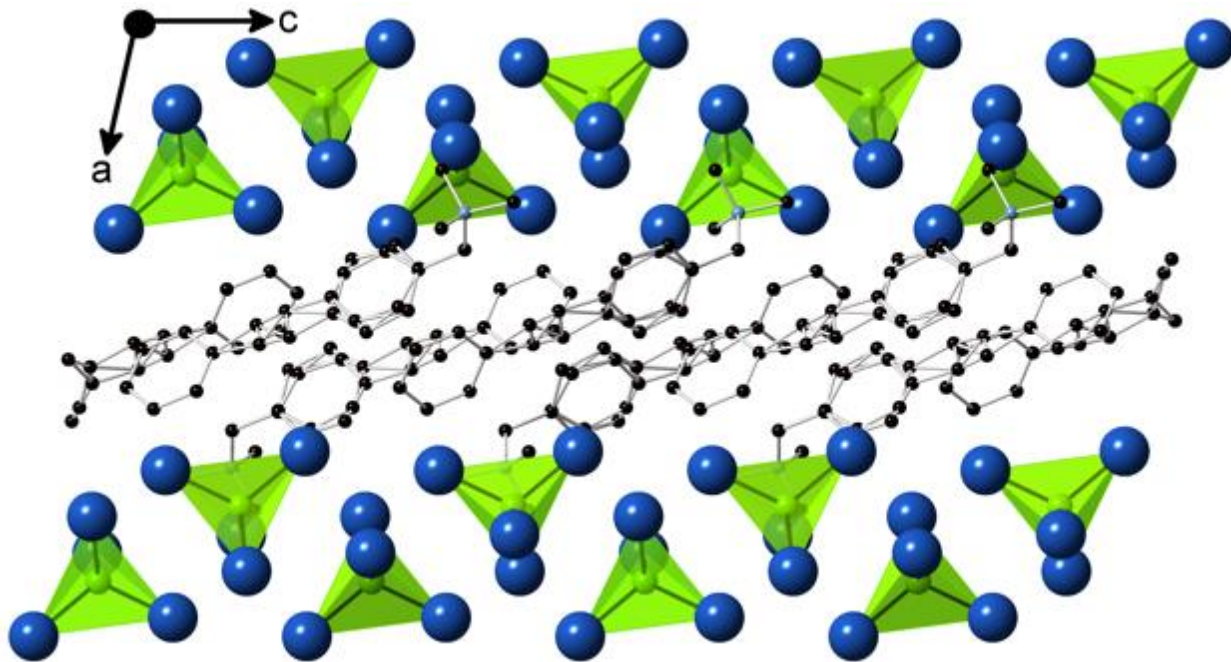


**Figure 46.** A polyhedral view of the 0D crystal structure of  $RInBr_4$ . C, N, M and Br atoms are shown in black, light blue, green and navy blue, respectively; H atoms are omitted for clarity.

$RInBr_4$  crystallizes in the monoclinic space group  $P2_1/c$ , and its structure is composed of molecular  $InBr_4^-$  anions separated by  $R^+$  cations. Although there is no chemical bonding connectivity between the tetrahedral  $InBr_4^-$  anions, i.e., the crystal structure of  $RInBr_4$  is 0D,  $InBr_4^-$  anions and  $R^+$  cations group into distinctly separate parts of the structure forming alternating inorganic anionic layers and organic cationic layers along the  $a$ -axis. Interestingly, similar pseudo-layered crystal structures have been reported for several other 0D halides of group 12 metals.<sup>18,38–40</sup> For  $RInBr_4$ , the formation of such pseudo-2D layered structure can be related to the optimized electrostatic interactions between the ammonium functional groups of  $R^+$  and  $InBr_4^-$ , and nonpolar interactions between the nonpolar tails of the organic cations, which is a common observation for low-dimensional metal halide perovskites.<sup>25</sup>

**Table 7.** Single crystal data and structure refinement parameters for  $RInBr_4$ .

Formula	RInBr <sub>4</sub>
Formula weight (g/mol)	686.82
Temperature (K)	100(2)
Wavelength (Å)	0.71073
Crystal system	Monoclinic
Space group	<i>P</i> 2 <sub>1</sub> / <i>c</i>
<i>Z</i>	4
Unit cell parameters (Å)	<i>a</i> = 12.1901(3) <i>b</i> = 11.6607(3) <i>c</i> = 16.0220(4)
Volume (Å <sup>3</sup> )	2229.16(10)
Density (g/cm <sup>3</sup> )	2.047
Absorption coefficient ( $\mu$ ) (mm <sup>-1</sup> )	8.231
$\theta_{\min}$ - $\theta_{\max}$ (°)	2.176 to 35.007
Reflections collected	106469
Independent reflections	9805
$R^a$ indices ( $I > 2\sigma(I)$ )	$R_1 = 0.0262$ $wR_2 = 0.0719$
Goodness-of-fit on $F^2$	1.000
Largest diff. peak and hole (e <sup>-</sup> /Å <sup>3</sup> )	1.444 and -1.358

$^aR_1 = \sum||F_o| - |F_c|| / \sum|F_o|$ ;  $wR_2 = |\sum|w(F_o^2 - F_c^2)^2| / \sum|w(F_o^2)||^{1/2}$ , where  $w = 1/|\sigma^2 F_o^2 + (AP)^2 + BP|$ , with  $P = (F_o^2 + 2F_c^2)/3$  and weight coefficients A and B.

Unlike trivalent bismuth and antimony halides, in which metals predominantly adopt octahedral coordination environment, In<sup>3+</sup> has a tetrahedral coordination in RInBr<sub>4</sub>. Indium is known in literature for its diversity of coordination environments in bromides. For instance, In<sup>3+</sup> takes a tetrahedral environment in InBr<sub>2</sub>, octahedral coordination in In<sub>7</sub>Br<sub>9</sub>, and both octahedral and tetrahedral geometries in In<sub>4</sub>Br<sub>7</sub>.<sup>35,41-43</sup> Only a few examples of ternary indium halides are known to date. Among them is the mixed-valent CsInBr<sub>3</sub>, in which In<sup>3+</sup> has an octahedral environment.<sup>35</sup> In Cs<sub>2</sub>InBr<sub>5</sub>·H<sub>2</sub>O, In<sup>3+</sup> also adopts an octahedral coordination environment.<sup>31</sup> However, In<sup>3+</sup> adopts both tetrahedral and octahedral coordination environments in (C<sub>4</sub>H<sub>14</sub>N<sub>2</sub>)<sub>2</sub>In<sub>2</sub>Br<sub>10</sub>,<sup>32</sup> (C<sub>4</sub>H<sub>7</sub>N<sub>2</sub>)<sub>4</sub>[InBr<sub>6</sub>][InBr<sub>4</sub>]·2H<sub>2</sub>O,<sup>33</sup> and (C<sub>4</sub>H<sub>10</sub>N)<sub>6</sub>[InBr<sub>6</sub>][InBr<sub>4</sub>]<sub>3</sub>·H<sub>2</sub>O.<sup>34</sup> Based

on Pauling's Radius-Ratio Rule ( $\mu = R_B/R_X$ , where  $R_B$  and  $R_X$  are ionic radii of the B metal and X anion), the acceptable octahedral factor  $\mu_{\text{oct}}$  range is 0.414 – 0.732 and the tetrahedral  $\mu_{\text{tet}}$  range is 0.225 – 0.414. For  $\text{In}^{3+}$  bromides,  $\mu_{\text{oct}}$  and  $\mu_{\text{tet}}$  are 0.408 and 0.316, respectively, which suggests a slight preference of tetrahedral coordination environment. However, the octahedral factor of  $\mu_{\text{oct}} = 0.408$  is close to the threshold value of 0.414, which can explain the empirical observation of both octahedral or tetrahedral coordination geometries in indium bromides.<sup>32,33,44</sup> It must also be noted that although the Pauling rules are frequently used for crystal structure rationalization, it has recently been shown that the Pauling rules, including the Radius-Ratio Rule, have only a limited predictive power when used for oxides.<sup>45</sup> Important for future work, the flexibility of the coordination environment of indium provides a route for obtaining chemical compositions and crystal structures that are not available through the use of commonly used B metal elements such as lead and tin in hybrid organic-inorganic metal halides.

The  $\text{InBr}_4^-$  tetrahedra in  $\text{RInBr}_4$  are slightly distorted with  $\text{In}^{\text{III}}\text{-Br}$  bond distances ranging from 2.35-2.5 Å (Table A10). Since trivalent indium has no lone pair of *s*-electrons (i.e.,  $\text{In}^{3+}$  has an electronic configuration of  $[\text{Kr}] 5s^0$ ), the observed distortions of  $\text{InBr}_4^-$  are attributed to the afore-mentioned optimized electrostatic interactions and packing of organic molecular cations and inorganic molecular anions. This conjecture is supported by the fact that in binary  $\text{In}(\text{III})$  bromides such as  $\text{In}_7\text{Br}_9$  and  $\text{InBr}_2$ , the  $\text{In}^{\text{III}}\text{Br}_4$  tetrahedra are regular with  $\text{In}^{\text{III}}\text{-Br}$  bond distances ranging from 2.4 – 2.5 Å, in agreement with the estimates based on the sum of Shannon ionic radii.<sup>46</sup> In comparison, indium(III) containing pseudo – ternary hybrid bromides such as  $(\text{C}_4\text{H}_7\text{N}_2)_4[\text{InBr}_6][\text{InBr}_4] \cdot 2\text{H}_2\text{O}$ ,  $(\text{C}_4\text{H}_{10}\text{N})_6[\text{InBr}_6][\text{InBr}_4]_3 \cdot \text{H}_2\text{O}$ , and  $(\text{C}_4\text{H}_{14}\text{N}_2)_2\text{In}_2\text{Br}_{10}$  feature more distorted coordination polyhedra, pointing to the important role of the constituent organic cations in the observed distortions of the inorganic building blocks.<sup>32–34</sup> The  $\text{In}^{\text{III}}\text{-Br}$  bond lengths in  $\text{InBr}_4$

tetrahedra in these compounds range from 2.47 to 2.62 Å, which are comparable to that observed for RInBr<sub>4</sub>. The slightly longer distances reported in literature can be attributed to the higher data collection temperatures of 150 K. The trends in tetrahedral bond angles also largely follow the same trends as that described for bond distances showing that InBr<sub>4</sub><sup>-</sup> tetrahedra undergo distortions when placed in a hybrid matrix.<sup>33,34</sup>

#### 4.1.4 Optical Properties

The optical band gap of RInBr<sub>4</sub> was estimated using diffuse reflectance measurements at room temperature. The band gap extrapolated from the linear region of the Kubelka-Munk plot is 3.1 eV (Figure A41). The onset of optical absorption is fairly sharp, suggesting a direct nature of the band gap in RInBr<sub>4</sub>. The estimated band gaps from direct and indirect fittings of the Tauc plots are 3.2 eV and 3.3 eV, respectively (Figure A41b – c).

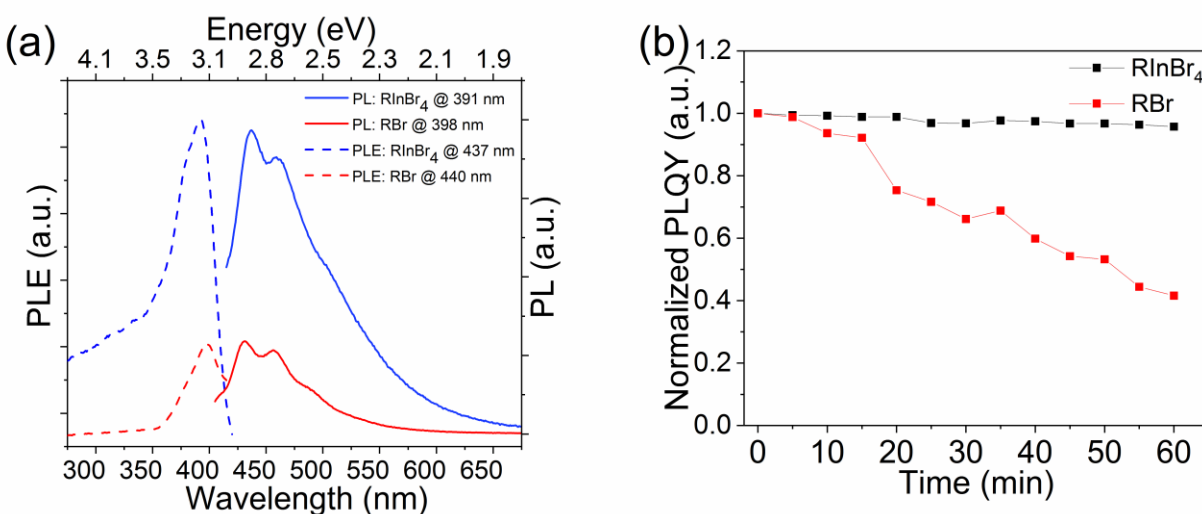


**Figure 47.** (a) Photoluminescence emission (PL) and excitation (PLE) spectra of RInBr<sub>4</sub> and RBr. (b) Normalized photoluminescence quantum yield (PLQY) values of RInBr<sub>4</sub> and RBr under a continuous irradiation at their respective PLE<sub>max</sub>.

Room temperature photoluminescence emission (PL) and excitation (PLE) spectra for RInBr<sub>4</sub> and the precursor organic salt RBr are presented in Figure 47a. Both excitation and emission spectra for RInBr<sub>4</sub> and RBr have similar wavelength ranges and peak shapes, suggesting



that the organic cations may be contributing to the observed blue emission in RInBr<sub>4</sub>. However, there are subtle differences between the two materials as it applies to their optical properties. The maximum excitation wavelength (PLE<sub>max</sub>) of 391 nm for RInBr<sub>4</sub> matches onset of optical absorption measured via diffuse reflectance (Figure A41). In comparison, PLE<sub>max</sub> of 398 nm was measured for the precursor RBr. The PL spectrum for the precursor salt RBr exhibits a broad emission peak with PL<sub>max</sub> of 440 nm and a full width at half maximum (FWHM) value of ~71.3 nm. Notably, the PL spectrum of RBr contains a characteristic two peaks at 432 and 457 nm, and a broad shoulder located at 488 nm. In contrast, RInBr<sub>4</sub> has a broader emission peak with PL<sub>max</sub> of 437 nm and a FWHM value of 95.3 nm, giving it a lighter blue tone with the Commission Internationale de l'Eclairage (CIE) color coordinates of (0.19, 0.20), which can be seen in the emission color for RInBr<sub>4</sub> (Figure 48 a – b).

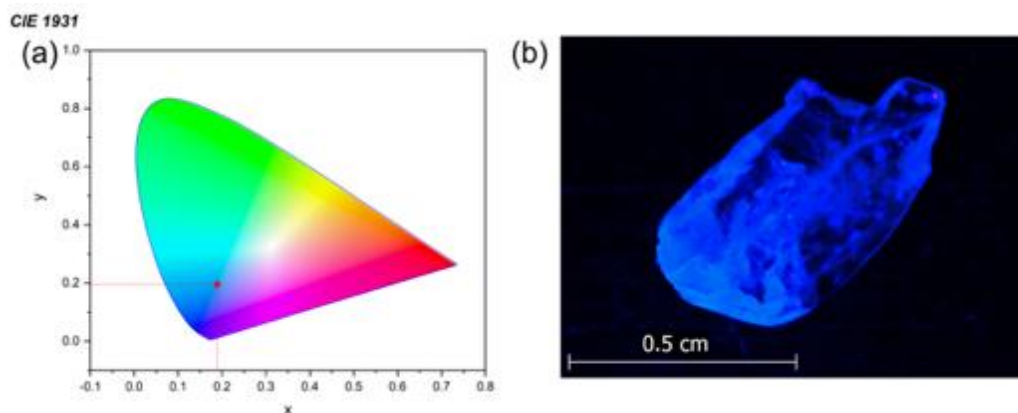


**Figure 48.** (a) A CIE 1931 chromaticity plot for RInBr<sub>4</sub> and (b) the luminescence color of the crystal. It has a clear match to the calculated color from the chromaticity plot.

Immediately noticeable is that the PL peak shape for RInBr<sub>4</sub> including 2 peaks at 437 nm, 451 nm, and a broader shoulder at 506 nm is nearly identical to that measured for RBr. Therefore, based on the measured PL results, the origin of emission in RInBr<sub>4</sub> seems to be the organic component. This is sharply different from the reported PL properties for most of the hybrid metal halides, which typically exhibit PL emission stemming from the inorganic structural segments.<sup>47,48</sup>

As mentioned above,  $\text{In}^{3+}$  is capable of adapting both octahedral or tetrahedral coordination geometries; however, only the octahedrally coordinated  $\text{In}^{\text{III}}\text{Br}_6$  unit was shown to be emissive in  $(\text{C}_4\text{H}_{14}\text{N}_2)_2\text{In}_2\text{Br}_{10}$ .<sup>32</sup> This is attributed to the more pronounced structural distortions of the  $\text{InBr}_6$  octahedra as compared to the  $\text{InBr}_4$  tetrahedra, which helps stabilize STEs in the former. In the case of  $\text{RInBr}_4$ , the presence of emissive organic counteranion together with non-emissive  $\text{InBr}_4^-$  tetrahedra may explain the observed PL properties. Importantly, our results seem to confirm the validity of our original materials design concept, which was based on the utilization of emission organic molecules for the preparation of a rare example of a highly luminescent hybrid metal halide in which the emission originates from the organic component.

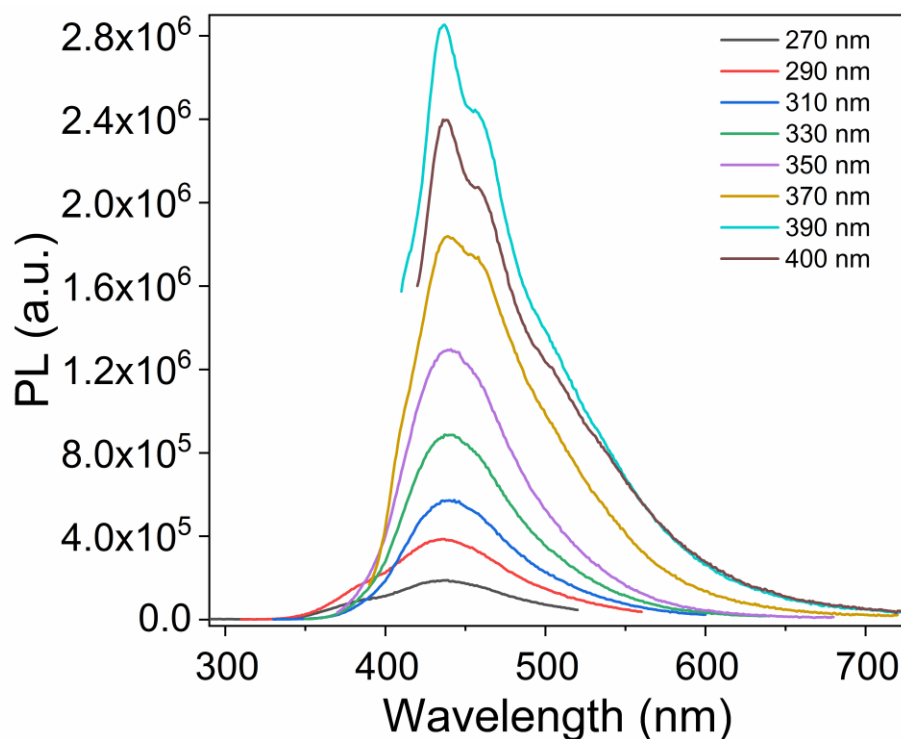


**Figure 49.** Excitation wavelength dependent PL spectra of  $\text{RInBr}_4$ . The optimal excitation wavelength is determined to be  $\text{PLE}_{\text{max}} = 390 \text{ nm}$ .

In order to further ascertain the mechanism of emission for  $\text{RInBr}_4$ , measurements of PL on single crystals and powder samples, PL measurements at low temperature, and excitation-dependent PL were carried out (Figure 49 and Figures A43 and A44). PL spectra measured on

single crystals and powder samples are nearly identical with a minor drop in intensity, ruling out the possible contribution from surface defects to the PL emission of RInBr<sub>4</sub> (Figure A44). We notice that changing the excitation wavelength does not cause a shift in the PL peak position (Figure 49 and A43). In fact, notwithstanding the emergence of a higher energy shoulder peak when higher excitation energy is used, the PL spectra are largely independent of the excitation wavelength. The peak that emerges at a higher excitation energy is present in the literature concerning various stilbene – based compounds, and is attributed to a  $\pi - \pi^*$  transition.<sup>49</sup> Note that when the optimal excitation energy is used (i.e., at PLE<sub>max</sub>), this shoulder is cutoff by the allowable emission monochromator scan range. More specifically, our excitation wavelength dependence of PL spectra shows a peak appearing at 395 nm when our excitation source was below 300 nm. This observation is in agreement with the PL behavior of previously-studied stilbene based compounds.<sup>50</sup> Therefore, our excitation-dependent PL results suggest that there is only one emission mechanism – emission from the organic component. This is further supported by our low temperature PL results taken at 4 K (Figure A42). The comparison of room temperature and low temperature PL spectra suggests that peak shape is largely preserved upon cooling, i.e., there are no new low temperature PL peaks attributable to a possible inorganic emission center. The lack of significant thermal broadening supports the assignment of the emission to the organic molecules in RInBr<sub>4</sub>. This is because organic molecules have stronger bonds and are less deformable by an exciton, and therefore, the phonon participation in the exciton emission is not as strong as in the inorganic anion.<sup>51</sup> Note that the reported fluorescence spectra for various parent *trans*-stilbene compounds are nearly identical in shape to the one reported in this paper.<sup>49,50</sup>

Figure 50 shows the time – resolved photoluminescence measurements (TRPL) for RInBr<sub>4</sub>. The decay profiles were fitted using the following equation

$$I(t) = \int_{-\infty}^t IRF(t') \sum_{i=1}^n A_i e^{-\frac{t-t'}{\tau_i}} dt'$$

where IRF is the instrument response function,  $A_i$  is the coefficient of the exponential decay, and  $\tau_i$  is the PL lifetime. According to the refinement results,  $\tau_1$  is the dominant lifetime at 178 ns. Radiative and non – radiative rates were calculated to be  $9.19 \times 10^5 \text{ s}^{-1}$  and  $4.70 \times 10^6 \text{ s}^{-1}$ , respectively. They were calculated using the following equation

$$\frac{1}{\tau} = \frac{1}{\tau_0} + A_{nr}$$

where  $\tau$  is the lifetime and  $\tau_0$  is the radiative lifetime and  $A_{nr}$  is the non-radiative rate. Full fitting parameters for the TRPL can be found in Table A11. Previous studies report that organic molecules typically have faster emission lifetimes.<sup>52,53</sup> Therefore, the observed longer emission lifetimes is unusual, and possibly, is indicative of greater lattice coupling of the photoemissive state in RInBr<sub>4</sub>.

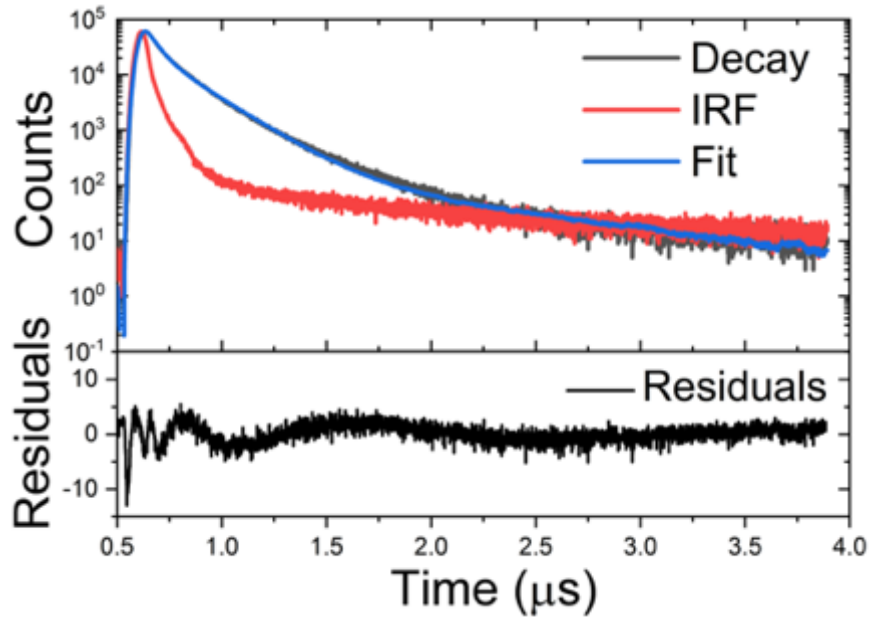


**Figure 50.** Room temperature time-resolved PL data for RInBr<sub>4</sub> obtained using 3.5 eV excitation energy.

#### 4.1.5 Stability Measurements

Important for practical applications, incorporation of emissive organic molecule into a hybrid metal halide can yield substantial improvements in both optical properties and material's stability. Thus, although PL and PLE are largely similar for RBr and RInBr<sub>4</sub>, light emission efficiency is doubled in the hybrid RInBr<sub>4</sub> with a photoluminescence quantum yield (PLQY) value of 16.36% compared to the PLQY of 8.15% for RBr. The high room-temperature PLQY value of 16.36% demonstrated by RInBr<sub>4</sub> is comparable to that shown by several other recently reported hybrid organic-inorganic blue emitters (Table 8). Figure 47b shows periodic PLQY measurements under a continuous exposure to light over the course of one hour for both RBr and RInBr<sub>4</sub>. The PLQY of RBr drops 40% within one hour, whereas the PL emission intensity of RInBr<sub>4</sub> remains almost unchanged with PLQY dropping only 4%. The photo-instability of stilbene (and stilbene-derived organics) has been attributed to its photochemical changes (e.g., photoisomerization and photodimerization) that quench PL; for example, Saltiel et al. reported that the photoisomerization of stilbene resulted in the quenching of the quantum yield.<sup>64</sup> In order for the photochemical reactions to occur, the stilbene molecules must be at an optimal distance from one another (between 3.5 and 4.2 Å), whereas any distance above 4.7 Å will not result in harmful changes.<sup>65</sup> In the hybrid compound RInBr<sub>4</sub>, the longer intermolecular distances between stilbene molecules (>4.7 Å), therefore, explains the improved stability. Therefore, these results suggest a substantial improvement of photostability of the hybrid material as compared to the precursor organic salt RBr. The observed optical property improvements in RInBr<sub>4</sub> as compared to RBr is also in line with the literature reports of synergistic combination of photoluminescent properties of organic and inorganic units and improved stability of resultant low-dimensional hybrid organic-inorganic metal halides.<sup>40</sup> Briefly, low-dimensional hybrid metal halides exhibit increased charge

localization as compared to organic and inorganic precursors (irrespective of the emission origin), which leads to enhanced excitonic properties and improved light emission properties. In the case of  $RInBr_4$ , the greater separation of organic  $R^+$  units not only improves its light emission efficiency but also can lead to reduced harmful PL quenching photochemical reactions, which are observed for stilbene-derived organics, resulting in improved photostability.

**Table 8.** A comparison of the photophysical properties of blue emitting hybrid organic-inorganic halides.<sup>3,18,40,54–59</sup>

Compound	PLQY (%)	PL <sub>max</sub> (nm)	PLE <sub>max</sub> (nm)	Stokes Shift (nm)	FWHM (nm)	Ref
RInBr <sub>4</sub>	16.36	437	391	46	95.3	this work
(C <sub>5</sub> H <sub>7</sub> N <sub>2</sub> ) <sub>2</sub> ZnBr <sub>4</sub>	19.18	438	320	118	-	[18]
[C <sub>6</sub> (CH <sub>3</sub> ) <sub>5</sub> CH <sub>2</sub> N(CH <sub>3</sub> ) <sub>3</sub> ] <sub>2</sub> CdBr <sub>4</sub> ·DMSO	0.32	501	399	102	164	[40]
(C <sub>6</sub> (CH <sub>3</sub> ) <sub>5</sub> CH <sub>2</sub> N(CH <sub>3</sub> ) <sub>3</sub> )ZnBr <sub>3</sub> (DMSO)	3.07	491	386	105	188	[40]
[(NH <sub>4</sub> ) <sub>2</sub> ]CuPbBr <sub>5</sub>	32	441	288	153	107	[54]
[BAPrEDA]PbCl <sub>6</sub>	21.3	390	300	100	73	[55]
PEA <sub>2</sub> (Rb <sub>0.6</sub> Cs <sub>0.4</sub> ) <sub>2</sub> Pb <sub>3</sub> Br <sub>10</sub>	58.3	475	-	-	20	[56]
Cl-MA <sub>3</sub> Bi <sub>2</sub> Br <sub>9</sub>	54.1	422	376	46	41	[57]
(R-mBZA) <sub>2</sub> PbBr <sub>4</sub>	3.430	373	325	48	48	[58]
(C <sub>9</sub> NH <sub>20</sub> ) <sub>7</sub> (PbCl <sub>4</sub> )Pb <sub>3</sub> Cl <sub>11</sub>	83	470	348	122	84	[3]
(C <sub>6</sub> N <sub>2</sub> H <sub>16</sub> Cl) <sub>2</sub> SnCl <sub>6</sub>	8.1	450	375	75	125	[59]

In order to test for the thermal stability of the compound, simultaneous TGA/DSC studies were performed on RInBr<sub>4</sub> and RBr (Figure A45 and A46). For RInBr<sub>4</sub>, the onset temperature at 177.65 °C represents the melting transition of the compound, also confirmed by measurements on our Mel-Temp melting point apparatus, which yields a value of 178.5 °C. The hybrid RInBr<sub>4</sub> demonstrates improved thermal stability with no significant loss in weight up to 250 °C compared to the precursor salt RBr, which shows a significant weight drop above 200 °C. The onset point of 209.67 °C in Figure A46 likely represents the trimethyl ammine group being thermally removed from the material. This is corroborated by the weight loss of 18%, an exact match to the mass percent of trimethyl ammine. Therefore, the measured thermal properties of RInBr<sub>4</sub> suggest a significant advantage of this material, and potentially its other hybrid In(III) bromide derivatives – RInBr<sub>4</sub> may be amenable for melt-processing, which has a set of distinct advantages over solution processing.<sup>60,61</sup> Furthermore, as another test for thermal and air stability, we carried out experiments aimed at studying RInBr<sub>4</sub> under constant heating in ambient air. For this, single

crystals and powdered samples of RInBr<sub>4</sub> were placed on a hotplate at 100°C for one week. The PXRD measurements taken before and after heating indicate that although sample crystallinity is decreased upon continuous heating in air as judged by lowered diffraction peak intensities, RInBr<sub>4</sub> remained crystalline with no signs of impurity evolution (Figure A47 and A48). In addition to structural stability, only a modest drop in the measured PLQY of RInBr<sub>4</sub> from 16.36% to 10.76% is observed after heating at 100°C for one week. Longer term air stability studies with no heating suggests that RInBr<sub>4</sub> is stable up to 2 weeks, after which an impurity peak appears (Figure A49). For the samples kept in ambient air for one week, a PLQY decrease of only 0.13% was recorded. A clear degradation of sample purity and crystallinity can be observed at 2 months (Figure A49). These air-stability and photostability stability metrics for RInBr<sub>4</sub> compare favorably to many of the reported hybrid lead halide phosphors in literature.<sup>62,63</sup>

#### **4.1.6 Electronic Band Structure**



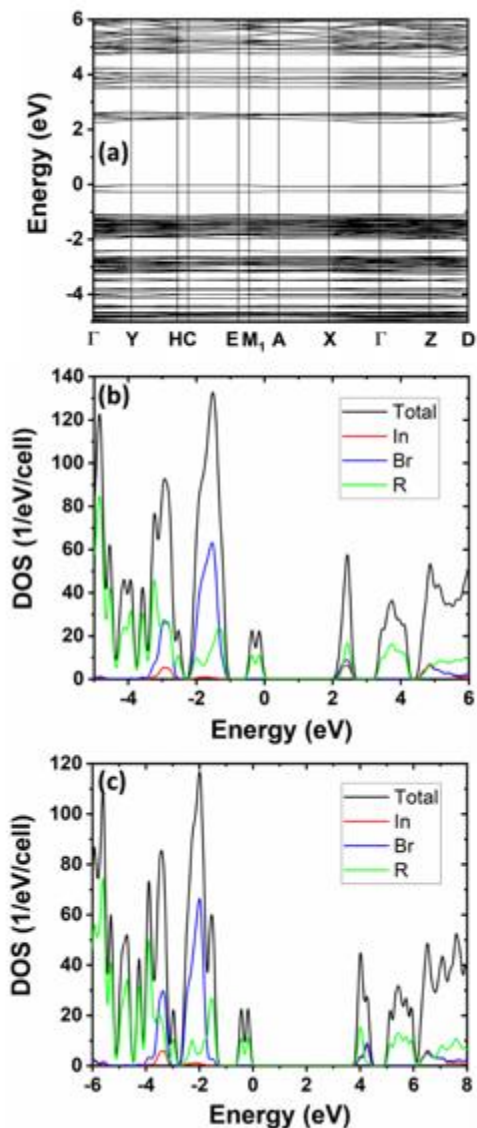


**Figure 51.** (a) Electronic band structure and (b) density of states (DOS) of RInBr<sub>4</sub> calculated using the PBE functional as well as (c) the DOS calculated using the more advanced hybrid PBE0 functional. Note that the PBE band gap in (a) and (b) is underestimated and the band gap is corrected by the PBE0 calculation in (c).

Figure 51a – b show the electronic band structure and DOS of RInBr<sub>4</sub> calculated using the PBE functional. Since the PBE calculation typically underestimates the band gap, the DOS was further corrected by using the hybrid PBE0 functional (Figure 51c), which was shown to improve the band gap description significantly.<sup>66–68</sup> The band structure (Figure 51a) shows extremely flat bands, indicating very weak intermolecular coupling as is expected for a 0D hybrid metal halide

featuring large, bulky organic cations. The PBE0-corrected band gap is about 4.1 eV. The top valence band is derived from  $\pi$  orbitals of the organic cation  $R^+$  while the filled states of  $\text{InBr}_4$  is much lower in energy between -4 eV and -1 eV as shown in the DOS (Figure 51c). The conduction band is made up of both  $R^+$  and  $\text{InBr}_4^-$  states. Since the energy gap between filled and empty  $\text{InBr}_4^-$  states is much larger than that of  $R^+$ , the emission and the lowest-energy excitation should be due to the molecular cation  $R^+$ , consistent with our experimental result. Our computational work reveals that the observed blue emission is due to the transition between  $\pi$  orbitals on stilbene (Figure 52). In contrast, the reported band structures for hybrid indium bromides such as that for  $(\text{C}_4\text{H}_{14}\text{N}_2)_2\text{In}_2\text{Br}_{10}$ <sup>32</sup> show valence and conduction bands dominated by the inorganic components, leading to more dispersive bands.

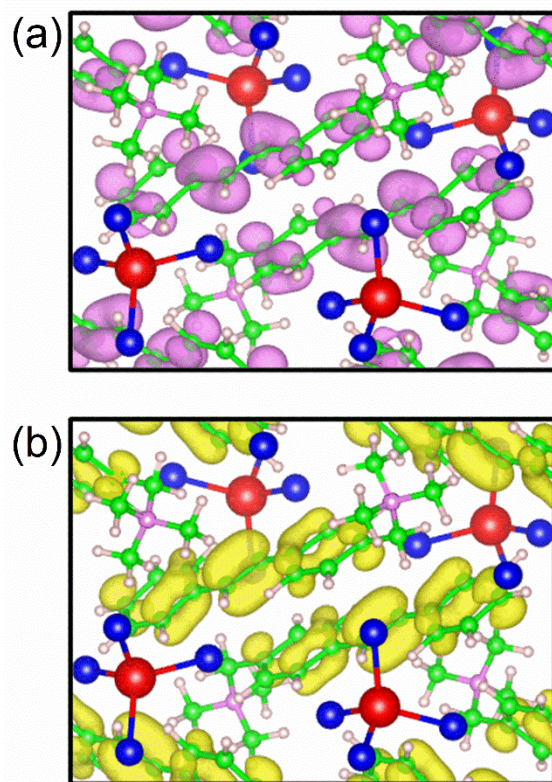


**Figure 52.** (a) Conduction band minimum and (b) valence band maximum at the  $\Gamma$  point for  $\text{RInBr}_4$ .

#### 4.1.7 Conclusions

In conclusion, a novel hybrid organic-inorganic 0D metal halide  $RInBr_4$  featuring photoemissive organic  $R^+$  cation and non-emissive tetrahedral  $InBr_4^-$  anion was prepared and characterized.  $RInBr_4$  shows a visible bright blue emission at room temperature with a measured PLQY of 16.36%, a two-fold improvement over the precursor organic salt  $RBr$ . Based on our combined computational and experimental work, the blue emission from  $RInBr_4$  is attributed to the organic component, which is the main contributor to both the valence and conduction band edge states. In addition to the two-fold improvement in PLQY, the incorporation of organic emitter into a hybrid metal halide material results in a substantial improvement of thermal stability and photo-stability. Of special note is that  $RInBr_4$  melts congruently at 177.65 °C and shows no signs of mass loss up to 250 °C. Together with the promising light emission properties, improved air- and thermal-stability of hybrid In(III) halides make this class of compounds promising for future fundamental research and practical applications. More broadly, our work also highlights the potential benefits of using luminescent organics based on stilbene, which can be incorporated to hybrid metal halide structures, and afford large single crystals through low temperature solution methods.

## Chapter 5: Conclusion and Future Work

### 5.1 Summary of Work Presented

The work presented herein lays the foundation needed to develop novel luminescent materials for various optoelectronic applications. Inspiration for the presented work came from the progress that has been made in lead halide perovskites and alternative lead-free halides, including  $\text{Cs}_3\text{Cu}_2\text{I}_5$  and  $\text{CsCu}_2\text{I}_3$ . As brand new materials systems, Cu(I) halides remain underexplored, and our work presented herein focused on the fundamental materials design principles needed to understand the structure, elemental composition, and optical property relationships.

The model system  $\text{A}_2\text{CuX}_3$  (A= K, Rb and X= Cl, Br) was investigated to reveal up to unity PLQY, bright blue emitters. While the optical properties of all four compounds were similar, they varied heavily in environmental stability and photostability. As one replaces rubidium with potassium, many advantages are revealed. For example,  $\text{Rb}_2\text{CuCl}_3$  undergoes oxidation to form  $\text{Rb}_2\text{CuCl}_4$ , a perovskite-like phase with quenched photoluminescence at room temperature. In contrast,  $\text{K}_2\text{CuCl}_3$  is found to be stable for months; a significant improvement compared to the rapid degradation of  $\text{Rb}_2\text{CuCl}_3$  within a day. The potassium family was also optimized in synthesis with the ability to be grown on larger scales and in the open air with the addition of a reducing agent.

From an optical properties perspective, the compounds were quite interesting as they demonstrated up to unity blue light emission. Blue light is traditionally more challenging to achieve as the formation of mid-gap states lead to off-color emission or reduced efficiency. In all four compounds ( $\text{Rb}_2\text{CuCl}_3$ ,  $\text{Rb}_2\text{CuBr}_3$ ,  $\text{K}_2\text{CuCl}_3$ , and  $\text{K}_2\text{CuBr}_3$ ), the emission is nearly identical, with approximately 300 nm absorption and 400 nm emission, leading to an approximately 1 eV Stoke's shift. The emission was studied through a variety of photoluminescent techniques to reveal

a single, long-lived, intrinsic emission mechanism. When combined with DFT calculations, the emission mechanism was attributed to the recombination of self-trapped excitons located on the copper(I) crystallographic site. This localization on copper explains why elemental substitution yields change only in the non-optical properties, with the exception of photostability. This work is summarized below in Table 9.

**Table 9.** A comparison of the photophysical properties of compounds reported in this work

<b>Compound</b>	<b>PL<sub>max</sub> (nm)</b>	<b>PLE<sub>max</sub> (nm)</b>	<b>Lifetime (<math>\mu</math>s)</b>	<b>FWHM (nm)</b>	<b>Visible PL Color</b>	<b>Primary Source of Emission</b>
Rb <sub>2</sub> CuCl <sub>3</sub>	400	300	12.21	52	Blue	STE
Rb <sub>2</sub> CuBr <sub>3</sub>	385	300	-	~54	Blue	STE
K <sub>2</sub> CuCl <sub>3</sub>	392	291	12.97	54	Blue	STE
K <sub>2</sub> CuBr <sub>3</sub>	388	296	-	54	Blue	STE
Rb <sub>2</sub> AgCl <sub>3</sub>	537	275	0.62	~200	White	DBE
Rb <sub>2</sub> AgBr <sub>3</sub>	485	283	0.77	~225	White (tunable)	STE & DBE
Rb <sub>2</sub> AgI <sub>3</sub>	485	304	1.15	~165	White	DBE
Cs <sub>2</sub> AgBr <sub>3</sub>	524	292	59	-	White (tunable)	STE & DBE
Cs <sub>2</sub> AgI <sub>3</sub>	595	310	15	-	White (tunable)	STE & DBE
(NH <sub>4</sub> ) <sub>2</sub> AgBr <sub>3</sub>	394	275	0.995	142	White (tunable)	STE & DBE
(NH <sub>4</sub> ) <sub>2</sub> AgI <sub>3</sub>	534	303	1.25	114	White (tunable)	STE & DBE
RInBr <sub>4</sub>	437	391	0.178	95	Sky-blue	Organic Cation

Success in the copper(I) halides answered some questions but opened many more on the impact of the metal center on the emission mechanism. Chapter 3 addresses many questions as it

focuses on  $A_2AgX_3$  ( $A = (NH)_4, Rb, Cs$  and  $X = Cl, Br, I$ ), the expanded silver analogs of the compounds explored in chapter 2. These studies looked at a broader range of elemental substitution while exploring the critical switch from copper(I) to silver. This work found that all of the silver halides had a remarkably different emission profile compared to the copper (I) analogs. The compounds displayed tunable white light emission with relatively low PLQY. The compounds performed much better with facile open-air synthesis and high environmental stability from a synthesis and stability perspective. The change in emission profile was attributed to the appearance of a second emission mechanism. In the silver halides, both STEs and low-energy DBEs form. The ratio of STE to DBE emission is controlled directly by the number of halide vacancies, which was found to be created via prolonged vacuum exposure. The halide vacancies could be healed via exposure to a halogen atmosphere. By changing between these two environmental control mechanisms, the optical emission mechanisms were also affected, changing emission from blue to white to red and back again. With their high stability and promising optical properties, multiple luminescent inks were fabricated to show potential for application.

All-inorganic group 11 halides show great promise; however, only a limited number of structures were found in the A-Cu-X ( $A = (NH)_4, K, Rb, Cs$ , and  $X = Cl, Br, I$ ) ternary systems. The work expanded into the broad area of organic-inorganic hybrid materials in chapter 4. The concept of using an organic cation as the emission source, as opposed to the standard metal-halide polyhedra, was investigated. When designing a new compound, the emission is often unpredictable to a certain degree. To get around this, a known emissive organic cation with strong photoluminescent potential was selected. The main issue with this compound and other organic emitters is photoinstability. Upon photoexcitation, the organic salt undergoes photodimerization, quenching photoluminescence. To achieve stable emission, the organic cation was integrated into

an organic-inorganic hybrid compound. This led to full stabilization of the emission, as well as a two-fold improvement in PLQY. The emission profile of the salt was maintained in the hybrid to give an overall improved photoluminescent emission profile. This work opens the door for other organic cation-focused hybrid compounds as a luminescent materials design strategy. All three chapters combined give insight into new strategies to design novel, lead-free, high-intensity emitters.

## **5.2 Future Work**

The path is clear moving forward; the primary objective is to better understand how changing the structure of copper/silver halides can lead to tunable and even brighter photoluminescent materials. As the work above revealed the limitations of elemental substitution, a systematic change in structure would likely lead to a better understanding of why different metal-halide polyhedra create different emission profiles. The most straightforward way to achieve this is to leave the all-inorganic families and begin an exploration of the hybrid families. Using organic cations expands the structures to a near-limitless combination of metal-halide networks.

The work has already begun with some new reports using small molecules that were popular with lead halide perovskites. Guanidinium copper(I) halides were synthesized and reported, yielding white light emission. These compounds have a soft lattice, similar to the silver halides, yet still, have copper(I) as the metal center. This resulted in a highly tunable dual emission from the recombination of both STEs and DBEs. While this was the first foray into the hybrid copper(I) halides, it will not be the last.

Recent work has evolved beyond using organic cations with ammonium as the center of positive charge and instead relies on phosphonium and sulphonium compounds. The resulting compounds have significantly expanded the structural diversity of the metal halide polyhedra.



Species include the simple linear  $\text{CuX}_2$ , through more complex clusters of copper(I) halides previously unreported. There is a full relationship between these structural changes, and the emission is not yet fully understood.

While organic cations can be useful for evoking new structures, they can also be utilized as a source of emission, as seen in chapter 4. A clear extension of this work would be to utilize both an emissive organic cation and metal-halide polyhedra in the same compound. This would require heavy optimization to prevent one emission center from dominating the main profile; however, if achieved, it is a clear route to tunable or white emission.

The last clear route to continue this work is through the incorporation of multiple metals into one compound. There exist many challenges for this path. The first is that the simple formability of the crystals may be unfavored compared to simply forming two ternary compounds. Once formed, the energy levels would have lined up so that both emission centers are optically active. One route around both of these issues is the doping of copper or silver with known emissive metals. This would allow targeted emission profiles and possibly expand copper halides more into the realm of white light emission if blue-emitting copper halides were doped with yellow or red-emitting metals.

## References

- (1) 2022 Solid-State Lighting R&D Opportunities. Energy, U. D. o., Ed.; 2022.
- (2) Gupta, S. K.; Sudarshan, K.; Kadam, R. M. Optical nanomaterials with focus on rare earth doped oxide: A Review. *Materials Today Communications* **2021**, *27*, 102277. DOI: <https://doi.org/10.1016/j.mtcomm.2021.102277>.
- (3) Sato, M.; Kim, S. W.; Shimomura, Y.; Hasegawa, T.; Toda, K.; Adachi, G. Chapter 278 - Rare Earth-Doped Phosphors for White Light-Emitting Diodes. In *Handbook on the Physics and Chemistry of Rare Earths*, Jean-Claude, B., Vitalij K, P. Eds.; Vol. 49; Elsevier, 2016; pp 1-128.
- (4) Kim, K.-B.; Kim, Y.-I.; Chun, H.-G.; Cho, T.-Y.; Jung, J.-S.; Kang, J.-G. Structural and Optical Properties of BaMgAl10O17:Eu<sup>2+</sup> Phosphor. *Chem. Mat.* **2002**, *14* (12), 5045-5052. DOI: 10.1021/cm020592f.
- (5) Li, L.; Lu, F.; Xiong, W.; Ding, Y.; Lu, Y.; Xiao, Y.; Tong, X.; Wang, Y.; Jia, S.; Wang, J.; et al. General synthesis of 2D rare-earth oxide single crystals with tailorable facets. *National Science Review* **2021**, *9* (5). DOI: 10.1093/nsr/nwab153 (accessed 9/12/2022).
- (6) Jha, M. K.; Kumari, A.; Panda, R.; Rajesh Kumar, J.; Yoo, K.; Lee, J. Y. Review on hydrometallurgical recovery of rare earth metals. *Hydrometallurgy* **2016**, *161*, 77. DOI: 10.1016/j.hydromet.2016.01.003.
- (7) Merzhanov, A. G.; Nersesyan, M. D. Self-propagating high-temperature synthesis of oxide materials. *Zh. Vses. Khim. O-va. im. D. I. Mendeleeva* **1990**, *35* (6), 700.
- (8) Hariyani, S.; Brgoch, J. Spectral Design of Phosphor-Converted LED Lighting Guided by Color Theory. *Inorg. Chem.* **2022**, *61* (10), 4205-4218. DOI: 10.1021/acs.inorgchem.1c02975.
- (9) Kumar, V.; Ntwaeaborwa, O. M.; Soga, T.; Dutta, V.; Swart, H. C. Rare Earth Doped Zinc Oxide Nanophosphor Powder: A Future Material for Solid State Lighting and Solar Cells. *ACS Photonics* **2017**, *4* (11), 2613-2637, 10.1021/acsphotonics.7b00777. DOI: 10.1021/acsphotonics.7b00777. Daksh, D.; Agrawal, Y. K. Rare earth-doped zinc oxide nanostructures: a review. *Rev. Nanosci. Nanotechnol.* **2016**, *5* (1), 1-27, 10.1166/rnn.2016.1071. DOI: 10.1166/rnn.2016.1071.
- (10) Saparov, B.; Mitzi, D. B. Organic–Inorganic Perovskites: Structural Versatility for Functional Materials Design. *Chem. Rev.* **2016**, *116* (7), 4558-4596. DOI: 10.1021/acs.chemrev.5b00715 From NLM PubMed-not-MEDLINE.
- (11) Kim, M.; Jeong, J.; Lu, H.; Lee, T. K.; Eickemeyer, F. T.; Liu, Y.; Choi, I. W.; Choi, S. J.; Jo, Y.; Kim, H.-B.; et al. Conformal quantum dot–SnO<sub>2</sub> layers as electron transporters for efficient perovskite solar cells. *Science* **2022**, *375* (6578), 302-306. DOI: 10.1126/science.abh1885 (accessed 2022/08/28).
- (12) Webb, T.; Sweeney, S. J.; Zhang, W. Device Architecture Engineering: Progress toward Next Generation Perovskite Solar Cells. *Advanced Functional Materials* **2021**, *31* (35), 2103121. DOI: <https://doi.org/10.1002/adfm.202103121>.
- (13) Wu, H.; Yao, L.; Cao, W.; Yang, Y.; Cui, Y.; Yang, D.; Qian, G. Stable and wide-wavelength tunable luminescence of CsPbX<sub>3</sub> nanocrystals encapsulated in metal–organic frameworks. *J. Mater. Chem. C.* **2022**, *10* (14), 5550-5558, 10.1039/D2TC00075J. DOI: 10.1039/D2TC00075J.
- (14) Protesescu, L.; Yakunin, S.; Bodnarchuk, M. I.; Krieg, F.; Caputo, R.; Hendon, C. H.; Yang, R. X.; Walsh, A.; Kovalenko, M. V. Nanocrystals of Cesium Lead Halide Perovskites (CsPbX<sub>3</sub>, X = Cl, Br, and I): Novel Optoelectronic Materials Showing Bright Emission with Wide Color Gamut. *Nano Lett.* **2015**, *15* (6), 3692-3696. DOI: 10.1021/nl5048779 From NLM PubMed-not-MEDLINE.

- (15) Zu, Y.; Dai, J.; Li, L.; Yuan, F.; Chen, X.; Feng, Z.; Li, K.; Song, X.; Yun, F.; Yu, Y.; et al. Ultra-stable CsPbBr<sub>3</sub> nanocrystals with near-unity photoluminescence quantum yield via postsynthetic surface engineering. *Journal of Materials Chemistry A* **2019**, *7* (45), 26116-26122, 10.1039/C9TA08421E. DOI: 10.1039/C9TA08421E.
- (16) Qiu, L.; Ono, L. K.; Qi, Y. Advances and challenges to the commercialization of organic–inorganic halide perovskite solar cell technology. *Materials Today Energy* **2018**, *7*, 169-189. DOI: <https://doi.org/10.1016/j.mtener.2017.09.008>.
- (17) Li, J.; Cao, H.-L.; Jiao, W.-B.; Wang, Q.; Wei, M.; Cantone, I.; Lü, J.; Abate, A. Biological impact of lead from halide perovskites reveals the risk of introducing a safe threshold. *Nature Communications* **2020**, *11* (1), 310. DOI: 10.1038/s41467-019-13910-y From NLM Medline.
- (18) Fang, H.-H.; Yang, J.; Tao, S.; Adjokatse, S.; Kamminga, M. E.; Ye, J.; Blake, G. R.; Even, J.; Loi, M. A. Unravelling Light-Induced Degradation of Layered Perovskite Crystals and Design of Efficient Encapsulation for Improved Photostability. *Advanced Functional Materials* **2018**, *28* (21), 1800305, <https://doi.org/10.1002/adfm.201800305>. DOI: <https://doi.org/10.1002/adfm.201800305> (accessed 2022/04/25).
- (19) Li, C. H. A.; Zhou, Z.; Vashishtha, P.; Halpert, J. E. The Future Is Blue (LEDs): Why Chemistry Is the Key to Perovskite Displays. *Chem. Mat.* **2019**, *31* (16), 6003-6032. DOI: 10.1021/acs.chemmater.9b01650.
- (20) Zhang, X.; Wang, H.; Wang, S.; Hu, Y.; Liu, X.; Shi, Z.; Colvin, V. L.; Wang, S.; Yu, W. W.; Zhang, Y. Room Temperature Synthesis of All Inorganic Lead-Free Zero-Dimensional Cs<sub>4</sub>SnBr<sub>6</sub> and Cs<sub>3</sub>KSnBr<sub>6</sub> Perovskites. *Inorganic Chemistry* **2020**, *59* (1), 533-538. DOI: 10.1021/acs.inorgchem.9b02806.
- (21) Lanzetta, L.; Aristidou, N.; Haque, S. A. Stability of Lead and Tin Halide Perovskites: The Link between Defects and Degradation. *J. Phys. Chem. Lett.* **2020**, *11* (2), 574-585. DOI: 10.1021/acs.jpcclett.9b02191 From NLM PubMed-not-MEDLINE. Slavney, A. H.; Hu, T.; Lindenberg, A. M.; Karunadasa, H. I. A Bismuth-Halide Double Perovskite with Long Carrier Recombination Lifetime for Photovoltaic Applications. *J. Am. Chem. Soc.* **2016**, *138* (7), 2138-2141. DOI: 10.1021/jacs.5b13294 From NLM PubMed-not-MEDLINE. Bekenstein, Y.; Dahl, J. C.; Huang, J.; Osowiecki, W. T.; Swabeck, J. K.; Chan, E. M.; Yang, P.; Alivisatos, A. P. The Making and Breaking of Lead-Free Double Perovskite Nanocrystals of Cesium Silver–Bismuth Halide Compositions. *Nano Lett.* **2018**, *18* (6), 3502-3508. DOI: 10.1021/acs.nanolett.8b00560. Ahrland, S.; Grenthe, I.; Theander, O.; Schliack, J.; Reio, L. The Stability of Metal Halide Complexes in Aqueous Solution. III. The Chloride, Bromide, and Iodide Complexes of Bismuth. *Acta Chemica Scandinavica - ACTA CHEM SCAND* **1957**, *11*, 1111-1130. DOI: 10.3891/acta.chem.scand.11-1111.
- (22) Luo, J.; Wang, X.; Li, S.; Liu, J.; Guo, Y.; Niu, G.; Yao, L.; Fu, Y.; Gao, L.; Dong, Q.; et al. Efficient and stable emission of warm-white light from lead-free halide double perovskites. *Nature* **2018**, *563* (7732), 541-545. DOI: 10.1038/s41586-018-0691-0 From NLM PubMed-not-MEDLINE.
- (23) Jun, T.; Sim, K.; Iimura, S.; Sasase, M.; Kamioka, H.; Kim, J.; Hosono, H. Lead-Free Highly Efficient Blue-Emitting Cs<sub>3</sub>Cu<sub>2</sub>I<sub>5</sub> with 0D Electronic Structure. *Adv. Mater.* **2018**, *30* (43), 1804547. DOI: 10.1002/adma.201804547 From NLM PubMed-not-MEDLINE.
- (24) Roccanova, R.; Yangui, A.; Nhalil, H.; Shi, H.; Du, M.-H.; Saparov, B. Near-Unity Photoluminescence Quantum Yield in Blue-Emitting Cs<sub>3</sub>Cu<sub>2</sub>Br<sub>5-x</sub>I<sub>x</sub> (0 ≤ x ≤ 5). *ACS Appl. Electron. Mater.* **2019**, *1* (3), 269–274. DOI: 10.1021/acsaelm.9b00015.
- (25) P. Villars, K. C. Pearson's Crystal Data: Crystal Structure Database for Inorganic Compounds

- (on DVD). In *Materials Park, Ohio, USA*, International, A., Ed.; 2016.
- (26) Boullay, P. Iodures doubles d'argent et de potassium. *Annales de chimie et de physique* **1827**, 34, 377.
- (27) Brink, C.; Kroese, H. A. S. The crystal structure of  $K_2AgI_3$  and isomorphous substances. *Acta Crystallographica* **1952**, 5 (4), 433-436. DOI: 10.1107/S0365110X52001301. Brink, C.; MacGillavry, C. H. The crystal structure of  $K_2CuCl_3$  and isomorphous substances. *Acta Crystallographica* **1949**, 2 (3), 158-163. DOI: 10.1107/s0365110x49000436.
- (28) Hull, S.; Berastegui, P. Crystal structures and ionic conductivities of ternary derivatives of the silver and copper monohalides—II: ordered phases within the  $(AgX)_x-(MX)_{1-x}$  and  $(CuX)_x-(MX)_{1-x}$  (M=K, Rb and Cs; X=Cl, Br and I) systems. *J. Solid State Chem.* **2004**, 177 (9), 3156-3173. DOI: <https://doi.org/10.1016/j.jssc.2004.05.004>.
- (29) Awano, T.; Matsuyama, T. Self-trapped holes in ammonium silver bromide crystal. *Nuclear Instruments & Methods in Physics Research Section B-beam Interactions With Materials and Atoms - NUCL INSTRUM METH PHYS RES B* **1994**, 91 (1-4), 227-229. DOI: 10.1016/0168-583X(94)96222-7.
- (30) Shannon, R. Revised effective ionic radii and systematic studies of interatomic distances in halides and chalcogenides. *Acta Crystallogr. A.* **1976**, 32 (5), 751-767. DOI: doi:10.1107/S0567739476001551.
- (31) Brink, C.; Binnendijk, N. F.; van de Linde, J. The crystal structures of  $CsCu_2Cl_3$  and  $CsAg_2I_3$ . *Acta Crystallographica* **1954**, 7 (2), 176-180. DOI: doi:10.1107/S0365110X54000503.
- (32) Roccanova, R.; Yangui, A.; Seo, G.; Creason, T. D.; Wu, Y.; Kim, D. Y.; Du, M.-H.; Saparov, B. Bright Luminescence from Nontoxic  $CsCu_2X_3$  (X = Cl, Br, I). *ACS Materials Lett.* **2019**, 1 (4), 459-465. DOI: 10.1021/acsmaterialslett.9b00274.
- (33) Bradley, J. N.; Greene, P. D. Relationship of structure and ionic mobility in solid  $Mg_4I_5$ . *Transactions of the Faraday Society* **1967**, 63 (0), 2516-2521, 10.1039/TF9676302516. DOI: 10.1039/TF9676302516.
- (34) Wojakowska, A.; Krzyżak, E.; Wojakowski, A. Phase Diagram for the  $RbBr-CuBr$  System. *J. Therm. Anal. Calorim* **2001**, 65 (2), 491-495. DOI: 10.1023/A:1012481105117.
- (35) Awano, T.; Matsuyama, T. Color centers in mixed crystals of alkali silver halides and ammonium silver halides. *Radiation Effects and Defects in Solids* **1995**, 134 (1-4), 389-393. DOI: 10.1080/10420159508227255. Awano, T.; Bczawa, M.; Matsuyama, T.; Yamaoka, H. Defect in Insulating Materials. World Scientific, Singapore: 1993. Awano, T.; Nanba, T.; Ikezawa, M.; Matsuyama, T.; Yamaoka, H. A Self-Trapped Hole in Alkali Silver Halide Crystals. *Journal of the Physical Society of Japan* **1989**, 58 (7), 2570-2577. DOI: 10.1143/JPSJ.58.2570 (accessed 2022/09/04).
- (36) Farnell, G. C.; Hallama, R.; Burton, P. C. Luminescence of Silver Halides at Low Temperatures. *Nature* **1949**, 164 (4160), 146-147. DOI: 10.1038/164146a0. Farnell, G. C.; Burton, P. C.; Hallama, R. XIV. The fluorescence of silver halides at low temperatures. *The London, Edinburgh, and Dublin Philosophical Magazine and Journal of Science* **1950**, 41 (313), 157-168. DOI: 10.1080/14786445008521778.
- (37) Wang, Z.; Marin, G.; Naterer, G. F.; Gabriel, K. S. Thermodynamics and kinetics of the thermal decomposition of cupric chloride in its hydrolysis reaction. *Journal of Thermal Analysis and Calorimetry* **2015**, 119 (2), 815-823. DOI: 10.1007/s10973-014-3929-6.
- (38) Harada, M.; Katagiri, E. Mechanism of Silver Particle Formation during Photoreduction Using In Situ Time-Resolved SAXS Analysis. *Langmuir* **2010**, 26 (23), 17896-17905. DOI: 10.1021/la102705h.

- (39) Pollack, H. *Materials Science and Metallurgy*; Reston Publishing Company, 1973.
- (40) Merkle, R.; Maier, J. On the Tammann–Rule. *Zeitschrift für anorganische und allgemeine Chemie* **2005**, *631* (6-7), 1163-1166. DOI: <https://doi.org/10.1002/zaac.200400540>.
- (41) Batch crystallization. In *Industrial Crystallization: Fundamentals and Applications*, Lewis, A., van Rosmalen, G., Kramer, H., Seckler, M. Eds.; Cambridge University Press, 2015; pp 178-191.
- (42) Stepanova, L. V.; Skripkin, M. Y.; Chernykh, L. V. Comparative analysis of solubility in CuCl-MCl-H<sub>2</sub>O systems at 25°C (M<sup>+</sup> = Li<sup>+</sup>, Cs<sup>+</sup>, NH<sub>4</sub><sup>+</sup>). *Russian Journal of Applied Chemistry* **2006**, *79* (4), 549-554. DOI: 10.1134/S1070427206040082.
- (43) Creason, T. D.; McWhorter, T. M.; Bell, Z.; Du, M.-H.; Saporov, B. K<sub>2</sub>CuX<sub>3</sub> (X = Cl, Br): All-Inorganic Lead-Free Blue Emitters with Near-Unity Photoluminescence Quantum Yield. *Chem. Mat.* **2020**, *32* (14), 6197-6205. DOI: 10.1021/acs.chemmater.0c02098.
- (44) Wang, F.; Liu, X.-K.; Gao, F. Chapter 1 - Fundamentals of Solar Cells and Light-Emitting Diodes. In *Advanced Nanomaterials for Solar Cells and Light Emitting Diodes*, Gao, F. Ed.; Elsevier, 2019; pp 1-35.
- (45) Aaron Wold, K. D. *Solid State Chemistry*; Chapman and Hall Inc, 1993.
- (46) Govorov, A.; Hernández Martínez, P. L.; Demir, H. V. Theoretical Approaches: Exciton Theory, Coulomb Interactions and Fluctuation-Dissipation Theorem. In *Understanding and Modeling Förster-type Resonance Energy Transfer (FRET): Introduction to FRET, Vol. 1*, Govorov, A., Hernández Martínez, P. L., Demir, H. V. Eds.; Springer Singapore, 2016; pp 41-51.
- (47) Jose Solé, L. B., Daniel Jaque. *An Introduction to the Optical Spectroscopy of Inorganic Solids*; 2005.
- (48) Li, S.; Luo, J.; Liu, J.; Tang, J. Self-Trapped Excitons in All-Inorganic Halide Perovskites: Fundamentals, Status, and Potential Applications. *J. Phys. Chem. Lett.* **2019**, *10* (8), 1999-2007. DOI: 10.1021/acs.jpcclett.8b03604 From NLM PubMed-not-MEDLINE.
- (49) Yangui, A.; Rocanova, R.; Wu, Y.; Du, M.-H.; Saporov, B. Highly Efficient Broad-Band Luminescence Involving Organic and Inorganic Molecules in a Zero-Dimensional Hybrid Lead Chloride. *The Journal of Physical Chemistry C* **2019**, *123* (36), 22470-22477. DOI: 10.1021/acs.jpcc.9b05509.
- (50) Yangui, A.; Pillet, S.; Mlayah, A.; Lusson, A.; Bouchez, G.; Triki, S.; Abid, Y.; Boukhedaden, K. Structural phase transition causing anomalous photoluminescence behavior in perovskite (C<sub>6</sub>H<sub>11</sub>NH<sub>3</sub>)<sub>2</sub>[PbI<sub>4</sub>]. *J. Chem. Phys.* **2015**, *143* (22), 224201. DOI: <http://dx.doi.org/10.1063/1.4936776> From NLM PubMed-not-MEDLINE.
- (51) Mauck, C. M.; Tisdale, W. A. Excitons in 2D Organic–Inorganic Halide Perovskites. *Trends in Chemistry* **2019**, *1* (4), 380-393. DOI: <https://doi.org/10.1016/j.trechm.2019.04.003>.
- (52) Zhao, X.; Niu, G.; Zhu, J.; Yang, B.; Yuan, J.-H.; Li, S.; Gao, W.; Hu, Q.; Yin, L.; Xue, K.-H.; et al. All-Inorganic Copper Halide as a Stable and Self-Absorption-Free X-ray Scintillator. *J. Phys. Chem. Lett.* **2020**, *11* (5), 1873-1880. DOI: 10.1021/acs.jpcclett.0c00161 From NLM Medline.
- (53) Gao, W.; Yin, L.; Yuan, J.-H.; Xue, K.-H.; Niu, G.; Yang, B.; Hu, Q.; Liu, X.; Tang, J. Lead-free violet-emitting K<sub>2</sub>CuCl<sub>3</sub> single crystal with high photoluminescence quantum yield. *Org. Electron.* **2020**, *86*, 105903. DOI: <https://doi.org/10.1016/j.orgel.2020.105903>.
- (54) Lin, Y.-C.; Karlsson, M.; Bettinelli, M. Inorganic Phosphor Materials for Lighting. *Topics in Current Chemistry* **2016**, *374* (2), 21. DOI: 10.1007/s41061-016-0023-5.
- (55) Lin, C. C.; Liu, R.-S. Advances in Phosphors for Light-emitting Diodes. *J. Phys. Chem. Lett.* **2011**, *2* (11), 1268-1277. DOI: 10.1021/jz2002452.

- (56) Creason, T. D.; Yangui, A.; Roccanova, R.; Strom, A.; Du, M.-H.; Saparov, B. All-Inorganic Halides: Rb<sub>2</sub>CuX<sub>3</sub> (X = Cl, Br): 1D All-Inorganic Copper Halides with Ultrabright Blue Emission and Up-Conversion Photoluminescence (Advanced Optical Materials 2/2020). *Adv. Opt. Mat.* **2020**, *8* (2), 2070005. DOI: 10.1002/adom.202070005.
- (57) <https://www.energy.gov/eere/ssl/ssl-forecast-report>.
- (58) Gong, X.; Voznyy, O.; Jain, A.; Liu, W.; Sabatini, R.; Piontkowski, Z.; Walters, G.; Bappi, G.; Nokhrin, S.; Bushuyev, O.; et al. Electron–phonon interaction in efficient perovskite blue emitters. *Nat. Mater.* **2018**, *17* (6), 550-556. DOI: 10.1038/s41563-018-0081-x.
- (59) Xing, J.; Zhao, Y.; Askerka, M.; Quan, L. N.; Gong, X.; Zhao, W.; Zhao, J.; Tan, H.; Long, G.; Gao, L.; et al. Color-stable highly luminescent sky-blue perovskite light-emitting diodes. *Nat. Commun.* **2018**, *9* (1), 3541. DOI: 10.1038/s41467-018-05909-8 From NLM PubMed-not-MEDLINE.
- (60) Xu, W.; Hu, Q.; Bai, S.; Bao, C.; Miao, Y.; Yuan, Z.; Borzda, T.; Barker, A. J.; Tyukalova, E.; Hu, Z.; et al. Rational molecular passivation for high-performance perovskite light-emitting diodes. *Nat. Photonics* **2019**, *13* (6), 418-424. DOI: 10.1038/s41566-019-0390-x.
- (61) Bi, C.; Wang, S.; Kershaw, S. V.; Zheng, K.; Pullerits, T.; Gaponenko, S.; Tian, J.; Rogach, A. L. Spontaneous Self-Assembly of Cesium Lead Halide Perovskite Nanoplatelets into Cuboid Crystals with High Intensity Blue Emission. *Adv. Sci.* **2019**, *6* (13), 1900462. DOI: 10.1002/advs.201900462 (accessed 2019/09/17). From NLM PubMed-not-MEDLINE.
- (62) Bi, C.; Wang, S.; Li, Q.; Kershaw, S. V.; Tian, J.; Rogach, A. L. Thermally Stable Copper(II)-Doped Cesium Lead Halide Perovskite Quantum Dots with Strong Blue Emission. *J. Phys. Chem. Lett.* **2019**, *10* (5), 943-952. DOI: 10.1021/acs.jpcclett.9b00290 From NLM PubMed-not-MEDLINE.
- (63) Liu, Y.; Cui, J.; Du, K.; Tian, H.; He, Z.; Zhou, Q.; Yang, Z.; Deng, Y.; Chen, D.; Zuo, X.; et al. Efficient blue light-emitting diodes based on quantum-confined bromide perovskite nanostructures. *Nat. Photonics* **2019**, doi: 10.1038/s41566-019-0505-4. DOI: 10.1038/s41566-019-0505-4.
- (64) Roccanova, R.; Yangui, A.; Seo, G.; Creason, T. D.; Wu, Y.; Kim, D. Y.; Du, M.-H.; Saparov, B. Bright Luminescence from Nontoxic CsCu<sub>2</sub>X<sub>3</sub> (X = Cl, Br, I). *ACS Materials Lett.* **2019**, *1*, 459-465. DOI: 10.1021/acsmaterialslett.9b00274.
- (65) Seletskiy, D. V.; Melgaard, S. D.; Bigotta, S.; Di Lieto, A.; Tonelli, M.; Sheik-Bahae, M. Laser cooling of solids to cryogenic temperatures. *Nat. Photonics* **2010**, *4*, 161-164. DOI: 10.1038/nphoton.2009.269.
- (66) Zhang, J.; Li, D.; Chen, R.; Xiong, Q. Laser cooling of a semiconductor by 40 kelvin. *Nature* **2013**, *493*, 504-508. DOI: 10.1038/nature11721
- <https://www.nature.com/articles/nature11721#supplementary-information>.
- (67) Ha, S.-T.; Shen, C.; Zhang, J.; Xiong, Q. Laser cooling of organic–inorganic lead halide perovskites. *Nat. Photonics* **2015**, *10*, 115, Article. DOI: 10.1038/nphoton.2015.243
- <https://www.nature.com/articles/nphoton.2015.243#supplementary-information>.
- (68) Cai, P.; Huang, Y.; Seo, H. J. Anti-Stokes Ultraviolet Luminescence and Exciton Detrapping in the Two-Dimensional Perovskite (C<sub>6</sub>H<sub>5</sub>C<sub>2</sub>H<sub>4</sub>NH<sub>3</sub>)<sub>2</sub>PbCl<sub>4</sub>. *J. Phys. Chem. Lett.* **2019**, *10* (14), 4095-4102. DOI: 10.1021/acs.jpcclett.9b01604 From NLM PubMed-not-MEDLINE.
- (69) Morozov, Y. V.; Zhang, S.; Brennan, M. C.; Janko, B.; Kuno, M. Photoluminescence Up-Conversion in CsPbBr<sub>3</sub> Nanocrystals. *ACS Energy Lett.* **2017**, *2* (10), 2514-2515. DOI: 10.1021/acsenerylett.7b00902.

- (70) Dong, Q.; Fang, Y.; Shao, Y.; Mulligan, P.; Qiu, J.; Cao, L.; Huang, J. Electron-hole diffusion lengths  $>175\ \mu\text{m}$  in solution-grown  $\text{CH}_3\text{NH}_3\text{PbI}_3$  single crystals. *Science* **2015**, *347* (6225), 967-970. DOI: 10.1126/science.aaa5760 From NLM PubMed-not-MEDLINE.
- (71) PDXL2. *Rigaku Corporation: Tokyo, Japan* **2012**.
- (72) Roccanova, R.; Ming, W.; Whiteside, V. R.; McGuire, M. A.; Sellers, I. R.; Du, M. H.; Saparov, B. Synthesis, Crystal and Electronic Structures, and Optical Properties of  $(\text{CH}_3\text{NH}_3)_2\text{CdX}_4$  ( $X = \text{Cl}, \text{Br}, \text{I}$ ). *Inorg. Chem.* **2017**, *56* (22), 13878-13888. DOI: 10.1021/acs.inorgchem.7b01986 From NLM PubMed-not-MEDLINE.
- (73) Cowley, A. Novel ultra-violet/blue optoelectronic materials and devices based on copper halides (CuHa). Dublin City University, 2012.
- (74) O'Reilly, L. Growth and characterisation of wide-bandgap  $\gamma\text{-CuCl}$  on near lattice-matched Si. Dublin City University, 2006.
- (75) Sharma, M.; Yangui, A.; Whiteside, V. R.; Sellers, I. R.; Han, D.; Chen, S.; Du, M.-H.; Saparov, B.  $\text{Rb}_4\text{Ag}_2\text{BiBr}_9$ : A Lead-Free Visible Light Absorbing Halide Semiconductor with Improved Stability. *Inorg. Chem.* **2019**, *58* (7), 4446–4455. DOI: 10.1021/acs.inorgchem.8b03623 From NLM PubMed-not-MEDLINE.
- (76) Kanno, R.; Takeda, Y.; Masuyama, Y.; Yamamoto, O.; Takahashi, T. Phase diagram and high copper ion conductivity of the copper(I) chloride-rubidium chloride system. *Solid State Ionics* **1983**, *11* (3), 221-226. DOI: [https://doi.org/10.1016/0167-2738\(83\)90027-9](https://doi.org/10.1016/0167-2738(83)90027-9).
- (77) Saparov, B.; Sun, J.-P.; Meng, W.; Xiao, Z.; Duan, H.-S.; Gunawan, O.; Shin, D.; Hill, I. G.; Yan, Y.; Mitzi, D. B. Thin-Film Deposition and Characterization of a Sn-Deficient Perovskite Derivative  $\text{Cs}_2\text{SnI}_6$ . *Chem. Mater.* **2016**, *28* (7), 2315-2322. DOI: 10.1021/acs.chemmater.6b00433.
- (78) Kresse, G.; Furthmüller, J. Efficiency of ab-initio total energy calculations for metals and semiconductors using a plane-wave basis set. *Computational Materials Science* **1996**, *6* (1), 15-50.
- (79) Kresse, G.; Joubert, D. From ultrasoft pseudopotentials to the projector augmented-wave method. *Physical Review B* **1999**, *59* (3), 1758.
- (80) Perdew, J. P.; Burke, K.; Ernzerhof, M. Generalized gradient approximation made simple. *Physical review letters* **1996**, *77* (18), 3865.
- (81) Perdew, J. P.; Ernzerhof, M.; Burke, K. Rationale for mixing exact exchange with density functional approximations. *Journal of Chemical Physics* **1996**, *105* (22), 9982-9985. DOI: 10.1063/1.472933.
- (82) Heyd, J.; Scuseria, G. E.; Ernzerhof, M. Hybrid functionals based on a screened Coulomb potential. *Journal of Chemical Physics* **2003**, *118* (18), 8207-8215. DOI: 10.1063/1.1564060.
- Paier, J.; Marsman, M.; Hummer, K.; Kresse, G.; Gerber, I. C.; Angyan, J. G. Screened hybrid density functionals applied to solids. *Journal of Chemical Physics* **2006**, *124* (15). DOI: 10.1063/1.2187006.
- (83) Du, M.-H.; Zhang, S. B. Impurity-bound small polarons in ZnO: Hybrid density functional calculations. *Physical Review B* **2009**, *80* (11), 115217. DOI: 10.1103/PhysRevB.80.115217.
- Janotti, A.; Franchini, C.; Varley, J. B.; Kresse, G.; Van de Walle, C. G. Dual behavior of excess electrons in rutile  $\text{TiO}_2$ . *physica status solidi (RRL) – Rapid Research Letters* **2013**, *7* (3), 199-203. DOI: doi:10.1002/pssr.201206464.
- Bjaalie, L.; Ouellette, D. G.; Moetakef, P.; Cain, T. A.; Janotti, A.; Himmetoglu, B.; Allen, S. J.; Stemmer, S.; Walle, C. G. V. d. Small hole polarons in rare-earth titanates. *Applied Physics Letters* **2015**, *106* (23), 232103. DOI: 10.1063/1.4922316.
- (84) Janotti, A.; Varley, J. B.; Choi, M.; Van de Walle, C. G. Vacancies and small polarons in

- $\{\mathrm{SrTiO}\}_3$ . *Physical Review B* **2014**, 90 (8), 085202. DOI: 10.1103/PhysRevB.90.085202.
- (85) Biswas, K.; Du, M. H. Energy transport and scintillation of cerium-doped elpasolite Cs<sub>2</sub>LiYCl<sub>6</sub>: Hybrid density functional calculations. *Physical Review B* **2012**, 86 (1), 014102, Article. DOI: 10.1103/PhysRevB.86.014102.
- (86) Du, M. H. Chemical trends of electronic and optical properties of ns(2) ions in halides. *Journal of Materials Chemistry C* **2014**, 2 (24), 4784-4791. DOI: 10.1039/c4tc00485j. Du, M. H. Using DFT Methods to Study Activators in Optical Materials. *ECS J. Solid State Sci. Technol.* **2016**, 5 (1), R3007-R3018, Article. DOI: 10.1149/2.0011601jss.
- (87) Jones, R. O.; Gunnarsson, O. The density functional formalism, its applications and prospects. *Reviews of Modern Physics* **1989**, 61 (3), 689-746. DOI: 10.1103/RevModPhys.61.689. Görling, A. Density-functional theory beyond the Hohenberg-Kohn theorem. *Physical Review A* **1999**, 59 (5), 3359-3374. DOI: 10.1103/PhysRevA.59.3359. Hellman, A.; Razaznejad, B.; Lundqvist, B. I. Potential-energy surfaces for excited states in extended systems. *The Journal of Chemical Physics* **2004**, 120 (10), 4593-4602. DOI: 10.1063/1.1645787.
- (88) Han, D.; Shi, H.; Ming, W.; Zhou, C.; Ma, B.; Saparov, B.; Ma, Y.-Z.; Chen, S.; Du, M.-H. Unraveling luminescence mechanisms in zero-dimensional halide perovskites. *J. Mater. Chem. C* **2018**, 6 (24), 6398-6405, 10.1039/C8TC01291A. DOI: 10.1039/C8TC01291A.
- (89) Du, M.-H. Zero-dimensional metal oxide Li<sub>4</sub>TiO<sub>4</sub>. *Journal of Materials Chemistry C* **2019**, 7 (19), 5710-5715, 10.1039/C9TC00197B. DOI: 10.1039/C9TC00197B.
- (90) Zhou, C.; Lin, H.; He, Q.; Xu, L.; Worku, M.; Chaaban, M.; Lee, S.; Shi, X.; Du, M.-H.; Ma, B. Low dimensional metal halide perovskites and hybrids. *Materials Science and Engineering: R: Reports* **2019**, 137, 38-65.
- (91) Shi, H.; Han, D.; Chen, S.; Du, M.-H. Impact of metal  $\{\mathrm{n}\}\{\mathrm{s}\}^2$  lone pair on luminescence quantum efficiency in low-dimensional halide perovskites. *Physical Review Materials* **2019**, 3 (3), 034604. DOI: 10.1103/PhysRevMaterials.3.034604. Wu, G.; Zhou, C.; Ming, W.; Han, D.; Chen, S.; Yang, D.; Besara, T.; Neu, J.; Siegrist, T.; Du, M.-H.; et al. A One-Dimensional Organic Lead Chloride Hybrid with Excitation-Dependent Broadband Emissions. *ACS Energy Letters* **2018**, 3 (6), 1443-1449. DOI: 10.1021/acsenergylett.8b00661. Zhou, C.; Lin, H.; Shi, H.; Tian, Y.; Pak, C.; Shatruk, M.; Zhou, Y.; Djurovich, P.; Du, M.-H.; Ma, B. A Zero-Dimensional Organic Seesaw-Shaped Tin Bromide with Highly Efficient Strongly Stokes-Shifted Deep-Red Emission. *Angewandte Chemie International Edition* **2018**, 57, 1021. DOI: 10.1002/anie.201710383. Zhou, C.; Worku, M.; Neu, J.; Lin, H.; Tian, Y.; Lee, S.; Zhou, Y.; Han, D.; Chen, S.; Hao, A.; et al. Facile Preparation of Light Emitting Organic Metal Halide Crystals with Near-Unity Quantum Efficiency. *Chemistry of Materials* **2018**, 30 (7), 2374-2378. DOI: 10.1021/acs.chemmater.8b00129.
- (92) Roccanova, R.; Yangui, A.; Nhalil, H.; Shi, H.; Du, M.-H.; Saparov, B. Near-Unity Photoluminescence Quantum Yield in Blue-Emitting Cs<sub>3</sub>Cu<sub>2</sub>Br<sub>5-x</sub>I<sub>x</sub> (0 ≤ x ≤ 5). *ACS Applied Electronic Materials* **2019**, 1 (3), 269-274. DOI: 10.1021/acsaelm.9b00015.
- (93) Zhou, C.; Lin, H.; He, Q.; Xu, L.; Worku, M.; Chaaban, M.; Lee, S.; Shi, X.; Du, M.-H.; Ma, B. Low dimensional metal halide perovskites and hybrids. *Mater. Sci. Eng., R* **2019**, 137, 38-65. DOI: <https://doi.org/10.1016/j.mser.2018.12.001>. Han, D.; Shi, H.; Ming, W.; Zhou, C.; Ma, B.; Saparov, B.; Ma, Y.-Z.; Chen, S.; Du, M.-H. Unraveling luminescence mechanisms in zero-dimensional halide perovskites. *J. Mater. Chem. C* **2018**, 6 (24), 6398-6405, 10.1039/C8TC01291A. DOI: 10.1039/C8TC01291A. Cortecchia, D.; Yin, J.; Bruno, A.; Lo, S. Z. A.; Gurzadyan, G. G.; Mhaisalkar, S. G.; Brédas, J. L.; Soci, C. Polaron Self-Localization in



White-light Emitting Hybrid Perovskites. *J. Mater. Chem. C* **2017**, *5*, 2771. Dammak, H.; Yangui, A.; Triki, S.; Abid, Y.; Feki, H. Structural characterization, vibrational, optical properties and DFT investigation of a new luminescent organic–inorganic material: (C<sub>6</sub>H<sub>14</sub>N)<sub>3</sub>Bi<sub>2</sub>I<sub>9</sub>. *J. Lumin.* **2015**, *161*, 214-220. DOI: <http://dx.doi.org/10.1016/j.jlumin.2015.01.010>.

(94) Morad, V.; Shynkarenko, Y.; Yakunin, S.; Brumberg, A.; Schaller, R. D.; Kovalenko, M. V. Disphenoidal Zero-Dimensional Lead, Tin, and Germanium Halides: Highly Emissive Singlet and Triplet Self-Trapped Excitons and X-ray Scintillation. *J. Am. Chem. Soc.* **2019**. Zhou, C.; Lin, H.; Worku, M.; Neu, J.; Zhou, Y.; Tian, Y.; Lee, S.; Djurovich, P.; Siegrist, T.; Ma, B. Blue Emitting Single Crystalline Assembly of Metal Halide Clusters. *J. Am. Chem. Soc.* **2018**, *140* (41), 13181-13184. DOI: 10.1021/jacs.8b07731 From NLM PubMed-not-MEDLINE.

(95) Yangui, A.; Garrot, D.; Lauret, J. S.; Lusson, A.; Bouchez, G.; Deleporte, E.; Pillet, S.; Bendeif, E. E.; Castro, M.; Triki, S.; et al. Optical Investigation of Broadband White-Light Emission in Self-Assembled Organic–Inorganic Perovskite (C<sub>6</sub>H<sub>11</sub>NH<sub>3</sub>)<sub>2</sub>PbBr<sub>4</sub>. *J. Phys. Chem. C* **2015**, *119* (41), 23638-23647. DOI: 10.1021/acs.jpcc.5b06211. Yangui, A.; Roccanova, R.; McWhorter, T. M.; Wu, Y.; Du, M.-H.; Saparov, B. Hybrid Organic–Inorganic Halides (C<sub>5</sub>H<sub>7</sub>N<sub>2</sub>)<sub>2</sub>MBr<sub>4</sub> (M = Hg, Zn) with High Color Rendering Index and High-Efficiency White-Light Emission. *Chem. Mater.* **2019**, *31* (8), 2983-2991. DOI: 10.1021/acs.chemmater.9b00537.

(96) Li, S.; Luo, J.; Liu, J.; Tang, J. Self-Trapped Excitons in All-Inorganic Halide Perovskites: Fundamentals, Status, and Potential Applications. *J. Phys. Chem. Lett.* **2019**, 1999-2007. DOI: 10.1021/acs.jpcclett.8b03604.

(97) Cowley, A.; Foy, B.; Danilieuk, D.; McNally, P. J.; Bradley, A. L.; McGlynn, E.; Danilewsky, A. N. UV emission on a Si substrate: Optical and structural properties of  $\gamma$ -CuCl on Si grown using liquid phase epitaxy techniques. *physica status solidi (a)* **2009**, *206* (5), 923-926. DOI: 10.1002/pssa.200881282.

(98) Vijayaraghavan, R. K.; Chandran, D.; Vijayaraghavan, R. K.; McCoy, A. P.; Daniels, S.; McNally, P. J. Highly enhanced UV responsive conductivity and blue emission in transparent CuBr films: implication for emitter and dosimeter applications. *J. Mater. Chem. C* **2017**, *5* (39), 10270-10279, 10.1039/C7TC02838E. DOI: 10.1039/C7TC02838E.

(99) Saparov, B.; Mitzi, D. B. Organic–Inorganic Perovskites: Structural Versatility for Functional Materials Design. *Chem. Rev.* **2016**, *116*, 4558-4596.

(100) Roccanova, R.; Houck, M.; Yangui, A.; Han, D.; Shi, H.; Wu, Y.; Glatzhofer, D. T.; Powell, D. R.; Chen, S.; Fourati, H.; et al. Broadband Emission in Hybrid Organic–Inorganic Halides of Group 12 Metals. *ACS Omega* **2018**, *3* (12), 18791-18802. DOI: 10.1021/acsomega.8b02883 From NLM PubMed-not-MEDLINE.

(101) Barkaoui, H.; Abid, H.; Yangui, A.; Triki, S.; Boukheddaden, K.; Abid, Y. Yellowish White-Light Emission Involving Resonant Energy Transfer in a New One-Dimensional Hybrid Material: (C<sub>9</sub>H<sub>10</sub>N<sub>2</sub>)PbCl<sub>4</sub>. *J. Phys. Chem. C* **2018**, *122* (42), 24253-24261. DOI: 10.1021/acs.jpcc.8b06850.

(102) Shinada, M.; Sugano, S. Interband optical transitions in extremely anisotropic semiconductors. I. Bound and unbound exciton absorption. *J. Phys. Soc. Jpn.* **1966**, *21* (10), 1936-1946. DOI: Doi 10.1143/Jpsj.21.1936.

(103) Lin, H.; Zhou, C.; Tian, Y.; Siegrist, T.; Ma, B. Low-Dimensional Organometal Halide Perovskites. *ACS Energy Lett.* **2018**, *3* (1), 54-62. DOI: 10.1021/acseenergylett.7b00926.

(104) Jain, A.; Ong, S. P.; Hautier, G.; Chen, W.; Richards, W. D.; Dacek, S.; Cholia, S.; Gunter, D.; Skinner, D.; Ceder, G.; et al. Commentary: The Materials Project: A materials genome approach to accelerating materials innovation. *APL Materials* **2013**, *1* (1), 011002. DOI:

10.1063/1.4812323.

(105) Morozov, Y. V.; Draguta, S.; Zhang, S.; Cadranet, A.; Wang, Y.; Janko, B.; Kuno, M. Defect-Mediated CdS Nanobelt Photoluminescence Up-Conversion. *J. Phys. Chem. C* **2017**, *121* (30), 16607-16616. DOI: 10.1021/acs.jpcc.7b05095. Sheik-Bahae, M.; Epstein, R. I. Optical refrigeration. *Nat. Photonics* **2007**, *1*, 693-699. DOI: 10.1038/nphoton.2007.244. Sheik-Bahae, M.; Epstein, R. I. Can Laser Light Cool Semiconductors? *Phys. Rev. Lett.* **2004**, *92* (24), 247403. DOI: 10.1103/PhysRevLett.92.247403 From NLM PubMed-not-MEDLINE.

(106) Yamada, T.; Aharen, T.; Kanemitsu, Y. Up-converted photoluminescence from (CH<sub>3</sub>NH<sub>3</sub>)PbI<sub>3</sub> perovskite semiconductors: Implications for laser cooling. *Phys. Rev. Mater.* **2019**, *3* (2), 024601. DOI: 10.1103/PhysRevMaterials.3.024601.

(107) Roman, B. J.; Sheldon, M. T. Six-fold plasmonic enhancement of thermal scavenging via CsPbBr<sub>3</sub> anti-Stokes photoluminescence. *Nanophotonics* **2019**, *8* (4), 599-605.

(108) Zhang, Q.; Yin, Y. All-inorganic metal halide perovskite nanocrystals: opportunities and challenges. *ACS central science* **2018**, *4* (6), 668-679. Li, S.; Luo, J.; Liu, J.; Tang, J. Self-Trapped Excitons in All-Inorganic Halide Perovskites: Fundamentals, Status, and Potential Applications. *J. Phys. Chem. Lett.* **2019**, *10* (8), 1999-2007. DOI: 10.1021/acs.jpcllett.8b03604. Ghosh, S.; Pradhan, B. Lead-Free Metal Halide Perovskite Nanocrystals: Challenges, Applications, and Future Aspects. *ChemNanoMat* **2019**, *5* (3), 300-312.

(109) Du, P.; Luo, L.; Cheng, W. Neoteric Mn<sup>2+</sup>-activated Cs<sub>3</sub>Cu<sub>2</sub>I<sub>5</sub> dazzling yellow-emitting phosphors for white-LED. *Journal of the American Ceramic Society* **2020**, *103* (2), 1149-1155. Luo, Z.; Li, Q.; Zhang, L.; Wu, X.; Tan, L.; Zou, C.; Liu, Y.; Quan, Z. 0D Cs<sub>3</sub>Cu<sub>2</sub>X<sub>5</sub> (X= I, Br, and Cl) Nanocrystals: Colloidal Syntheses and Optical Properties. *Small* **2020**, *16* (3), 1905226. Lin, R.; Guo, Q.; Zhu, Q.; Zhu, Y.; Zheng, W.; Huang, F. All-Inorganic CsCu<sub>2</sub>I<sub>3</sub> Single Crystal with High-PLQY (≈ 15.7%) Intrinsic White-Light Emission via Strongly Localized 1D Excitonic Recombination. *Advanced Materials* **2019**, *31* (46), 1905079. Li, T.; Mo, X.; Peng, C.; Lu, Q.; Qi, C.; Tao, X.; Ouyang, Y.; Zhou, Y. Distinct green electroluminescence from lead-free CsCuBr<sub>2</sub> halide micro-crosses. *Chemical Communications* **2019**, *55* (31), 4554-4557. Zhou, L.; Liao, J. F.; Huang, Z. G.; Wei, J. H.; Wang, X. D.; Li, W. G.; Chen, H. Y.; Kuang, D. B.; Su, C. Y. A Highly Red-Emissive Lead-Free Indium-Based Perovskite Single Crystal for Sensitive Water Detection. *Angewandte Chemie International Edition* **2019**, *58* (16), 5277-5281. Zhou, C.; Lin, H.; Tian, Y.; Yuan, Z.; Clark, R.; Chen, B.; van de Burgt, L. J.; Wang, J. C.; Zhou, Y.; Hanson, K. Luminescent zero-dimensional organic metal halide hybrids with near-unity quantum efficiency. *Chemical science* **2018**, *9* (3), 586-593. Zhang, R.; Mao, X.; Zheng, D.; Yang, Y.; Yang, S.; Han, K. A Lead-Free All-Inorganic Metal Halide with Near-Unity Green Luminescence. *Laser & Photonics Reviews*, 2000027. Zhou, C.; Lin, H.; Shi, H.; Tian, Y.; Pak, C.; Shatruk, M.; Zhou, Y.; Djurovich, P.; Du, M. H.; Ma, B. A zero-dimensional organic seesaw-shaped tin bromide with highly efficient strongly stokes-shifted deep-red emission. *Angewandte Chemie International Edition* **2018**, *57* (4), 1021-1024. Majher, J. D.; Gray, M. B.; Strom, T. A.; Woodward, P. M. Cs<sub>2</sub>NaBiCl<sub>6</sub>: Mn<sup>2+</sup>—A New Orange-Red Halide Double Perovskite Phosphor. *Chemistry of Materials* **2019**, *31* (5), 1738-1744.

(110) Yang, B.; Yin, L.; Niu, G.; Yuan, J. H.; Xue, K. H.; Tan, Z.; Miao, X. S.; Niu, M.; Du, X.; Song, H. Lead-Free Halide Rb<sub>2</sub>CuBr<sub>3</sub> as Sensitive X-Ray Scintillator. *Advanced Materials* **2019**, *31* (44), 1904711.

(111) Creason, T. D.; Yangui, A.; Roccanova, R.; Strom, A.; Du, M. H.; Saporov, B. Rb<sub>2</sub>CuX<sub>3</sub> (X= Cl, Br): 1D All-Inorganic Copper Halides with Ultrabright Blue Emission and Up-Conversion Photoluminescence. *Advanced Optical Materials* **2020**, *8* (2), 1901338.

- (112) Bi, C.; Wang, S.; Kershaw, S. V.; Zheng, K.; Pullerits, T.; Gaponenko, S.; Tian, J.; Rogach, A. L. Spontaneous Self-Assembly of Cesium Lead Halide Perovskite Nanoplatelets into Cuboid Crystals with High Intensity Blue Emission. *Advanced Science* **2019**, *6* (13), 1900462. Morad, V.; Shynkarenko, Y.; Yakunin, S.; Brumberg, A.; Schaller, R. D.; Kovalenko, M. V. Disphenoidal Zero-Dimensional Lead, Tin, and Germanium Halides: Highly Emissive Singlet and Triplet Self-Trapped Excitons and X-ray Scintillation. *Journal of the American Chemical Society* **2019**, *141* (25), 9764-9768. Zhou, C.; Lin, H.; Worku, M.; Neu, J.; Zhou, Y.; Tian, Y.; Lee, S.; Djurovich, P.; Siegrist, T.; Ma, B. Blue emitting single crystalline assembly of metal halide clusters. *Journal of the American Chemical Society* **2018**, *140* (41), 13181-13184.
- (113) Jun, T.; Sim, K.; Iimura, S.; Sasase, M.; Kamioka, H.; Kim, J.; Hosono, H. Lead-Free Highly Efficient Blue-Emitting Cs<sub>3</sub>Cu<sub>2</sub>I<sub>5</sub> with 0D Electronic Structure. *Advanced Materials* **2018**, *30* (43), 1804547.
- (114) Xing, J.; Zhao, Y.; Askerka, M.; Quan, L. N.; Gong, X.; Zhao, W.; Zhao, J.; Tan, H.; Long, G.; Gao, L. Color-stable highly luminescent sky-blue perovskite light-emitting diodes. *Nature communications* **2018**, *9* (1), 1-8. Gong, X.; Voznyy, O.; Jain, A.; Liu, W.; Sabatini, R.; Piontkowski, Z.; Walters, G.; Bappi, G.; Nokhrin, S.; Bushuyev, O. Electron-phonon interaction in efficient perovskite blue emitters. *Nature materials* **2018**, *17* (6), 550-556. Bi, C.; Wang, S.; Li, Q.; Kershaw, S. V.; Tian, J.; Rogach, A. L. Thermally stable copper (II)-Doped cesium lead halide perovskite quantum dots with strong blue emission. *The journal of physical chemistry letters* **2019**, *10* (5), 943-952. Steckel, J. S.; Zimmer, J. P.; Coe-Sullivan, S.; Stott, N. E.; Bulović, V.; Bawendi, M. G. Blue luminescence from (CdS) ZnS core-shell nanocrystals. *Angewandte Chemie International Edition* **2004**, *43* (16), 2154-2158. Wang, L.; Nagesha, D. K.; Selvarasah, S.; Dokmeci, M. R.; Carrier, R. L. Toxicity of CdSe nanoparticles in Caco-2 cell cultures. *Journal of nanobiotechnology* **2008**, *6* (1), 11.
- (115) Zhang, R.; Mao, X.; Zheng, D.; Yang, Y.; Yang, S.; Han, K. A Lead-Free All-Inorganic Metal Halide with Near-Unity Green Luminescence. *Laser & Photonics Reviews* **2020**, *14* (5), 2000027. DOI: 10.1002/lpor.202000027 (accessed 2020/04/30).
- (116) Zhao, X.; Niu, G.; Zhu, J.; Yang, B.; Yuan, J. H.; Li, S.; Gao, W.; Hu, Q.; Yin, L.; Xue, K. H.; et al. All-Inorganic Copper Halide as a Stable and Self-Absorption-Free X-ray Scintillator. *J Phys Chem Lett* **2020**, *11* (5), 1873-1880. DOI: 10.1021/acs.jpcllett.0c00161.
- (117) Yang, B.; Yin, L.; Niu, G.; Yuan, J.-H.; Xue, K.-H.; Tan, Z.; Miao, X.-S.; Niu, M.; Du, X.; Song, H.; et al. Lead-Free Halide Rb<sub>2</sub>CuBr<sub>3</sub> as Sensitive X-Ray Scintillator. *Advanced Materials* **2019**, *31* (44), 1904711. DOI: 10.1002/adma.201904711 (accessed 2020/02/19). From NLM PubMed-not-MEDLINE.
- (118) Roccanova, R.; Yangui, A.; Seo, G.; Creason, T. D.; Wu, Y.; Kim, D. Y.; Du, M.-H.; Saparov, B. Bright Luminescence from Nontoxic CsCu<sub>2</sub>X<sub>3</sub> (X = Cl, Br, I). *ACS Materials Letters* **2019**, *1* (4), 459-465. DOI: 10.1021/acsmaterialslett.9b00274.
- (119) Li, Q.; Chen, Z.; Yang, B.; Tan, L.; Xu, B.; Han, J.; Zhao, Y.; Tang, J.; Quan, Z. Pressure-Induced Remarkable Enhancement of Self-Trapped Exciton Emission in One-Dimensional CsCu<sub>2</sub>I<sub>3</sub> with Tetrahedral Units. *Journal of the American Chemical Society* **2020**, *142* (4), 1786-1791. DOI: 10.1021/jacs.9b13419.
- (120) Janotti, A.; Varley, J. B.; Choi, M.; Van de Walle, C. G. Vacancies and small polarons in SrTiO<sub>3</sub>. *Physical Review B* **2014**, *90* (8), 085202. DOI: 10.1103/PhysRevB.90.085202.
- (121) Du, M.-H. Microscopic origin of multiple exciton emission in low-dimensional lead halide perovskites. *The Journal of Chemical Physics* **2019**, *151* (18), 181101. DOI: 10.1063/1.5127933.
- (122) Cheng, P.; Sun, L.; Feng, L.; Yang, S.; Yang, Y.; Zheng, D.; Zhao, Y.; Sang, Y.; Zhang, R.;

- Wei, D.; et al. Colloidal Synthesis and Optical Properties of All-Inorganic Low-Dimensional Cesium Copper Halide Nanocrystals. *Angewandte Chemie* **2019**, *131* (45), 16233-16237. DOI: 10.1002/ange.201909129. Shi, H.; Han, D.; Chen, S.; Du, M.-H. Impact of metal ns<sup>2</sup> lone pair on luminescence quantum efficiency in low-dimensional halide perovskites. *Physical Review Materials* **2019**, *3* (3), 034604. DOI: 10.1103/PhysRevMaterials.3.034604.
- (123) Du, M.-H. Emission Trend of Multiple Self-Trapped Excitons in Luminescent 1D Copper Halides. *ACS Energy Letters* **2020**, *5*, 464-469. DOI: 10.1021/acseenergylett.9b02688.
- (124) Saparov, B.; Sun, J.-P.; Meng, W.; Xiao, Z.; Duan, H.-S.; Gunawan, O.; Shin, D.; Hill, I. G.; Yan, Y.; Mitzi, D. B. Thin-film deposition and characterization of a Sn-deficient perovskite derivative Cs<sub>2</sub>SnI<sub>6</sub>. *Chemistry of Materials* **2016**, *28* (7), 2315-2322. Sharma, M.; Yangui, A.; Whiteside, V. R.; Sellers, I. R.; Han, D.; Chen, S.; Du, M.-H.; Saparov, B. Rb<sub>4</sub>Ag<sub>2</sub>BiBr<sub>9</sub>: A Lead-Free Visible Light Absorbing Halide Semiconductor with Improved Stability. *Inorganic chemistry* **2019**, *58* (7), 4446-4455.
- (125) Biefeld, R. M. The KBr-CuBr and NaBr-CuBr phase diagrams. *Materials Research Bulletin* **1975**, *10* (11), 1151-1156. DOI: [https://doi.org/10.1016/0025-5408\(75\)90019-7](https://doi.org/10.1016/0025-5408(75)90019-7). Etter, D. E.; Wiedenheft, C. J. The study of KCl-CuCl eutectic fused salt as a potential intermediate temperature heat transfer and storage medium. *Solar Energy Materials* **1980**, *2* (4), 423-431. DOI: [https://doi.org/10.1016/0165-1633\(80\)90037-4](https://doi.org/10.1016/0165-1633(80)90037-4).
- (126) Cortecchia, D.; Yin, J.; Bruno, A.; Lo, S.-Z. A.; Gurzadyan, G. G.; Mhaisalkar, S.; Brédas, J.-L.; Soci, C. Polaron self-localization in white-light emitting hybrid perovskites. *Journal of Materials Chemistry C* **2017**, *5* (11), 2771-2780.
- (127) Ziegler, J. F. *INTERACTIONS OF IONS WITH MATTER*. <http://srin.org/index.htm#HOMETOP> (accessed 5/15/20).
- (128) M.J. Berger, J. H. H., S.M. Seltzer, J. Chang, J.S. Coursey, R. Sukumar, D.S. Zucker, and K. Olsen. *XCOM: Photon Cross Sections Database*. <https://physics.nist.gov/PhysRefData/Xcom/html/xcom1.html> (accessed 5/15/20).
- (129) M.J. Berger, J. S. C., M.A. Zucker and J. Chang. *Stopping-Power & Range Tables for Electrons, Protons, and Helium Ions*. 2017. <https://physics.nist.gov/PhysRefData/Star/Text/ESTAR.html> (accessed 5/15/20).
- (130) Kumar, P.; Creason, T. D.; Fattal, H.; Sharma, M.; Du, M. H.; Saparov, B. Composition-Dependent Photoluminescence Properties and Anti-Counterfeiting Applications of A<sub>2</sub>AgX<sub>3</sub> (A = Rb, Cs; X = Cl, Br, I). *Advanced Functional Materials* **2021**, *31* (48). DOI: 10.1002/adfm.202104941.
- (131) Creason, T. D.; Fattal, H.; Gilley, I. W.; McWhorter, T. M.; Du, M.-H.; Saparov, B. (NH<sub>4</sub>)<sub>2</sub>AgX<sub>3</sub> (X = Br, I): 1D Silver Halides with Broadband White Light Emission and Improved Stability. *ACS Mater. Au* **2021**, *1* (1), 62-68. DOI: 10.1021/acsmaterialsau.1c00009.
- (132) Green, M. A.; Ho-Baillie, A.; Snaith, H. J. The emergence of perovskite solar cells. *Nat Photonics* **2014**, *8* (7), 506-514, 10.1038/nphoton.2014.134. DOI: 10.1038/Nphoton.2014.134. Cai, M.; Wu, Y.; Chen, H.; Yang, X.; Qiang, Y.; Han, L. Cost-Performance Analysis of Perovskite Solar Modules. *Advanced Science* **2017**, *4* (1), 1600269. DOI: 10.1002/advs.201600269 From NLM PMC. Sum, T. C.; Mathews, N. Advancements in perovskite solar cells: photophysics behind the photovoltaics. *Energy & Environmental Science* **2014**, *7* (8), 2518-2534, 10.1039/C4EE00673A. DOI: 10.1039/C4EE00673A.
- (133) Yang, Z.; Gao, M.; Wu, W.; Yang, X.; Sun, X. W.; Zhang, J.; Wang, H.-C.; Liu, R.-S.; Han, C.-Y.; Yang, H.; et al. Recent advances in quantum dot-based light-emitting devices: Challenges and possible solutions. *Materials Today* **2019**, *24*, 69-93. DOI:

<https://doi.org/10.1016/j.mattod.2018.09.002>.

(134) Wei, Y.; Cheng, Z.; Lin, J. An overview on enhancing the stability of lead halide perovskite quantum dots and their applications in phosphor-converted LEDs. *Chem. Soc. Rev.* **2019**, *48* (1), 310-350, 10.1039/C8CS00740C. DOI: 10.1039/C8CS00740C From NLM PubMed-not-MEDLINE.

(135) Ono, L. K.; Qi, Y.; Liu, S. Progress toward Stable Lead Halide Perovskite Solar Cells. *Joule* **2018**, *2* (10), 1961-1990, 10.1016/j.joule.2018.07.007. DOI: 10.1016/j.joule.2018.07.007.

(136) Creason, T. D.; Yangui, A.; Roccanova, R.; Strom, A.; Du, M.-H.; Saparov, B. Rb<sub>2</sub>CuX<sub>3</sub> (X = Cl, Br): 1D All-Inorganic Copper Halides with Ultrabright Blue Emission and Up-Conversion Photoluminescence. *Adv. Opt. Mat.* **2020**, *8* (2), 1901338. DOI: 10.1002/adom.201901338.

(137) Wu, M.; Haji Ladi, N.; Yi, Z.; Li, H.; Shen, Y.; Wang, M. Stability Issue of Perovskite Solar Cells under Real-World Operating Conditions. *Energy Technol. (Weinheim, Ger.)* **2020**, *8* (4), 1900744, 10.1002/ente.201900744. DOI: 10.1002/ente.201900744.

(138) Dai, X.; Deng, Y.; Peng, X.; Jin, Y. Quantum-Dot Light-Emitting Diodes for Large-Area Displays: Towards the Dawn of Commercialization. *Advanced Materials* **2017**, *29* (14), 1607022. DOI: 10.1002/adma.201607022 (accessed 2020/02/24). From NLM PubMed-not-MEDLINE.

(139) Huang, H.; Polavarapu, L.; Sichert, J. A.; Susha, A. S.; Urban, A. S.; Rogach, A. L. Colloidal lead halide perovskite nanocrystals: synthesis, optical properties and applications. *Npg Asia Materials* **2016**, *8*, e328, Review. DOI: 10.1038/am.2016.167.

(140) Lu, S.; Zhou, Q.; Ouyang, Y.; Guo, Y.; Li, Q.; Wang, J. Accelerated discovery of stable lead-free hybrid organic-inorganic perovskites via machine learning. *Nature Communications* **2018**, *9* (1), 3405. DOI: 10.1038/s41467-018-05761-w From NLM PubMed-not-MEDLINE. Luo, J.; Hu, M.; Niu, G.; Tang, J. Lead-Free Halide Perovskites and Perovskite Variants as Phosphors toward Light-Emitting Applications. *ACS Applied Materials & Interfaces* **2019**, *11* (35), 31575-31584. DOI: 10.1021/acsami.9b08407 From NLM PubMed-not-MEDLINE. Li, Y.; Yang, K. High-throughput computational design of organic-inorganic hybrid halide semiconductors beyond perovskites for optoelectronics. *Energy & Environmental Science* **2019**, *12* (7), 2233-2243, 10.1039/C9EE01371G. DOI: 10.1039/C9EE01371G. Sun, J.; Yang, J.; Lee, J. I.; Cho, J. H.; Kang, M. S. Lead-Free Perovskite Nanocrystals for Light-Emitting Devices. *J. Phys. Chem. Lett.* **2018**, *9* (7), 1573-1583. DOI: 10.1021/acs.jpcllett.8b00301 From NLM PubMed-not-MEDLINE. Chakraborty, S.; Xie, W.; Mathews, N.; Sherburne, M.; Ahuja, R.; Asta, M.; Mhaisalkar, S. G. Rational Design: A High-Throughput Computational Screening and Experimental Validation Methodology for Lead-Free and Emergent Hybrid Perovskites. *ACS Energy Letters* **2017**, *2* (4), 837-845. DOI: 10.1021/acsenerylett.7b00035.

(141) Mo, X.; Li, T.; Huang, F.; Li, Z.; Zhou, Y.; Lin, T.; Ouyang, Y.; Tao, X.; Pan, C. Highly-efficient all-inorganic lead-free 1D CsCu<sub>2</sub>I<sub>3</sub> single crystal for white-light emitting diodes and UV photodetection. *Nano Energy* **2020**, *81*, 105570. DOI: <https://doi.org/10.1016/j.nanoen.2020.105570>.

(142) Morad, V.; Shynkarenko, Y.; Yakunin, S.; Brumberg, A.; Schaller, R. D.; Kovalenko, M. V. Disphenoidal Zero-Dimensional Lead, Tin, and Germanium Halides: Highly Emissive Singlet and Triplet Self-Trapped Excitons and X-ray Scintillation. *J. Am. Chem. Soc.* **2019**, *141* (25), 9764-9768. DOI: 10.1021/jacs.9b02365 From NLM PubMed-not-MEDLINE.

(143) Peng, H.; Yao, S.; Guo, Y.; Zhi, R.; Wang, X.; Ge, F.; Tian, Y.; Wang, J.; Zou, B. Highly Efficient Self-Trapped Exciton Emission of a (MA)<sub>4</sub>Cu<sub>2</sub>Br<sub>6</sub> Single Crystal. *J. Phys. Chem. Lett.* **2020**, *11* (12), 4703-4710. DOI: 10.1021/acs.jpcllett.0c01162 From NLM PubMed-not-MEDLINE.

- (144) Roccanova, R.; Yangui, A.; Nhalil, H.; Shi, H.; Du, M.-H.; Saparov, B. Near-Unity Photoluminescence Quantum Yield in Blue-Emitting  $\text{Cs}_3\text{Cu}_2\text{Br}_{5-x}\text{I}_x$  ( $0 \leq x \leq 5$ ). *ACS Appl. Electron. Mater.* **2019**, *1* (3), 269-274. DOI: 10.1021/acsaelm.9b00015.
- (145) Dou, L.; Lai, M.; Kley, C. S.; Yang, Y.; Bischak, C. G.; Zhang, D.; Eaton, S. W.; Ginsberg, N. S.; Yang, P. Spatially resolved multicolor  $\text{CsPbX}_3$  nanowire heterojunctions via anion exchange. *PNAS* **2017**, *114* (28), 201703860. DOI: 10.1073/pnas.1703860114 From NLM PubMed-not-MEDLINE.
- (146) Zhang, F.; Zhong, H.; Chen, C.; Wu, X.-g.; Hu, X.; Huang, H.; Han, J.; Zou, B.; Dong, Y. Brightly Luminescent and Color-Tunable Colloidal  $\text{CH}_3\text{NH}_3\text{PbX}_3$  ( $X = \text{Br}, \text{I}, \text{Cl}$ ) Quantum Dots: Potential Alternatives for Display Technology. *ACS Nano* **2015**, *9* (4), 4533-4542. DOI: 10.1021/acsnano.5b01154 From NLM PubMed-not-MEDLINE.
- (147) Du, M.-H. Emission Trend of Multiple Self-Trapped Excitons in Luminescent 1D Copper Halides. *ACS Energy Letters* **2020**, *5* (2), 464-469. DOI: 10.1021/acsenerylett.9b02688.
- (148) Zhao, X.; Niu, G.; Zhu, J.; Yang, B.; Yuan, J.-H.; Li, S.; Gao, W.; Hu, Q.; Yin, L.; Xue, K.-H.; et al. All-Inorganic Copper Halide as Stable and Self-Absorption Free X-Ray Scintillator. *J. Phys. Chem. Lett.* **2020**, *11* (5), 1873-1880. DOI: 10.1021/acs.jpcclett.0c00161 From NLM Medline.
- (149) Seo, G.; Jung, H.; Creason, T. D.; Yeddu, V.; Bamidele, M.; Echeverria, E.; Lee, J.; McIlroy, D.; Saparov, B.; Kim, D. Y. Lead-Free Halide Light-Emitting Diodes with External Quantum Efficiency Exceeding 7% Using Host–Dopant Strategy. *ACS Energy Letters* **2021**, *6* (7), 2584-2593. DOI: 10.1021/acsenerylett.1c01117.
- (150) Ding, M.; Dong, B.; Lu, Y.; Yang, X.; Yuan, Y.; Bai, W.; Wu, S.; Ji, Z.; Lu, C.; Zhang, K.; et al. Energy Manipulation in Lanthanide-Doped Core-Shell Nanoparticles for Tunable Dual-Mode Luminescence toward Advanced Anti-Counterfeiting. *Adv Mater* **2020**, *32* (45), e2002121. DOI: 10.1002/adma.202002121 From NLM PubMed-not-MEDLINE.
- (151) Liu, Y.; Han, F.; Li, F.; Zhao, Y.; Chen, M.; Xu, Z.; Zheng, X.; Hu, H.; Yao, J.; Guo, T.; et al. Inkjet-printed unclonable quantum dot fluorescent anti-counterfeiting labels with artificial intelligence authentication. *Nature Communications* **2019**, *10* (1), 2409. DOI: 10.1038/s41467-019-10406-7 From NLM PubMed-not-MEDLINE.
- (152) Martins, D. T. A.-A. Compact ion-source based on superionic rubidium silver iodide ( $\text{RbAg}_4\text{I}_5$ ) solid electrolyte. 2013. Bradley, J. N.; Greene, P. D. Solids with high ionic conductivity in group 1 halide systems. *Transactions of the Faraday Society* **1967**, *63* (0), 424-430, 10.1039/TF9676300424. DOI: 10.1039/TF9676300424.
- (153) Zhang, M.; Wang, X.; Yang, B.; Zhu, J.; Niu, G.; Wu, H.; Yin, L.; Du, X.; Niu, M.; Ge, Y.; et al. Metal Halide Scintillators with Fast and Self-Absorption-Free Defect-Bound Excitonic Radioluminescence for Dynamic X-Ray Imaging. *Advanced Functional Materials* **2021**, *31* (9), 2007921, <https://doi.org/10.1002/adfm.202007921>. DOI: <https://doi.org/10.1002/adfm.202007921> (accessed 2021/03/25).
- (154) Zhang, Z.; Zhao, R.; Teng, S.; Huang, K.; Zhang, L.; Wang, D.; Yang, W.; Xie, R.; Pradhan, N. Color Tunable Self-Trapped Emissions from Lead-Free All Inorganic IA-IB Bimetallic Halides  $\text{Cs-Ag-X}$  ( $X = \text{Cl}, \text{Br}, \text{I}$ ). *Small* **2020**, *16* (44), 2004272, <https://doi.org/10.1002/sml.202004272>. DOI: <https://doi.org/10.1002/sml.202004272> (accessed 2021/04/02).
- (155) Bill, H.; Hollingsworth, G. J.; McClure, D. S.; Moine, B.; Pedrini, C. Optical spectroscopy of the  $\text{Ag}^+$  ion in  $\text{NaF}$ : Experimental results and analysis of manifestations of the Jahn–Teller effect. *J. Chem. Phys.* **1998**, *109* (17), 7328-7337. DOI: 10.1063/1.477362 (accessed 2021/03/03).

- (156) Yanagida, T. Inorganic scintillating materials and scintillation detectors. *Proc Jpn Acad Ser B Phys Biol Sci* **2018**, *94* (2), 75-97. DOI: 10.2183/pjab.94.007 From NLM PubMed.
- (157) Nikl, M.; Yoshikawa, A. Recent R&D Trends in Inorganic Single-Crystal Scintillator Materials for Radiation Detection. *Adv. Opt. Mat.* **2015**, *3* (4), 463-481. DOI: 10.1002/adom.201400571 (accessed 2020/02/19).
- (158) Bhaumik, S.; Bruno, A.; Mhaisalkar, S. Broadband emission from zero-dimensional Cs<sub>4</sub>PbI<sub>6</sub> perovskite nanocrystals. *RSC Advances* **2020**, *10* (23), 13431-13436, 10.1039/D0RA00467G. DOI: 10.1039/D0RA00467G From NLM PubMed-not-MEDLINE.
- Baranowski, M.; Plochocka, P. Excitons in Metal-Halide Perovskites. *Advanced Energy Materials* **2020**, *10* (26). DOI: 10.1002/aenm.201903659.
- (159) Bramble, S. K.; Creer, K. E.; Gui Qiang, W.; Sheard, B. Ultraviolet luminescence from latent fingerprints. *Forensic Science International* **1993**, *59* (1), 3-14. DOI: [https://doi.org/10.1016/0379-0738\(93\)90306-U](https://doi.org/10.1016/0379-0738(93)90306-U) From NLM Medline.
- (160) Huang, H.; Susha, A. S.; Kershaw, S. V.; Hung, T. F.; Rogach, A. L. Control of Emission Color of High Quantum Yield CH<sub>3</sub>NH<sub>3</sub>PbBr<sub>3</sub> Perovskite Quantum Dots by Precipitation Temperature. *Advanced Science* **2015**, *2* (9), 1500194. DOI: 10.1002/advs.201500194 From NLM PubMed-not-MEDLINE.
- (161) Sun, C.; Guo, Y.-H.; Yuan, Y.; Chu, W.-X.; He, W.-L.; Che, H.-X.; Jing, Z.-H.; Yue, C.-Y.; Lei, X.-W. Broadband White-Light Emission in One-Dimensional Organic-Inorganic Hybrid Silver Halide. *Inorg. Chem.* **2020**, *59* (7), 4311-4319. DOI: 10.1021/acs.inorgchem.9b03139 From NLM PubMed-not-MEDLINE.
- (162) Thackeray, M. M.; Coetzer, J. Dipotassium silver triiodide. *Acta Crystallographica Section B Structural Crystallography and Crystal Chemistry* **1975**, *31* (9), 2339-2340. DOI: 10.1107/s0567740875007510.
- (163) Trivelli, A. P. H.; Sheppard, S. E. On the Visible Decomposition of Silver Halide Grains by Light. *J. Phys. Chem.* **1925**, *29* (12), 1568-1582. DOI: 10.1021/j150258a009.
- (164) Gao, W.; Niu, G.; Yin, L.; Yang, B.; Yuan, J.-H.; Zhang, D.; Xue, K.-H.; Miao, X.; Hu, Q.; Du, X.; et al. One-Dimensional All-Inorganic K<sub>2</sub>CuBr<sub>3</sub> with Violet Emission as Efficient X-ray Scintillators. *ACS Applied Electronic Materials* **2020**, *2* (7), 2242-2249. DOI: 10.1021/acsaelm.0c00414.
- (165) Fattal, H.; Creason, T. D.; Delzer, C. J.; Yangui, A.; Hayward, J. P.; Ross, B. J.; Du, M.-H.; Glatzhofer, D. T.; Saporov, B. Zero-Dimensional Hybrid Organic-Inorganic Indium Bromide with Blue Emission. *Inorg. Chem.* **2021**, *60* (2), 1045-1054. DOI: 10.1021/acs.inorgchem.0c03164 From NLM PubMed-not-MEDLINE.

## Appendix: Supplemental Figures and Tables

### A1.1 Chapter 2 Figures and Tables

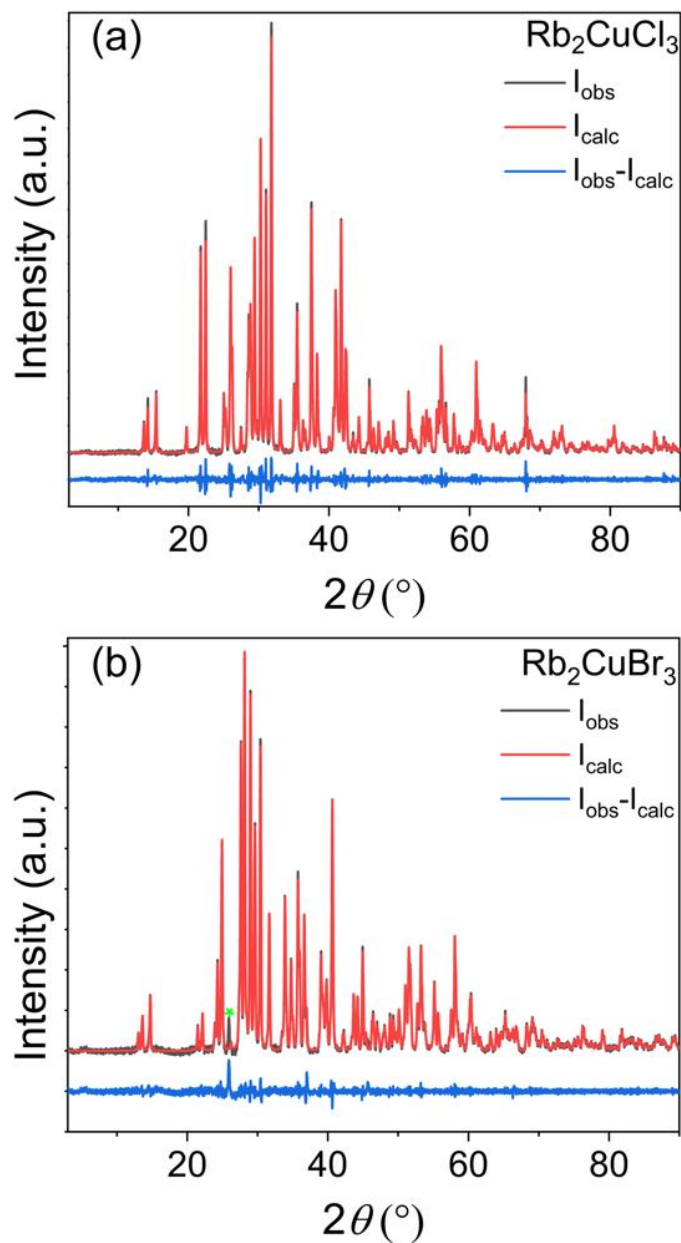


**Figure A1.** Room temperature PXRD patterns (black) for (a) Rb<sub>2</sub>CuCl<sub>3</sub> and (b) Rb<sub>2</sub>CuBr<sub>3</sub> refined using the Pawley method. Difference maps between the measured and calculated patterns are shown in blue. The presence of an impurity peak (green asterisk) belonging to RbBr is noticeable for Rb<sub>2</sub>CuBr<sub>3</sub>.



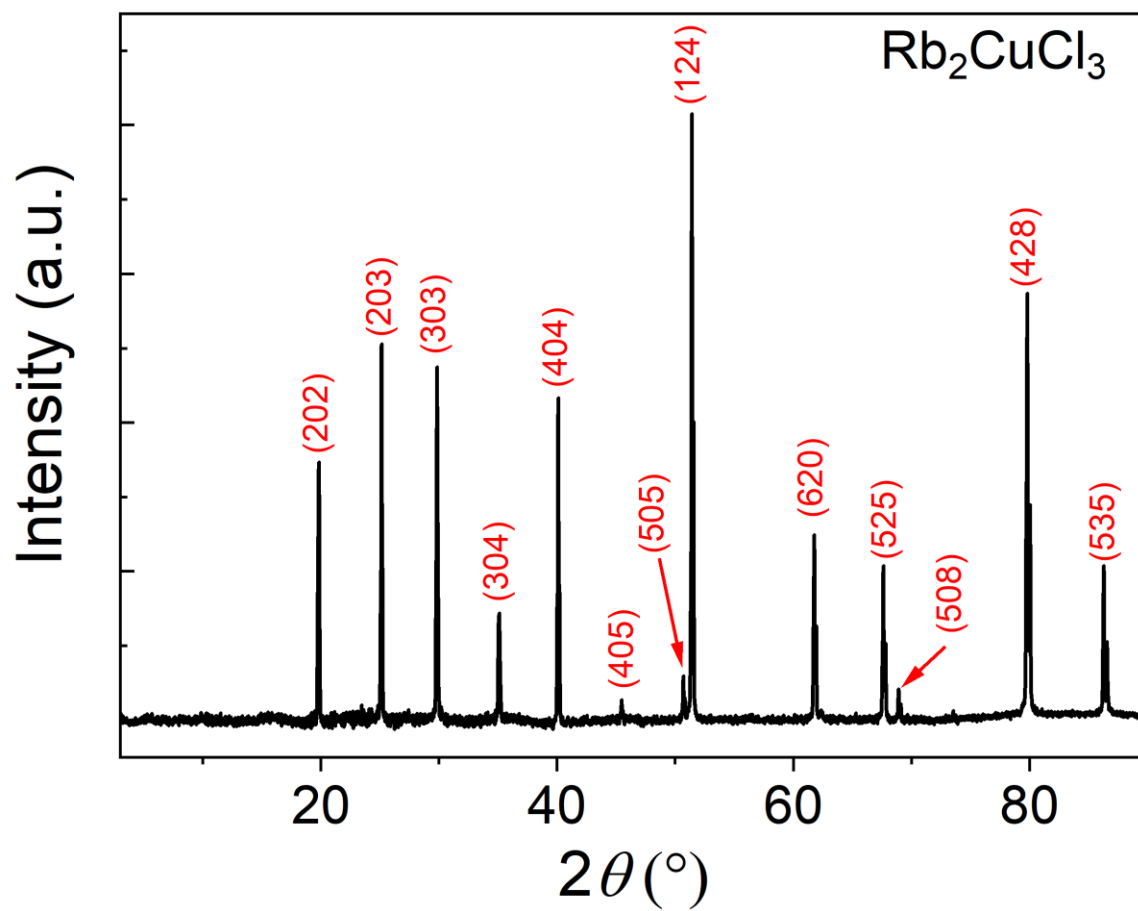


**Figure A2.** A room temperature PXRD pattern of a single crystal of  $\text{Rb}_2\text{CuCl}_3$ .<sup>28</sup>

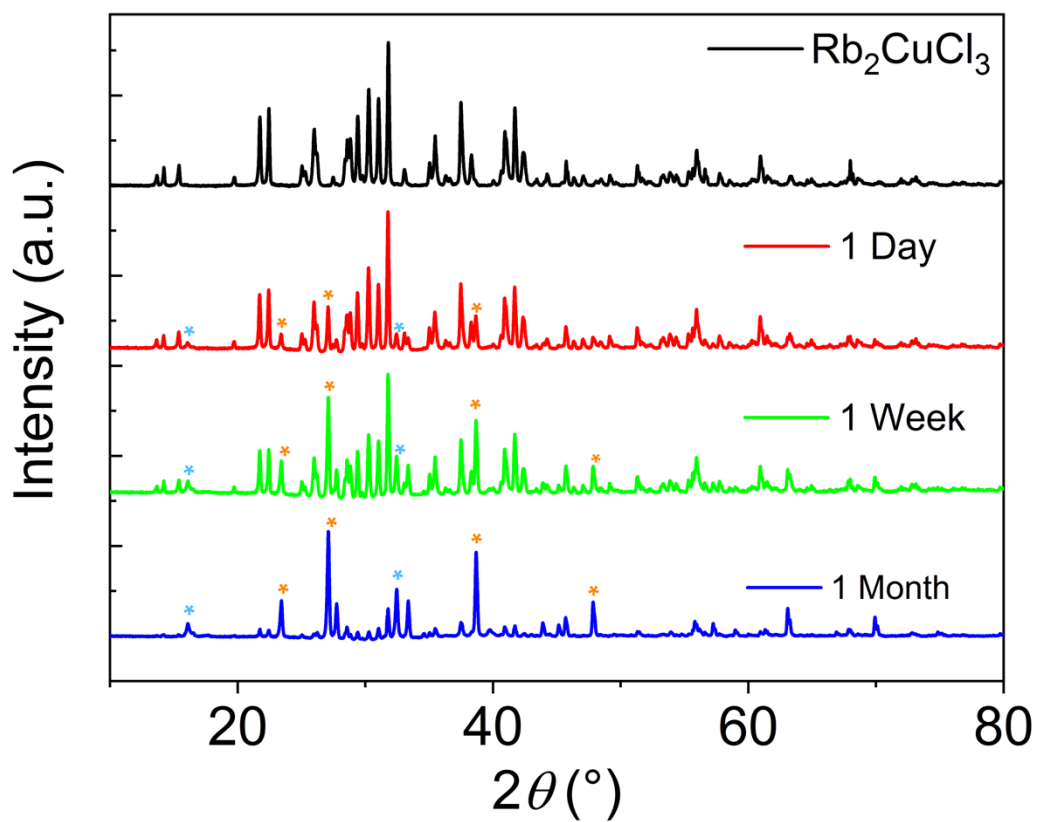


**Figure A3.** PXR D patterns of a polycrystalline powder sample of  $\text{Rb}_2\text{CuCl}_3$  measured over a period of 1-2 months. Orange and blue asterisks represent impurity peaks of  $\text{RbCl}$  and  $\text{Rb}_2\text{CuCl}_4 \cdot 2\text{H}_2\text{O}$ , respectively.

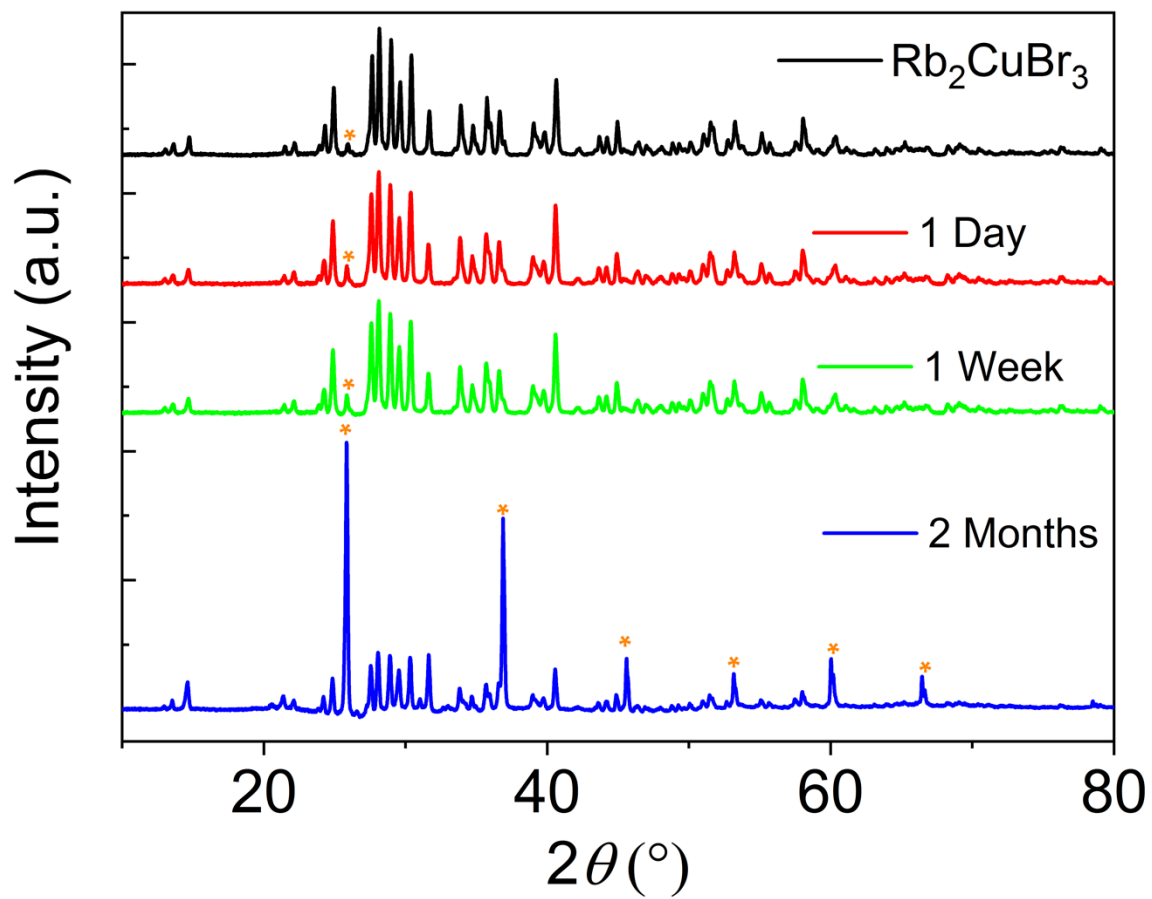


**Figure A4.** PXRD patterns of a powder sample of  $\text{Rb}_2\text{CuBr}_3$  measured over a period of 1-2 months. Orange asterisks represent RbBr impurity peaks.

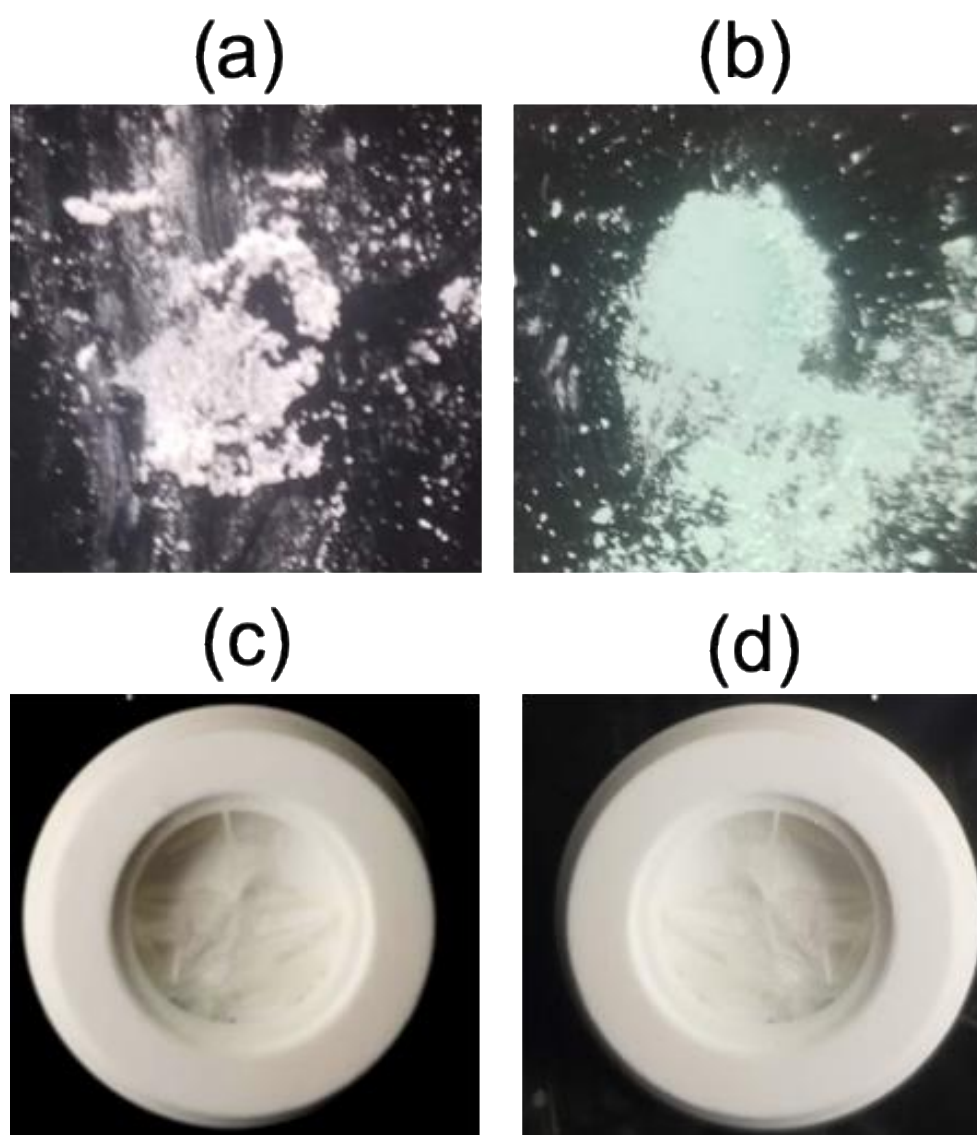


**Figure A5.** (a) A fresh white polycrystalline powder sample of  $\text{Rb}_2\text{CuCl}_3$  degrades in ambient air as is evident from the green color of (b) the air-exposed sample due to Cu(I) oxidation. In contrast, (c) single crystals of  $\text{Rb}_2\text{CuCl}_3$  do not show any noticeable degradation in air (d) after exposure to ambient air for days.

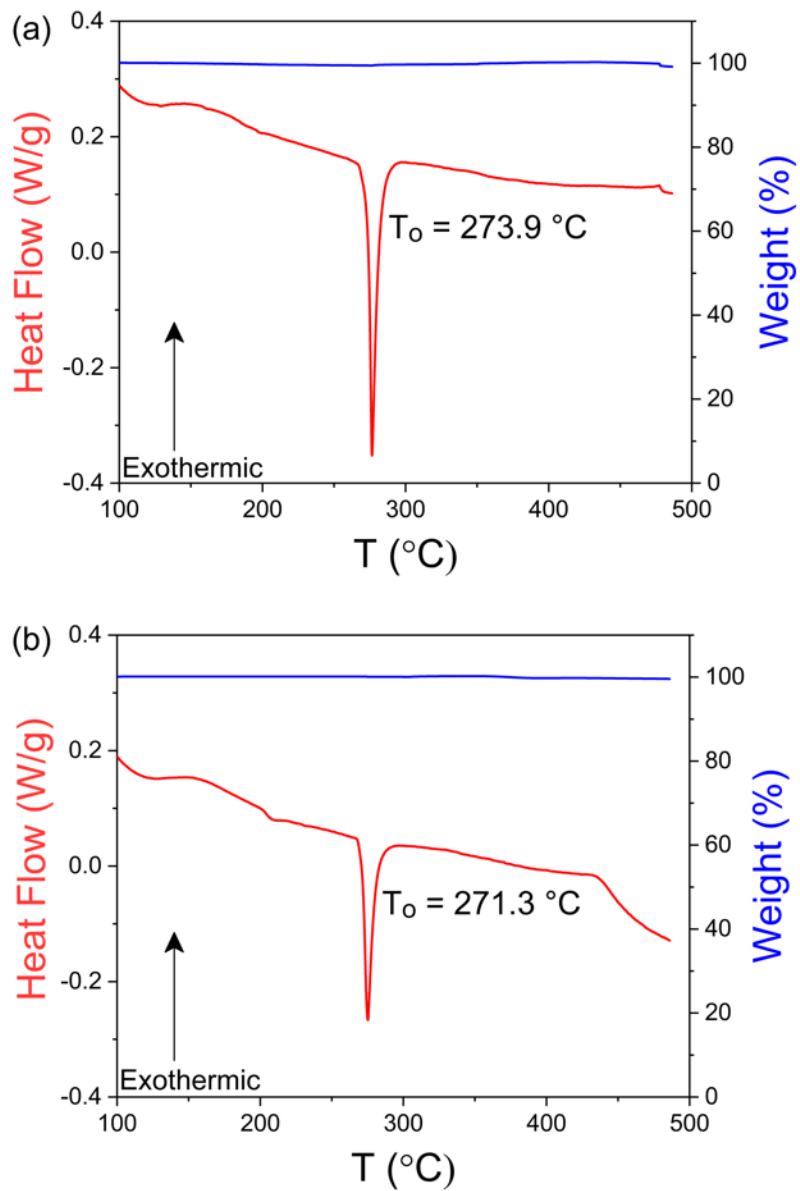


**Figure A6.** Thermogravimetric analysis (TGA, in blue) and differential scanning calorimetry (DSC, in red) plots for (a)  $\text{Rb}_2\text{CuCl}_3$  and (b)  $\text{Rb}_2\text{CuBr}_3$ .

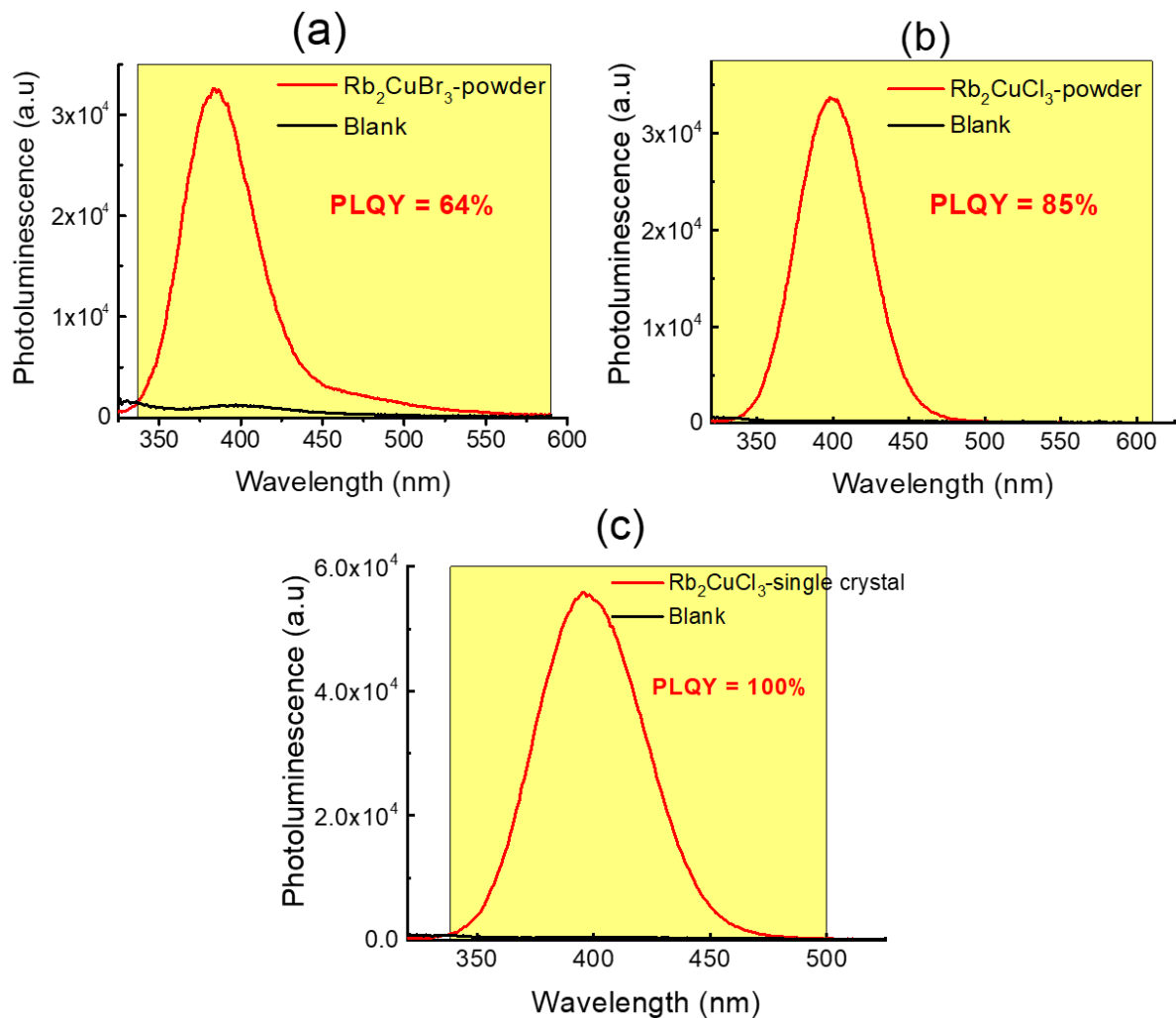


**Figure A7.** Room temperature PLQY measurements for (a) powder of  $\text{Rb}_2\text{CuBr}_3$  and (b) powder and (c) single crystal samples of  $\text{Rb}_2\text{CuCl}_3$ , under 300nm UV excitation.

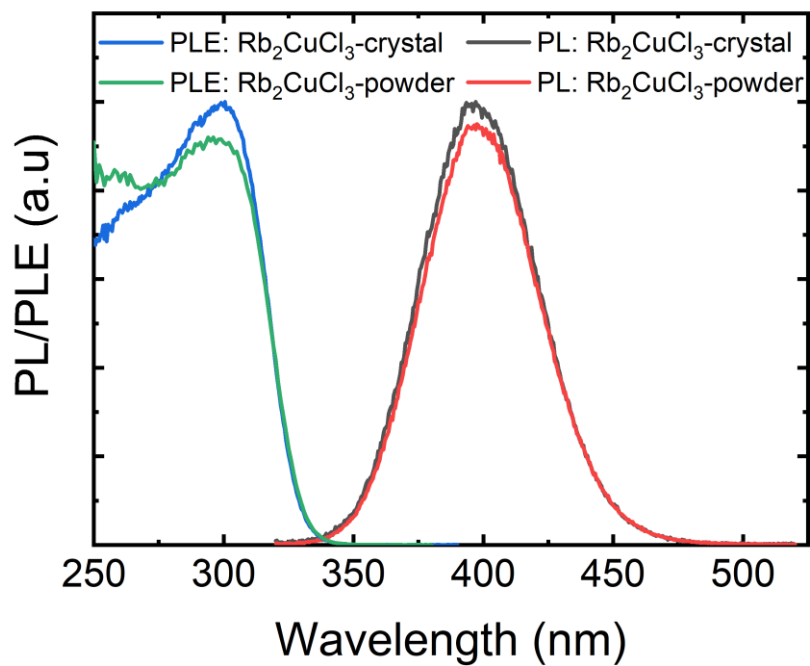


**Figure A8.** Room temperature PL ( $\lambda_{\text{ex}} = 300 \text{ nm}$ ) and PLE ( $\lambda_{\text{em}} = 398 \text{ nm}$ ) spectra of single crystal and powder samples of  $\text{Rb}_2\text{CuCl}_3$ .

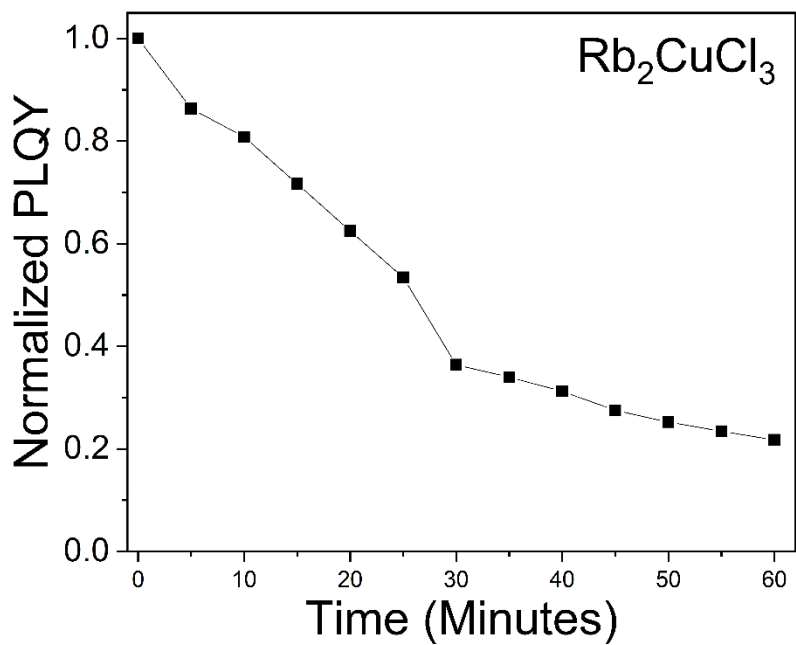


**Figure A9.** Periodic measurements of PLQY under continuous irradiation of  $\text{Rb}_2\text{CuCl}_3$  at its  $\text{PLE}_{\text{max}}$ .



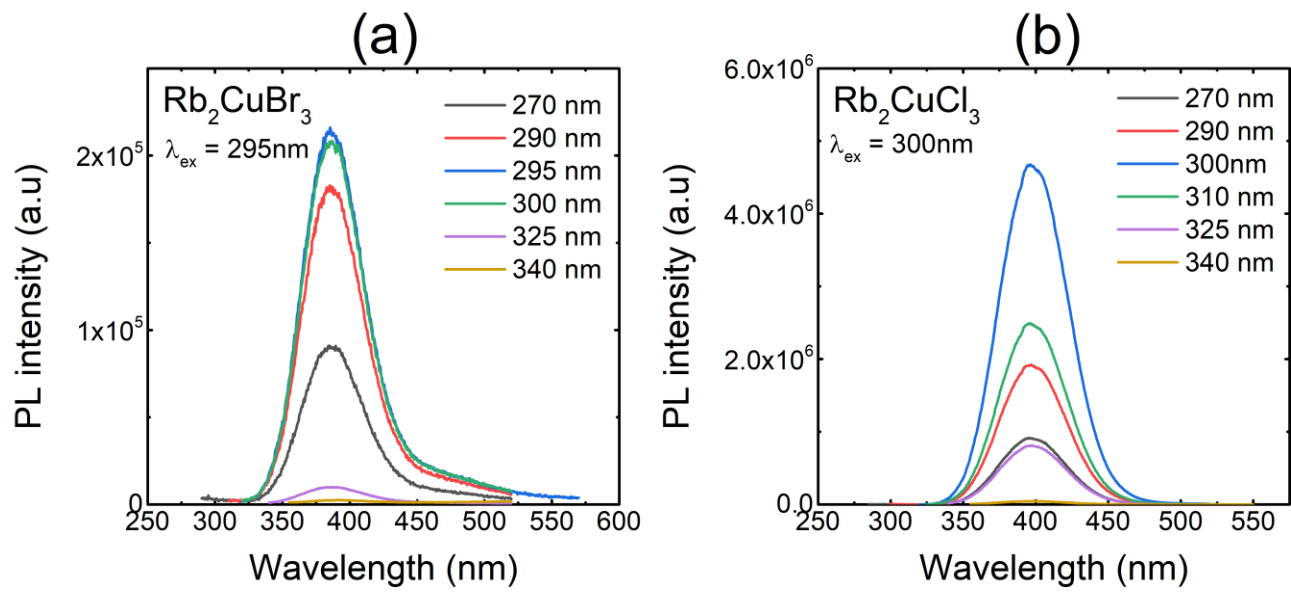


**Figure A10.** Excitation dependence PL measurements for (a)  $\text{Rb}_2\text{CuBr}_3$  and (b)  $\text{Rb}_2\text{CuCl}_3$ .

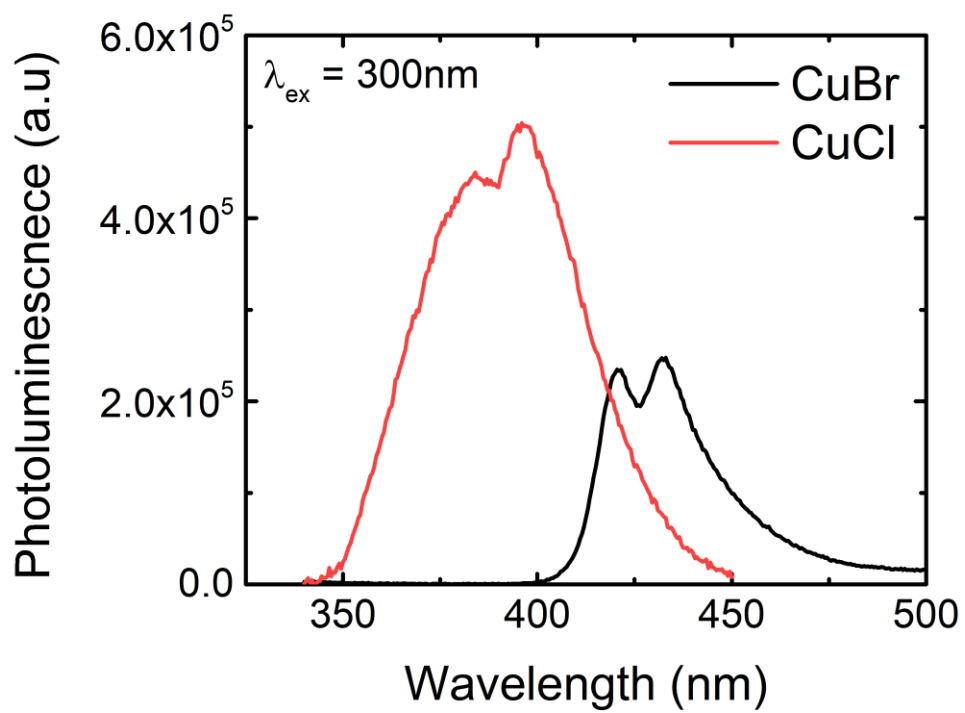


**Figure A11.** Room temperature PL spectra for (a) CuBr and (b) CuCl under 295 nm excitation.

**Table A1.** Atomic coordinates and equivalent isotropic displacement parameters ( $U_{\text{eq}}^a$ ) for  $\text{K}_2\text{CuCl}_3$  and  $\text{K}_2\text{CuBr}_3$ .

Atom	x	y	z	$U_{\text{eq}}, \text{\AA}^2$
<hr/> $\text{K}_2\text{CuCl}_3$ <hr/>				
K1	0.82716(3)	0.250000	0.48236(3)	0.01028(6)
K2	0.48778(3)	0.250000	0.67425(3)	0.01011(6)
Cu	0.75408(2)	0.750000	0.69905(2)	0.01139(5)
Cl1	0.63409(3)	0.750000	0.55196(3)	0.00982(7)
Cl2	0.72323(3)	0.250000	0.79223(3)	0.00917(7)
Cl3	0.94091(3)	0.750000	0.64054(3)	0.00989(7)
 <hr/> $\text{K}_2\text{CuBr}_3$ <hr/>				
K1	0.17576(9)	0.250000	0.48432(8)	0.0140(2)
K2	0.51318(9)	0.250000	0.67681(8)	0.0138(2)
Cu	0.24555(5)	0.750000	0.69721(5)	0.01465(14)
Br1	0.36891(4)	0.750000	0.55239(4)	0.01229(12)
Br2	0.05805(4)	0.750000	0.63876(4)	0.01260(12)
Br3	0.27719(4)	1.250000	0.79305(4)	0.01170(11)

<sup>a</sup> $U_{\text{eq}}$  is defined as one-third of the trace of the orthogonalized  $U_{ij}$  tensor.

**Table A2.** A comparison of bond distances and angles within the 1D  $\infty[\text{CuX}_3]^{2-}$  chains in  $\text{Rb}_2\text{CuCl}_3$ ,  $\text{K}_2\text{CuCl}_3$  and  $\text{K}_2\text{CuBr}_3$ .<sup>111</sup>

Atom pair	Distance (Å)	Label	Angle (°)
<b>Rb<sub>2</sub>CuCl<sub>3</sub></b>			
Cu – Cl1 (×2)	2.4243(3)	Cl1-Cu-Cl2	106.160(17)
Cu – Cl2	2.3363(6)	Cl1-Cu-Cl3	106.471(16)
Cu – Cl3	2.3480(7)	Cl2-Cu-Cl3	111.58(2)
<b>K<sub>2</sub>CuCl<sub>3</sub></b>			
Cu – Cl1	2.3319(4)	Cl1-Cu-Cl2	106.853(11)
Cu – Cl2 (×2)	2.3916(2)	Cl1-Cu-Cl3	109.736(16)
Cu – Cl3	2.3475(4)	Cl2-Cu-Cl3	107.357(11)
<b>K<sub>2</sub>CuBr<sub>3</sub></b>			
Cu – Br1	2.4529(8)	Br1-Cu-Br2	110.83(3)
Cu – Br2	2.4688(9)	Br1-Cu-Br3	106.86(2)
Cu – Br3 (×2)	2.5215(4)	Br2-Cu-Br3	107.77(2)

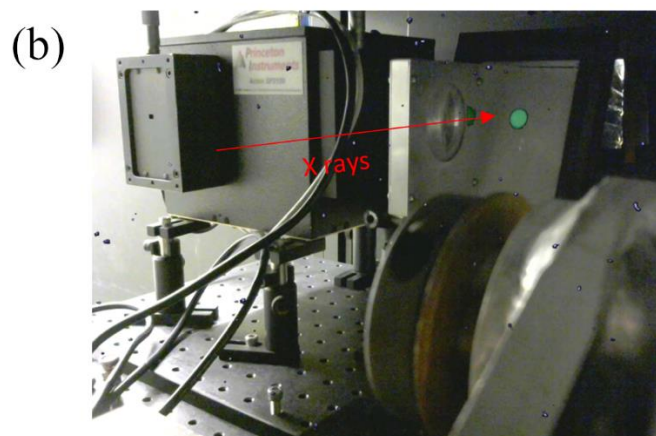
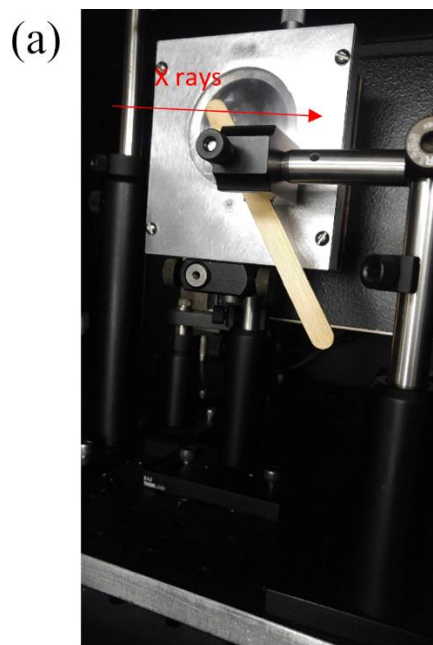


**Figure A12.** UV-VIS spectrometer and sample in the irradiation cabinet. The direction of X rays is indicated by the arrows. (a) Wooden stick holding sample (hidden between stick and spectrometer) mounted in the beam in front of the spectrometer. (b) Downstream view of apparatus with no sample present. The green circle is the image of the beam on a gadolinium oxysulfide scintillator screen; the beam diameter is 1 cm. The bright flecks scattered throughout the image are caused by direct conversion of X rays in the camera's CCD chip.

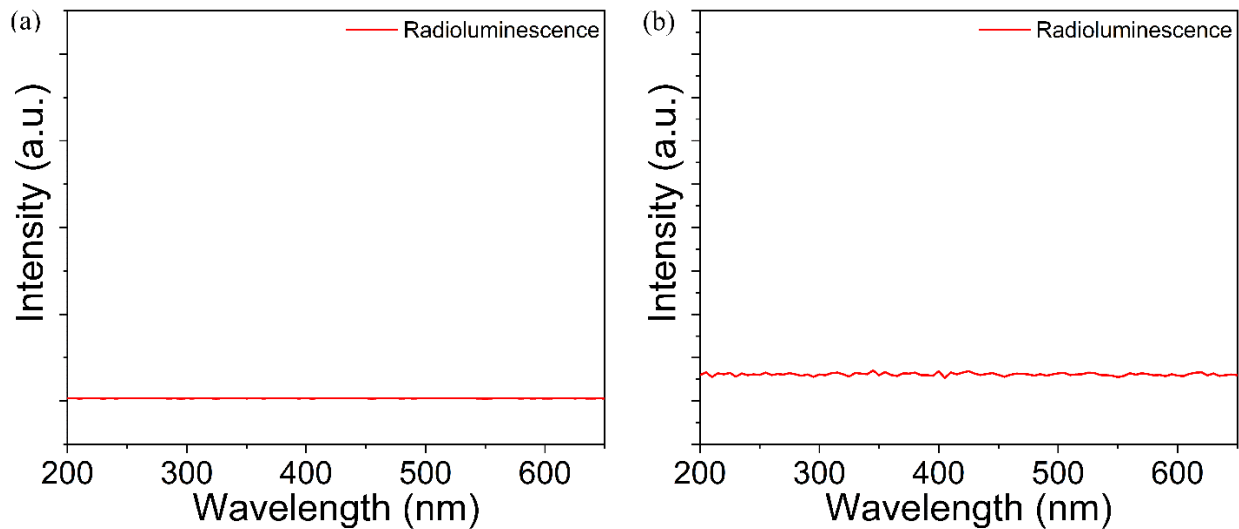


**Figure A13.** (a) Radioluminescence spectrum of a wooden stick coated with BC-630 optical grease using the same vertical scale as Figure 3d and (b) at a magnification of the vertical scale by a factor of 10. There is no luminescence of the grease/stick combination, confirming that the 404 nm emission (Figure 3d) comes from the sample.

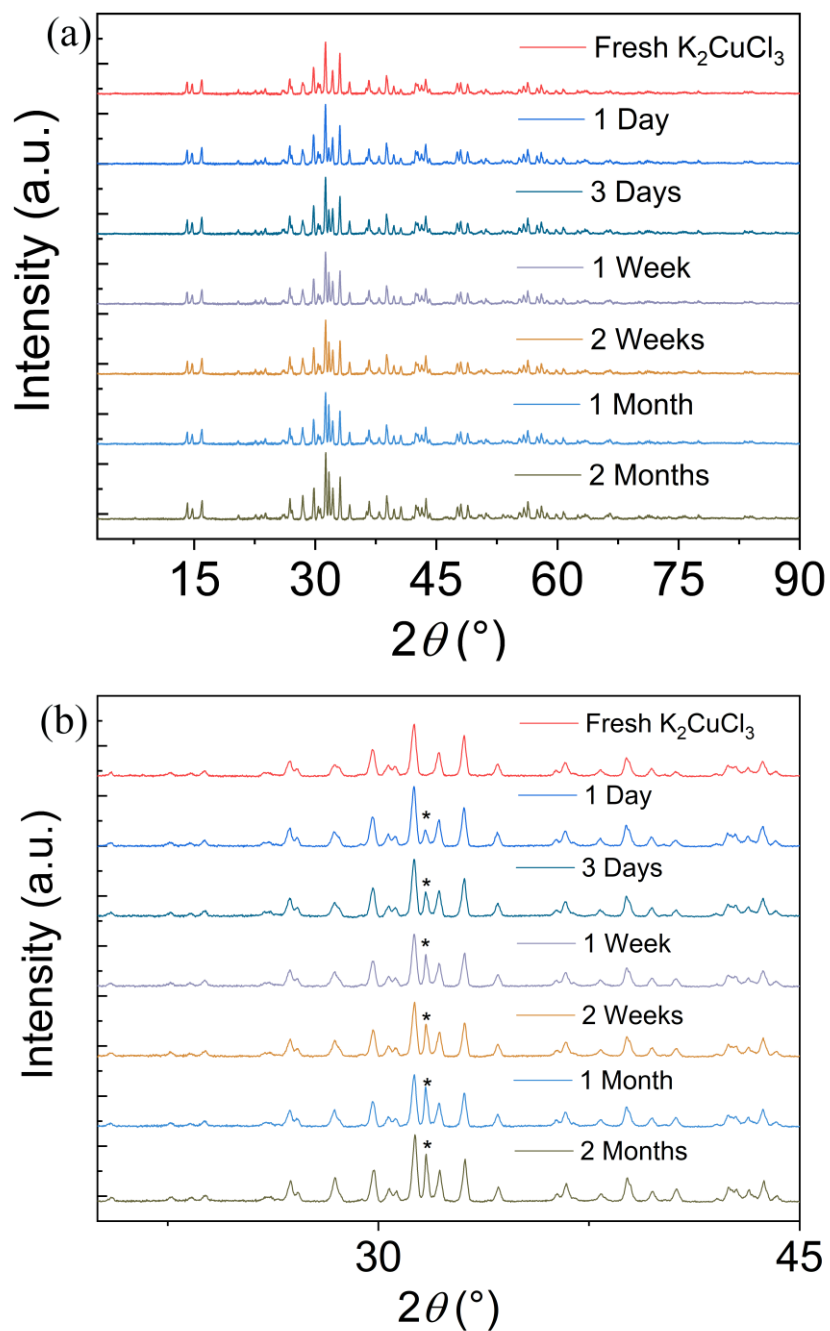


**Figure A14.** (a) PXR D patterns of  $K_2CuCl_3$  prepared using the solid-state synthesis technique. (b) When left in ambient air for a period of 2 months, evolution of a single impurity peak attributed to  $KCuO$  (marked with a black asterisk) was observed.

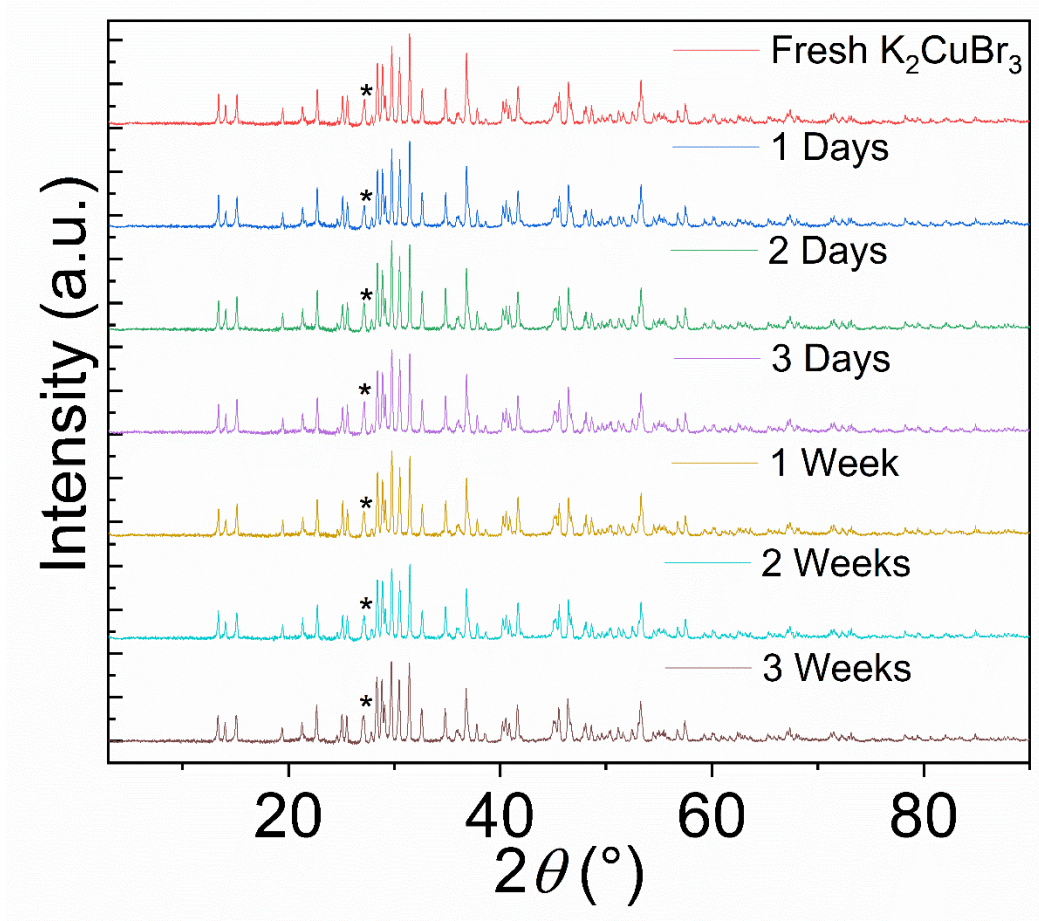


**Figure A15.** PXRD patterns of  $Rb_2CuBr_3$  synthesized using the solid-state method. Black asterisks represent the  $CuBr$  impurity peaks. No measurable change was observed for the  $K_2CuBr_3$  sample left in air for over 3 weeks.



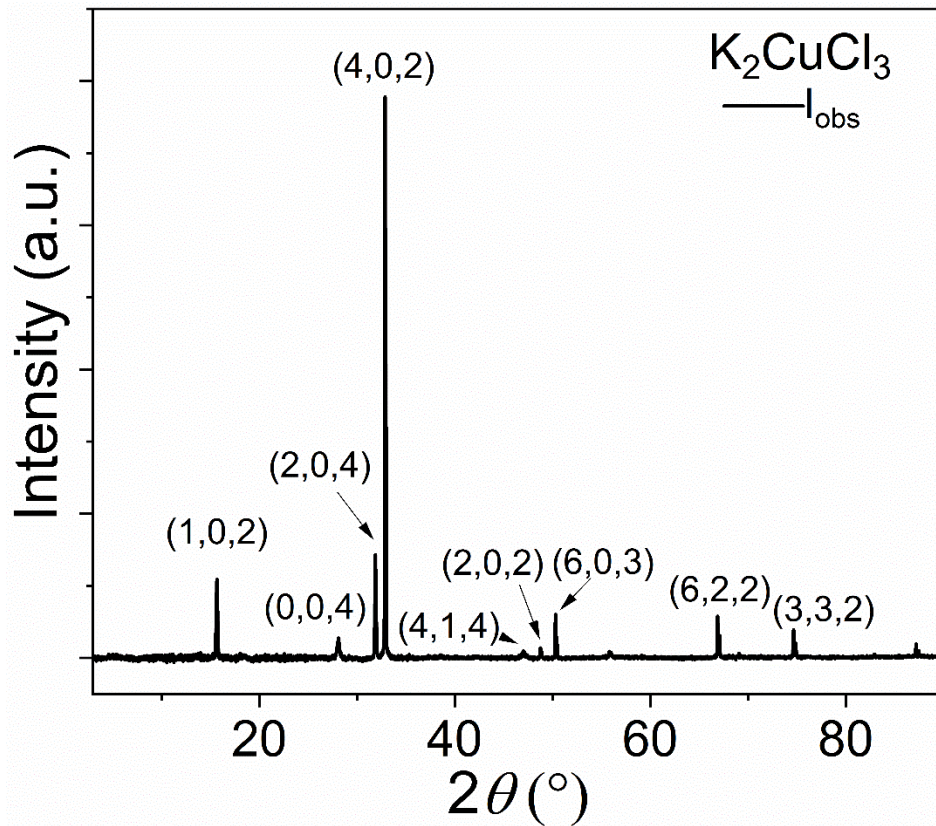


**Figure A16.** An indexed room temperature PXRD pattern of a single crystal grown from slow evaporation of  $K_2CuCl_3$ .

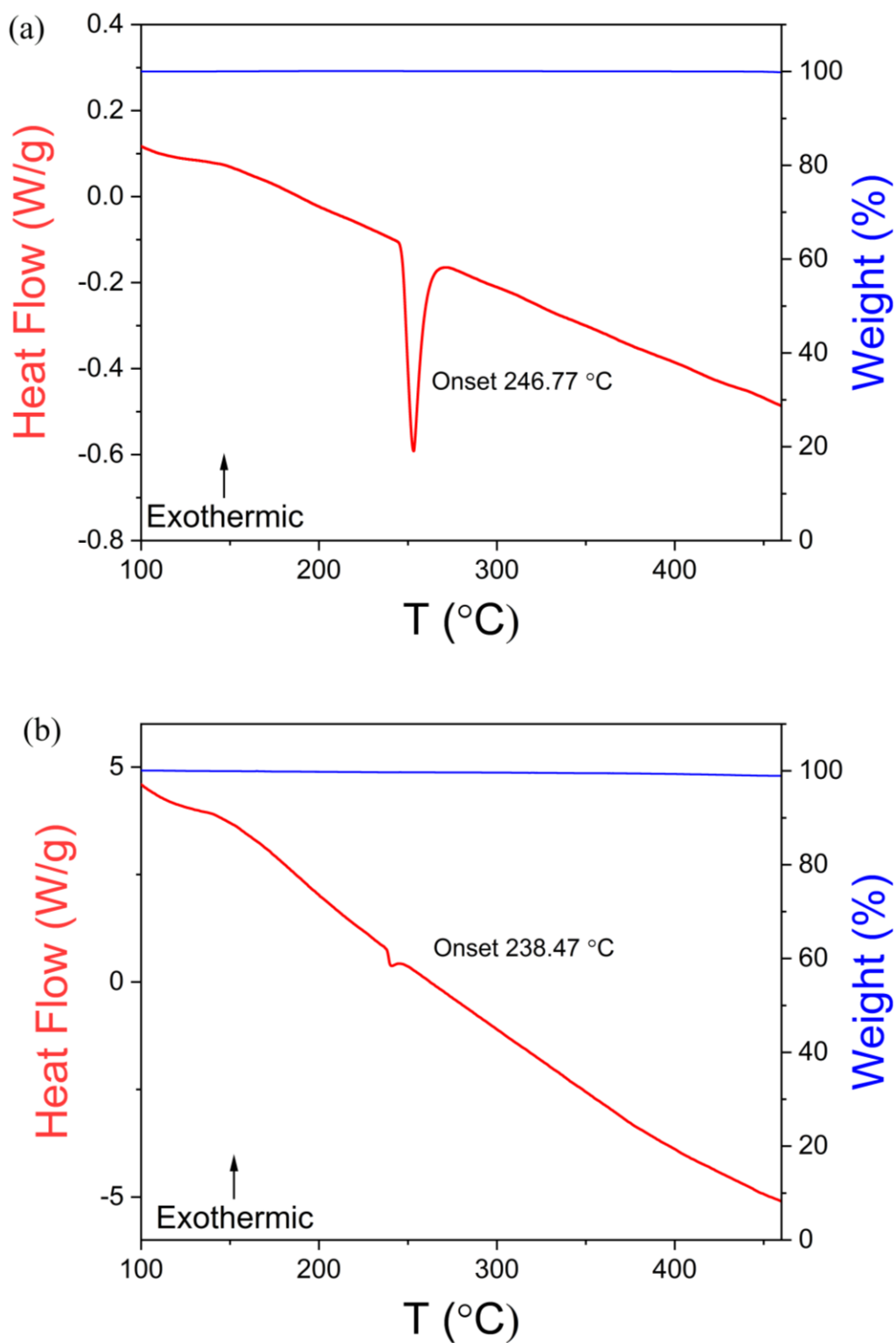


**Figure A17.** Thermogravimetric analysis (TGA, in blue) and differential scanning calorimetry (DSC, in red) plots for (a)  $K_2CuCl_3$  and (b)  $K_2CuBr_3$ .

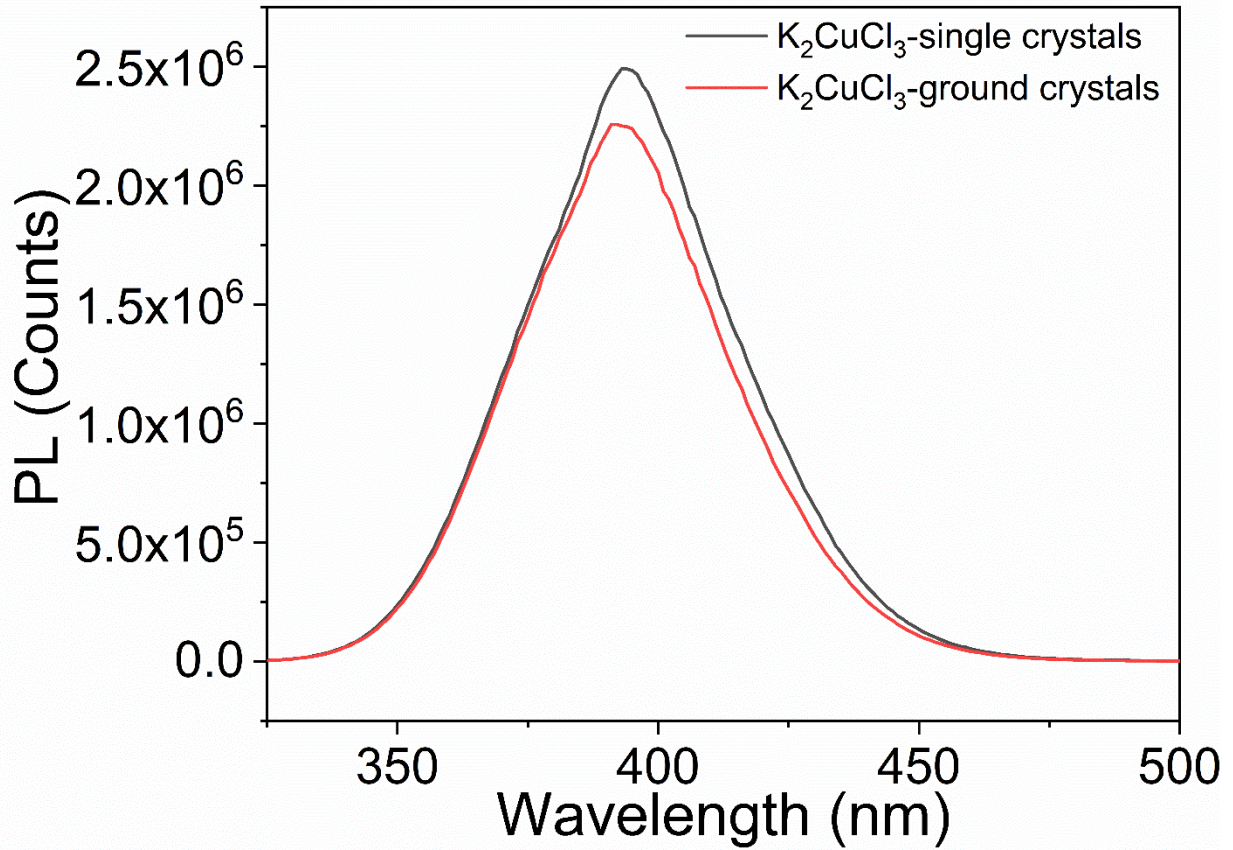


**Figure A18.** Room temperature PL ( $\lambda_{\text{ex}} = 291$  nm) spectra of a single crystal and powder samples of  $K_2CuCl_3$ .

## A1.2 Chapter 3 Figures and Tables

**Table A3.** Summary of the time-resolved photoluminescence (TRPL) refinement parameters for exponential fitting of TRPL spectra of  $A_2AgX_3$ .

Parameter	$Rb_2AgCl_3$	$Rb_2AgBr_3$	$Rb_2AgI_3$	$Cs_2AgBr_3$	$Cs_2AgBr_3$
$A_1$ (Cnts)	45.57	24.52	28.64	48.45	83.61
$\tau_1$ ( $\mu$ s)	0.05 $\mu$ s	0.11 $\mu$ s	0.16 $\mu$ s	19.79 $\mu$ s	13.81 $\mu$ s
$A_2$ (Cnts)	54.43	75.48	71.36	51.55	25.44
$\tau_2$ ( $\mu$ s)	0.65 $\mu$ s	0.80 $\mu$ s	1.2 $\mu$ s	68.86 $\mu$ s	16.39 $\mu$ s
Average lifetime	0.62 $\mu$ s	0.77 $\mu$ s	1.15 $\mu$ s	58.82 $\mu$ s	14.87 $\mu$ s

**Table A4.** Direct band gaps (in eV) at the  $\Gamma$  point of  $\text{Rb}_2\text{AgCl}_3$ ,  $\text{Rb}_2\text{AgBr}_3$ , and  $\text{Rb}_2\text{AgI}_3$ , respectively, obtained by PBE and PBE0 calculations.

<b>Compound</b>	<b><math>\text{Rb}_2\text{AgCl}_3</math></b>	<b><math>\text{Rb}_2\text{AgBr}_3</math></b>	<b><math>\text{Rb}_2\text{AgI}_3</math></b>
<b>PBE Band Gap</b>	2.91 eV	2.68 eV	2.60 eV
<b>PBE0 Band Gap</b>	5.55 eV	5.10 eV	4.81 eV

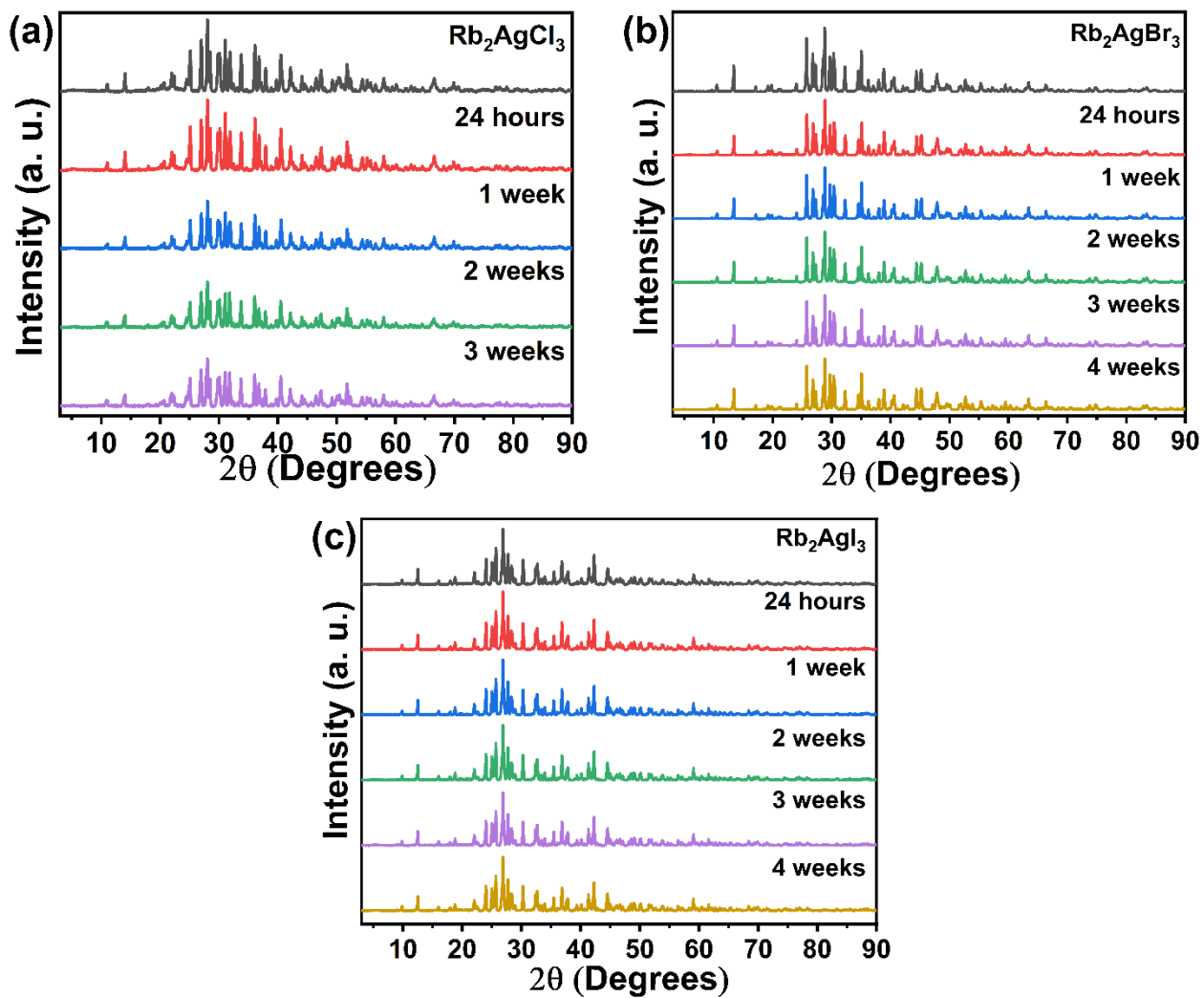


**Figure A19.** The room temperature PXRD patterns of (a)  $\text{Rb}_2\text{AgCl}_3$ , (b)  $\text{Rb}_2\text{AgBr}_3$ , and (c)  $\text{Rb}_2\text{AgI}_3$ , left in ambient air for a period of up to four weeks.

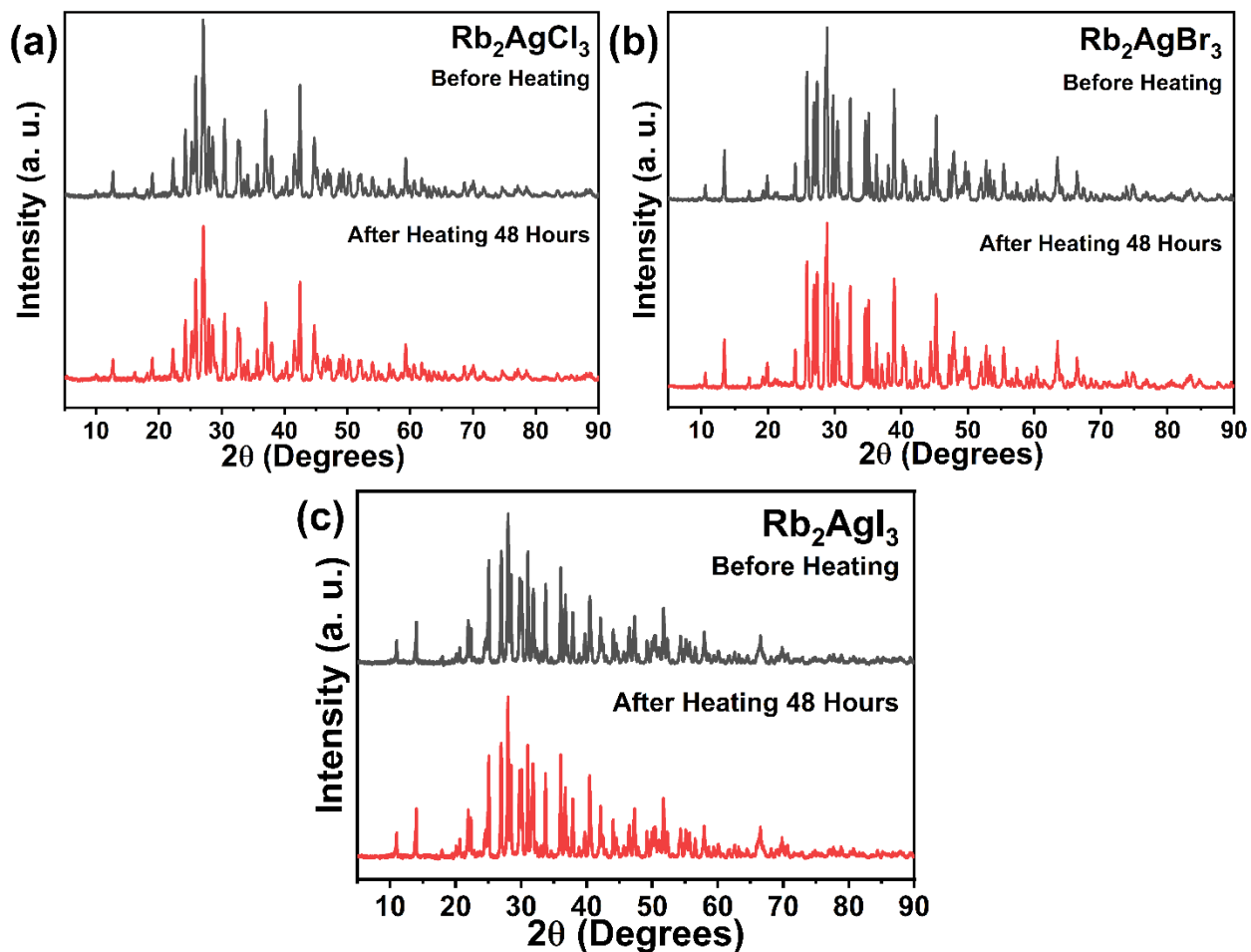


**Figure A20.** (a)  $\text{Rb}_2\text{AgCl}_3$ , (b)  $\text{Rb}_2\text{AgBr}_3$  and (c)  $\text{Rb}_2\text{AgI}_3$  demonstrate improved thermal stability as evidenced by the PXRD patterns before and after heating at 100°C for 48 hours.

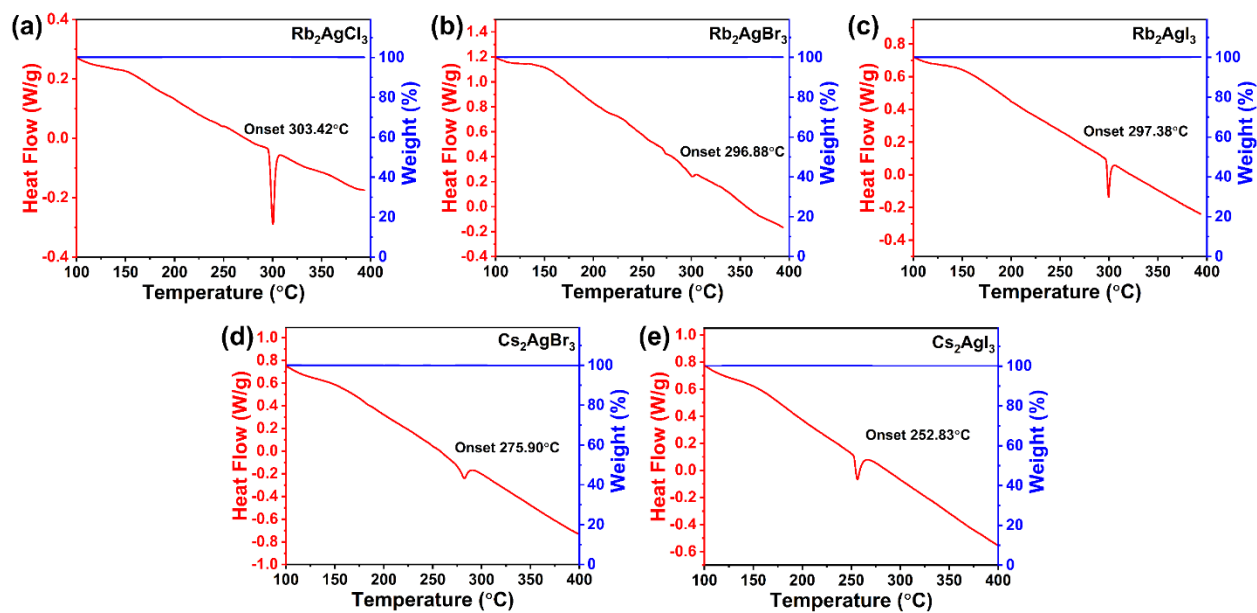


**Figure A21.** Thermogravimetric analysis (TGA, blue) and differential scanning calorimetry (DSC, red) plots for  $\text{A}_2\text{AgX}_3$  (A = Rb, Cs; X = Cl, Br, I).



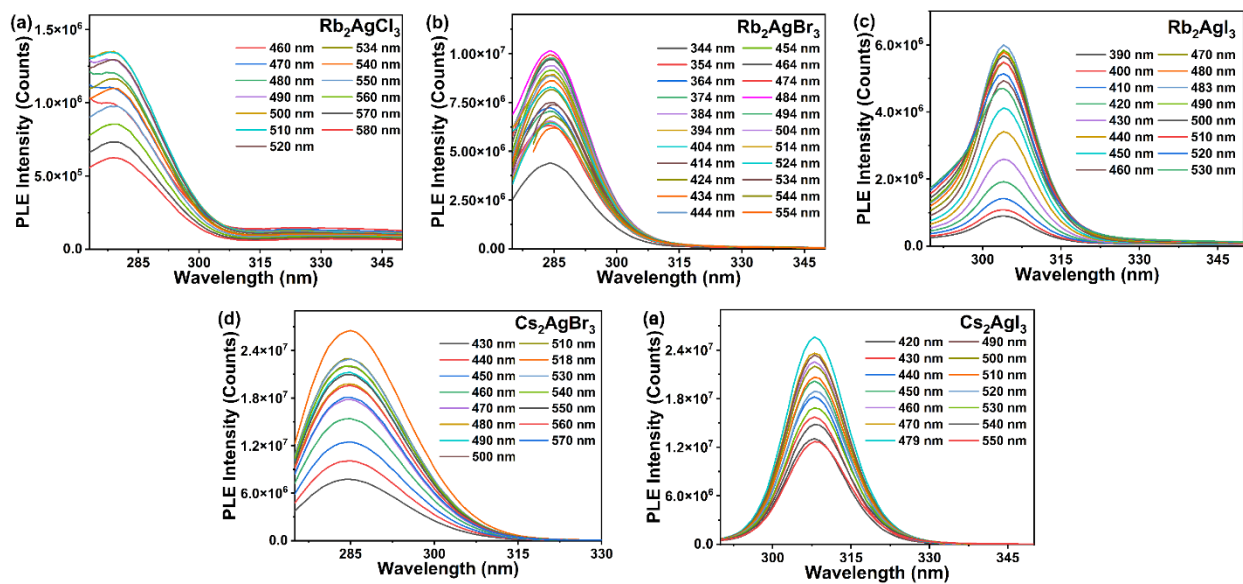


**Figure A22.** Emission-dependent PLE measurements for (a)  $\text{Rb}_2\text{AgCl}_3$ , (b)  $\text{Rb}_2\text{AgBr}_3$ , (c)  $\text{Rb}_2\text{AgI}_3$ , (d)  $\text{Cs}_2\text{AgBr}_3$ , and (e)  $\text{Cs}_2\text{AgI}_3$ .

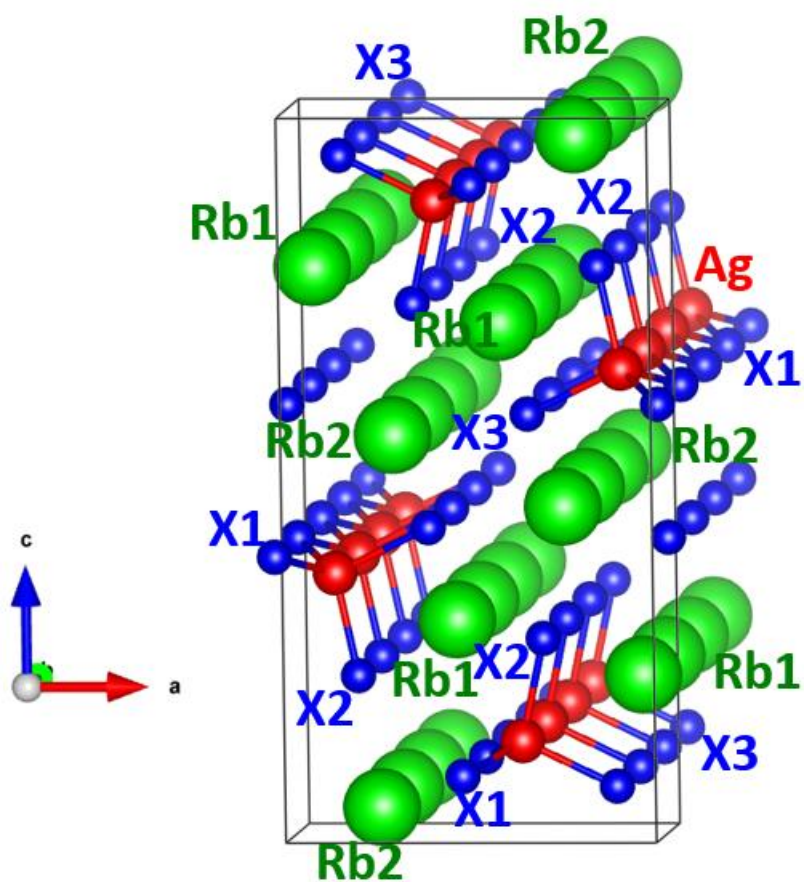


**Figure A23.** Vacancy sites that trap the defect-bound excitons (DBEs) in the  $\text{Rb}_2\text{AgX}_3$  family.

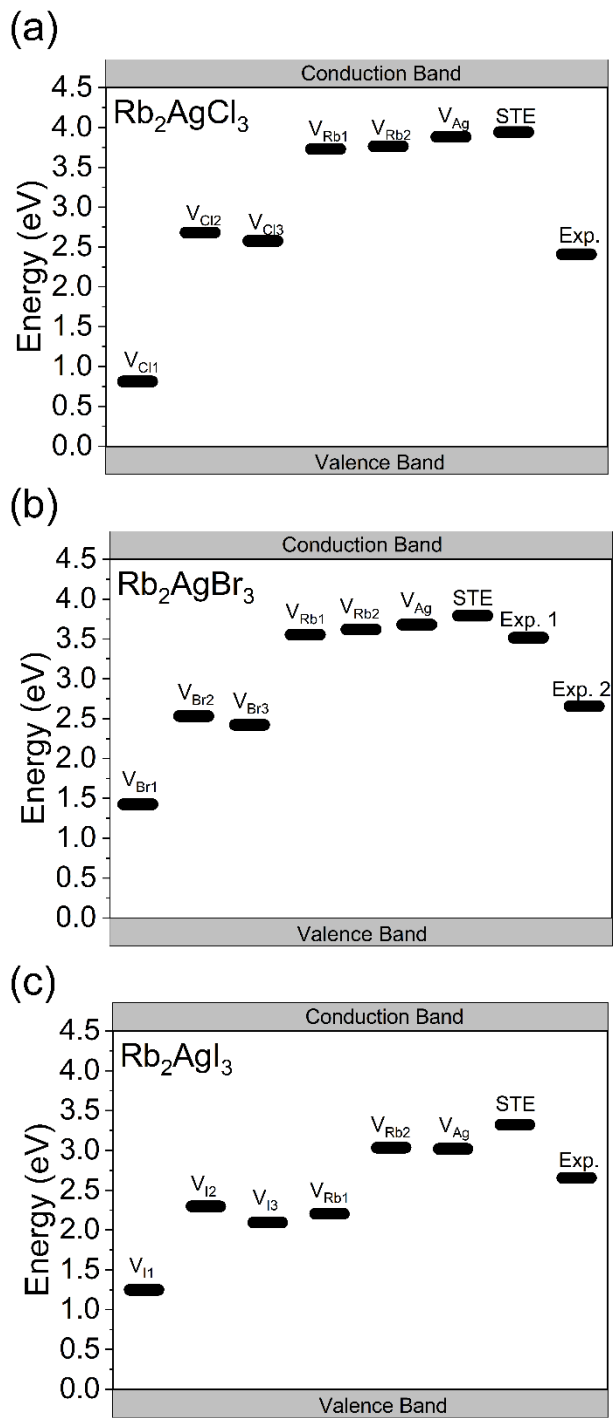


**Figure A24.** A comparison of the calculated energy levels of vacancies and self-trapped excitons (STE) and experimentally determined transition levels (Exp.) in  $\text{Rb}_2\text{AgX}_3$ .

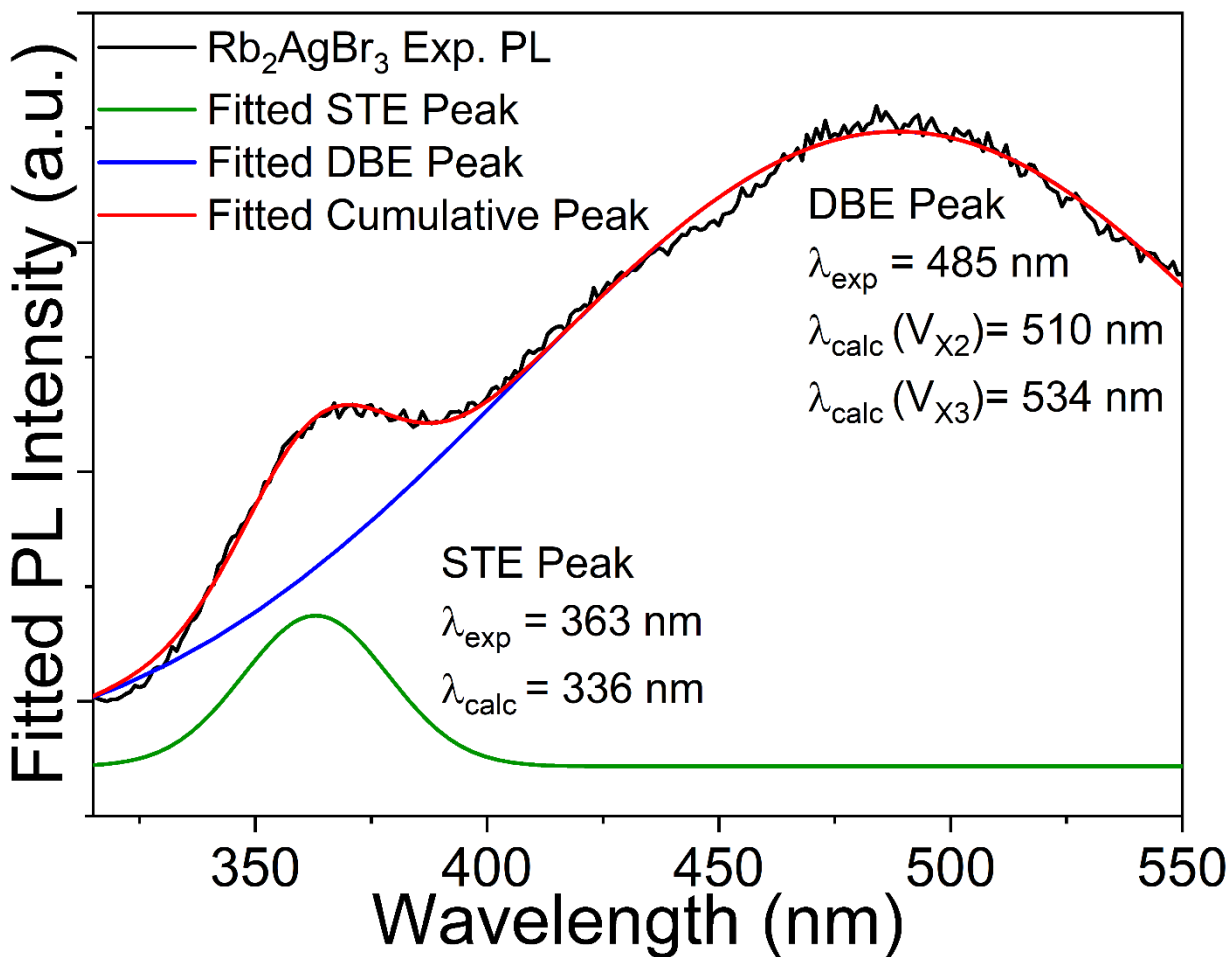


**Figure A25.** The PL spectrum of Rb<sub>2</sub>AgBr<sub>3</sub> includes a narrower higher peak attributed to self-trapped exciton (STE) emission and a lower energy broad peak attributed to defect-bound excitons (DBE) located on halogen vacancies. The calculation STE and DBE emission energies are provided for comparison.

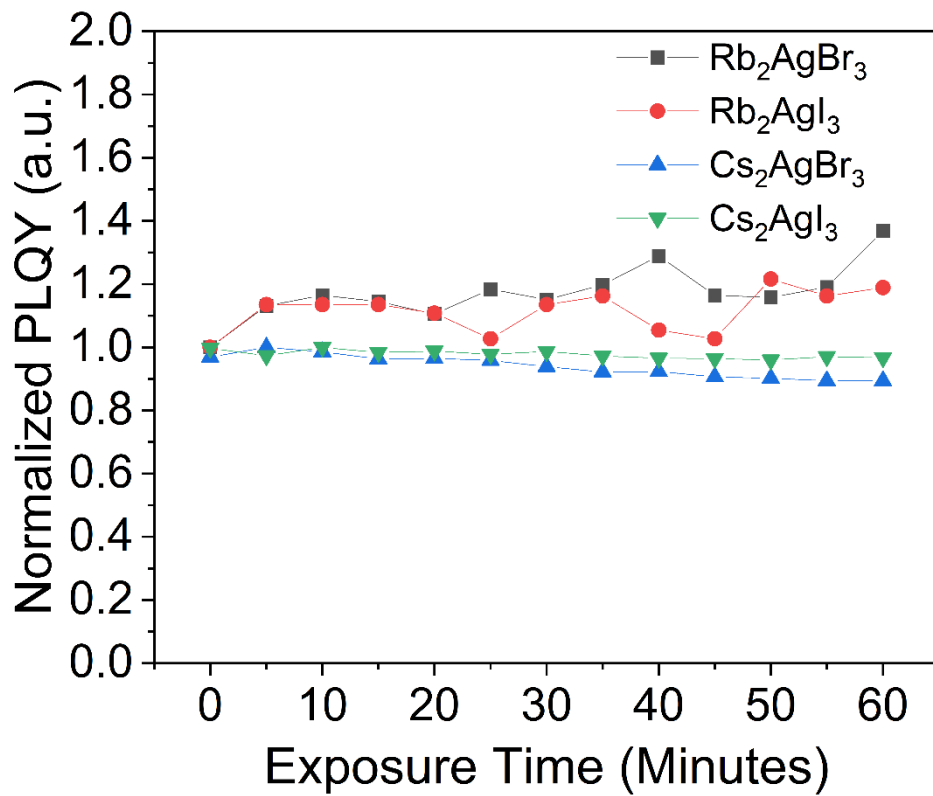


**Figure A26.** Comparison of the normalized photoluminescence quantum yields (PLQYs) of Rb<sub>2</sub>AgBr<sub>3</sub>, Rb<sub>2</sub>AgI<sub>3</sub>, and Cs<sub>2</sub>AgBr<sub>3</sub> and Cs<sub>2</sub>AgI<sub>3</sub> under continuous UV irradiation

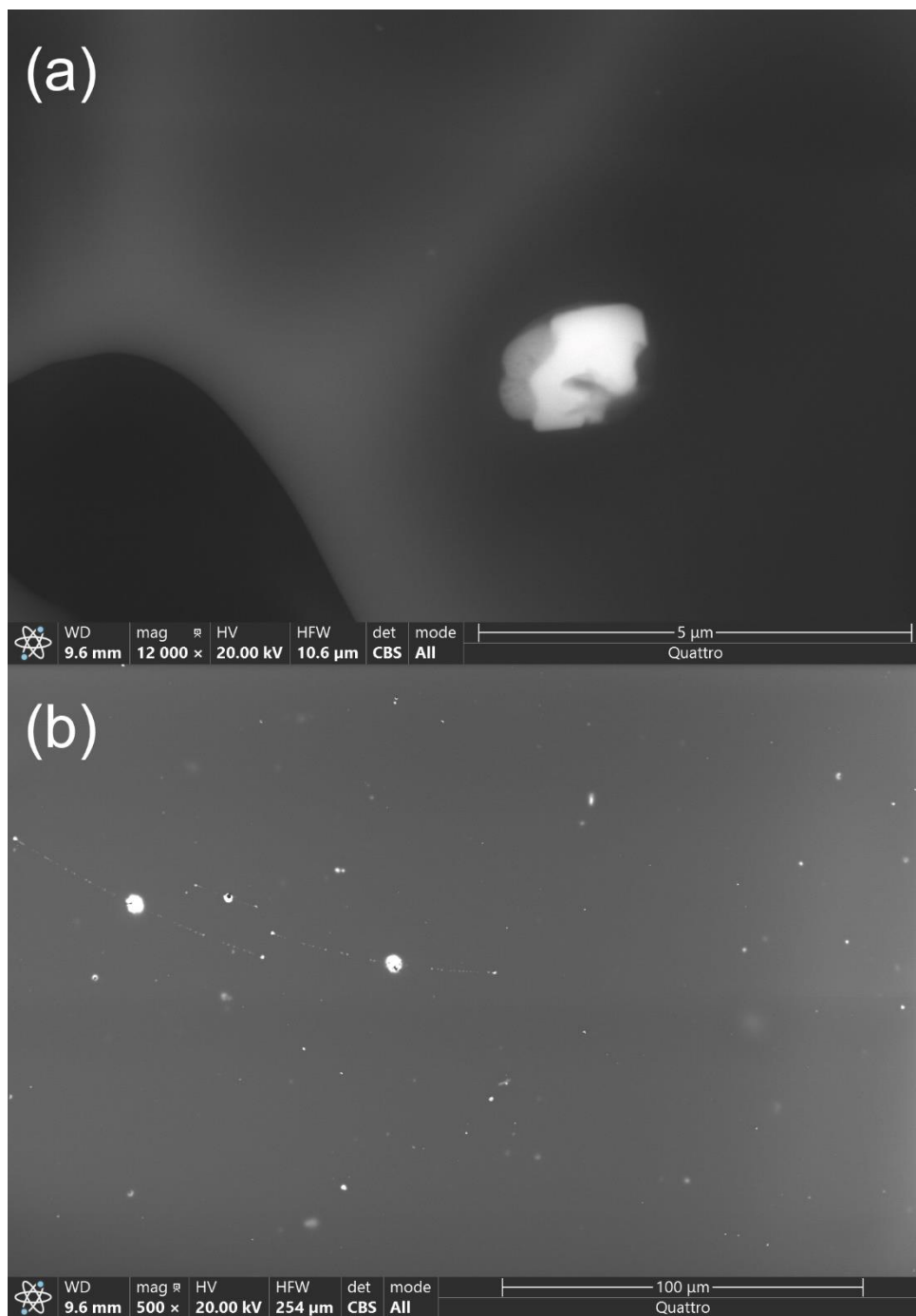


**Figure A27.** Backscattered ESEM image of (a)  $\text{Rb}_2\text{AgBr}_3$  particle aggregate dispersed in luminescent ink. Image (b) shows large differences in particles and aggregates formed in  $\text{Rb}_2\text{AgBr}_3$ .

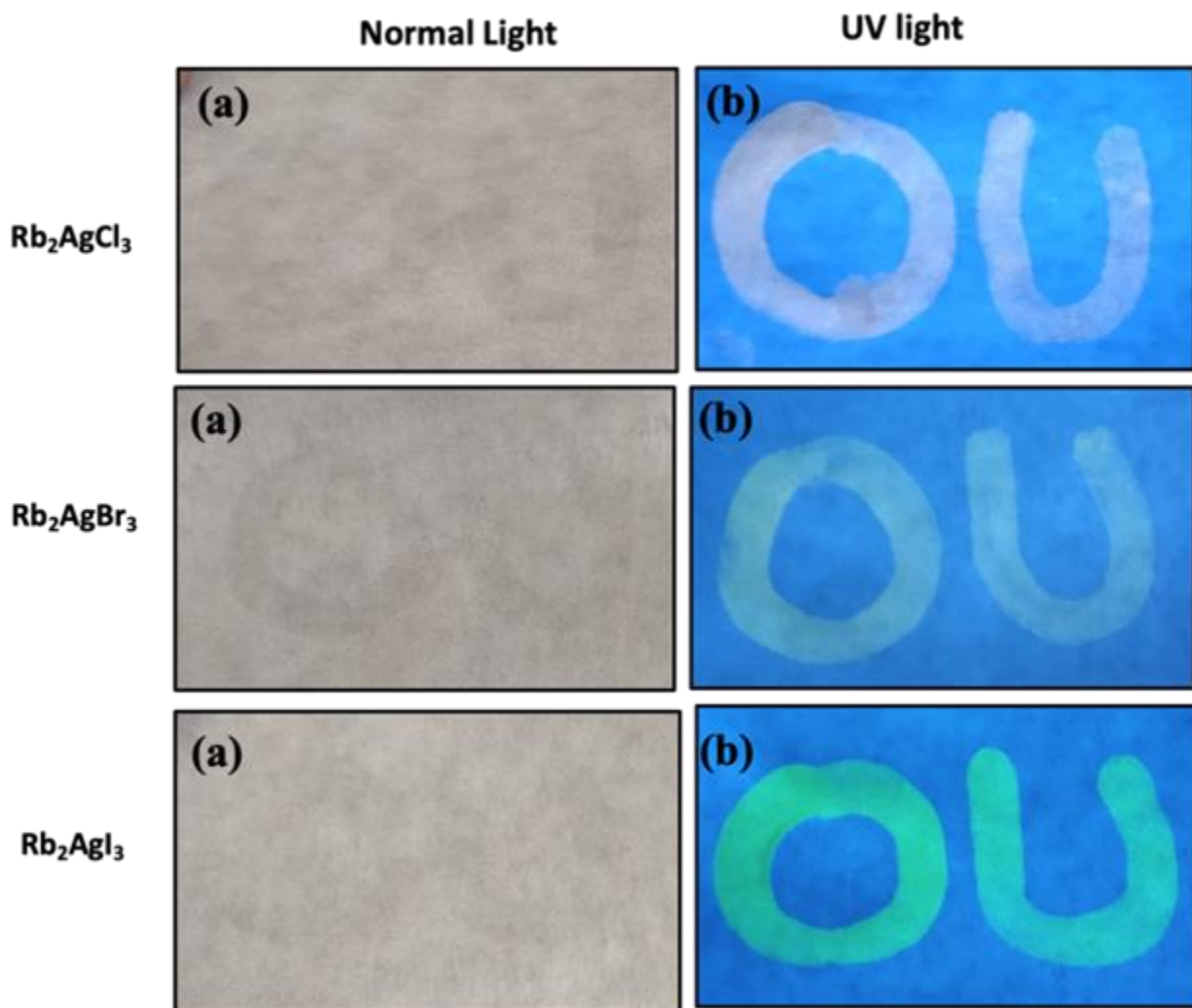


**Figure A28.** “OU” printed on white weighing papers using  $\text{Rb}_2\text{AgX}_3$  ( $\text{X} = \text{Cl}, \text{Br}, \text{I}$ ) based inks under normal light (left side) and UV light (right side, 365 nm).

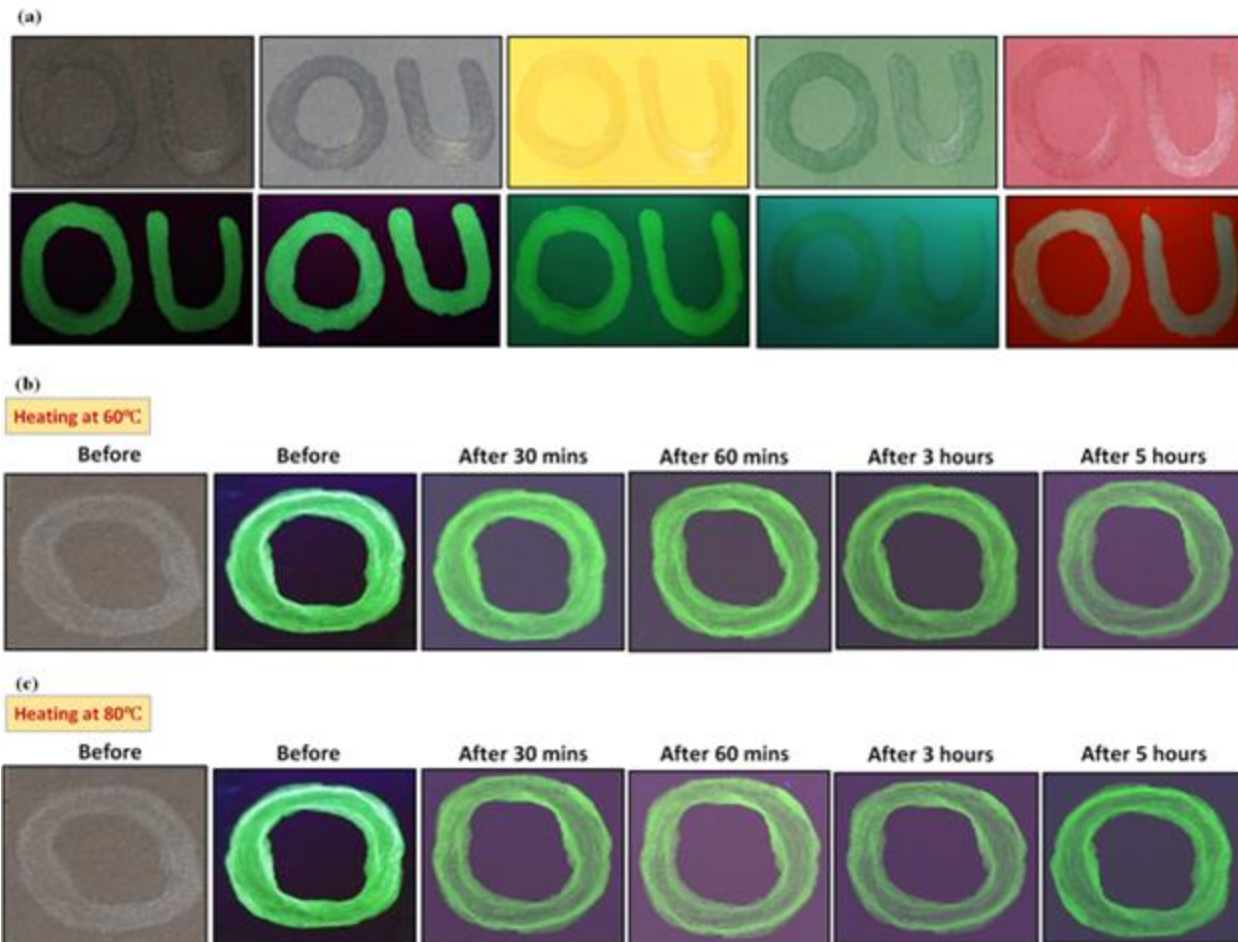


**Figure A29.** (a) Images of “OU” printed on different color backgrounds using a  $\text{Rb}_2\text{AgI}_3$  based luminescent ink under normal and UV light conditions (365 nm). (b) Images of the letter “O” printed on a black paper with a  $\text{Rb}_2\text{AgI}_3$  based luminescent ink under normal and UV light at (b) 60°C and (c) 80°C.



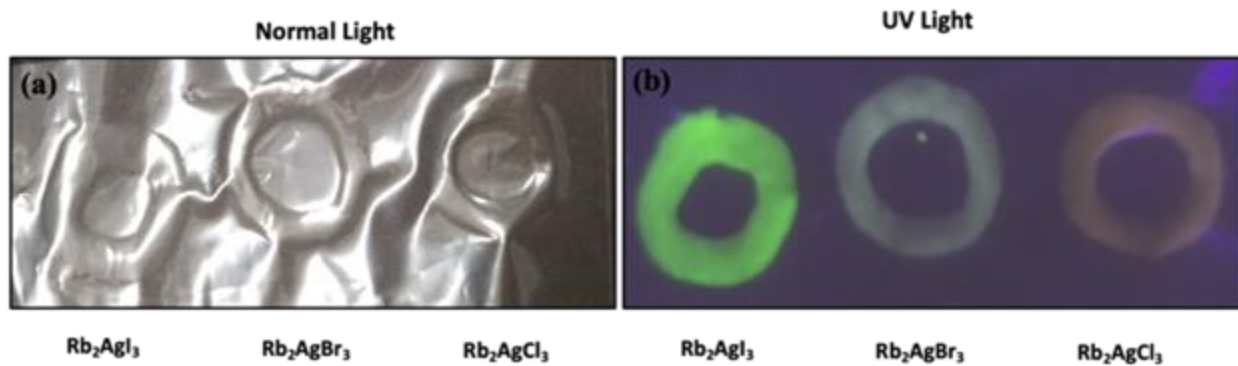


**Figure A30.** The letter “O” printed on a piece of transparent polyethylene bag with  $\text{Rb}_2\text{AgCl}_3$ ,  $\text{Rb}_2\text{AgBr}_3$  and  $\text{Rb}_2\text{AgI}_3$  based luminescent inks under normal and UV light conditions (365 nm).

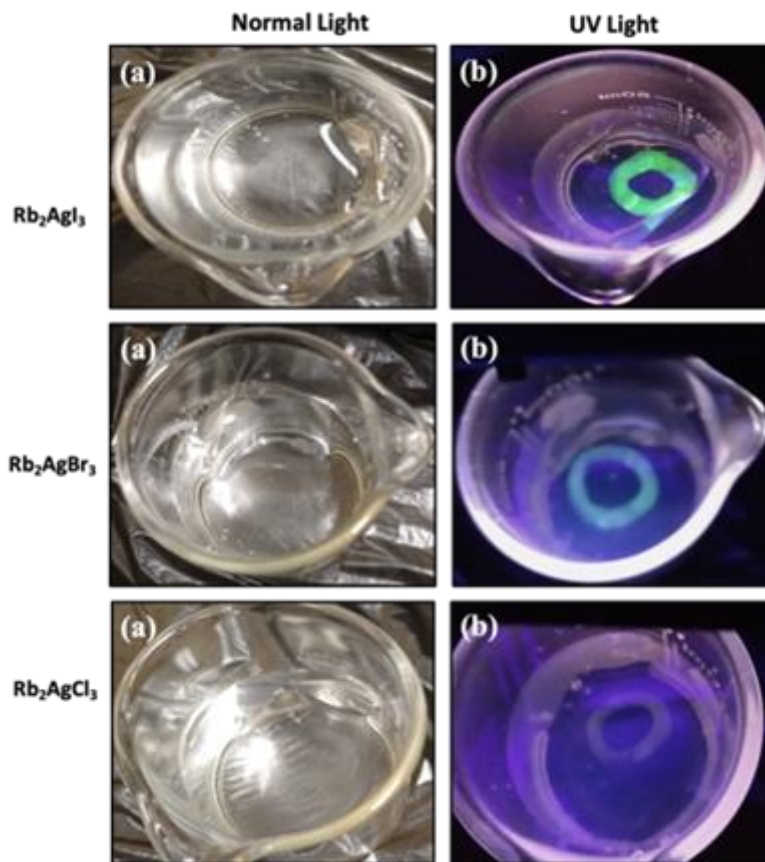


**Figure A31.** The letter “O” printed on a piece of transparent polyethylene bag with  $\text{Rb}_2\text{AgCl}_3$ ,  $\text{Rb}_2\text{AgBr}_3$  and  $\text{Rb}_2\text{AgI}_3$  based luminescent inks dispersed in water under normal and UV light conditions (365 nm).

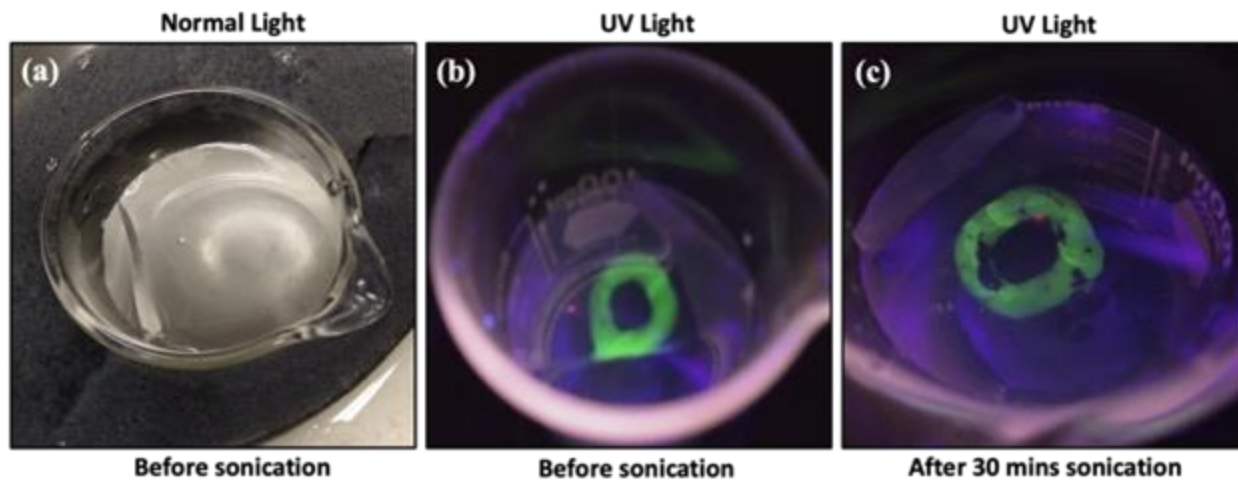


**Figure A32.** The letter “O” printed on a piece of transparent polyethylene bag with  $\text{Rb}_2\text{AgI}_3$  based luminescent inks dispersed in water before and after ultrasonication under normal light and UV light (365 nm).

**Table A5.** Selected single crystal data and structure refinement parameters for (NH<sub>4</sub>)<sub>2</sub>AgBr<sub>3</sub> and (NH<sub>4</sub>)<sub>2</sub>AgI<sub>3</sub>.

Formula	(NH <sub>4</sub> ) <sub>2</sub> AgBr <sub>3</sub>	(NH <sub>4</sub> ) <sub>2</sub> AgI <sub>3</sub>
Formula weight (g/mol)	383.68	524.65
Temperature (K)	295(2)	
Radiation, wavelength (Å)	Mo Kα, 0.71073	
Crystal system	Orthorhombic	
Space group	Pnma	
Z	4	
Unit cell parameters (Å)	$a = 9.5890(3)$	$a = 10.1968(16)$
	$b = 4.5949(2)$	$b = 4.8347(7)$
	$c = 18.5212(6)$	$c = 19.847(4)$
Volume (Å <sup>3</sup> )	816.05(5)	978.4(3)
Density ( $\rho_{\text{calc}}$ ) (g/cm <sup>3</sup> )	3.123	3.562
Absorption coefficient ( $\mu$ ) (mm <sup>-1</sup> )	17.060	11.445
$\theta_{\text{min}} - \theta_{\text{max}}$ (°)	3.93 – 32.50	2.864 – 30.603
Reflections collected	18128	18780
Independent reflections	1796	1514
$R^a$ indices ( $I > 2\sigma(I)$ )	$R_1 = 0.0275$	$R_1 = 0.0202$
	$wR_2 = 0.0507$	$wR_2 = 0.0389$
Goodness-of-fit on $F^2$	1.006	1.069
Largest diff. peak and hole (e <sup>-</sup> /Å <sup>3</sup> )	1.511 and -1.468	1.535 and -1.183

$${}^aR_1 = \sum ||F_0| - |F_c|| / \sum |F_0|; WR_2 = |\sum |w(F_0^2 - F_c^2)|^2 / \sum |wF_0^2|^{1/2},$$

where  $w = 1/|\sigma^2 F_0^2 + (AP)^2 + BP|$ , with  $P = (F_0^2 + 2F_c^2)/3$  and weight coefficients A and B

**Table A6.** Atomic coordinates and equivalent isotropic displacement parameters ( $U_{\text{eq}}^a$ ) for  $(\text{NH}_4)_2\text{AgBr}_3$  and  $(\text{NH}_4)_2\text{AgI}_3$ .

Atom	x	y	z	$U_{\text{eq}}, \text{\AA}^2$
<hr/>				
$(\text{NH}_4)_2\text{AgBr}_3$				
<hr/>				
N1	0.2438(4)	0.250000	0.5426(2)	0.0385(8)
N2	0.5731(4)	0.250000	0.2119(2)	0.0371(8)
Ag	0.37369(4)	0.750000	0.36795(2)	0.04454(11)
Br1	0.50543(5)	0.250000	0.40239(3)	0.03634(11)
Br2	0.11781(4)	0.750000	0.42793(2)	0.03461(11)
Br3	0.30945(5)	0.750000	0.22524(2)	0.03436(11)
$(\text{NH}_4)_2\text{AgI}_3$				
<hr/>				
N1	0.0743(4)	0.250000	0.7110(2)	0.0432(10)
N2	0.2519(5)	0.250000	0.4577(2)	0.0457(10)
Ag	0.36573(4)	0.750000	0.63506(2)	0.04790(11)
I1	0.50037(3)	0.250000	0.60023(2)	0.03764(9)
I2	0.30864(3)	0.750000	0.77602(2)	0.03687(9)
I3	0.11746(3)	0.750000	0.57080(2)	0.03735(9)

<sup>a</sup> $U_{\text{eq}}$  is defined as one-third of the trace of the orthogonalized  $U_{ij}$  tensor.

**Table A7.** A comparison of bond distances and angles within the 1D  $\infty[\text{AgX}_3]^{2-}$  chains in  $(\text{NH}_4)_2\text{AgBr}_3$  and  $(\text{NH}_4)_2\text{AgI}_3$ .

Atom pair	Distance (Å)	Label	Angle (°)
$(\text{NH}_4)_2\text{AgBr}_3$			
Ag – Br1 (×2)	2.6983(3)	Br1-Ag-Br2	109.207(14)
Ag – Br2	2.6934(3)	Br1-Ag-Br3	109.664(14)
Ag – Br3	2.7139(6)	Br2-Ag-Br3	101.239(19)
$(\text{NH}_4)_2\text{AgI}_3$			
Ag – I1 (×2)	2.8647(4)	I1-Ag-I2	109.505(12)
Ag – I2	2.8576(8)	I1-Ag-I3	108.630(14)
Ag – I3	2.8345(7)	I2-Ag-I3	104.982(19)

**Table A8.** Summary of time-resolved photoluminescence (TRPL) refinement parameters for  $(\text{NH}_4)_2\text{AgBr}_3$  and  $(\text{NH}_4)_2\text{AgI}_3$ .

<b>Parameter</b>	<b><math>(\text{NH}_4)_2\text{AgBr}_3</math></b>	<b><math>(\text{NH}_4)_2\text{AgI}_3</math></b>
<b>A<sub>1</sub> (Cnts)</b>	532.3859	62.81477
<b><math>\tau_1</math> (<math>\mu\text{s}</math>)</b>	0.521073 $\mu\text{s}$	5.994375 $\mu\text{s}$
<b>A<sub>2</sub> (Cnts)</b>	72.95995	434.3554
<b><math>\tau_2</math> (<math>\mu\text{s}</math>)</b>	4.455118 $\mu\text{s}$	0.5617258 $\mu\text{s}$
<b>Average lifetime</b>	0.995 $\mu\text{s}$	1.25 $\mu\text{s}$



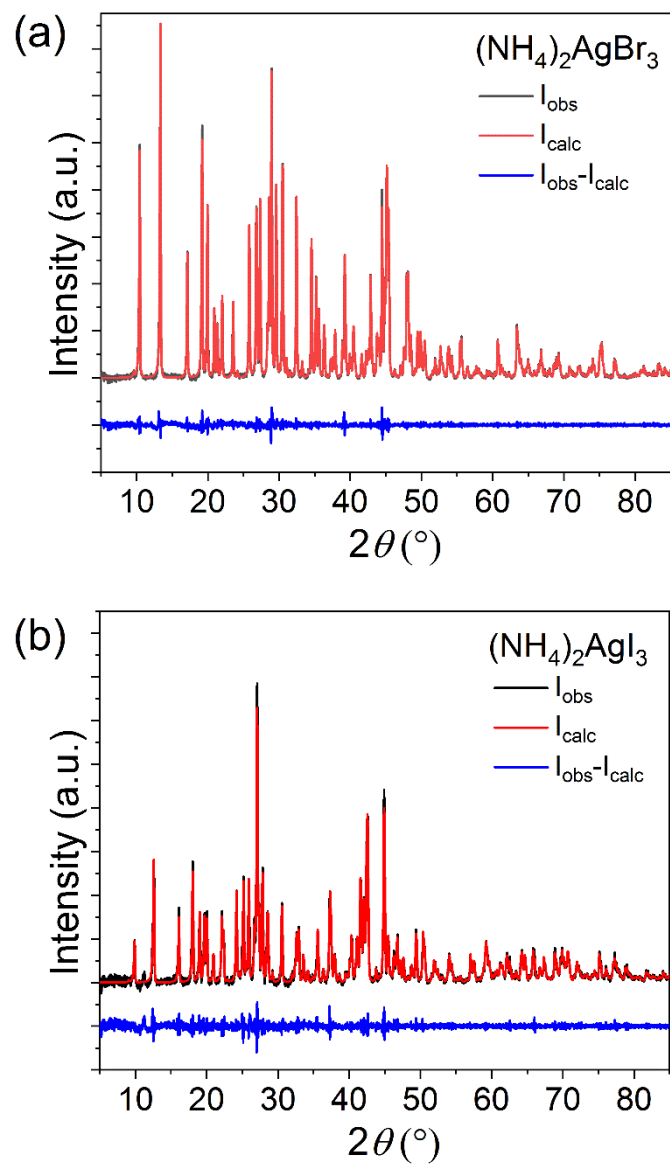


**Figure A33.** Room temperature PXRD patterns (black) fitted using the Pawley method (red) for (a)  $(\text{NH}_4)_2\text{AgBr}_3$  and (b)  $(\text{NH}_4)_2\text{AgI}_3$  prepared through hydrothermal synthesis.

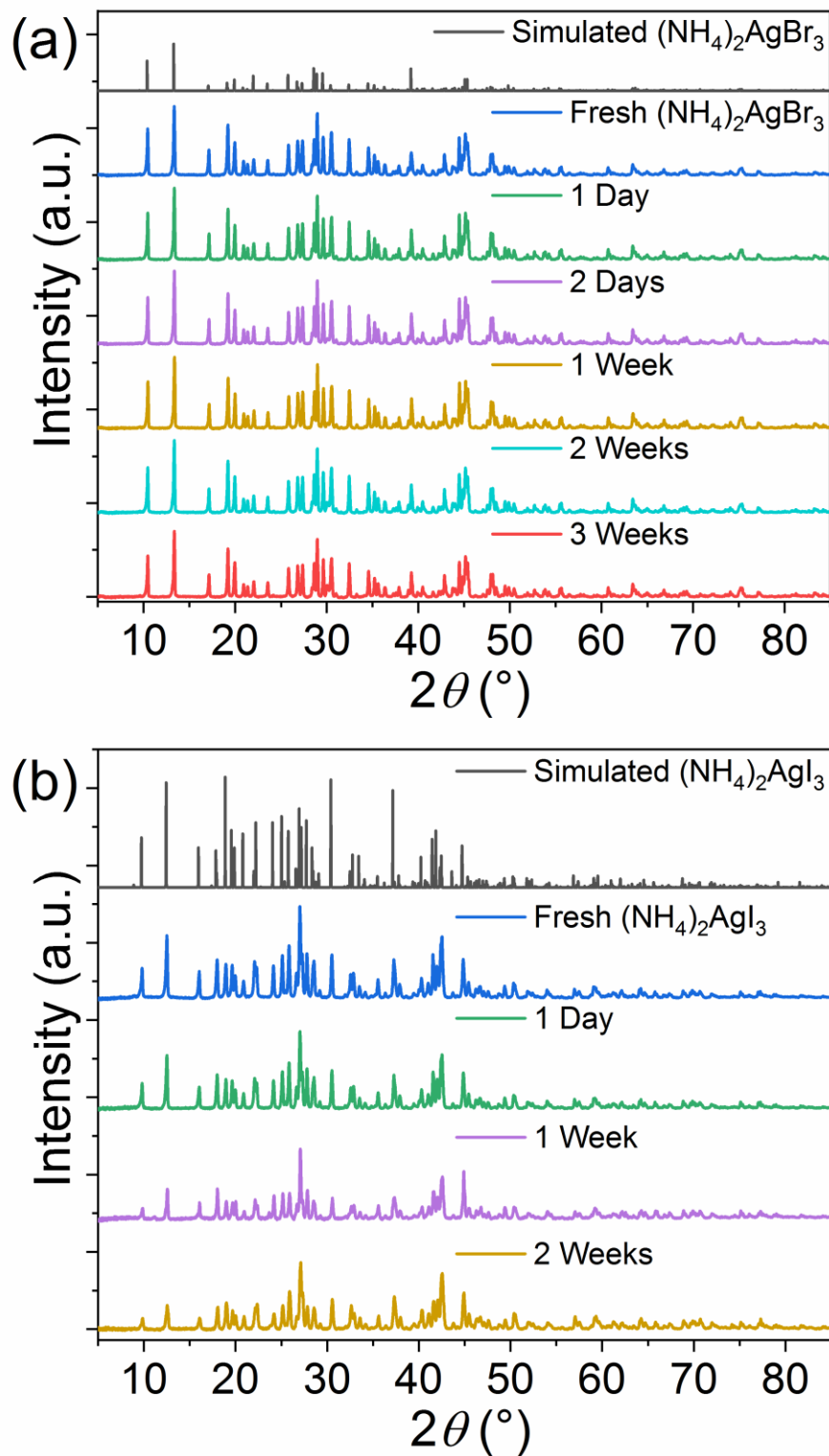


**Figure A34.** PXRD patterns of polycrystalline samples of (a)  $(\text{NH}_4)_2\text{AgBr}_3$  and (b)  $(\text{NH}_4)_2\text{AgI}_3$  left in ambient air for 3 weeks.

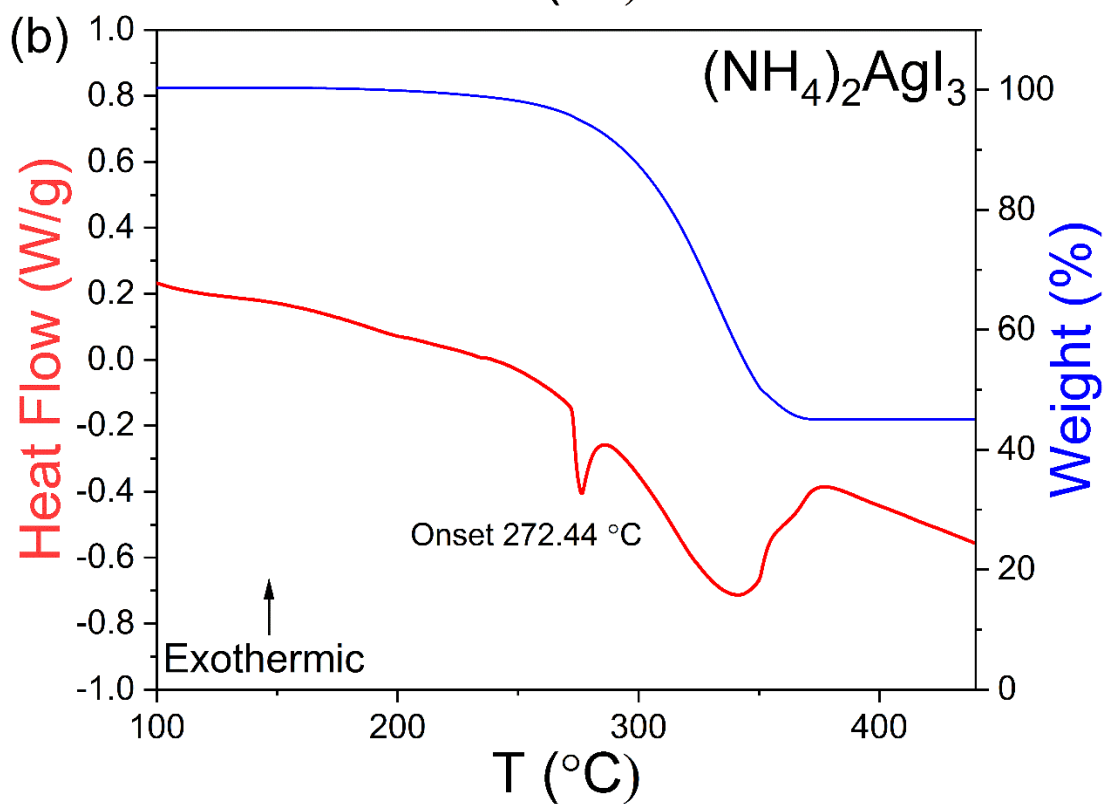
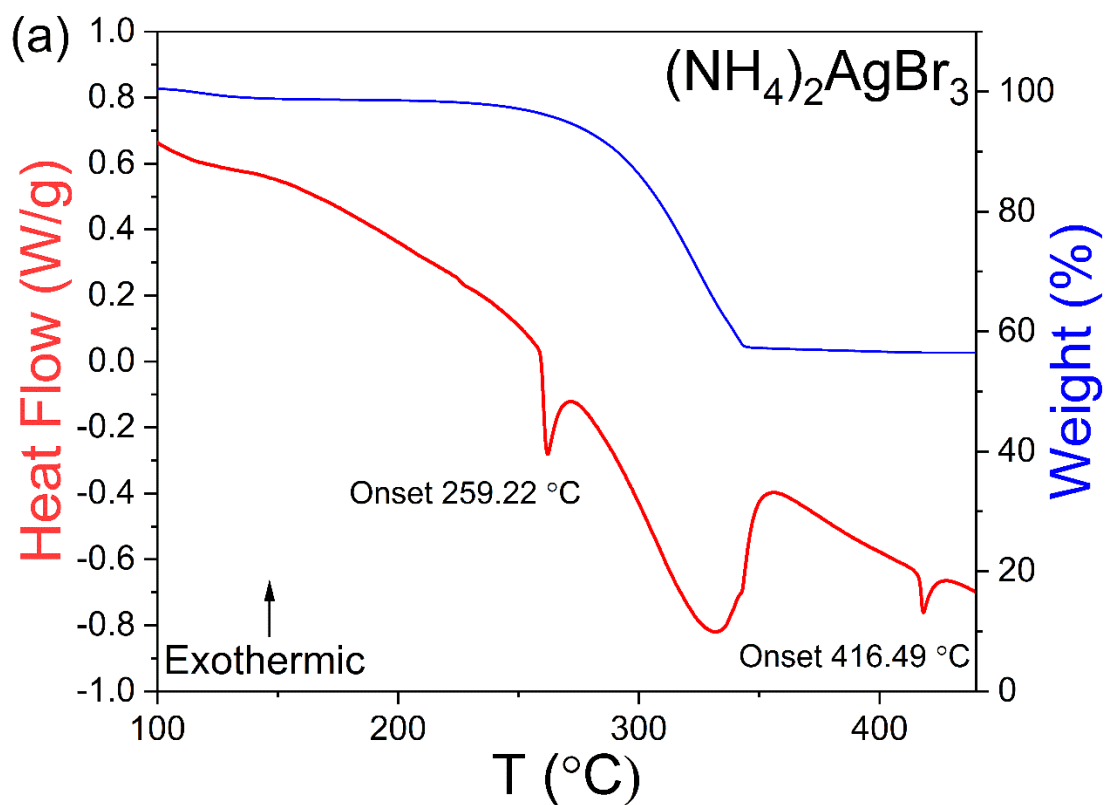


**Figure A35.** Differential scanning calorimetry (DSC, in red) and thermogravimetric analysis (TGA, in blue) plots for (a)  $(\text{NH}_4)_2\text{AgBr}_3$  and (b)  $(\text{NH}_4)_2\text{AgI}_3$ .

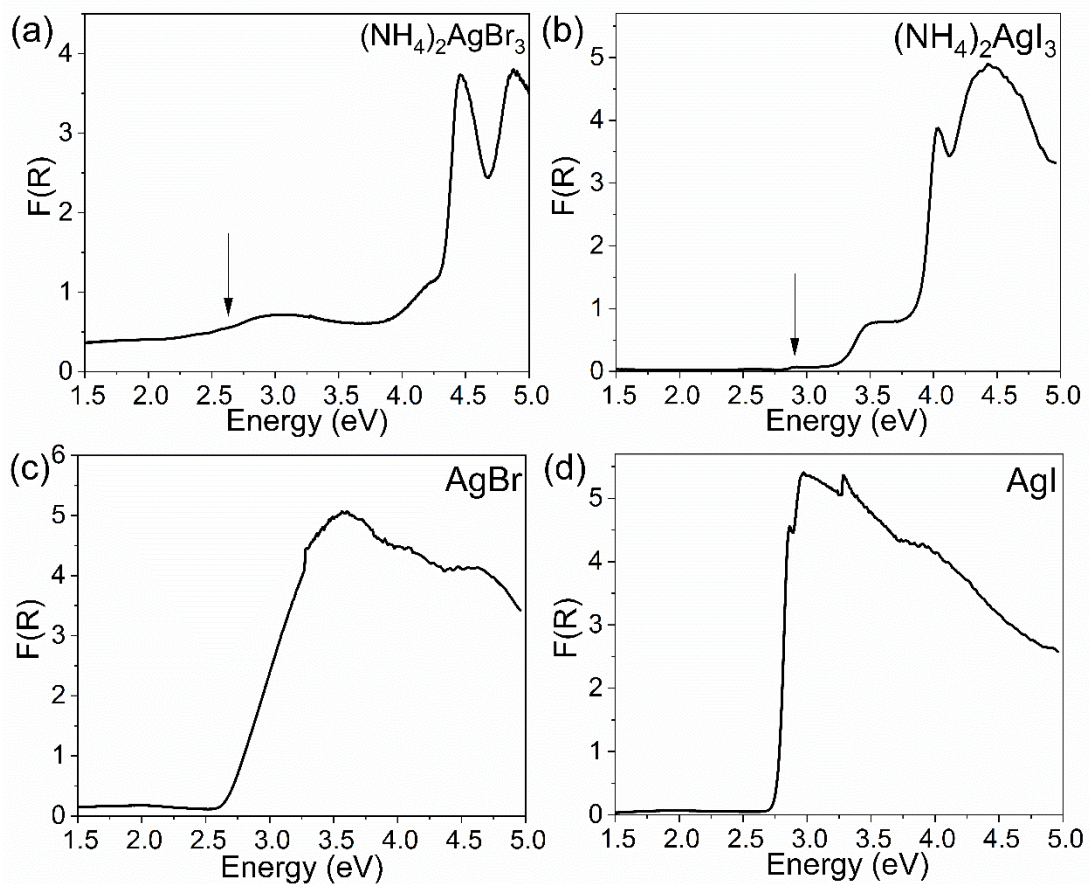


**Figure A36.** Kubelka-Munk transformed diffuse reflectance plot for (a)  $(\text{NH}_4)_2\text{AgBr}_3$ , (b)  $(\text{NH}_4)_2\text{AgI}_3$ , (c) AgBr, and (d) AgI. Arrows indicate minor impurities of AgX.

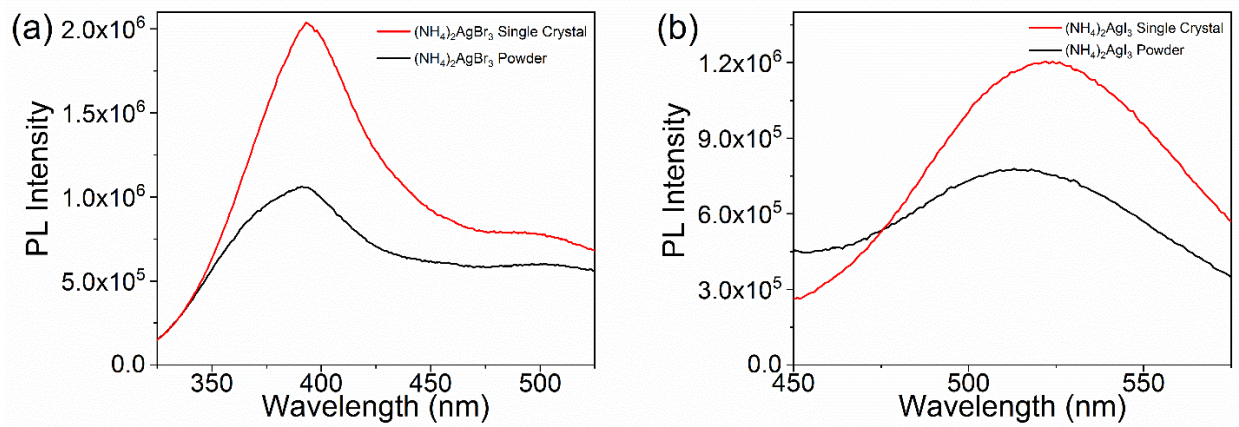


**Figure A37.** Comparisons of PL emission from single crystals and polycrystalline powders of (a)  $(\text{NH}_4)_2\text{AgBr}_3$  and (b)  $(\text{NH}_4)_2\text{AgI}_3$ .

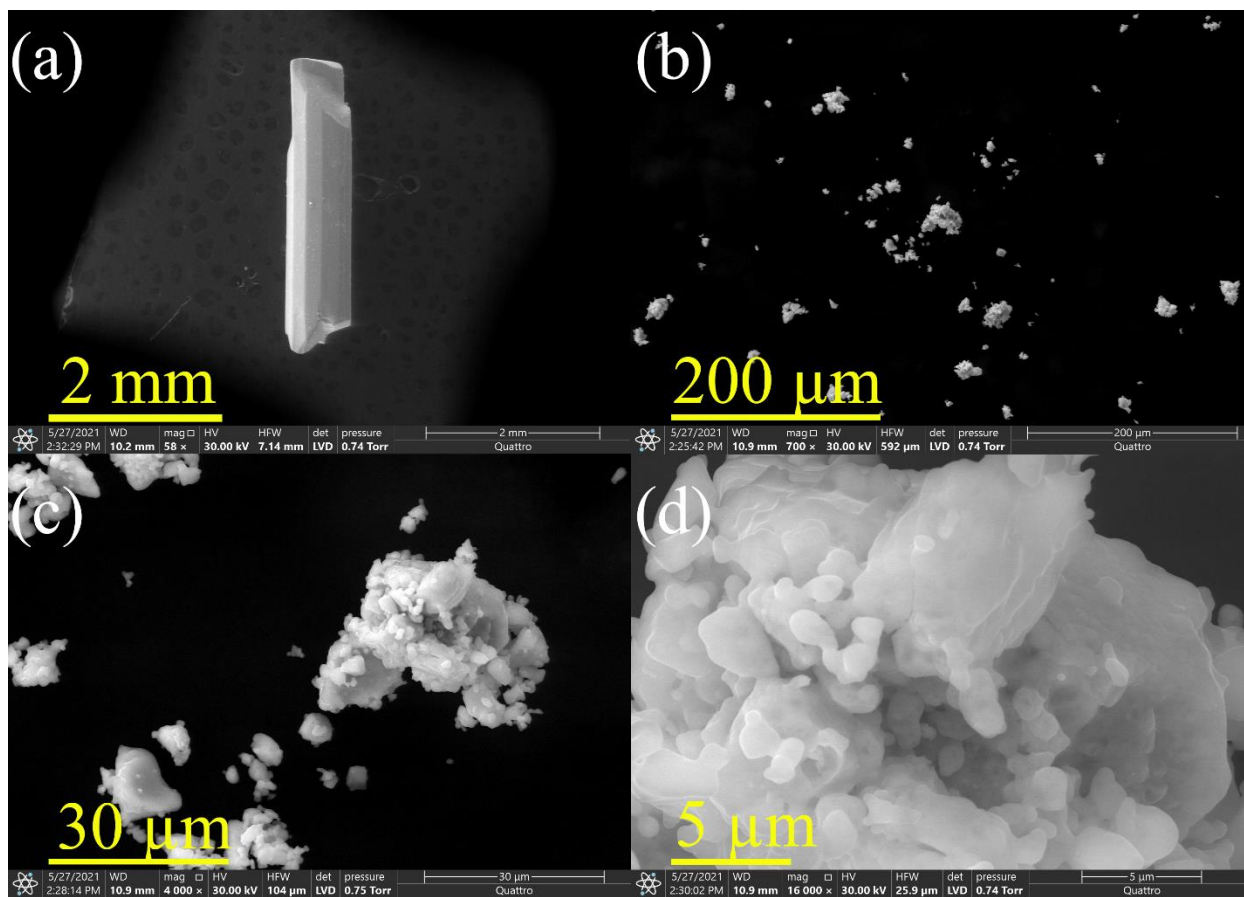


**Figure A38.** Environmental scanning electron microscope (ESEM) images of (a) a single crystal and (b-d) ground polycrystalline powders of  $(\text{NH}_4)_2\text{AgI}_3$ .

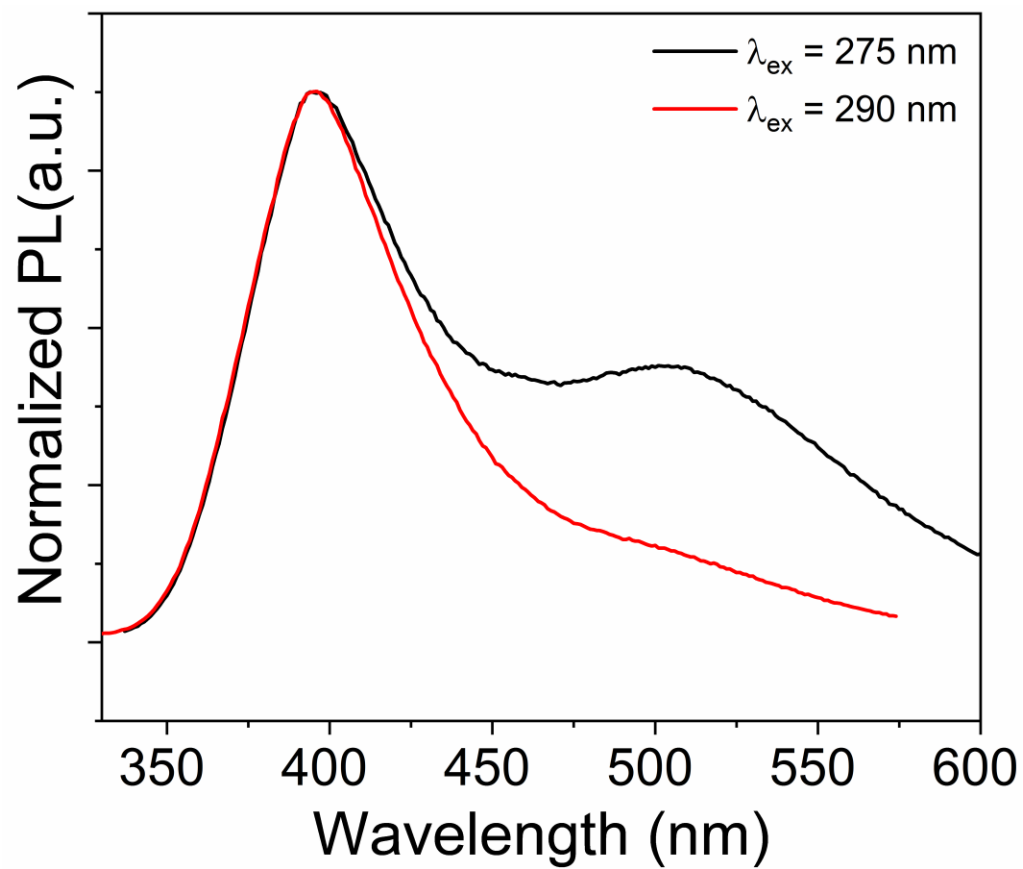


**Figure A39.** A comparison of PL emission using different excitation energies for  $(\text{NH}_4)_2\text{AgBr}_3$ .

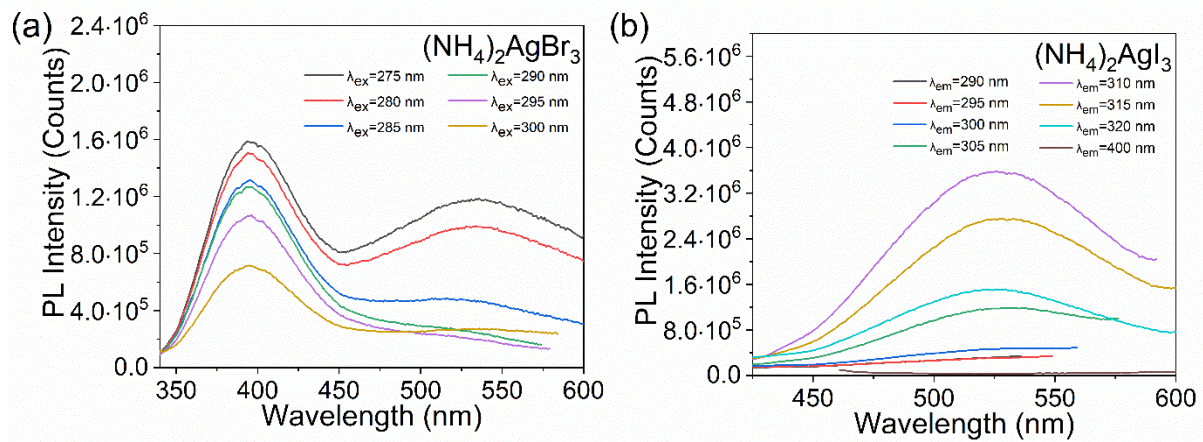


**Figure A40.** Excitation-dependent PL emission spectra for (a)  $(\text{NH}_4)_2\text{AgBr}_3$  and (b)  $(\text{NH}_4)_2\text{AgI}_3$ .



### A1.3 Chapter 4 Figures and Tables

**Table A9.** Atomic coordinates and equivalent isotropic displacement parameters ( $U_{\text{eq}}^a$ ) for RInBr<sub>4</sub>.

Atom	x	y	z	$U_{\text{eq}}, \text{\AA}^2$
In1	0.40750(2)	0.70882(2)	0.86534(2)	0.01787(4)
Br1	0.56693(2)	0.57044(2)	0.90193(2)	0.02594(5)
Br2	0.47657(2)	0.91075(2)	0.87790(2)	0.02811(5)
Br3	0.31904(2)	0.65708(2)	0.71516(2)	0.02801(5)
Br4	0.27309(2)	0.68829(2)	0.96278(2)	0.02515(5)
N1	0.68708(15)	0.77714(15)	0.66438(12)	0.0209(3)
C1	0.77834(18)	0.68544(18)	0.67806(13)	0.0240(4)
C2	0.8268(3)	0.6599(3)	0.60130(16)	0.017(2)
C3	0.9273(4)	0.7161(4)	0.5977(3)	0.0186(10)
C4	0.9800(3)	0.6980(3)	0.5297(2)	0.0193(7)
C5	0.9344(3)	0.6253(3)	0.46244(19)	0.0155(6)
C6	0.8350(3)	0.5689(3)	0.4662(2)	0.0182(7)
C7	0.7822(4)	0.5853(4)	0.5344(3)	0.0187(10)
C8	0.9928(3)	0.6104(3)	0.3912(2)	0.0182(7)
C9	0.9624(3)	0.5401(3)	0.3258(2)	0.0178(7)
C10	1.0311(2)	0.5357(2)	0.25718(15)	0.0348(6)
C11	1.1251(2)	0.5915(2)	0.24172(16)	0.0327(5)
C12	1.1688(2)	0.5663(2)	0.17002(17)	0.0302(5)
C13	1.1162(2)	0.4858(2)	0.11213(14)	0.0274(4)
C14	1.0223(2)	0.4303(2)	0.12655(17)	0.0313(5)

C15	0.9804(2)	0.4542(2)	0.19873(19)	0.0347(6)
C16	0.72553(19)	0.88376(18)	0.62731(16)	0.0262(4)
C17	0.6609(3)	0.8051(3)	0.74970(19)	0.0412(6)
C18	0.58236(19)	0.7348(2)	0.60610(19)	0.0319(5)

<sup>a</sup> $U_{eq}$  is defined as one third of the trace of the orthogonalized  $U_{ij}$  tensor.

**Table A10.** A comparison of bond distances and angles within the OD  $\infty^1$ [InBr<sub>4</sub>]<sup>-</sup>.

Atom pair	Distance (Å)	Label	Angle (°)
In – Br1	2.5015(2)	Br2-In-Br4	107.100(9)
In – Br2	2.4949(3)	Br2-In-Br3	112.160(10)
In – Br3	2.5006(3)	Br4-In-Br3	111.706(10)
In – Br4	2.4954(2)	Br2-In-Br1	110.899(9)
		Br4-In-Br1	111.696(9)
		Br3-In-Br1	103.360(9)

**Table A11.** Summary of time-resolved photoluminescence (TRPL) refinement parameters for RInBr<sub>4</sub>.

<b>Parameter</b>	<b>Value</b>
<b>A<sub>1</sub> (Cnts)</b>	4110.3
<b>τ<sub>1</sub> (μs)</b>	0.178149 μs
<b>A<sub>2</sub> (Cnts)</b>	14051
<b>τ<sub>2</sub> (μs)</b>	0.040379 μs
<b>A<sub>3</sub> (Cnts)</b>	3.774
<b>τ<sub>3</sub> (μs)</b>	3.783 μs
<b>Average lifetime (intensity weighted)</b>	0.077286 μs
<b>Average lifetime (amplitude weighted)</b>	0.070788 μs

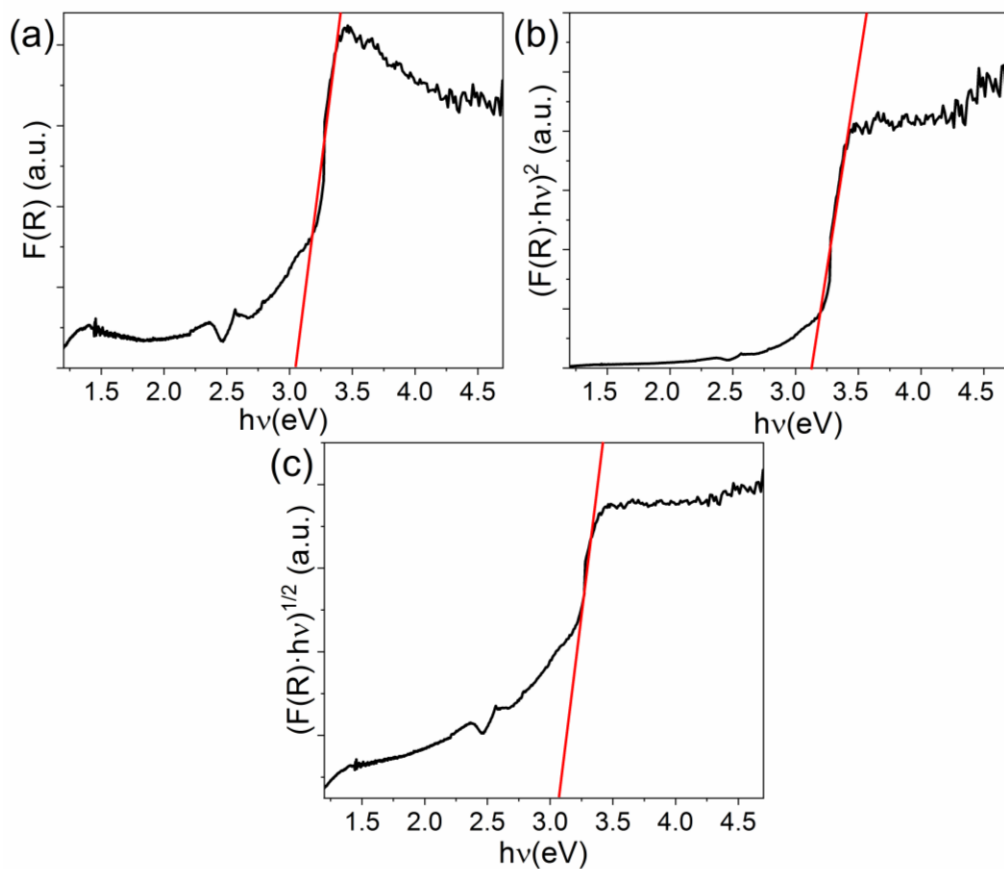


**Figure A41.** (a) Diffuse reflectance data converted to pseudo – absorbance via the Kubelka-Munk ( $F(R)$ ) function and plotted against photon energy. (b) Tauc plots with a direct band gap and (c) an indirect band gap fits.

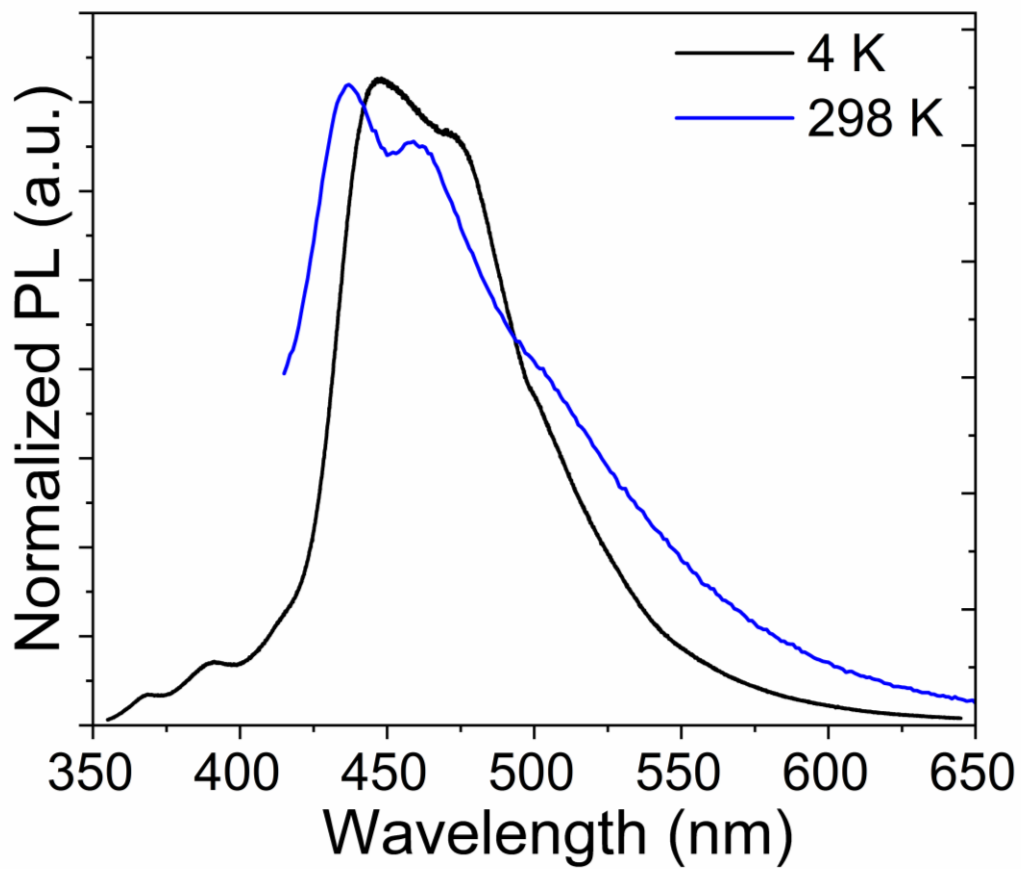


**Figure A42.** Low temperature PL data collected under an excitation by 325 nm laser at 4 K as compared to room temperature emission collected under an excitation by Xenon lamp at  $\text{PLE}_{\text{max}}$ .

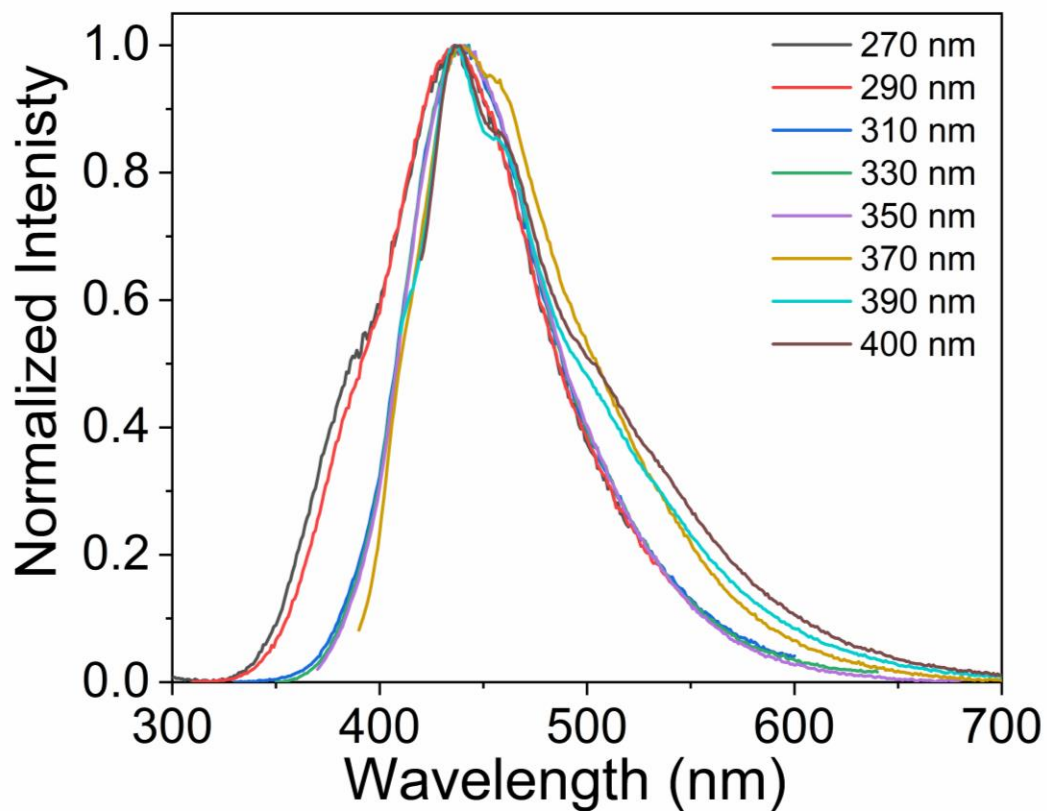


**Figure A43.** Normalized excitation wavelength-dependent photoluminescence spectra for RInBr<sub>4</sub>.

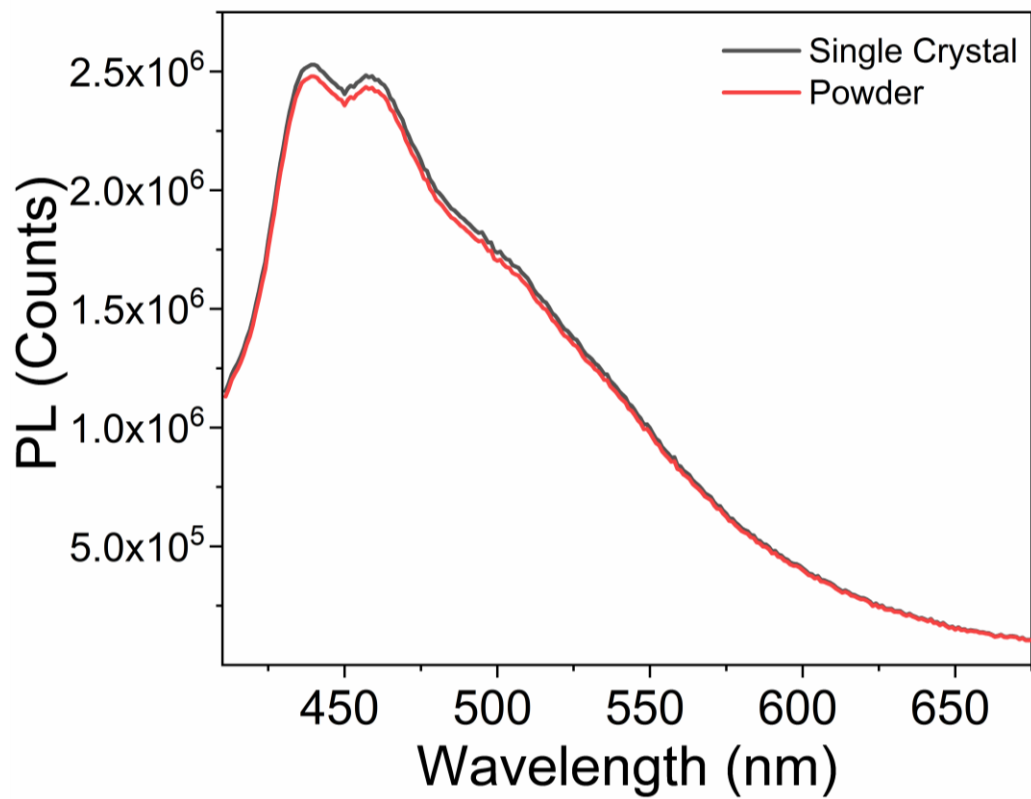


**Figure A44.** A comparison of photoluminescence emission spectra of single crystal and powder samples of RInBr<sub>4</sub>.



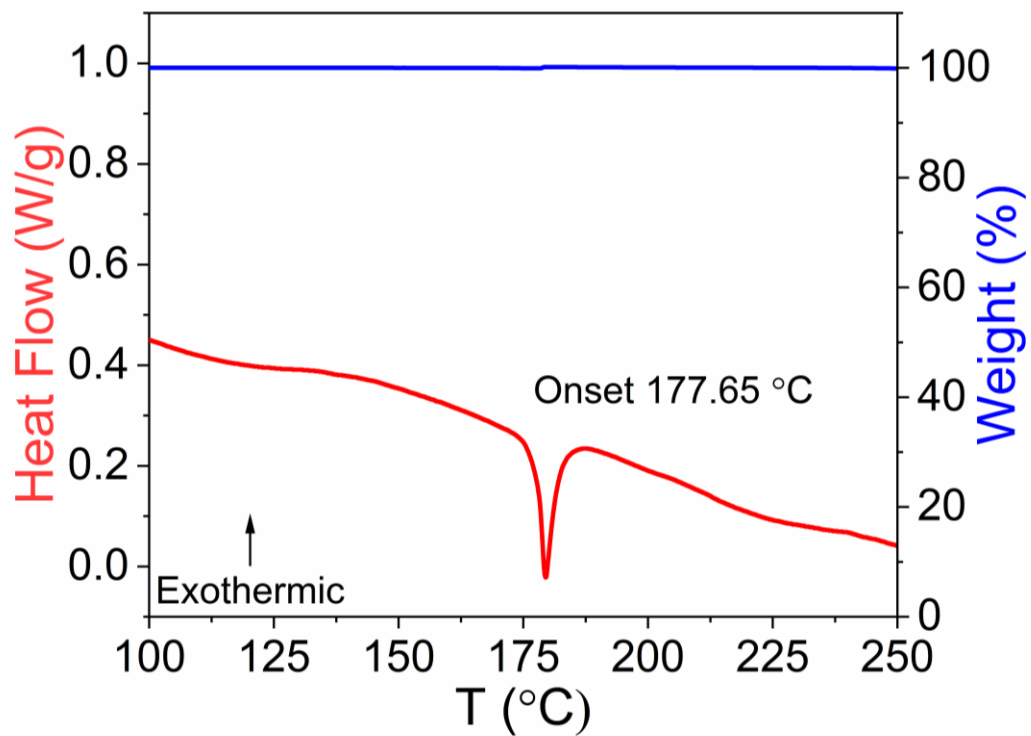


**Figure A45.** Thermogravimetric analysis (TGA, blue) and differential scanning calorimetry (DSC, red) for RInBr<sub>4</sub>.

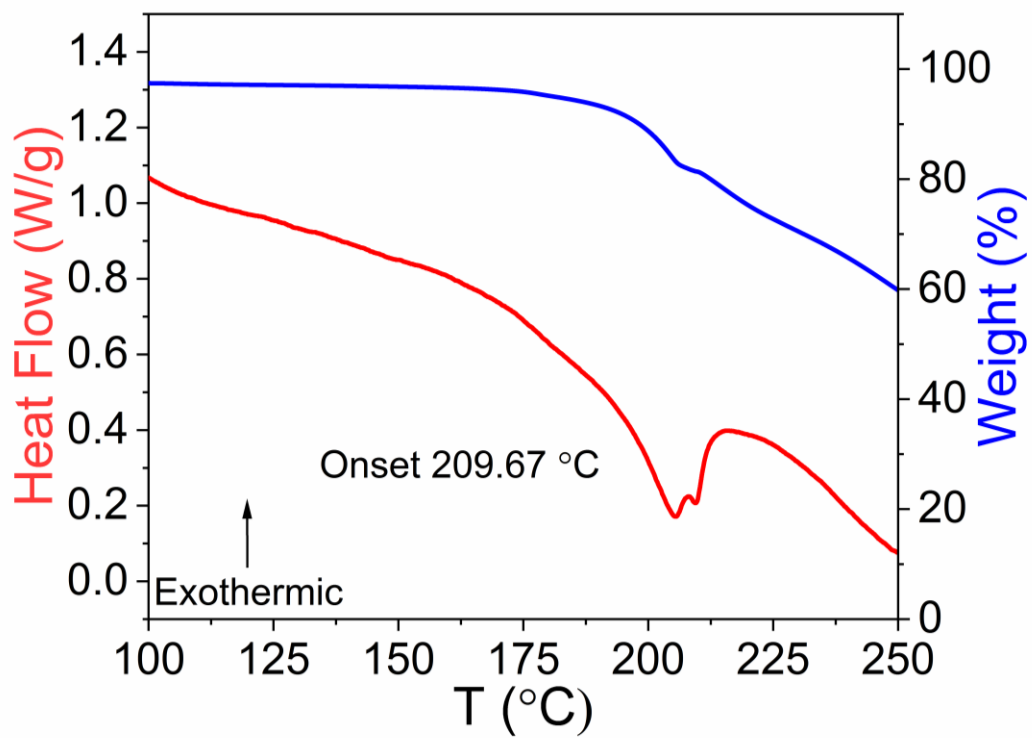


**Figure A46.** Thermogravimetric analysis (TGA, blue) and differential scanning calorimetry (DSC, red) for RBr.

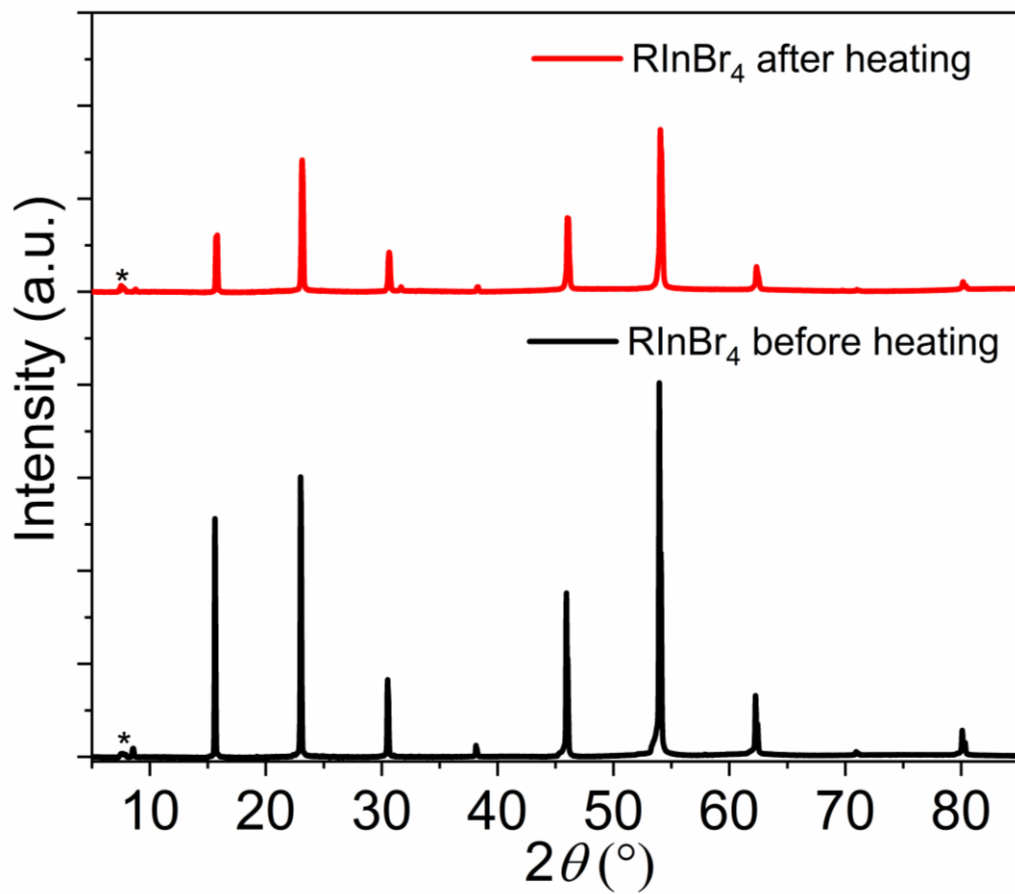


**Figure A47.** PXRd patterns of a crystal of RInBr<sub>4</sub> before and after heating at 100°C for 1 week. The asterisk under 10° represent InBr<sub>3</sub> impurities.

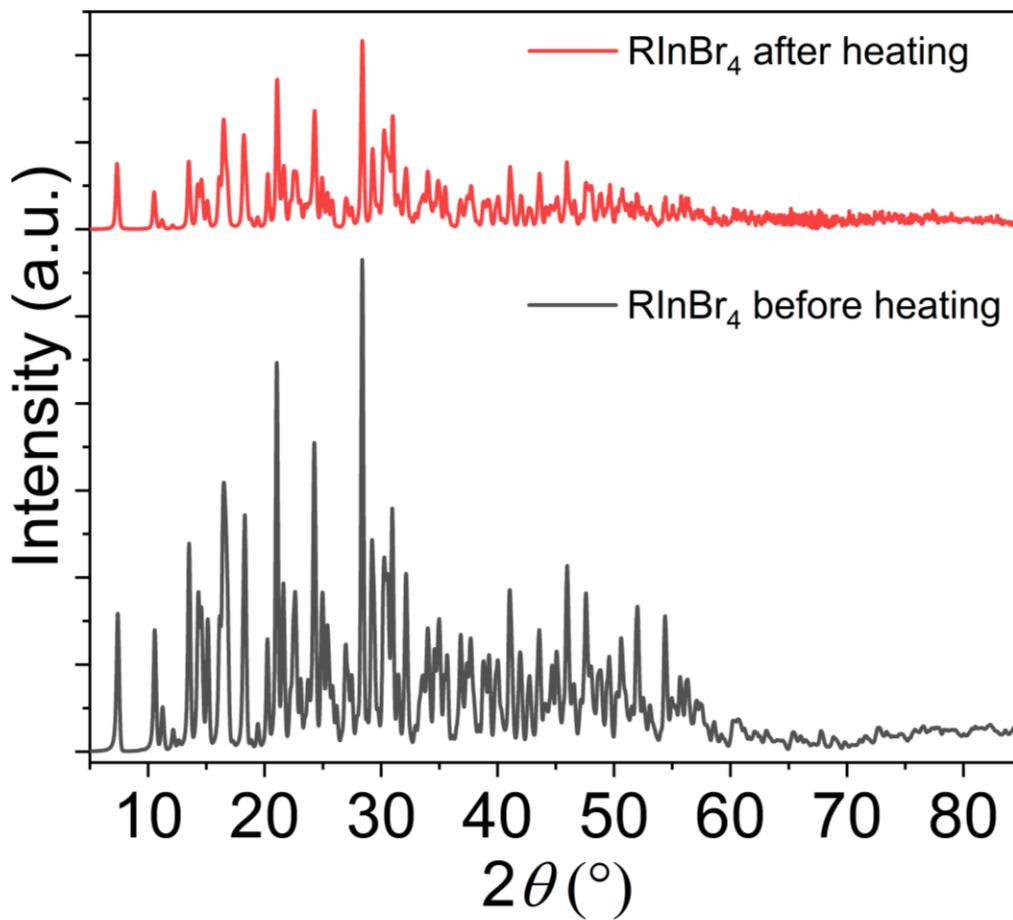


**Figure A48.** PXRD patterns of a powdered sample of  $\text{RInBr}_4$  before and after heating at 100 °C for 1 week. Although emergence of impurity peaks is not observed, a significant drop in intensity is noticeable.

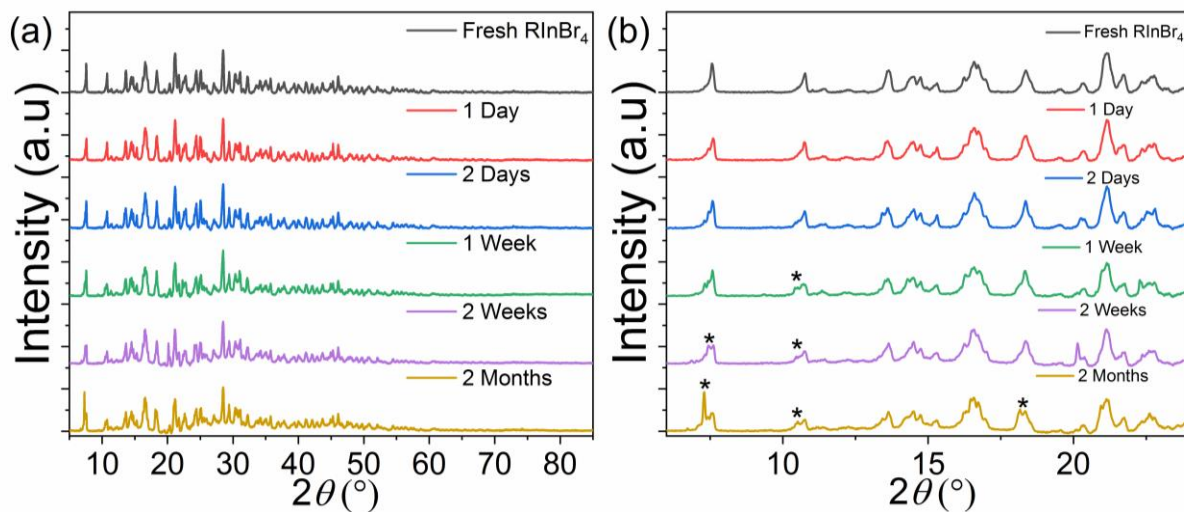


**Figure A49.** (a) PXRD patterns of a polycrystalline sample of RInBr<sub>4</sub> left in ambient air for 2 months. (b) A close-up view of the  $6 - 24^\circ$  region shows the emergence of InBr<sub>3</sub> impurity (marked with a black asterisk) over time.



**Figure A50.** A solution-grown crystal of RInBr<sub>4</sub>.

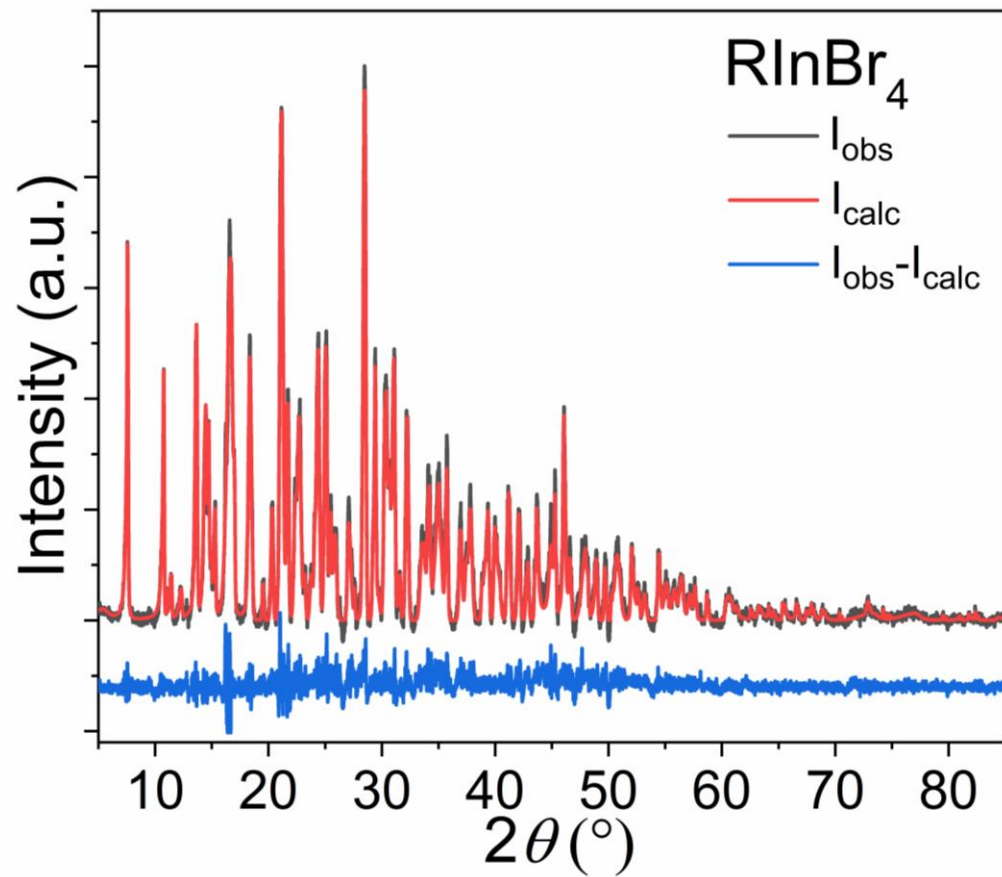


**Figure A51.** Room temperature PXRD pattern (black) for  $\text{RInBr}_4$  fitted using the decomposition method (red). The difference plot is shown in blue.